# PORTUGALIAE PHYSICA

**VOLUME 19**
FASCÍCULO 3-4
**1988**

SOCIEDADE PORTUGUESA DE FÍSICA

# PORTUGALIAE PHYSICA

Fundada em 1943 por A. Cyrillo Soares, M. Telles Antunes, A. Marques da Silva e M. Valadares

Publicação subsidiada pelo INSTITUTO NACIONAL DE INVESTIGAÇÃO CIENTÍFICA

ISSN 0048 - 4903

# PORTUGALIAE PHYSICA

VOLUME 19

FASCÍCULO 3-4

1988

# PROCEEDINGS
# OF
# SAGAMORE IX

## Conference on Charge, Spin and Momentum Densities

Luso (Coimbra) - Portugal

26 June - 2 July 1988

## Part II — Poster Communications
## Part III — Workshop on Density Matrices (Satellite Meeting)

*Guest Editors* *: Luís Alte da Veiga
M. Margarida R. R. Costa
Maria José B. M. de Almeida

* Appointed in December 1989

# Part II – Poster Communications

# X-RAY DIFFRACTION, ELECTRON DENSITIES AND CHEMICAL BONDING

W. H. E. SCHWARZ and L. MENSCHING
Theoretical Chemistry Group, The University, D5900 Siegen, West Germany

K. RUEDENBERG, R. JACOBSON and L. L. MILLER
Ames Laboratory USDOE and Department of Chemistry,
Iowa State University, Ames, IA50010, USA

*ABSTRACT* — The «Chemical Deformation Density» (CDD) is defined as the minimal electron density difference between the molecule or crystal, and the optimally and uniquely positioned *and* oriented ground state atoms. The CDD offers a coherent picture of bond and lone pair deformations. Fluorine, oxygen, and nitrogen compounds do no longer exhibit exceptional features. Even carbon ground states may be strongly quadrupolar at asymmetric sites. Intermolecular interactions may strongly influence the conventional difference densities by changing the orientations of the atomic quadrupoles without changing the genuine CDD significantly.

## 1 — INTRODUCTION

Molecular electron densities are often examined in the form of difference densities (DDs) [1]. Conventionally they are defined with respect to the superimposed densities of the *sperically averaged* atoms. These DDs are denoted here as «*Total Difference Densities*» (TDDs). They are particularly useful for the discussion of the electrostatic fields created by the molecules in the space around them. However, only atoms with spatially nondegenerate ground states are of necessity spherical. Most atoms with open p and d shells are not, and consequently their TDDs are often dominated by *quadrupolar* density distributions [2], which are the result of the *orientation of the undeformed atoms*. These orientational effects can be quite large and hide the genuine *atomic deformations* [3], which are associated with bond formation. Because of this superposition of atomic orientation as well as chemical deformation effects, it is intrinsically quite difficult to interpret TDDs and to compare them for different systems. Therefore, we shall *not* use the term «deformation densities» for them.

As a more appropriate quantity for the elucidation of the nature of chemical bonds, the «*Chemical Deformation Density*» (CDD) is defined here with respect to the reference density of a promolecule whose *unperturbed* atoms, in addition to

*Portgal. Phys.* — Vol. 19, fasc. 3-4, pp. 185-189, 1988

being *positioned* at their correct places in the molecule, also have their multipoles appropriately *oriented* [4]. The orientation is accomplished by chosing the atomic reference densities so as to minimize the norm of the DD. The approach has been applied to theoretical densities of a series of small molecules [5] in section 2, and to experimental X-ray scattering data of a series of organic molecular crystals [6], see section 3.

## 2 — THEORETICAL DENSITIES OF HF AND $CH_2$

The TDD of the HF molecule (Fig. 1a) is dominated by a strong quadrupolar distribution around the F nucleus. It shows that the $^2P$ ground state of the F atom in HF should not be spherically averaged to $(1/3\ {}^2P_x + 1/3\ {}^2P_y + 1/3\ {}^2P_z)$. Instead, the referred to orientation procedure yields the non-spherical average $(0.21\ {}^2P_x + 0.21\ {}^2P_y + 0.58\ {}^2P_z)$, corresponding to the orbital population $p_x^{1.79}\ p_y^{1.79}\ p_z^{1.42}$ as most appropriate for the CDD construction. It indicates a superposition of about 0.4 oriented F ($^2P_z$) and 0.6 spherical F, corresponding to a mixture of covalent $Fp\sigma - Hs$ and ionic $F^- - H^+$ bonding, respectively. The Mulliken charge of −0.53 on F is in reasonable agreement with this.

The CDD of HF in Fig. 1b shows three characteristic features:

1. the electron charge deficit «*behind*» the proton indicates the positive partial charge attributable to H in HF;

2. the «bond charge» with maximum CDD value of 0.6 e/Å$^3$ is typical for σ-covalencies;

3. the *dipolar* density shift around the F nucleus describes the lone pair formation on F.

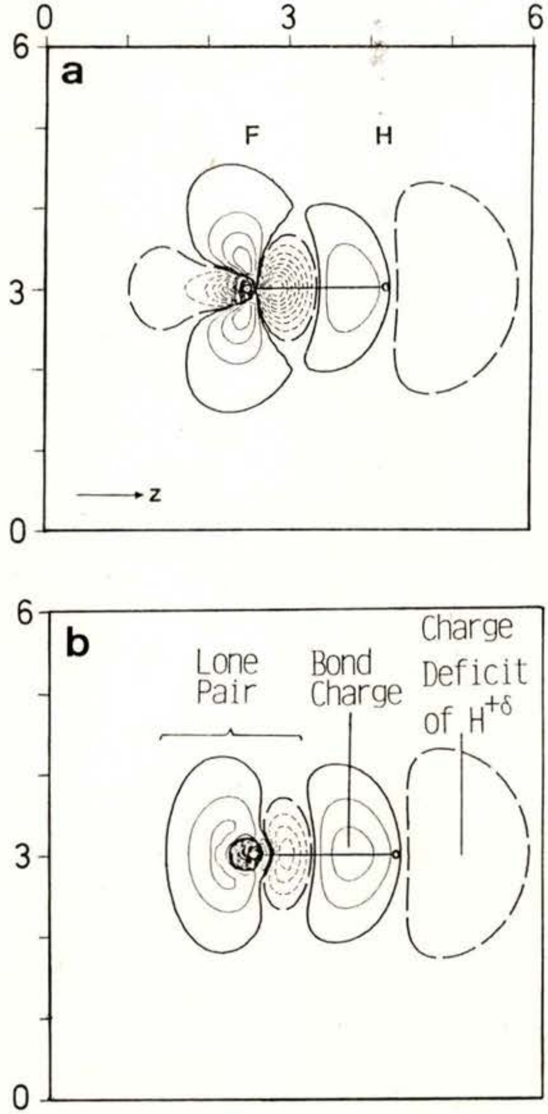

Fig. 1 — SCF difference density maps of HF [5]. *a*) TDD, molecular density minus sphericalized atoms. *b*) CDD, molecular density minus optimally oriented atomic ground states. Length scale in $a_0$. Density contour lines: 0.01, 0.04, 0.08, 0.12,... e/$a_0^3$; broken lines: negative values.

Features 2, and especially 3, are covered up in the TDD by the large fluorine quadrupole. The norm of the TDD (0.026 a. u.) is nearly twice as large as the value for the CDD (0.015 a. u.).

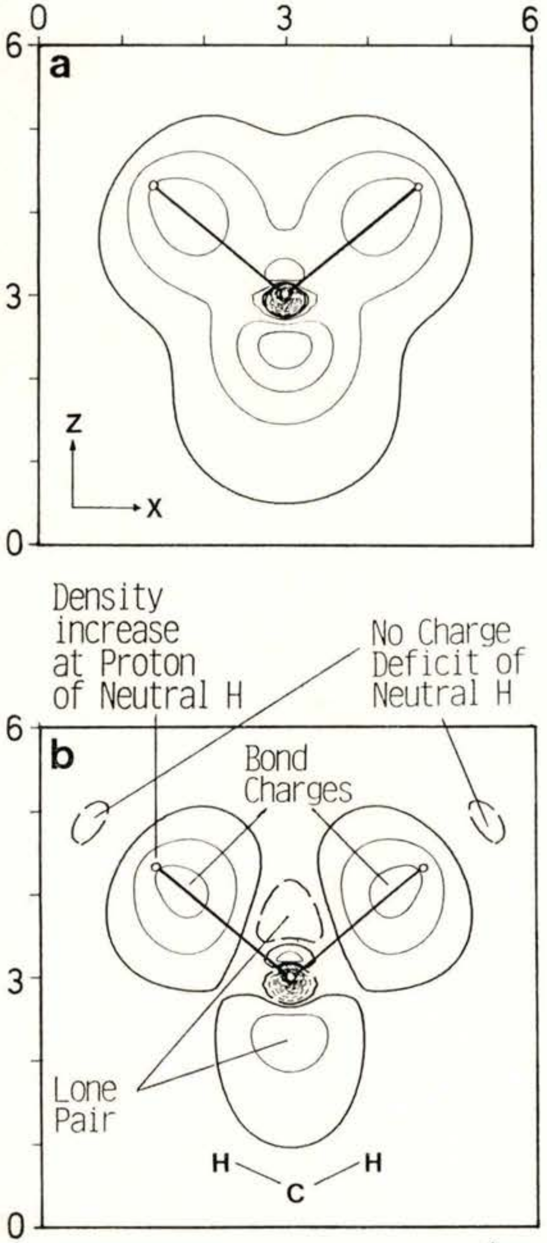

Fig. 2 — SCF difference density maps of $^1CH_2$. *a*) TDD. *b*) CDD. See caption of Fig. 1.

While the open shell $p^2$ $^3P$ ground state of carbon atoms is evenly populated in aliphatic compounds, this is not always so for asymmetrically coordinated C-atoms. The simplest example, singlet methylen $^1CH_2$, is shown in Fig. 2. The large positive TDD values in the whole molecular plane demonstrate that the $Cp_x$ and $Cp_z$ AOs have a higher population than according to the spherical average of the $^3P$ state. Optimal orientation reduces the norm from 0.055 a. u. for the TDD down to 0.021 a. u. for the CDD, corresponding to a $(0.06\ ^3P_x + 0.94\ ^3P_y)$ reference density on C with orbital population $p_x^{0.94}\ p_y^{0.06}\ p_z^{1.00}$. The CDD (Fig. 2b) exhibits various density features, which are covered up in the TDD (Fig. 2a). Further examples are given in Refs. [5, 8].

## 3 — EXPERIMENTAL DENSITIES OF 9-t-BUTYL-ANTHRACENE AND 1,2,3-TRIAZINE

Miller et al. [6] have analyzed the X-ray scattering data of Angermund et al. [7] on butyl-anthracene (BA) and triazine. The predominantly positive TDD of BA (Fig. 3a) again indicates uneven population of the C2p-shells. The optimized populations of the p-orbitals are rather similar for all ring-C-atoms: $p_\pi^{0.1}\ p_{rad}^{1.0}\ p_{tang}^{0.9}$. The CDD bond charges in Fig. 3b (maxima of $0.50 \pm 0.05\ e/Å^3$) scatter less than the TDD ones (maxima of $0.66 \pm 0.12\ e/Å^3$).

The low $p_\pi$-population deserves an explanation. Since the X-ray scattering from the 2s density is nearly identical to that from the average 2p density, experimental density determinations from X-rays cannot detect $2s \rightarrow 2p$ promotion. The $C2s^2$ density of the promolecule simulates some of the $C2p_x\,2p_y\,2p_z$ density so that a correspondingly reduced p-population is calculated.

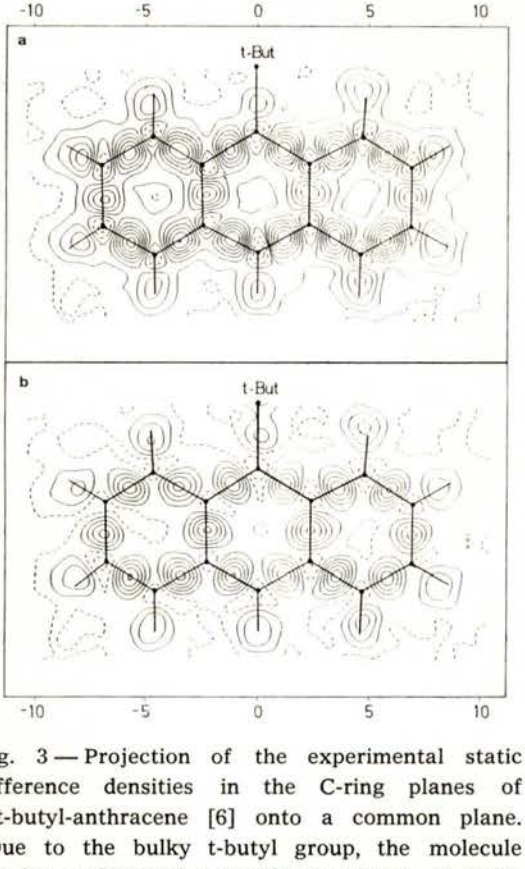

Fig. 3 — Projection of the experimental static difference densities in the C-ring planes of 9-t-butyl-anthracene [6] onto a common plane. (Due to the bulky t-butyl group, the molecule obtains a distorted butterfly structure). *a*) TDD. *b*) CDD. Length scale in $a_0$. Density contour lines: 0.1, 0.2, 0.3,...e/Å$^3$; broken lines: negative values.

Due to strong intermolecular interactions in the crystal, the TDD of triazine (Fig. 4a) does not reflect the nearly perfect symmetry of the molecule. The same problem will also show up, if density derivatives (the Laplacian, [9]) are preferred instead of total density differences.

The optimized p-shell populations of similar atoms are rather similar ($p_\pi^{0.2}\ p_{\rm rad}^{0.7}\ p_{\rm tang}^{1.1}$ for C, $p_\pi^{0.55}\ p_{\rm rad}^{1.4}\ p_{\rm tang}^{1.05}$ for N). The corresponding CDD (Fig. 4b) reflects the molecular symmetry and the order of bond strengths, $C-C > C-N > N-N$. The intermolecular interactions, however, change the orientation of the tangential and radial $p_\sigma$-AOs significantly, and that of the $p_\pi$-AOs still by up to 10°.

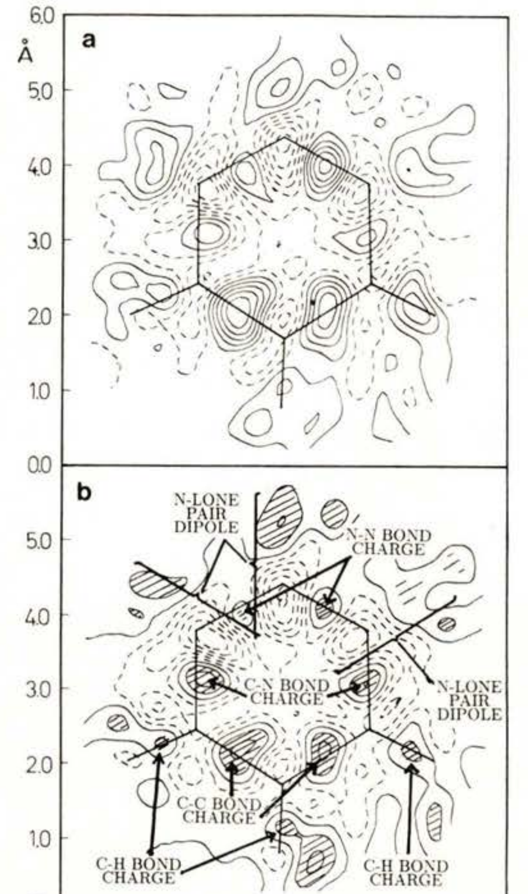

Fig. 4 — Experimental static difference densities of 1,2,3-triazine [6]. *a*) TDD. *b*) CDD (promolecule from orientated C-$^3$P/$^2$D and N-$^4$S/$^2$D states). Length scale in Å. Density lines as in Fig. 3.

## REFERENCES

[1] COPPENS, P., STEVENS, E. D., Adv. Quantum Chem. **10**, 1 (1977).

[2] BADER, R. F. W., The Force Concept in Chemistry, Ed. Debb B. M., p. 39 Van Nostrand Reinhold, New York, 1981.

[3] DUNITZ, J. D., SEILER, P., J. Am. Chem. Soc. **105**, 7056 (1983).

[4] SCHWARZ, W. H. E., RUEDENBERG, K., MENSCHING, L., J. Am. Chem. Soc. **111**, 6926 (1989). RUEDENBERG, K., SCHWARZ, W. H. E., J. Chem. Phys. **92**, 4956 (1989).

[5] SCHWARZ, W. H. E., MENSCHING, L., VALTAZANOS, P., VONNIESSEN, W., Int. J. Quantum Chem. **29**, 909 (1986), for correct order of paragraphs see ibid. **30**, 439 (1986). MENSCHING, L., VONNIESSEN, W., VALTAZANOS, P., RUEDENBERG, K., SCHWARZ, W. H. E., J. Am. Chem. Soc. **111**, 6933 (1989).

[6] MILLER, L. L., Thesis, Iowa State University, Ames, 1988.
MILLER, L. L., RUEDENBERG, K., JACOBSON, R., in preparation.

[7] ANGERMUND, K. P., Thesis, Universität Wuppertal, 1986.
ANGERMUND, K. P., CLAUS, K. H., GODDARD, R., KRÜGER, C., Angew. Chem. Int. Ed. **24**, 237 (1985).

[8] SCHWARZ, W. H. E., MENSCHING, L., RUEDENBERG, K., VALTAZANOS, P., MILLER, L. L., VONNIESSEN, W., JACOBSON, R., Angew. Chem. Int. Ed. **28**, 597 (1989).

[9] BADER, R. F. W., NGUYEN-DANG, T. T., TAL, Y., Rep. Prog. Phys. **44**, 893 (1981).

# THE EFFECTS OF HYBRIDIZATION, CHARGE TRANSFER, DELOCALIZATION AND CONSTRUCTIVE INTERFERENCE ON THE ELECTRON DEFORMATION DENSITY MAPS OF THE FIRST-ROW HYDRIDES

ARTUR A. LOW and MICHAEL B. HALL

Department of Chemistry
Texas A&M University
College Station, TX 77843-3255

*ABSTRACT* — Standard deformation density maps, molecular density minus the sum of the spherical atom densities, may show some features contrary to what is expected by chemical intuition. This is due to the effects of hybridization and charge transfer on these maps which can mask the effects of construtive interference of atomic orbitals. Changing the choice of promolecule to the sum of valence-state hybrid atoms partitions the effects of hybridization out of the standard deformation density maps. Another choice of promolecule, namely the sum of the densities of the singly occupied GVB pair orbitals, subtracted from the total GVB molecular density, produces deformation density maps which partition out the effects of charge transfer and delocalization. This produces deformation density maps which only show the effects of the constructive interference and delocalization. These deformation density maps and various difference density maps of the first-row hydrides, $AH_x$ ($A$ = Li-F, $x$ = 1-4) are computed in order to observe the effects of hybridization, charge transfer, delocalization and constructive interference on their deformation density maps.

As illustrated in Figure 1, the standard deformation density, shown for LiH in Figure 2a, may be considered to be the sum of different effects. The first is the

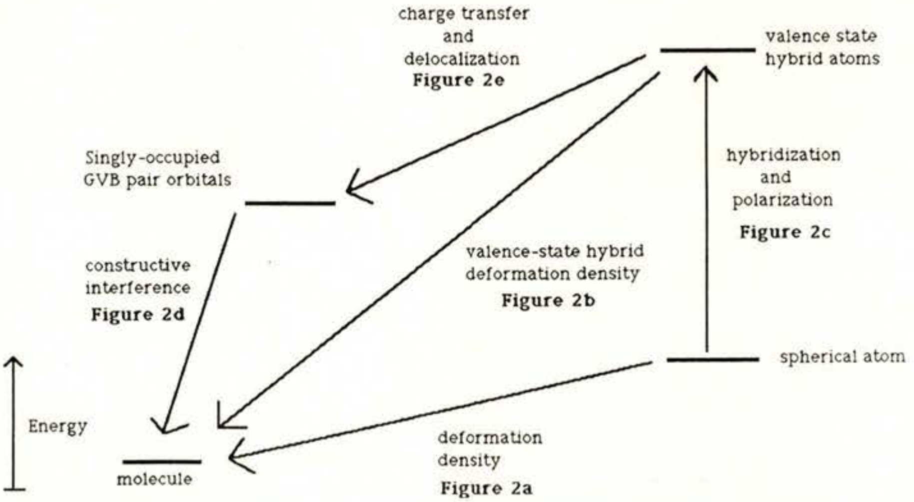

Fig. 1 — Energy diagram representing the partioning scheme of the standard deformation density map of LiH used in this abstract.

energy required for electron promotion, hybridization and polarization of the atomic orbitals in preparation for bonding. The use of valence-state hybrid atoms obtained from truncation of the GVB pair orbitals from each A-H bond as the promolecule will produce the valence-state hybrid deformation density map shown for LiH in Figure 2b. A similar procedure has been used to produce hybrid deformation density maps of $F_2$ [1]. The difference of the densities of the valence-state hybrid atoms and the spherical atom promolecule shows the density changes due to hybridization and polarization (shown for LiH in Figure 2c).

The second effect is due to polar charge transfer and delocalization between the constituent atoms. We can separate this from the deformation density maps (along

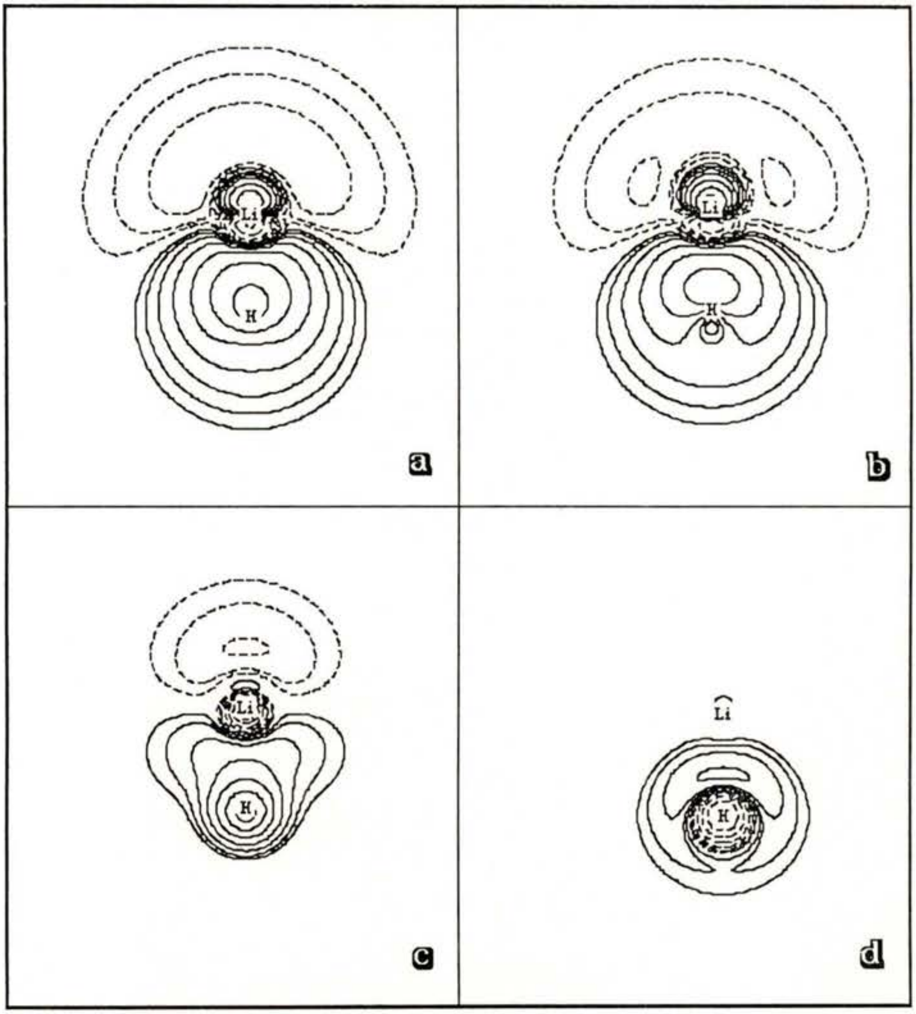

Fig. 2 a) Standard deformation density map of LiH; b) GVB valence state hybrid minus spherical atoms for LiH; c) Valence state hybrid deformation density; d) Delocalization difference density map of LiH.

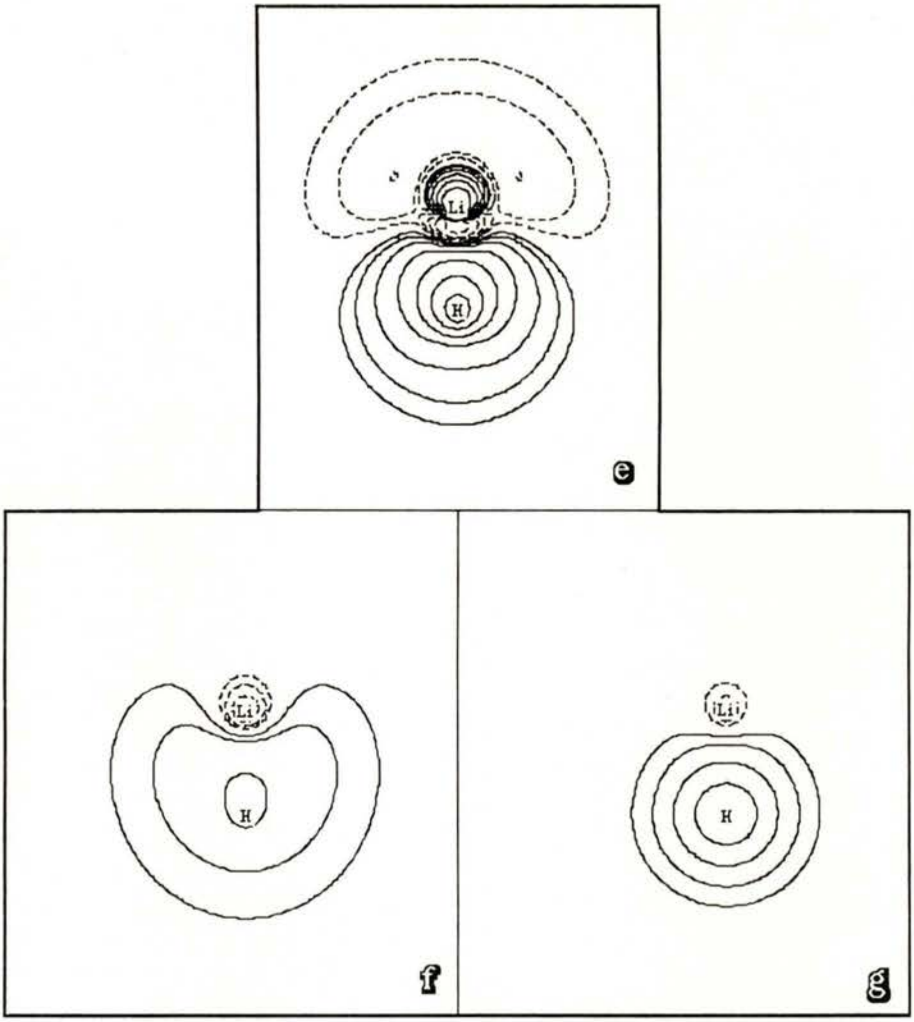

Fig. 2 e) Constructive interference deformation density map; f) GVB pair orbital centered on Li for LiH; g) GVB pair orbital centered on H for LiH. All difference density plots are contoured geometrically with a factor of two between consecutive contours. The smallest positive and negative contour have a value of $\pm 2^{-12}$ electrons (au)$^{-3}$ $(2.4414 \times 10^{-4})$. Negative contours are dashed. For the orbital plots, the smallest positive and negative contours have a value of ±2-7 electrons (au)$^{-3}$ $(\pm 7.813 \times 10^{-3})$.

with hybridization and polarization effects) by using the density of the singly-occupied GVB pair orbitals (on A and H) from each A-H bond along with the atomic core orbitals as the promolecule. The use of this promolecule results in a deformation density map which shows the effect of constructive interference of the GVB pair orbitals only (shown for LiH in Figure 2d). The difference between the densities of the GVB pair orbital and the valence state hybrid atom promolecules will show the density changes due to polar charge transfer and delocalization (shown for LiH in Figure 2e).

The standard deformation density map of LiH shows a large accumulation near the H atom on the bonding side of the H atom. About the Li atom is a dipolar pattern of deficit and accumulation with the accumulation on the non-bonding side of the Li atom. The same pattern has been observed previously by Bader, et al. [2] and was attributed to polarization of the Li ls core away from the negatively charged H atom. The density changes due to hybridization and polarization show a contraction of the valence state hybrid orbital on hydrogen resulting in the accumulation region near H. The valence-state hybrid deformation density map of LiH shows an accumulation in the internuclear region which has shifted significantly towards the internuclear region when compared to the standard deformation density. There is a little notch on the nonbonding side of the H atom which may be the beginning of the formation of the deficit regions found at the back of the H atoms in the valence-state deformation density maps of the first row hydrides. The polarization of the Li ls core is still observed. When delocalization and charge transfer is removed from the maps resulting in the constructive interference deformation density map, there are few features about the Li atom. There is a ring of accumulation around the H atom with a central region of deficit near the H nucleus.

The constructive interference deformation density maps can be more easily understood by imagining the interaction of the two GVB pair orbitals for LiH. The GVB pair orbital centered on Li contains a substantial amount of H 1s character in addition to Li 2s and $2p_z$ character whereas the GVB pair orbital centered on H consists mostly of H 1s character with little Li character. When these orbitals approach and constructively interfere, one would expect most of the interaction to occur near the H atom with little interference near the Li atom.

Since the choice of the promolecule is arbitrary, a new choice of a promolecule is useful if it gives us more insight into the relationship of electron density and chemical bonding. Standard deformation density maps sometimes produce unexpected results due to the inclusion of the effects of hybridization, polarization, delocalization and charge transfer. The use of valence-state hybrid atoms and the singly occupied GVB pair atoms as promolecules serves the purpose of partitioning these effects in the standard deformation density maps and results in clearer understanding of the relationship of chemical bonding to electron density.

## REFERENCES

[1] K. L. KUNZE and M. B. HALL, *J. Am. Chem. Soc.*, 1986, **108**, 5122.

[2] R. F. W. BADER, W. H. HENNECKER and P. E. CADE, *J. Chem. Phys.*, 1964, **46**, 3341.

# POLARISATION EFFECTS IN Mg(WATER)6(HYDROGENMALEATE)2

F. VANHOUTEGHEM, A. T. H. LENSTRA and H. J. GEISE
U. I. Antwerpen, Dept. Chemistry,
Universiteitsplein 1,2610 Wilrijk (Belgium)

An electron density study of the title compound was carried out using low temperature (100 K) X-ray and neutron data.

Fig. 1

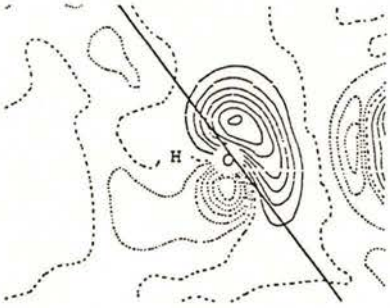

Fig. 2

A nearly symmetric deformation density was observed in the hydrogen maleate moiety, even though the moiety has no crystallographically imposed symmetry.

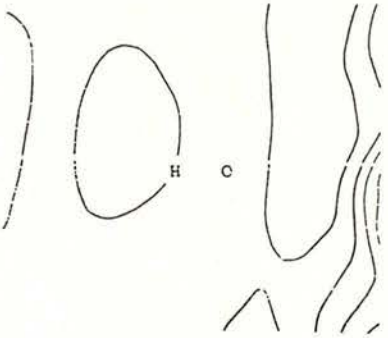

Fig. 3

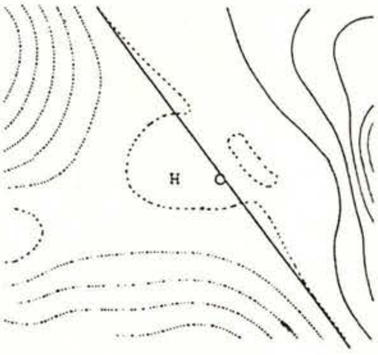

Fig. 4

This observation points towards a large internal consistency in the data. With the

*Portgal. Phys.* — Vol. 19, fasc. 3-4, pp. 195-196, 1988

Mg-ion at an inversion center, the metal coordination contains three independent water molecules. Only one shows a deformation density compatible with the distortion expected from an 'ab-initio' model (Fig. 1). The distortion observed in the $H_2O$ bisecting plane of the two other water molecules has no parallel in the theoretical model (Fig. 2), and is believed to be connected with the electrostatic potential created by the $H_2O$ neighbours. Hence, we calculated a deformation potential from the difference between the multipole and an independent atom model, leaving out the water molecule under investigation. For the 'normal' $H_2O$ we find a nearly constant deformation potential (Fig. 3), whereas the maps for the 'anomalous' $H_2O$ entities show much larger variations (Fig. 4). The observed polarisation follows an electronic redistribution along an equipotential plane.

# TRANSFERABILITY OF LOCALIZED CHARGE DISTRIBUTIONS

HARRY BRUNING and DIRK FEIL

Chemical Physics Laboratory
Twente University
PO 217
7500AE Enschede
the Netherlands

*ABSTRACT* — A comparison by means of the stockholder recipe of the quantum chemically derived electron density distributions in the $K^+ \ldots$18-crown-6 complex and small fragments of this complex leads to rules by which the electrostatic potential of large molecules can be derived out of the charge distribution of small molecules.

## INTRODUCTION

Complexes of macro cyclic compounds such as crown ethers with ions and neutral molecules derive their stability to a large extent from electrostatic interactions. So the electron density distribution in crown ether molecules plays an important role in their interaction with guest molecules. Quantum chemical calculations on these complexes are hampered by the size of the problem. The molecules are large forcing the use of small basis sets. It is known, however, that small basis sets give poor results for electrostatic properties like dipole moments [1]. The aim of this investigation is to find rules by which the electron density distribution of large molecules can be constructed out of the distribution of small fragment molecules. Results of calculations on 18-crown-6 and its complex with the potassium cation are compared with results on water, methanol, ethanol and dimethyl ether and their potassium cation complexes. The bond lengths and angles of the fragment molecules are chosen to be the same as in the $K^+ \ldots$18-crown-6 complex, to make a comparison of the charge density distributions possible.

## COMPUTATIONAL METHODS

### A. *HFS*

The charge distributions in the molecules and the complexes are calculated by the local density functional approximation using the X-alpha-LCAO-DVM method [2]. Double zeta Slater type basis sets, extended with polarization functions are used.

### B. *Atomic charge distribution*

The molecular charge distribution is projected in atomic charge distributions using Hirshfeld's 'stockholder'-recipe [3].

$$\rho_{\text{molecule}}(r) = \sum_i \rho_{\text{atom},\,i}(r) \qquad (1)$$

$$\rho_{\text{atom},\,i}(r) = w_i(r)\,\rho_{\text{molecule}}(r) \qquad (2)$$

$$w_i(r) = \rho_i^{\text{free}}(r) / \sum_j \rho_j^{\text{free}}(r) \qquad (3)$$

where $\rho^{\text{free}}(r)$ is the electron density distribution in free spherical atom. Atomic charges and dipole moments are calculated by integrating over the stockholder atomic charge distributions. The integration is carried out by Gauss quadrature, with an error of less than 1 promille.

## RESULTS

To give a detailed but qualitative illustration the transferability of the atomic charge distributions as defined by the stockholder recipe we draw contour plots of the atomic charge distributions for the oxygen and the carbon atoms. In figure 1 the difference between the charge density distribution of the stockholder atom and that of the free spherical averaged atomic density is depicted.

To give a more aggregate and quantitative qualification of the atomic charge distributions we calculated the charges and the dipole moments of the atoms. The results of the calculations are presented in table 1 and figure 2. The charges and dipole moments on the hydrogen atoms of the free molecules show good transferability. Their dipole moments are directed along the bonds. The charges on the oxygen atoms can be related to the number of hydrogen atoms bonded to the oxygen atom and to the neighbouring carbon atoms.

$$q_o = -0.154\,n_o - 0.028\,n_c \qquad (4)$$

$n_o$ : number of hydrogen atoms on oxygen

$n_c$ : number of hydrogen atoms on neighbouring carbons.

The coefficients are obtained by fitting the data of table 1 (variance 7.5 %). Assuming a fixed charge on the bonded oxygen atom the fit can be carried out with a variation of 4.6 %.

$$q_o = -0.130\,n_o - 0.019\,n_c - 0.048 \qquad (5)$$

The dipole moments on the oxygen atoms can be expanded in dipole moments along the bonds. The latter show good transferability (variance 11 %).

$$\mu_{O,\,OH} = 0.0515 \text{ a. u.} \qquad (6)$$

$$\mu_{O,\,OC} = 0.1054 \text{ a. u.} \qquad (7)$$

Given the transferability of the hydrogen and oxygen atomic charges, the carbon atomic charges follow from electroneutrality. The dipole moments on the carbon atoms are relatively small, probably as the result of four partly cancelling tetrahedraly arranged bond dipole moments.

In all molecules the complexation with $K^+$ results in a charge flow to the oxygen atom. Atomic dipoles are induced which point away from the cation. The polarization effects show good transferability.

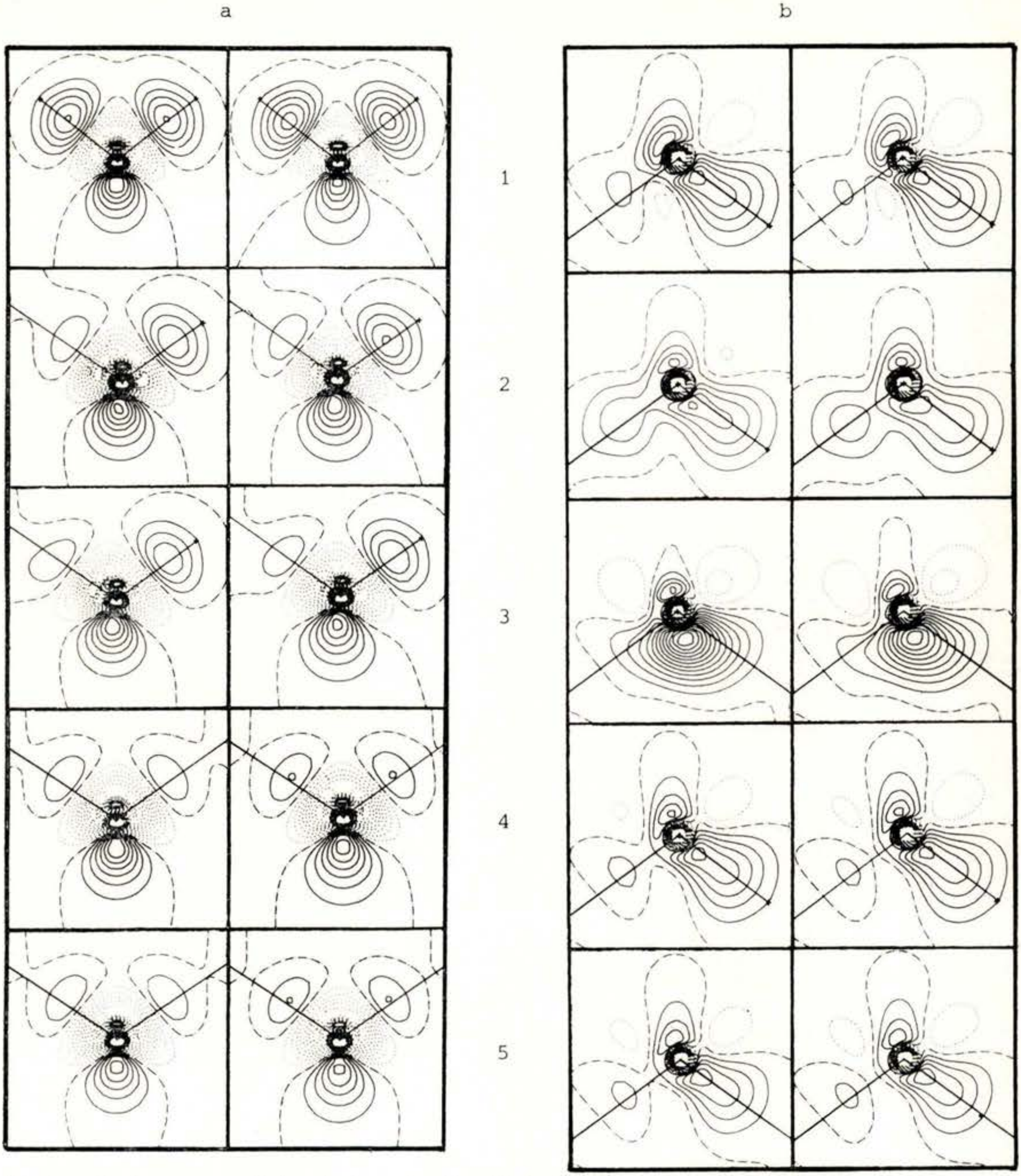

Fig. 1 — Contour maps of the electron density distribution in the stockholder atoms. Left: free molecule, right: $K^+$-complex. Contour interval .015 a. u. positive ———, zero - · - · -, negative .........

| | | |
|---|---|---|
| a. Oxygen | 1. $H_2O$ | H-O-H plane |
| | 2. $CH_3OH$ | C-O-H plane |
| | 3. $CH_3CH_2OH$ | C-O-H plane |
| | 4. $CH_3OCH_3$ | C-O-C plane |
| | 5. 18-crown-6 | C-O-C plane |
| b. Carbon | 1. $CH_3OH$ | O-C-H plane |
| | 2. $CH_3CH_2OH$ | C-C-H plane |
| | 3. $CH_3CH_2OH$ | O-C-C plane |
| | 4. $CH_3OCH_3$ | O-C-H plane |
| | 5. 18-crown-6 | O-C-C plane |

TABLE 1 — Atomic charges and dipole moments (a. u.).

| | host | | $K^+$-complex | | difference | |
|---|---|---|---|---|---|---|
| | charge | dipole | charge | dipole | charge | dipole |
| Oxygen: | | | | | | |
| $H_2O$ | −.312 | .068 | −.364 | .184 | −.052 | .116 |
| $CH_3OH$ | −.240 | .117 | −.290 | .192 | −.050 | .095 |
| $CH_3CH_2OH$ | −.202 | .104 | −.260 | .187 | −.058 | .099 |
| $CH_3OCH_3$ | −.161 | .107 | −.226 | .192 | −.065 | .098 |
| 18-crown-6 | −.132 | .111 | −.185 | .182 | −.050 | .075 |
| Carbon: | | | | | | |
| $CH_3OH$ | −.055 | .050 | −.049 | .049 | .006 | .072 |
| $CH_3CH_2OH$ | −.098 | .017 | −.107 | .090 | −.009 | .084 |
| $CH_3CH_2OH$ | −.076 | .100 | −.059 | .069 | .017 | .065 |
| $CH_3OCH_3$ | −.051 | .049 | −0.53 | .051 | −.002 | .079 |
| 18-crown-6 | −.016 | .051 | −.019 | .043 | −.003 | .044 |
| Hydrogen (OH): | | | | | | |
| $H_2O$ | .156 | .266 | .188 | .291 | .033 | .036 |
| $CH_3OH$ | .160 | .267 | .175 | .283 | .015 | .032 |
| $CH_3CH_2OH$ | .155 | .261 | .168 | .278 | .013 | .035 |
| Hydrogen (CH, in 18-crown-6 plane): | | | | | | |
| $CH_3OH$ | .037 | .196 | .070 | .220 | .033 | .027 |
| $\mathit{CH}_3\mathrm{CH}_2\mathrm{OH}$ | .053 | .205 | .084 | .230 | .031 | .026 |
| $\mathrm{CH}_3\mathit{CH}_2\mathrm{OH}$ | .027 | .215 | .059 | .237 | .032 | .023 |
| $CH_3OCH_3$ | .036 | .185 | .067 | .212 | .031 | .028 |
| 18-crown-6 | .042 | .194 | .066 | .219 | .024 | .026 |
| Hydrogen (CH, out of 18-crown-6 plane): | | | | | | |
| $CH_3OH$ | .038 | .193 | .048 | .208 | .010 | .030 |
| $\mathit{CH}_3\mathrm{CH}_2\mathrm{OH}$ | .056 | .202 | .062 | .215 | .006 | .030 |
| $\mathrm{CH}_3\mathit{CH}_2\mathrm{OH}$ | .032 | .161 | .038 | .174 | .006 | .022 |
| $CH_3OCH_3$ | .037 | .187 | .045 | .201 | .008 | .032 |
| 18-crown-6 | .041 | .186 | .046 | .196 | .005 | .018 |
| Hydrogen (CH, for saturation): | | | | | | |
| $CH_3OH$ | .058 | .210 | .058 | .214 | .000 | .030 |
| $\mathit{CH}_3\mathrm{CH}_2\mathrm{OH}$ | .051 | .201 | .009 | .162 | −.042 | .074 |
| $CH_3OCH_3$ | .057 | .210 | .053 | .212 | −.004 | .037 |
| Potassium: | | | | | | |
| $H_2O$ | 1.000 | .000 | .987 | .031 | −.013 | .031 |
| $CH_3OH$ | 1.000 | .000 | .987 | .035 | −.013 | .035 |
| $CH_3CH_2OH$ | 1.000 | .000 | 1.003 | .060 | .003 | .060 |
| $CH_3OCH_3$ | 1.000 | .000 | 1.002 | .061 | .002 | .061 |
| 18-crown-6 | 1.000 | .000 | .984 | .000 | −.016 | .000 |

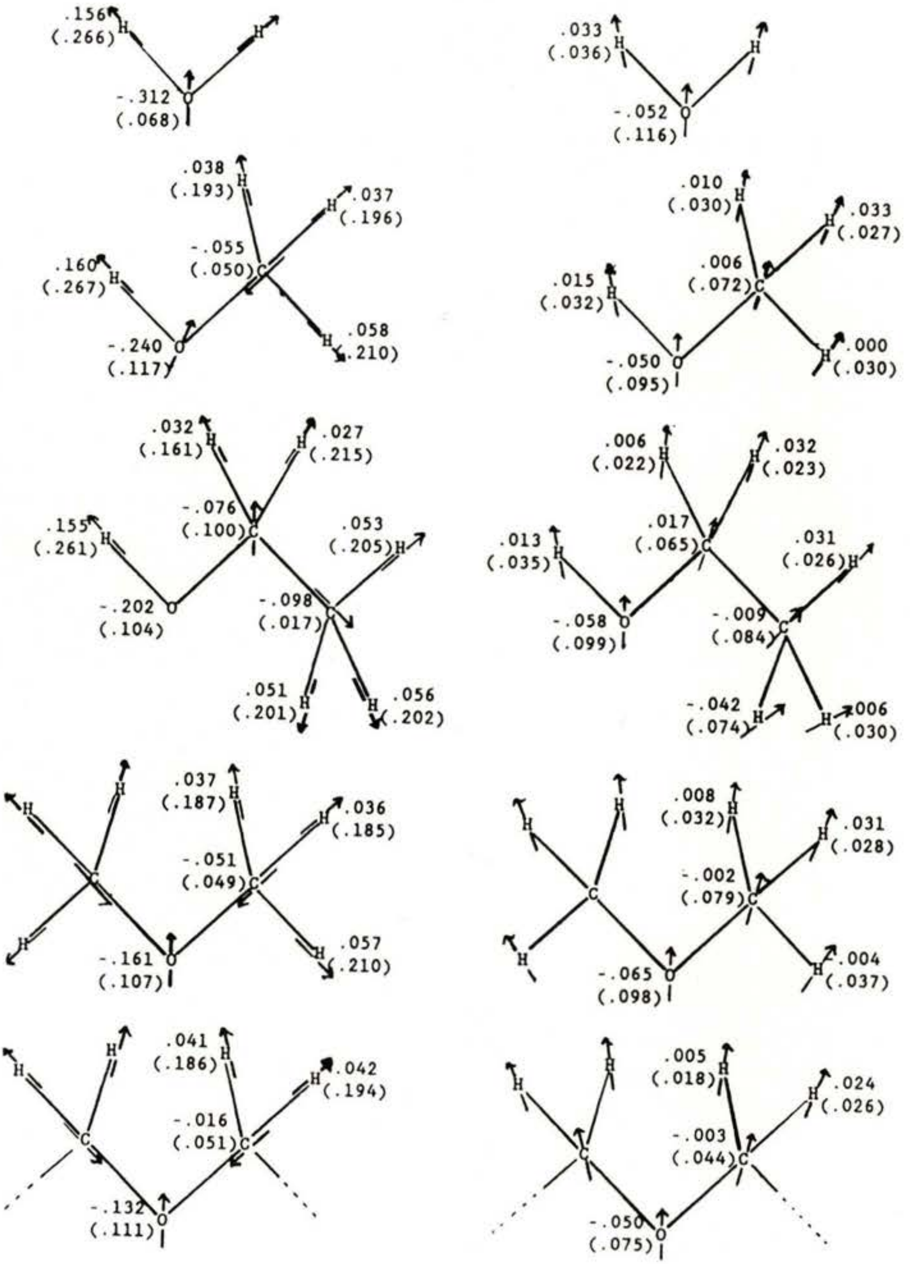

Fig. 2 — Atomic charges and dipole moments (parantheses) of the free host molecules and the polarization effects upon complexation (a. u.).

## CONCLUSIONS

The analysis of the electron density distribution by means of the stockholder recipe gives a good tool for finding rules to construct the electron density distribution in large molecules.

## REFERENCES

[1] E. J. BAERENDS, P. VERNOOYS, A. ROOZENDAAL, P. BOERRIGTER, M. P. C. M. KRIJN, D. FEIL and D. SUNDHOLM, J. Mol. Struct. **133**, 147 (1985).

[2] E. J. BAERENDS, D. E. ELLIS and P. ROSS, Chem. Phys. **2**, 41 (1973).
E. J. BAERENDS and P. ROSS, ibid. **2**, 52 (1973).
P. HOHENBERG and W. KOHN, Phys. Rev. **B136**, 864 (1964).
W. KOHN and L. J. SHAM, Phys. Rev. **A140**, 1133, (1965).
D. E. ELIS and G. S. PAINTER, Phys. Rev. **B2**, 2887 (1970).

[3] F. L. HIRSHFELD, Theor. Chim. Acta. **44**, 129 (1977).

# ELECTRON DENSITY IN ALKALI HALIDE CRYSTALS (*) (**)

G. BÖBEL, P. CORTONA, F. G. FUMI
Dipartimento di Fisica, Università di Genova and CISM/MPI
GNSM/CNR, unità di Genova (Italy)

The structure factors of alkali halide crystals derived from self-consistent charge densities generally agree very well with the experimental data [1, 2]. In particular in the case of isoelectronic alkali halides the low order difference reflections are very sensitive to the deformation of the electron cloud and the agreement between theoretical and experimental values indicates that the particular method used to compute the crystal charge densities is really able to take into account the crystal field effects.

However, a crucial point in the comparison between theoretical and experimental results is the use of the Debye-Waller (DW) factors in order to take into account the thermal effects. The general use of fitted DW factors may mask (possible) systematic discrepancies between theory and experiment.

Recently Jansen and Freeman (J&F) [3] have performed self-consistent calculations of the charge density of NaCl and have compared the ensuing structure factors with the X-ray data by Schoknecht (S) [4]. These data were reduced to the static crystal using theoretical DW factors calculated from the approximate Debye formula. J&F found that the values of the high order difference reflections differ by up to 100 % from the theoretical ones. They attribute these discrepancies to strong dynamical deformations of the ions and they conclude that the DW theory is not adequate to take into account the thermal effects in these crystals.

In fact it is not clear why these deformations should affect only the high order difference reflections and not the lower order ones, which are more sensitive to the outer electron distribution. Furthermore the J&F conclusion contradicts the results of preceeding theoretical studies [5] on the effect of the dynamical deformations on the structure factors.

In order to have more insight on this problem, we compute the structure factors at room temperature for the four salts LiF, NaF, NaCl and KCl and we compare them with the best available data. We use the ionic factors calculated using augmented spherical waves in LDA for NaF and KCl [2] and the Hartree-Fock free ions factors for LiF and NaCl: indeed for the latter two (non isoelectronic) salts the resulting structure factors for the static crystal differ only by a few percent (at most 4 %) from the values calculated by

---

(*) Supported in part by a grant from the Italian Research Council under the French-Italian Scientific Collaboration Agreement.

(**) A more detailed account of the work is in pubblication in Acta Cryst. A.

Zunger and Freeman for LiF [1] and by J&F for NaCl for all reflections, which is quite sufficient for our purposes. The theoretical DW factors that we use, are obtained from experimental phonon dispersion curves [6].

In table 1 to 4 we report for each salt the calculated values of the structure factors F(hkl) at room temperature and the percent deviation $\delta = (F(exp)-F(hkl))/F(hkl)$ from the experimental values [7, 8, 4, 10]. For LiF and KCl the agreement is excellent, with a mean deviation of about 1 %, the maximum discrepancy being of 3.2 %. For NaF the discrepancies are of comparable order of magnitude for the sum reflections and the low order difference reflection but they are greater for the high order difference reflection. However, these last reflections are very weak, owing to the isoelectronic nature of the salt, and thus rather uncertain (note the large difference between the equivalent pairs 551-711 and 553-731 which can be due only in part to aspherical effects). The values of $\delta$ tend to remain

TABLE 1 — LiF

| hkl | F | $\delta$ % |
|---|---|---|
| 111 | 4.77 | −0.4 |
| 220 | 5.22 | −1.0 |
| 311 | 2.17 | 1.8 |
| 222 | 4.03 | 0.5 |
| 331 | 1.43 | 1.4 |
| 422 | 2.33 | 2.1 |
| 511 | 1.12 | 2.7 |
| 333 | 1.12 | 0.0 |
| 442 | 1.62 | 1.8 |
| 600 | 1.62 | 0.6 |
| 444 | 1.23 | −0.8 |
| 800 | 0.90 | 0.0 |

$B(Li^+) = 0.958\ Å^2$
$B(F^-) = 0.655\ Å^2$

TABLE 2 — KCl

| hkl | F | $\delta$ % |
|---|---|---|
| 111 | 1.33 | 0.0 |
| 220 | 21.89 | 0.7 |
| 222 | 18.60 | −0.3 |
| 400 | 16.25 | −2.8 |
| 422 | 13.02 | −1.1 |
| 442 | 9.97 | −0.5 |
| 600 | 9.97 | −3.2 |
| 444 | 7.93 | −1.6 |
| 800 | 5.97 | −1.2 |
| 1000 | 3.25 | −0.9 |

$B(K^+) = 1.929\ Å^2$
$B(Cl^-) = 1.994\ Å^2$

TABLE 3 — NaF

| hkl | F | $\delta$ % |
|---|---|---|
| 111 | 1.25 | 0.0 |
| 220 | 10.74 | 1.4 |
| 311 | 1.57 | 0.0 |
| 222 | 8.64 | 1.8 |
| 331 | 1.21 | 1.6 |
| 422 | 5.22 | −0.8 |
| 333 | 0.93 | −5.4 |
| 511 | 0.93 | −4.3 |
| 440 | 4.03 | −2.0 |
| 531 | 0.69 | −4.3 |
| 620 | 3.24 | −2.2 |
| 533 | 0.49 | −2.0 |
| 444 | 2.69 | −3.0 |
| 551 | 0.36 | −22.2 |
| 711 | 0.36 | 0.0 |
| 642 | 2.27 | −3.1 |
| 553 | 0.28 | −7.1 |
| 731 | 0.28 | −17.8 |
| 800 | 1.94 | −2.6 |
| 733 | 0.22 | −18.2 |
| 660 | 1.69 | −5.3 |
| 822 | 1.69 | −2.9 |
| 842 | 1.41 | −6.4 |

$B(Na^+) = 0.868\ Å^2$
$B(F^-) = 0.867\ Å^2$

TABLE 4 — NaCl

| hkl | F | δ % | δ′ % |
|---|---|---|---|
| 111 | 4.51 | 12.0 | 3.6 |
| 200 | 20.56 | −0.3 | −0.9 |
| 222 | 14.11 | −2.3 | 1.7 |
| 400 | 12.30 | 1.3 | 0.8 |
| 331 | 2.31 | 11.7 | −1.5 |
| 333 | 2.32 | 22.8 | −2.7 |
| 600 | 7.35 | 13.9 | −9.5 |
| 442 | 7.35 | 12.5 | −10.1 |
| 533 | 2.17 | 14.3 | −9.9 |
| 444 | 5.71 | 17.7 | −15.4 |
| 551 | 2.02 | 16.3 | −13.7 |
| 800 | 4.18 | 18.9 | −18.4 |
| 555 | 1.48 | 11.5 | −17.2 |
| 771 | 1.03 | 20.4 | −19.9 |
| 1000 | 2.20 | 30.9 | −23.5 |
| 666 | 1.92 | 50.5 | −23.0 |
| 1200 | 1.08 | 44.4 | — |
| 777 | 0.49 | 26.5 | — |
| 1400 | 0.49 | 40.8 | — |

$B(Na^+) = 1.556$ Å$^2$

$B(Cl^-) = 1.348$ Å$^2$

negative, which could be due to a slight underestimate of the theoretical DW factors.

For NaCl there do not appear to exist really good data. The data by Schoknecht [4], or the rather equivalent data by Witte and Wölfel [9], are thirty years old and were not corrected for thermal diffuse scattering (TDS). Estimates of the TDS corrections to the structure factors were reported twenty years ago by Göttlicher (G) [10]: they increase with hkl reaching 20 % at 666. It should, however, be noted that the (uncorrected) G structure factors at high hkl are already appreciably smaller than those of the other sets, the ratio of the G to the S values reaching 0,6 at 666. Our computed values fall between the values of S and the corrected values of G. Indeed the δ's reported in table 4 for S and G are (mostly) positive and (mostly) negative, respectively: their magnitudes are large in both cases. The difference between our results and those reported by J&F are clearly due to the DW factors used.

The conclusion of our work is that there does not appear to be the need to question the validity of the DW theory as J&F seem to propose. In fact when good experimental data are available as it is the case for LiF, KCl and NaF the agreement between the structure factors calculated with the DW theory and the experimental values is generally good and the few discrepancies can be naturally attributed to specific deficiencies of the experimental data.

## REFERENCES

[1] A. Zunger & A. J. Freeman, Phys. Rev. **B16**, 2901 (1977).

[2] G. Böbel, P. Cortona, C. Sommers & F. G. Fumi, Acta Cryst. **A39**, 400 (1983); Acta Cryst. **A41**, 175 (1985).

[3] H. J. Jansen & A. J. Freeman, Phys. Rev. **B33**, 8629 (1986).

[4] G. Schoknecht, Z. Naturfor, **12**, 983 (1957).

[5] A. W. Pryor, Acta Cryst. **20**, 138 (1966); W. J. Buyers, J. D. Pirie & T. Smith, Phys. Rev. **165**, 999 (1968).

[6] G. Dolling, H. G. Smith, R. M. Nicklow, P. R. Vijayaraghavan & M. K. Wilkinson, Phys. Rev. **168**, 970 (1968), (LiF); J. S. Reid & T. Smith, J. Phys. Chem. Solids **31**, 2689 (1970).

[7] M. C. Schmidt, R. Colella & D. R. Yoder-Short, Acta Cryst. **A41**, 171 (1985), (LiF and KCl).

[8] C. J. Howard & R. D. G. Jones, Acta Cryst. **A33**, 776 (1977) (NaF).

[9] H. Witte & E. Wölfel, Z. Phys. Chem. **3**, 296 (1955).

[10] S. Göttlicher, Acta Cryst. **B24**, 122 (1968); see also B. T. M. Willis & A. W. Pryor, Thermal Vibrations in Crystallography, Cambridge Univ. Press (1975), § 9.4.

# ELECTRONIC DENSITY STUDY OF HEXACARBONYL-μ-di-t-BUTYLACETYLENE-di-IRON: A JOINT EXPERIMENTAL AND THEORETICAL STUDY

F. BAERT and A. LAAMYEN
UFR de physique Bat. P5 USTL 59655 Villeneuve d'Ascq France.

R. WIEST and M. BENARD
Lab. de chimie quantique Institut Le Bel Université L. Pasteur
F67000 Strasbourg France.

An experimental electronic density and a theoretical analysis of the title compound have been undertaken.

The deformation density calculated with $X - X_{HO}$ formalism at a resolution of 0.90 $Å^{-1}$ ($[>1\sigma(I)]$) shows four peaks around the Fe atoms. Multipole refinements with different models have been done using the Stewart modified by Hansen & Coppens formalism. The best results are obtained with the $4s^2$ incorporated in the core and the $3d^6$ represented by the monopole 1. There is good agreement between the model dynamic maps and the experimental ones. The d orbital occupancies have been calculated from the multipole parameters.

Interpretation of the experimental and theoretical results shows that the formal double metal-metal bond postulated for $Fe_2(CO)_6(HC_2H)$ does not involve any direct coupling between the metal d electrons. The metal-metal interactions are effective through back-donation processes involving either the semibridging carbonyl or the acetylenic group.

These results are compared to those of the $Co_2(CO)_8((CH_3)_2C_2)$ compound which has two more electrons.

# MEDIUM RANGE ATOMIC OVERLAP IN PEROVSKITE STRUCTURES

E. N. MASLEN and N. SPADACCINI
Crystallography Centre, University of WA, Nedlands 6009 Australia

The $KMF_3$ perovskites, M = Co, Fe, Co & Ni have been studied extensively [2, 3, 4]. The data from these studies were reanalysed [5] using spherically symmetric free atoms as the reference model. Confining the extinction correction to the isotropic model resulted in *R* factors and $\Delta\rho$ maps virtually identical to those reported by the original authors. Any anisotropy in the extinction must be small.

The divalent metal M is octahedrally coordinated to F atoms (2.0058-2.0945 Å), with eight second nearest neighbour K atoms located on the $< 111 >$ vectors (3.4741-3.6277 Å). With the exception of the $U_{11}$ term for the F atom in $KMnF_3$ the variation of the thermal parameters with cell dimension is close to linear. The magnitudes are lowest for the Ni structure. Because differences in bond and contact distances through the series are exact linear functions of the cell dimension, other or physical properties which are correlated to interatomic separation will display the same correlation with cell dimension.

The atomic charges determined by the Hirshfeld [1] method are a small fraction of their formal values and consistent with other reported values. The atoms become increasingly ionic in progressing from $KMnF_3$ to $KNiF_3$. The variation of charges with cell dimension is close to linear (the charges for Co and K for the Co structure deviate appreciably from the trend lines for the series as a whole).

$\Delta\rho$ in a plane containing four M-F bonds for these compounds are shown in Fig. 1. $\Delta\rho$ along the M-F bond shows effects commonly associated with overlap of the atomic orbitals. For Mn there is a peak, approximately 0.6 Å from the metal nucleus, $0.5e\text{Å}^{-3}$ in height. In the Fe compound the feature is minimum of $-0.3e\text{Å}^{-3}$ with similar radial dependence. This trend continues through the series, the feature having a depth of $-1.12e\text{Å}^{-3}$ for $KNiF_3$. As the contribution from the antibonding orbitals increases the electrons are repelled more strongly from the vicinity of the M-F bond. The depletion increases progressively, becoming more strongly antibonding from Mn to Ni, as the spin conflict due to overlap of the F atom electrons with the *3d* subshell increases. This is expected from the exclusion principle.

The topology of $\Delta\rho$ in Fig. 1 has a contrasting parallel in $\Delta\rho$ along the M-K interaction vector. There is a minor build up of density along the Mn-K direction. This feature becomes increasingly more positive as one progresses through the Fe, Co and Ni analogues, for which it maximises at $1.13 e\text{Å}^{-3}$. The peaks are aligned with their maxima along the M-K vectors. The variation of characteristics of $\Delta\rho$ with cell dimension through the series

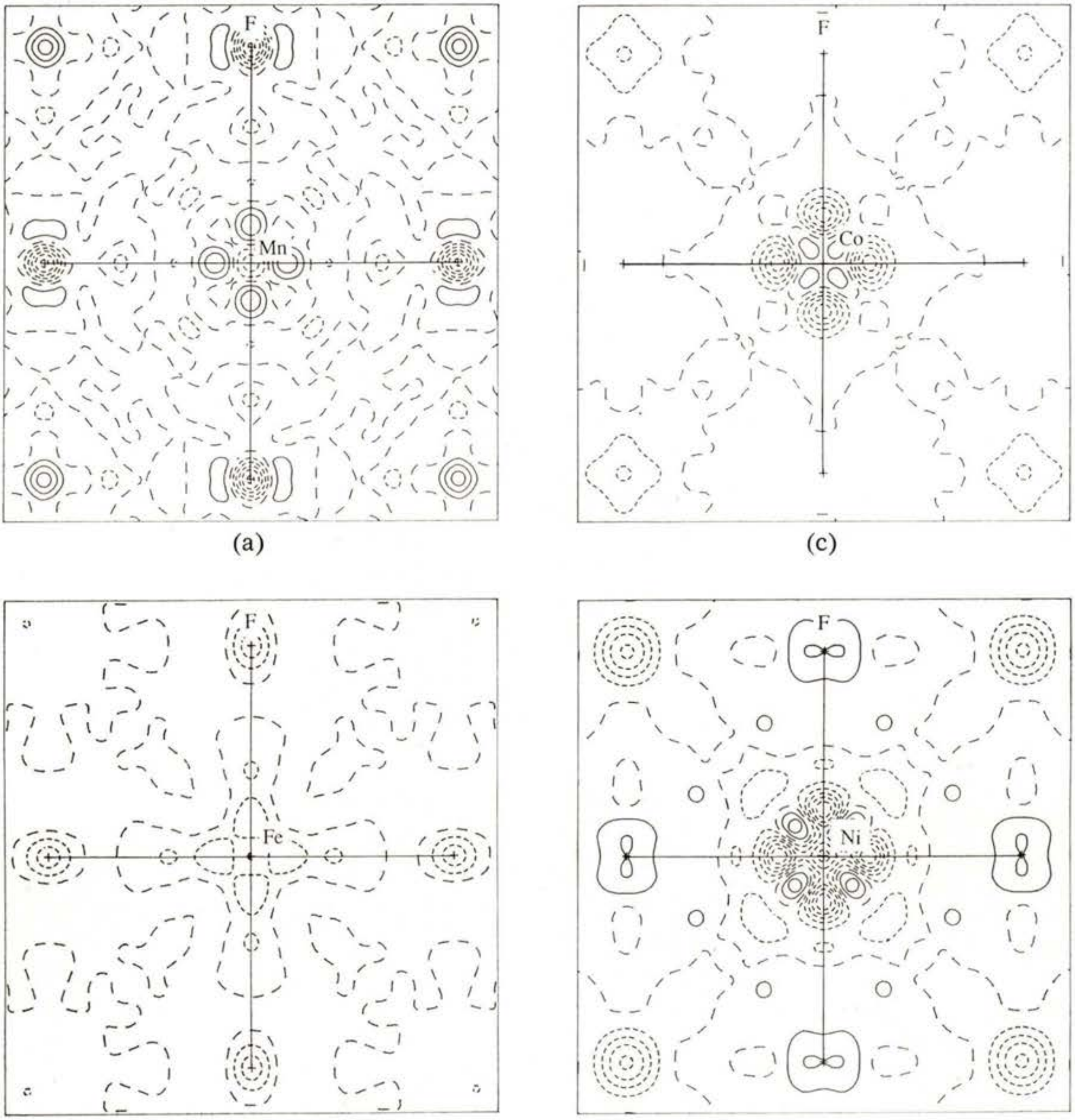

(a) (c)

(b) (d)

Fig. 1 — $\Delta\rho$ in a section through the M-F bonds(a) $KMnF_3$ (b) $KFeF_3$ (c) $KCoF_3$ (d) $KNiF_3$. Contour interval $0.2 e\text{Å}^{-3}$. Short dashed contour isnegative, solid - positive, long dash - zero. Map Map borders $5 \times 5$ Å.

is shown in Fig. 2, which depicts the heights at the F atom, in the $e_g$ orbital and in the $t_{2g}$ orbital projected on to the plane of Fig. 1. The variation is close to linear in all cases. This is not surprising since the overlap between the metal atom and the F ligands must vary in a regular manner.

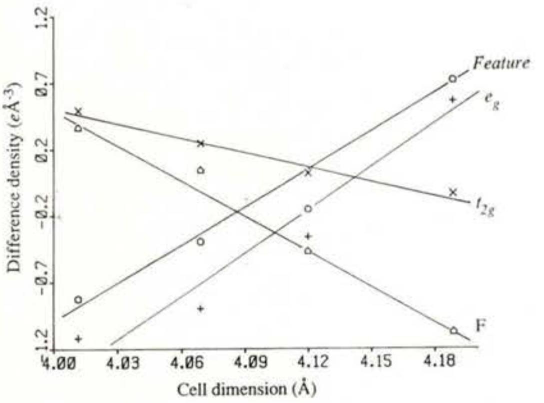

Fig. 2 — The magnitudes of $\Delta\rho$ at various points in the cell as a function of cell dimension.

The effect of increasing the $d$ subshell population for the M species on the orbital overlap can be understood qualitatively in terms of the changes in the electrostatic energy, $E_{es}$. This is the classical electrostatic interaction energy for overlapping, undeformed, spherically symmetric charge density clouds. It can be considered as the first order term in a perturbation expansion of the total energy and is often dominant. Changing the $d$ shell population has two competing effects on the bonding energy. Raising the number of $d$ electrons increases the degree of overlap, but at fixed separation this is outweighed by the contraction of the electron cloud due to the increased nuclear charge. The combined effect is to reduce the magnitude of the bonding *i.e.* to raise the bonding energy.

The bonding $E_{es}$ becomes more negative as the contact distance is compressed. In addition to the $E_{es}$, the total bonding energy includes contributions from $\Delta\rho$ associated with exchange and other polarisation terms. The sign of this contribution can be inferred from the $\Delta\rho$ topology in the interatomic region.

In Fig. 1*d* there is a large deficiency of electrons near the Ni atom, along the Ni-Ni (and Ni-F) vectors. This makes an antibonding contribution to the total bonding energy, which, for the Ni-Ni interactions, must be more positive than $E_{es}$ Conversely near the Mn atom there is electron excess along the Mn-Mn (and Mn-F) vector. In this case the contribution is bonding, lowering the total bonding energy below $E_{es}$. We conclude that the contribution of the polarisation on the M-M interactions is increasingly antibonding from $KMnF_3$ to $KNiF_3$.

M-K interactions are often neglected because of their supposedly small contribution to bonding. The sign of the contribution of the polarisation to the bonding energy is opposite to that for the M-M and M-F interactions, because of the increase in density along the M-K vector as M progresses towards Ni. In $KNiF_3$ there is a large excess of density directly along the Ni-K vector which makes a bonding contribution. The weak depletion of density along the Mn-K vector $KMnF_3$ will make a slightly antibonding contribution to that interaction energy. The total contribution of the M-K interaction to the bonding energy is increasingly bonding from $KMnF_3$ to $KNiF_3$.

There is a significant feature, midway between and 2 Å from the K atoms, which is 2 Å and 2.8 Å from the F and M atoms respectively (Fig. 1). $\Delta\rho$ is $0.6e\text{Å}^{-3}$ at that location for $KMnF_3$, progressively decreasing to a hollow of $-0.8e\text{Å}^{-3}$ in the Ni structure. The feature becomes more prominent and more localised with increasing data resolution. The rate of increase is slow, as expected of valence electron terms. It cannot result from random error and is highly unlikely to arise from similar systematic errors in four different experiments.

Although too far from the atomic centres to be attributed to well known chemical effects, the change through the series is highly correlated with those of other significant features. The variation of $\Delta\rho$ at this site, plotted against cell dimension in Fig. 2 (marked *Feature*), shows the same linear variation as those for the other characteristic features of known origin. This suggests that they arise in a similar way.

The structural cavity may be a local maximum or minimum in $\Delta\rho$ depending on the chemical species at the M site. Because the feature is far from the nuclei, at a site of low electrostatic potential, this has significant implications for the related high $T_c$ $LaBa_2Cu_3O_7$ superconductors.

This work was supported by the Australian Research Grants Scheme.

## REFERENCES

[1] HIRSHFELD, F. L. (1977). *Theor. Chim. Acta* **44**, 129-138.

[2] KIJIMA, N., TANAKA, K. & MARUMO, F. (1981). *Acta Cryst.* **B37**, 545-548.

[3] KIJIMA, N., TANAKA, K. & MARUMO, F. (1983). *Acta Cryst.* **B39**, 557-561.

[4] MIYATA, N., TANAKA, K. & MARUMO, F. (1983). *Acta Cryst.* **B39**, 561-564.

[5] SPADACCINI, N. (1988). *Ph. D. Thesis*, Univ. of Western Australia.

# QUANTUM TOPOLOGY APPROACH TO THE X-RAY DIFFRACTION RESULTS INTERPRETATION: ETHANE, ETHYLENE AND ACETYLENE

M. KAPPHAHN, V. G. TSIREL'SON, R. P. OZEROV
Mendeleev - Institute of Chemical Technology, Moscow, U.S.S.R.

*ABSTRACT* — The application of the topological approach [1] to the experimental electron density distribution has been attempted. The molecules $C_2H_6$, $C_2H_4$ and $C_2H_2$ have been choosen as examples. The low-temperature experimental data have been taken from [2].

The present work is concerned with the attempt to apply the quantum topology approach [1] to the interpretation of experimental dynamic electron densities in the crystals $C_2H_6$, $C_2H_4$ and $C_2H_2$. The electron density function $\rho$ for $C_2H_6$ was obtained from Eq. (1):

$$\rho(\mathbf{r}) = \delta_\rho(\mathbf{r}) + \sum_{j=1}^{N} \rho_{oj}(\mathbf{r} - \mathbf{R}_j), \qquad (1)$$

where $\delta\rho$ is the deformation density function and the second part — the promolecule contribution. For the other two crystals $\rho$ has been calculated as a superposition of multipole-pseudoatoms [3].

In all three crystals C - C bond critical points (3, - 1) have been observed in the inversion centres of the unit cells. The results of topological analysis have been compared with analogous results derived from ab-initio calculations for free molecules [4, 5] (Table 1). Experimental dynamic and theoretical static topological characteristics for $C_2H_6$ are in a good agreement. The only difference is the non-zero-ellipticity for crystal $C_2H_6$. Taking into account the non-coincidence of the Hessian-eigenvectors with the main directions of the thermal motion ellipsoids for carbon atoms we have concluded, that this effect is determined by intermolecular interactions in crystal $C_2H_6$. In fact, the direction of the most slowly decrease of charge density (Hessian-eigenvector $\mathbf{v}_2$) deviates from direction [100] by 15.4°. This is the direction to the nearest neighbouring molecules in the crystal.

There is some disagreement between dynamic and static topological characteristics for $C_2H_4$ and $C_2H_2$. In order to find out the dependence of thermal motion and internuclear distance on the topological characteristics of charge density in the C - C bond critical point, isotropic thermal parameteres $B_j$ [6] have been introduced in the promolecular part of Eq. (1):

$$\rho^{T}_{oj}(\mathbf{r}) = 8\pi^{3/2} \sum_{i=1}^{4} a_{ij} (b_{ij} + B_j)^{-3/2} \exp(-4\pi^2 r^2 / (b_{ij} + B_j)) \qquad (2)$$

*Portgal. Phys.* — Vol. 19, fasc. 3-4, pp. 213-216, 1988

TABLE 1 — Topological characteristics for the C — C bond ($C_2H_6$), C = C bond ($C_2H_4$), C ≡ C bond ($C_2H_2$) and C - H bonds in the bond critical points.

| Bond | | R, Å | $\rho$, e/Å$^3$ | $\nabla^2\rho$ e/Å$^5$ | $\lambda_1$, e/Å$^5$ | $\lambda_2$, e/Å$^5$ | $\lambda_3$, e/Å$^5$ | $\varepsilon$ |
|---|---|---|---|---|---|---|---|---|
| C — C | A1 | 1.510 | 1.611 | −16.13 | −12.09 | −11.49 | 5.21 | 0.05 |
| | B1 | 1.528 | 1.701 | −15.92 | −9.25 | −9.25 | 7.06 | 0.00 |
| C = C | A2 | 1.336 | 2.156 | −16.71 | −16.82 | −14.17 | 14.28 | 0.19 |
| | B2 | 1.306 | 2.286 | −22.42 | −16.68 | −13.63 | 7.89 | 0.22 |
| C ≡ C | A3 | 1.183 | 2.835 | −31.24 | −22.38 | −22.36 | 13.24 | 0.00 |
| | B3 | 1.190 | 2.737 | −31.25 | −16.21 | −16.21 | 1.17 | 0.00 |
| C - H | A1 | 0.960 | 1.546 | −8.78 | −13.01 | −13.01 | 16.24 | 0.00 |
| C - H | A2 | 1.071 | 1.396 | −5.47 | −13.22 | −5.24 | 12.99 | 1.52 |
| C - H | A3 | 1.043 | 1.419 | −7.12 | −10.26 | −10.24 | 13.38 | 0.00 |
| C - H | B | 1.086 | 1.881 | −23.71 | −17.47 | −17.47 | 11.07 | 0.00 |

Note: 1) «A» — molecule in the crystal (present work), «B» — ab-initio calculations for free molecules [4, 5], R — internuclear distance, $\rho$ and $\nabla^2\rho$ — values of electron density and Laplacian of electron density in the (3, - 1) — critical points, $\varepsilon$ — bond ellipticity.

2) The values for C - H bonds have been averaged.

TABLE 2 — The influence of atomic thermal motion on the topological characteristics in the (3, - 1) critical point of the $C_2H_6$, $C_2H_4$ and $C_2H_2$ promolecules.

| B, Å$^2$ | Fragment C — C | | | Fragment C = C | | | Fragment C ≡ C | | |
|---|---|---|---|---|---|---|---|---|---|
| | $\rho$, e/Å$^3$ | $\lambda_1=\lambda_2$, e/Å$^5$ | $\lambda_3$, e/Å$^5$ | $\rho$, e/Å$^3$ | $\lambda_1=\lambda_2$, e/Å$^5$ | $\lambda_3$, e/Å$^5$ | $\rho$, e/Å$^3$ | $\lambda_1=\lambda_2$, e/Å$^5$ | $\lambda_3$, e/Å$^5$ |
| 0.0 | 1.114 | −5.035 | 11.265 | 1.548 | −7.588 | 12.271 | 1.899 | −9.757 | 11.724 |
| 0.5 | 1.117 | −4.923 | 10.432 | 1.538 | −7.303 | 11.074 | 1.875 | −9.332 | 11.347 |
| 1.0 | 1.118 | −4.812 | 9.740 | 1.528 | −7.122 | 11.918 | 1.862 | −9.570 | 20.532 |
| 1.5 | 1.119 | −4.727 | 9.818 | 1.528 | −7.336 | 17.641 | 1.891 | −11.064 | 39.097 |
| 2.0 | 1.122 | −4.752 | 11.343 | 1.549 | −8.038 | 26.421 | 1.966 | −13.259 | 56.223 |
| 2.5 | 1.131 | −4.917 | 14.068 | 1.592 | −9.025 | 34.605 | 2.072 | −15.408 | 66.312 |
| 3.0 | 1.149 | −5.201 | 17.172 | 1.651 | −10.038 | 40.201 | 2.185 | −17.073 | 69.503 |
| 3.5 | 1.174 | −5.545 | 19.935 | 1.717 | −10.904 | 42.925 | 2.292 | −18.144 | 67.877 |
| 4.0 | 1.204 | −5.898 | 21.977 | 1.783 | −11.550 | 43.302 | 2.383 | −18.672 | 63.476 |

The deformation density $\delta\rho$ in the bond region depends much less on the atomic thermal motions [7].

The influence of thermal motions is increasing when bond order becomes bigger (Table 2). The static topological characteristics in the (3, - 1) - critical point for the C – C promolecular bond fragment have not been changed by thermal motion of carbon atoms (in crystal $C_2H_6$ at $T = 85$ K : $\bar{B}(C) = 2.1$ Å$^2$), unlike the C = C bond fragment (in crystal $C_2H_4$ at $T = 85$ K : $\bar{B}(C) = 2.8$ Å$^2$) and the C ≡ C bond fragment (in crystal $C_2H_2$ at $T = 141$ K : $\bar{B}(C) = 4.2$ Å$^2$). At first an intensification of thermal motion results in a primary increase of $\lambda_3$ (and $\nabla^2\rho = \lambda_3 - |\lambda_1| - |\lambda_2|$). Crystal $C_2H_4$ sets an example for this case. A further intensification of thermal motion results in a primary increase of $|\lambda_1|$ and $|\lambda_2|$, which will compensate for the former increased value of $\lambda_3$. That is why the $\nabla^2\rho$ — values for $C_2H_2$ have coincided.

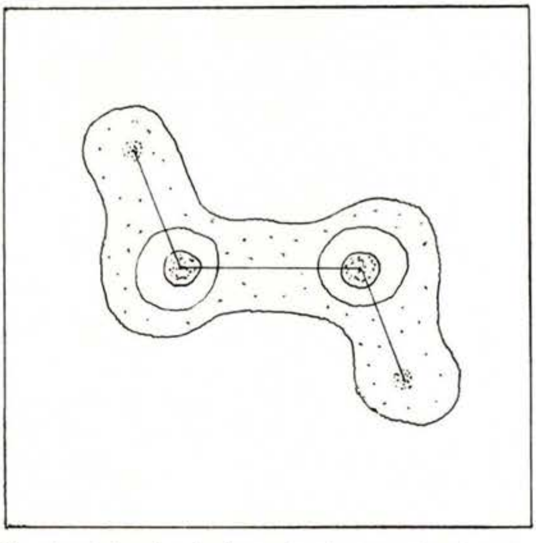

Fig. 1 — The Laplacian of electron density $\nabla^2\rho$ distribution in the H - C - C - H plane of crystal $C_2H_6$. In the dotted regions $\nabla^2\rho < 0$, around the nuclei $\nabla^2\rho << 0$.

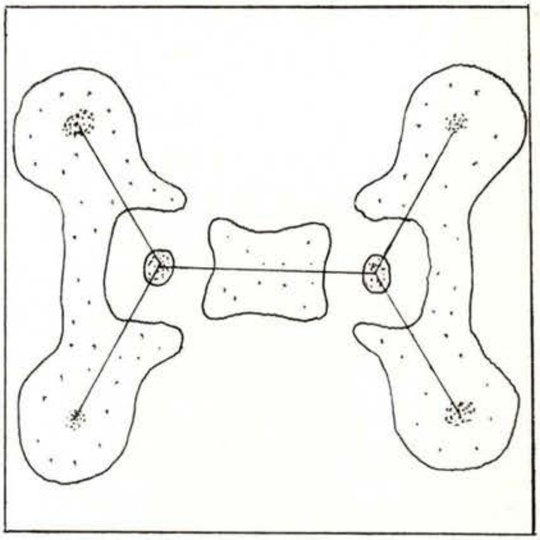

Fig. 2 — The Laplacian of electron density $\Delta^2\rho$ distribution in the molecular plane of crystal $C_2H_4$. In the dotted regions $\nabla^2\rho < 0$, around the nuclei $\nabla^2\rho << 0$.

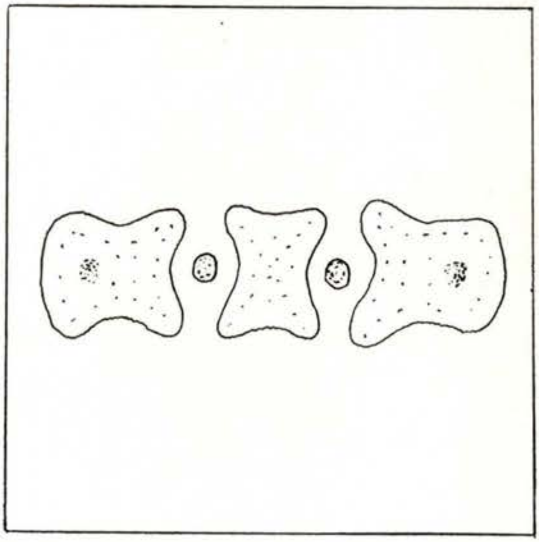

Fig. 3 — The Laplacian of electron density $\nabla^2\rho$ distribution in the molecular plane of crystal $C_2H_2$. In the dotted regions $\nabla^2\rho < 0$, around the nuclei $\nabla^2\rho << 0$.

The promolecular C - H bond fragment is much more sensible to thermal motion, which makes it difficult to apply the topological approach for the analysis of C - H bonds. A further temperature-fall for diffraction experiments will facilitate topological analysis for such bonds.

Figures 1 and 3 illustrate the $\Delta^2\rho$ — distributions for the given crystals. They are typical covalent binding charge density concentrations in the internuclear regions.

A further development of topological analysis for dynamic electron densities will allow more chemical significant information to be obtained directly from X-ray diffraction experiments.

## REFERENCES

[1] BADER, R. F. W., NGUYEN-DANG, T. T., TAL, Y., Rep. Prog. Phys., **44**, 893 (1981).

[2] NES, G. J. H. VAN, VOS, A., Acta Cryst., **B34**, 1947 (1978).

[3] STEWART, R. F., Acta Cryst., **A32**, 565 (1976).

[4] BADER, R. F. W. et al., J. Am. Chem. Soc., **109**, 985 (1983).

[5] WIBERG, K. B., BADER, R. F. W., LAU, C. D. H., J. Am. Chem. Soc., **109**, 985 (1987).

[6] SCHERINGER, C., Acta Cryst., **A35**, 838 (1979).

[7] EPSTEIN, J., SWANTON, D., J. Chem. Phys., **77**, 1048 (1982).

# CHARGE DENSITY DISTRIBUTION, ELECTROSTATIC POTENTIAL AND COMPLEX FORMATION ABILITY OF SOME NEUTRAL AGENTS

A. A. VARNEK, A. S. GLEBOV, A. N. KUZNETSOV
D. I. Mendeleev Institute of Chemical Technology, Moscow, 125820 U.S.S.R.

*ABSTRACT* — Quantum chemical, molecular mechanical and Monte-Carlo calculations have been carried out for explanation complexation and extraction ability of some neutral organophosphorus and macrocyclic agents.

The aim of this work is a theoretical investigation of the influence of substituents on some neutral macrocyclic and organophosphorus agents complexation and extraction processes.

1. According to experimental data [1, 2] the introduction in benzene rings of dibenzo-18-crown-6 (DB18C6) both electron donor substituents (Cl, $NO_2$) and electron acceptor ones decrease the stability of their complexes with alkaly cations.

Let us consider the metal cation ($M^{n+}$) complexation process with ligand (L) in the solvent (S):

$$(M_s^{n+}) + (L)_s \rightarrow (M)_s^{n+}, \qquad (1)$$

as a set of the following stages: cation (I) and agent (II) desolvatation, agent conformational transformation (III), agent-cation interaction (IV), complex solvation (V). In this case the complexation energy $E_c$ is determined as a sum of energy of the stage I-V.

Conformational transformation energy has been calculated by molecular mechanics method using MM2 programm [3]. The energy of ion-molecular and intermolecular interactions $\Delta E$ has been calculated by the method based on perturbation treatment:

$$E = E_{es} + E_{pl} + E_w \qquad (2)$$

where the electrostatic term $E_{es}$ is determined from the molecular electrostatic potential (MEP) of the agents, the polarization ($E_{pl}$) and van-der-Waals energy terms ($E_w$) — according to [4]. Solvation energy was estimated by means of Monte-Carlo method.

Calculations of crown-ethers (CE) atomic charge received from CNDO/2 are shown on Fig. 1.

The alkyl cation—CE interaction energy calculated according to equation (2) decreases in the series DB18C6-dichloro DB18C6-dinitroDB18C6. Adding the alkyl groups to BD18C6 did not change the interaction energy.

According to our results there are different reasons for the metallo-complexes stability decrease of in the case of DB18C6--substituted. The influence of electron--acceptor (Cl, NO) substituents is connected with decrease of cation-ligand interaction energy (Fig. 2). Decrease of the dialkyl--DB18C6 complexes stability is associated with hydrophobic interaction of CE, which becomes stronger with the increase of the alkyl chain size. Thus, the decrease of different terms $E_c$ results in the same effect — the decrease of total complexation energy, and, hence, the decrease of complex stability.

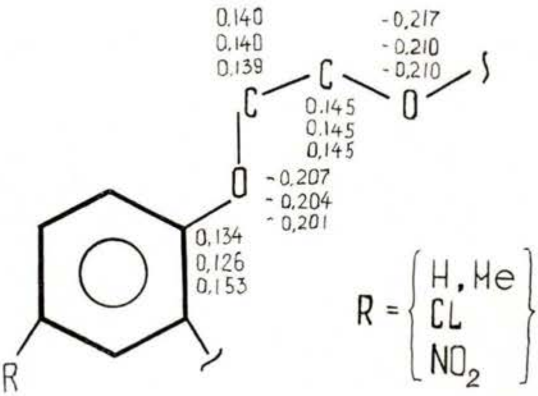

Fig. 1 — Charge distribution in fragments of the DB18C6 and its dichloro-, dinitro- and dialkyl substitueted.

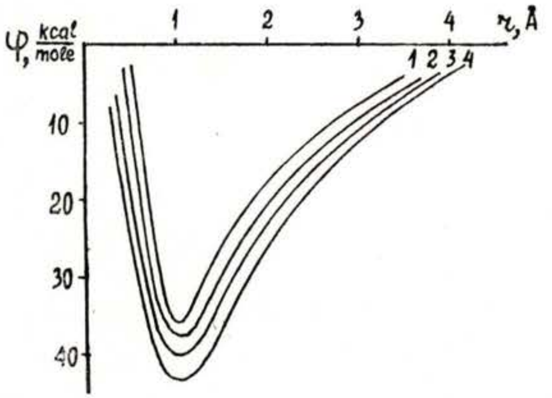

Fig. 2 — MEP distribution along the line of P = 0 bond; 1 — TMP, 2 — DMP, 3 — MDP, 4 — TMPO.

2. The molecular electrostatic potential (MEP) distribution [5] may be effectively used for estimation of agents extraction ability if E is approximated by the ion--molecular interaction energy. In the series trimethylphosphate (TMP) — dimethylmethylphosphonate (DMP) — methyldimethylphosphinate (MDP) — trimethylphosphine

TABLE 1 — Charge distribution on P = 0 fragment

| Calc. method | MNDO | | CNDO/2 (spd) | | CNDO/2 (sp) | |
|---|---|---|---|---|---|---|
| | $O_{ph}$ | P | $O_{ph}$ | P | $O^{ph}$ | P |
| $(CH_3O)_3PO$ | −0.695 | 1.467 | −0.342 | 0.566 | −0.490 | 1.361 |
| $(CH_3O)_2CH_3PO$ | −0.689 | 1.193 | −0.328 | 0.450 | −0.489 | 1.355 |
| $CH_3O(CH_3)_2PO$ | −0.668 | 0.893 | −0.311 | 0.351 | −0.480 | 0.904 |
| $(CH_3)_3PO$ | −0.639 | 0.579 | −0.297 | 0.276 | −0.467 | 0.676 |

oxide (TMPO) extraction ability decreases if the alkyl radical replaces the alkoxyl one.

The quantum chemical calculations for this series were accomplished by CNDO/2 (sp- and spd-basis) and MNDO methods. The charge distribution data in P = 0 fragments of investigated molecules received from calculations are present in Table 1.

The presented data indicate that negative charge on oxygen of phosphoryl group ($O_{ph}$) decreases from TMP to TMPO while the extraction ability in such series increases.

MEP distribution along the line of P = 0 bond for the series TMP-TMPO is presented in Fig. 2. The comparison of the curves evidences a shift of the corresponding curve to more negative MEP values when changing of alcoxyl substitutional group for alcyl group which correlates with known experimental data concerning extraction ability.

## REFERENCES

[1] IZATT, R. M. et al., Chem. Rev., v. 85, 472 (1985).

[2] PARPIEV, N. A., NOROV, S. K. and TASHMUHAMEDOV, B. A. et al., Biorg. Khim., v. 9, 1429 (1983).

[3] BURKERT, W., ALINGER, N., Molecular mechanics., Moscow, Mir., 364 p. (1986).

[4] GRESH, N., CLAVERIE, P., PULLMAN, A., Int. J. Quant. Chem. Symp., v. 13, 243 (1979).

[5] SCROCCO, E., TOMASI, I., Adv. Quant. Chem., v. 11, 115 (1978).

# THE ATOMIC AND ELECTRON STRUCTURE REFINEMENT WITH THE USE OF A-PRIORI CHEMICAL BOND DATA

KRASHENINNIKOV, M. V.
Mendeleev Institute of Chemical Technology,
Moscow 125820, Miusskaja Sq. 9, U.S.S.R.

The free spherical symmetric atom model is usualy used in the traditional methods of covalent crystal structure refinements. Some of the important atomic electron density distribution peculiarities are not taken into account in this model. This can influence the thermal parameters, scale factor and other refined values as well as the experimental electron density distribution. Many models (aspherical form factors, double atom, æ-technique; multipole decomposition) have been suggested in order to improve the situation.

An iteration refinement procedure is proposed that deals with the standard parameters determination as well as the full crystal potential distribution in reciprocal space calculation. The corrections to the experimental and calculated structure factors can also be determined in the linear quantum perturbation theory approach, the Fermi wave number being taken into account. By this procedure the results converge to the self consistent parameters, within acceptable limits.

# MÖSSBAUER-EFFECT AND SPIN-DENSITY-WAVES OF CHROMIUM (*)

S. M. DUBIEL
Institute of Metallurgy, A. G. H., Al. Mickiewicza 30,
PL-30-059 Kraków, Poland

Chromium is known as a spin-density-wave (SDW) antiferromagnet. The name follows from the fact that its magnetic moment $\vec{\mu}_{Cr}$ has not a constant magnitude, but it is modulated according to the following formula:

$$\vec{\mu}_{Cr} = \mu_o \mathbf{n} \sin \mathbf{Q} \cdot \mathbf{r} \qquad (1)$$

where $\mu_o = 0.59\, \mu_B$ is the maximum value of $|\vec{\mu}_{Cr}|$, $\hat{\eta}$ is the polarization unit vector and $\mathbf{Q} = 2\,\pi/\lambda\, \mathbf{q}$ is the wave vector. These are just SDW, because of their peculiar properties, which make chromium such a fascinating subject of research [1]:

(i) The polarization of SDW depends on the temperature T. For $T_{sf} < T < T_N$ the polarization is transverse i. e. $\mathbf{q} \cdot \mathbf{n} = 0$. $T_N = 312$ K is the Néel temperature and $T_{sf} = 123$ K is the so called spin-flip temperature. Below $T_{sf}$ the polarization is longitudinal i. e. $\mathbf{q} \cdot \mathbf{n} = 1$.

(ii) SDW are incommensurate with the underlying lattice, i. e. $Q \neq 2\,\pi/a$, where a is the lattice constant.

(iii) The modulation of the SDW is not purely sinusoidal but a second- and a third-order harmonics exist with a relative contribution of 0.16 % and 1.75 % respectively.

The aim of the present paper is to demonstrate that the Mössbauer-effect spectroscopy (MES) is a very suitable tool to study SDW of chromium and related effects. It is so because the hyperfine (hf) field, one of the three hf parameters which one measures through MES, is proportional to the spin-density of the s-like electrons which constitutes the SDW for chromium. Despite these favourable circumstances MES has not contributed to the investigation of SDW to the extent as e. g. diffraction techniques have. This may have resulted from a failure to successfully observe the spin-flip transition by means of $^{57}$Fe MES by Wertheim [2], which in fact was a first attempt to use MES in such an investigation. Few years later Pepper and Street [3] and Street and Window [4] succeeded to observe SDW by means of $^{119}$Sn MES. In particular, they demonstrated that SDW is incommensurate

---

(*) Supported in part by project n° 106/BP/87 - CPBPO1.04.

*Portgal. Phys.* — Vol. 19, fasc. 3-4, pp. 223-224, 1988

and they become commensurate on addition of Mn into Cr matrix. They could also determine the value of $T_N$.

$^{119}$Sn MES has also proved to be useful to study the spin-flip transition [5]; the third-order harmonic could have been detected in the same way [6].

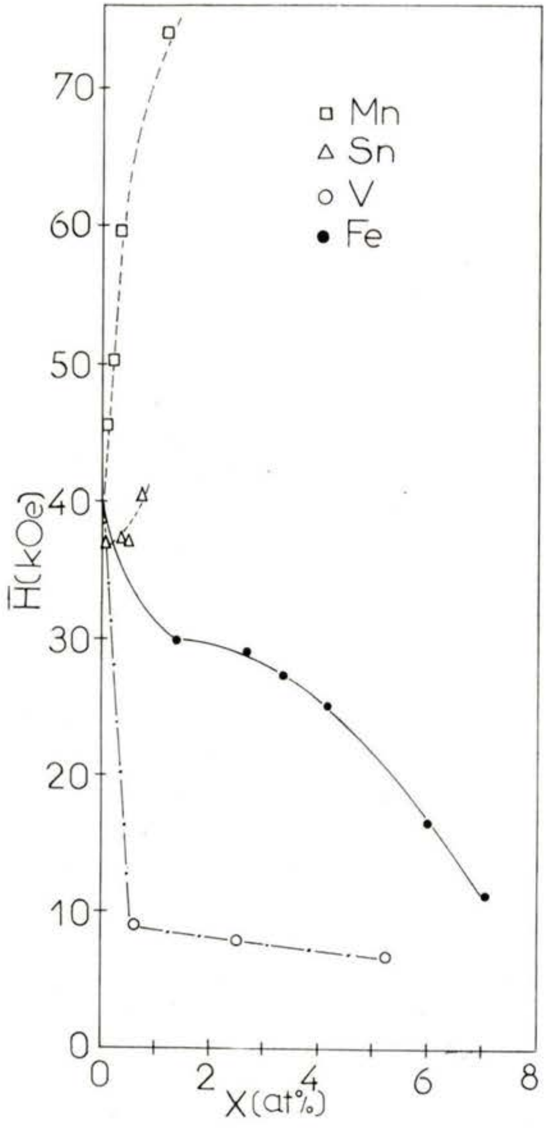

Fig. 1 — The average hf field, $\overline{H}$ versus solute atoms concentration, y, as deduced from room temperature $^{119}$Sn Mössbauer spectra [8].

The influence of different parameters like higher-order harmonics, their amplitudes and signs, on SDW has been recently studied by means of model calculations [7]. It has been shown that $^{119}$Sn Mössbauer-spectra sensitively depend on them.

As is well known the antiferromagnetic properties of chromium depend very much on foreign atoms. In terms of SDW it means that their properties are substantially modified by those atoms. In particular, vanadium is known to drastically quench SDW, while manganese acts in an opposite direction as it increases the amplitude of SDW and their wavelength finally making the SDW commensurate. Our recent investigation of several Cr-based alloys with Mn, V. Fe and Sn, by means of $^{119}$Sn MES has clearly shown that such conclusion can also be drawn from the Mössbauer spectra [8]. Figure 1 illustrates the average $^{119}$Sn hyperfine field versus the impurity concentration. We note that the above-mentioned influence of the impurities on SDW can be readily seen from that figure.

## REFERENCES

[1] FAWCETT, E., Rev. Mod. Phys., **60**, 209 (1988) and references therein.

[2] WERTHEIM, G. K., J. Appl. Phys., **32**, 110S (1961).

[3] PEPPER, A. R. and STREET, R., Proc. Phys. Soc. (London), **87**, 971 (1966).

[4] STREET, R. and WINDOW, B., Proc. Phys. Soc. (London), **89**, 587 (1966).

[5] DUBIEL, S. M., Phys. Rev., **B29**, 2816 (1984).

[6] DUBIEL, S. M. and LE CAËR, G., Europhys. Lett., **4**, 487 (1987).

[7] LE CAËR, G. and DUBIEL, S. M., to be published.

[8] DUBIEL, S. M., to be published.

# THE INFLUENCE OF INEQUIVALENT COBALT SITES ON THE SPIN AND ORBITAL MAGNETIC MOMENTS IN $YCo_5$

BARBARA SZPUNAR and VEDENE H. SMITH, JR.
Department of Chemistry, Queen's University, Kingston, Ontario, Canada K7L 3N6

*ABSTRACT* — Self-consistent band calculations for $YCo_5$ have been performed with the linear-muffin-tin-orbital, atomic-sphere approximation (LMTO-ASA) method. In contrast to earlier calculations in the literature, the 2c and 3g cobalt sites were not constrained to be equivalent. The resulting differences in the local electronic and magnetic structure of these cobalt sites are discussed.

Intermetallic rare earth-transition metal compounds, such as $Nd_2Fe_{14}B$, are known to be useful as permanent magnets. In order to understand these compounds, calculations of their electronic and magnetic structures would be invaluable. The crystal structure of $Nd_2Fe_{14}B$, for example, is very complicated and *ab initio* calculations would be very time consuming because there are 68 atoms per unit cell. However, these compounds have a tetragonal crystallographic structure which is related to the hexagonal $CaCu_5$ structure [1] (see Figure 1). As a result it is hoped that an accurate analysis of the simpler R(rare-earth)$Co_5$ compounds will lead to realistic progress in understanding the magnetic properties of these very complex compounds.

The first calculation [2] of the magnetic properties of such a compound $YCo_5$ were made using the self-consistent augmented plane-wave (APW) method but with the constraint of equivalence of both types (2c and 3g) of cobalt sites (see Fig. 1). This meant that the results could not predict a local magnetic anisotropy although it is known from polarized neutron diffrac-

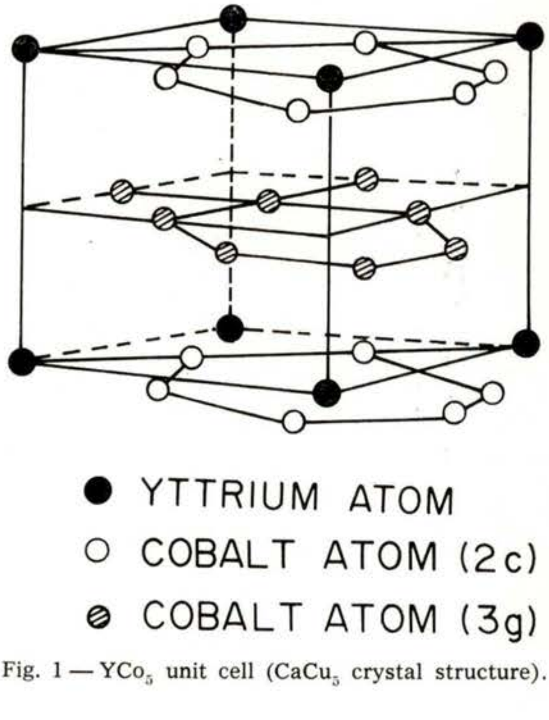

Fig. 1 — $YCo_5$ unit cell ($CaCu_5$ crystal structure).

*Portgal. Phys.* — Vol. 19, fasc. 3-4, pp. 225-228, 1988

tion [3] and NMR experiments [4] that there is a significant difference between the magnetic properties of these sites.

Subsequent theoretical calculations [5] of the local orbital moments by means of the recursion method supported the experimental results, namely that the two cobalt sites have different magnetic properties. On the other hand Kurihare et al. [6] found very poor agreement with experiment calculations of the anisotropy constants unless the drastic assumption was made that there were very small differences ($\sim 10^{-3}$) in the number of electrons for the different directions of magnetization.

The purpose of the present study was to investigate this problem by means of electronic structure calculations without the constraint of equivalent cobalt sites. The calculations were made using the linear muffin-tin orbital (LMTO) atomic sphere approximation (ASA) method [7-9] which is based on local spin-density (LSD) functional theory. This method is known to be quite good for close packed systems and has been successfully used for the study of rare earth and transition metals.

In the present self-consistent calculations, a basis set of s, p, d and f partial waves was used for the valence electrons

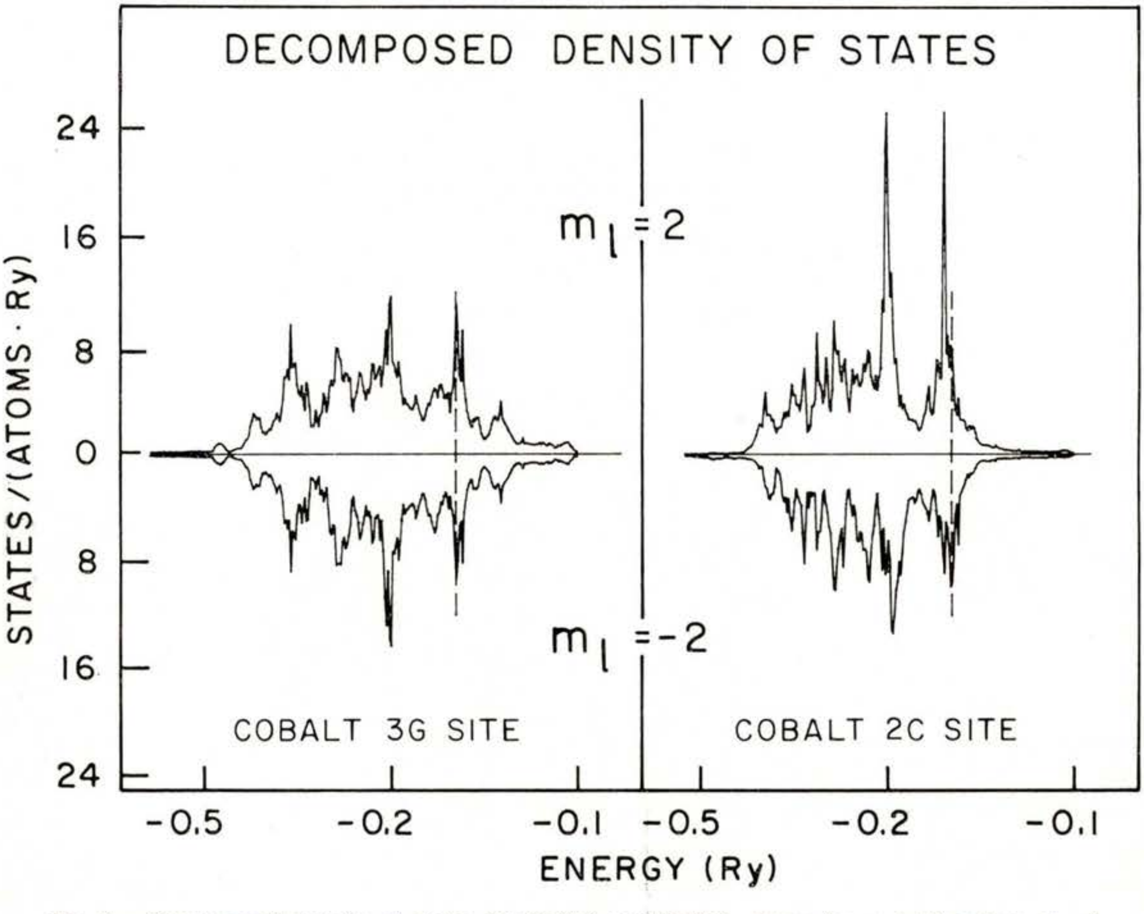

Fig. 2 — Decomposed density of states for Co(3g) and Co(2c) atoms for $m_l = 2$ and $m_l = -2$.

with the frozen core approximation (argon-like and krypton-like cores were used respectively for the cobalt and yttrium atoms). The von Barth-Hedin local (spin) density approximation was used to describe the exchange-correlation energy [10]. Calculations were made both with and without spin-orbit coupling — all other quasi-relativistic corrections were included.

It was noticed previously [2] in the case of the constrained self-consistent calculation that convergence was difficult for $YCo_5$. It is even more difficult when the two types of cobalt sites are allowed to differ. Convergence was obtained only by assuming a small mixing parameter (5 %) in the iterative process. Ninety points were sampled in the irreducible wedge of the Brillouin zone and the density of states (DOS) was integrated with an energy step of 0.5 mRy.

The convergence problem is probably due to the high density of states (DOS) of the minority spin electrons at the Fermi energy. In fact the peak of the minority spin DOS is at the Fermi energy. This is in agreement with experimental expectations [11] and also with previous calculations [2, 12].

There is not much difference between the band structure of pure cobalt [13] and that of $YCo_5$. The number of occupied d states is almost the same (pure cobalt $n_{d\uparrow\downarrow} = 7.515$ [13]) but in $YCo_5$ the minority d bands of cobalt are squeezed to lower energies due to different lattice parameters and hybridization with the yttrium d electrons. The main difference between the two different cobalt sites is that the DOS around the Fermi energy on Co(2c) is higher than on Co(3g).

The Fermi energy is shifted from $-0.1134$ Ry without spin-orbit coupling to a higher value of $-0.0963$ Ry with spin-orbit coupling. The calculated spin contributions to the magnetic moment [Co(2c): $1.29\,\mu_B$, Co(3g): $1.44\,\mu_B$ and Y: $-0.37\,\mu_B$] are in very good agreement with experiment [11]. The difference between the local orbital moment on the 2c and 3g sites was calculated to be equal to $0.18\,\mu_B$ The main contribution to this difference is due to the d electrons with azimuthal orbital quantum number $m_l = \pm 2$ on the Co(2c) and Co(3g) sites. The decomposed density of states for $m_l = \pm 2$ is presented in Fig. 2. There are two remarkable peaks on the Co(2c) site for $m_l = 2$. These peaks are the main contributors to the orbital moment on the Co(2c) site. The peak closer to the Fermi energy is due to the minority spin electrons on this site. We suggest that this feature of the electronic density on the Co(2c) site is responsible for the high anisotropy on this site.

Support of this research by the Natural Sciences and Engineering Research Council of Canada is gratefully acknowledged.

## REFERENCES

[1] D. GIVORD, M. S. LI and F. TASSET, J. Appl. Phys. **57**, 4100 (1985).

[2] S. K. MALIK, F. J. ARLINGHAUS and W. E. WALLACE, Phys. Rev. B **16**, 1242 (1977).

[3] J. SCHWEIZER and F. TASSET, J. Phys. F: Metal Phys. **10**, 1 (1980).

[4] R. L. STREEVER, Phys. Lett. **65A**, 360 (1978); Phys. Rev. B **19**, 2704 (1979).

[5] B. SZPUNAR and W. E. WALLACE, Lant. Act. Res. **1**, 335 (1986).

[6] K. KURIHARE, S. OHTSUKA, T. UKAI and N. MORI, Physica **130B**, 317 (1985).

[7] O. K. ANDERSEN, Phys. Rev. B **12**, 3060 (1975).

[8] H. L. SKRIVER, The LMTO Method, (Springer, Berlin, 1984).

[9] O. K. ANDERSEN, O. JEPSEN and D. GLOTZEL, in *Highlights of Condensed Matter Theory*, Proceedings of the International School of Physics, Enrico Fermi, Varenna, July 1983, edited by F. BASSANI *et al.* (Elsevier, Amsterdam, 1985).

[10] U. VON BARTH and L. HEDIN, J. Phys. C **5**, 1629 (1972).

[11] D. GIVORD, J. LAFOREST, R. LEMAIRE and Q. LU, J. Magn. Mat. **191**, 31 (1983).

[12] B. SZPUNAR, J. Phys. F: Metal Phys. **12**, 759 (1982); Physica **130B**, 29 (1985).

[13] B. SZPUNAR and P. STRANGE, J. Phys. F: Metal Phys. **15**, L165 (1985).

# ELECTRONIC AND MAGNETIC STRUCTURE OF SUPERCONDUCTING COPPER OXIDES

BARBARA SZPUNAR and VEDENE H. SMITH, JR.
Department of Chemistry, Queen's University, Kingston, Ontario, Canada K7L 3N6

*ABSTRACT* — The results of self-consistent spin-polarized band structure calculations on $YBa_2Cu_3O_6$ and $YBa_2Cu_3O_7$ are discussed. For $YBa_2Cu_3O_6$ a locally stable metamagnetic state is found with antiferromagnetic ordering of the copper magnetic moments in the Cu2-O plane, and with a Peirels-type gap around the Fermi energy such that it is a semiconductor. For $YBa_2Cu_3O_7$, results for a forced ferromagnetic state are discussed. The Cu1 sites in both compounds are not likely to form substantial local magnetic moments.

## 1 — INTRODUCTION

The recent, continuing, discoveries of classes of compounds containing copper oxide planes, some of whose members are superconductors with unusually high transition temperatures $T_c$, has prompted a large number of theoretical efforts to identify the mechanisms responsible and to understand the structure of these compounds.

To this end a series of self-consistent band structure calculations have been performed in our laboratory for several of the new families of materials namely the doped $La_{2-x}M_xCuO_4$ family, the $YBa_2Cu_3O_{6+y}$ family and more recently the $Tl_2Ba_2Ca_nCu_{n+1}O_{2n+6}$ and $Bi_2Sr_2Ca_nCu_{n+1}O_{2n+6}$ $(n = 0, 1, 2, 3)$ families.

In our studies we perform self-consistent band structure calculations using the linear muffin-tin orbital (LMTO) atomic sphere approximation (ASA) method [1] which is based on the local spin density (LSD) functional approximation (Hohenberg-Kohn-Sham). The exchange-correlation energy is described using either the von Barth-Hedin [2] or Vosko-Wilk-Nusair [3] approximations. These two potentials yield similar results but the calculations converge more rapidly with the latter. Spin-orbit coupling is usually neglected but all other quasi-relativistic effects are always included. Our calculations are either non-spin polarized or spin-polarized as appropriate for the problem under consideration. For spin-polarized calculations of metamagnetic antiferromagnetism, particular care must be taken in choosing a sufficient number of *k* points in the irreducible wedge of the Brillouin zone. The LMTO-ASA method is very suitable for such calculations as it is very transparent, quite efficient and appears to mimic well the results of calculations with highly precise methods such as (FP) LAPW.

*Portgal. Phys.* — Vol. 19, fasc. 3-4, pp. 229-232, 1988

## 2 — COMPARISON OF $YBa_2Cu_3O_6$ AND $YBa_2Cu_3O_7$

In an early study [4] we showed for $YBa_2Cu_3O_7$ the importance of the oxygen *p* electrons which dominate the density of states (DOS) in the region around the Fermi energy. In contrast, it is found for $YBa_2Cu_3O_6$ that Cu *d* electrons dominate the DOS in that region and are presumably

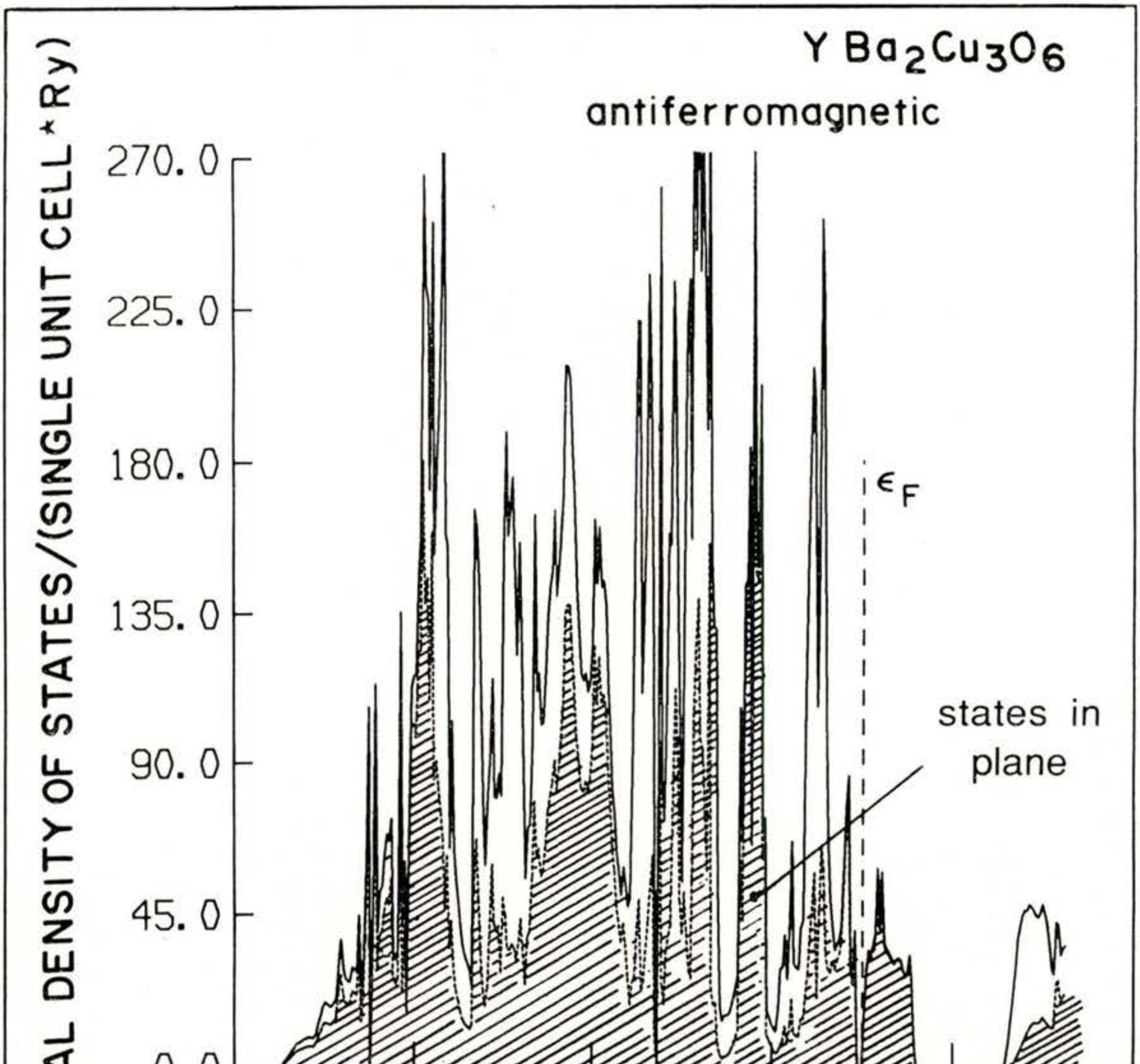

Fig. 1 — Density of states for the meta antiferromagnetic solution for $YBa_2Cu_3O_6$.

responsible for the magnetic interactions.

These non-spin polarized calculations exhibited metallic behaviour for both compounds. One would expect that the insulating character of $YBa_2Cu_3O_6$ (and $La_2CuO_4$) is related to the antiferromagnetic ordering expected (and now observed) at low temperatures. Spin-polarized calculations within the LSD approximation for $La_2CuO_{4-y}$ have not yet succeeded in finding a stable AFM ground state with an insulating gap.

Prior to the experimental determination [5] of the AFM structure of $YBa_2Cu_3O_6$, we demonstrated [6] that it was possible to find a stable insulating ground state. This calculation was done by forcing the AFM ordering for a half-filled band until an AFM «Peirels gap» opens up at the Fermi energy due to the doubling of the unit cell. The removal of the forcing magnetic field does not destroy the gap and the self-consistent solution subsequently obtained. The gap was called a «Peirels gap» as the effect of AFM ordering on the electronic structure is analogous to the Peirels lattice distortion effect.

This solution is analogous to metamagnetism [7]. Stability was only possible by the use of a large number of *k* points (≧ 108/irreducible wedge of the Brillouin zone).

In this calculation [6], a ferromagnetic (FM) ordering between the planes was assumed. We report now the results of assuming an AFM ordering between the planes. In Fig. 1 the DOS is shown for the stable AFM solution. As is always found in the LSD approximation, the gap at the Fermi energy, 0.1 eV, is smaller than experimentally found (~2 eV). Alternating moments of $0.3\,\mu_B$ were found on the Cu2 atoms (in the CuO plane) which are smaller than the experimental values ($\sim 0.5\,\mu_B$). Zero moments were found on the Cul and oxygen sites. The spherically averaged spin density of Cu2 atoms is presented in Fig. 2. The maximum is at a distance of 0.56 a. u. from the centre of a Cu2 atom.

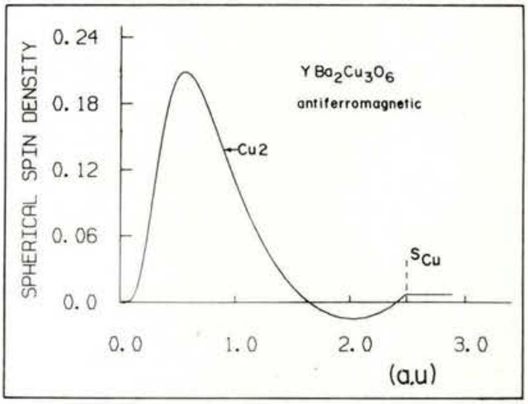

Fig. 2 — Spherically averaged spin density about a Cu2 atom in $YBa_2Cu_3O_6$ from the meta antiferromagnetic solution.

Forced FM calculations for $YBa_2Cu_3O_7$, (which collapse to the paramagnetic when the forcing field is removed) show that a very small moment can be formed on

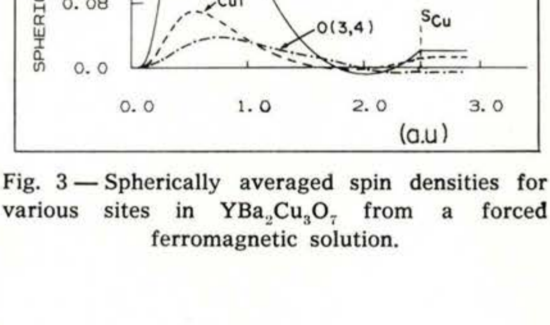

Fig. 3 — Spherically averaged spin densities for various sites in $YBa_2Cu_3O_7$ from a forced ferromagnetic solution.

Cu1 atoms in contrast to the case in $YBa_2Cu_3O_6$ where the Cu1 atoms are isolated and do not contribute to the DOS at the Fermi energy. In Fig. 3, the spherically averaged spin density is shown for the forced FM solution for $YBa_2Cu_3O_7$.

The stability of a moment in these compounds is dependent on the oxygen content. However the local moment on Cu2 site is very similar in both phases. This suggests that the moment in $YBa_2Cu_3O_7$ may be oscillating such that no static moment is observed.

Support of this research by the Natural Sciences and Engineering Research Council of Canada and the Ontario Centre for Materials Research is gratefully acknowledged.

## REFERENCES

[1] O. K. ANDERSEN, Phys. Rev. **B12**, 3060 (1975); H. L. SKRIVER, The LMTO Method, (Springer, Berlin, 1984); O. K. ANDERSEN, O. JEPSEN and D. GLOTZEL, in *Highlights of Condensed Matter Theory*, Proceedings of the International School of Physics, Enrico Fermi, edited by F. BASSANI *et al.* (Elsevier, Amsterdam, 1985).

[2] U. VON BARTH and L. HEDIN, J. Phys. **C5**, 1629 (1972).

[3] S. H. VOSKO, L. WILK and M. NUSAIR, Can. J. Phys. **58**, 1200 (1980).

[4] B. SZPUNAR and V. H. SMITH, JR., Phys. Rev. **B37**, 7525 (1988).

[5] J. M. TRANQUADA *et al.*, Phys. Rev. Lett. **60**, 156 (1988).

[6] B. SZPUNAR, V. H. SMITH, JR. and R. W. SMITH, Physica **C152**, 91 (1988).

[7] E. P. WOHLFARTH and P. RHODES, Phil. Mag. **7**, 1817 (1962).

# MAGNETISATION DENSITY DISTRIBUTION IN AN ORGANO-BIMETALLIC COMPLEX OF Cu(II), Ni(II)

B. GILLON
Laboratoire Léon Brillouin (CEA-CNRS), CEN-Saclay
91191 Gif-sur-Yvette cedex, France

Y. JOURNAUX, O. KAHN
Laboratoire de Spectrochimie des Eléments de Transition,
ERA 672, Université Paris-Sud, 91405 Orsay cedex, France

Organo-bimetallic complexes of 3d transition metals present a large variety of intramolecular magnetic interactions, at long distance, between the 3d ions, depending on the number and the nature of the ligands surrounding each metal. The determination of the magnetisation density in such systems, using the Polarised Neutron Diffraction method, yields direct information about the magnetic coupling and the role of the atoms of the organic bridge relating the metal ions.

In the complex Cu(Salen) Ni(hfa)$_2$, two oxygen atoms from the central bridge between the $Cu^{2+}$ and $Ni^{2+}$ ions:

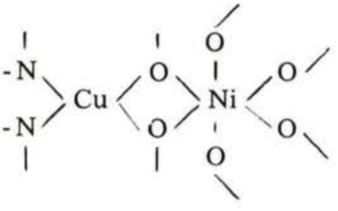

The experimental study was performed on the polarised neutron diffractometer 5Cl at the LLB in Saclay (France). Two sets of data have been collected using a lifting counter, for two different orientations (**a** vertical, then **b** vertical) of the same single crystal, at 2K, under an applied field of 5 teslas. The whole set of 362 reflections permitted to determine the three-dimensional image of the magnetisation density, using a multipole refinement method. A strong positive density on the Nickel and a weak negative density on the Copper are observed, in agreement with a fundamental doublet spin state. The spin delocalisation on the ligands is discussed.

# SPIN AND ORBITAL EFFECTS IN 5F COMPOUNDS

G. H. LANDER and M. WULFF
Commision of the European Communities, Joint Research Centre
European Institute for Transuranium Elements
Postfach 2340, D-7500 Karlsruhe
Federal Republic of Germany

*ABSTRACT* — The 5*f* electrons that surround the nucleus of the light actinide elements (U, Np, Pu, and Am) behave in a different way to the 4*f* electrons that one finds in the lanthanide series. The large spatial extent of these 5*f* electrons means that they interact strongly with electrons belonging to neighbouring atoms. In this sense, of course, they are not unlike 3*d* electrons. However, their *f* quantum number means that they have a strong orbital character. What happens to this orbital character when there is a strong hybridization between the 5*f* electrons and neighbouring *d* or *p* electrons? This is an important question in actinide physics. It has been addressed by theory and in this paper we shall discuss neutron experiments that address this issue.

In the light actinides with less than a half-filled shell the orbital (L) and spin (S) moments are opposite if we follow Hund's rule and Russell-Saunders coupling. The magnetization densities of the L and S components have a different spatial density. Thus, we can imagine a cancellation of L and S when integrated over all space, but for a certain Q (scattering vector) a finite moment exists. We will discuss the unusual magnetic form factors of PuSb, $PuFe_2$, and $UFe_2$ that demonstrate this point.

## REFERENCES

PuSb: G. H. LANDER et al., Phys. Rev. Letters **53**, 2262 (1985).

$PuF_2$: M. WULFF et al., Phys. Rev. **B37**, 5577 (1988).

$UF_2$: M. WULFF et al., Phys. Rev. **B39**, 4719 (1989).

See also M. WULFF et al., Europhysics Letters **11**, 269 (1990).

B. LEBECH, et al., J. Phys. Cond. Matt. **1**, 10, 229 (1989).

# COEXISTENCE OF MAGNETIC AND NON MAGNETIC CERIUM IN $Ce_2Sn_5$ AND $Ce_3Sn_7$ *

J. X. BOUCHERLE, J. SCHWEIZER and A. STUNAULT
DRF/SPh-MDN, CEA, CENG, 85X, 38041 Grenoble Cedex, France.

F. GIVORD
Lab. Louis Néel, CNRS, 166X, 38042 Grenoble Cedex, France.

P. LEJAY
CRTBT, CNRS, 166X, 38042 Grenoble Cedex, France.

The compound $CeSn_3$ is a typical intermediate valence system, with a very weak value of the magnetic susceptibility at low temperatures [1]. The two neighboring phases $Ce_2Sn_5$ and $Ce_3Sn_7$ are both superstructures of cubic $CeSn_3$ ($AuCu_3$ type) obtained by ordered substitutions of atoms [2]. Contrarily to $CeSn_3$, they are magnetic and order at low temperatures (2.9 K for $Ce_2Sn_5$ and 5.1 K for $Ce_3Sn_7$) [3].

Using polarized neutrons, we have investigated the magnetization density for the two compounds. Experiments were carried out at different wavelengths, ranging from 0.84 Å to 0.5 Å (LLB-5C1, ILL-D3), on large single crystals. $Ce_2Sn_5$ anisotropy: for both compounds, magnetization is much higher when the magnetic zation is much higher when the magnetic field is applied along **a** [3]. The samples were mounted in a cryomagnet (H = 4.6T), with their **a** axis vertical and parallel to the field [4]. The Fourier transform of the magnetic structure factors $F_M$ gives the projection of the magnetization density along the **a** axis. In the two compounds the maps (Fig. 1) show a different behavior for the two crystallographic sites of Ce: the $Ce_I$ site, which has practically the same environment as cerium in $CeSn_3$ (12 first neighbors which are all Sn atoms), is non magnetic in $Ce_2Sn_5$ and $Ce_3Sn_7$, as in $CeSn_3$ On the contrary, the $Ce_{II}$ site, which corresponds to the substitution zones at the origin of the superstructures, carries all the magnetization. Its environment is different from the previous site: among the 12 first neighbors of $Ce_{II}$, 10 are Sn atoms but 2 are $Ce_{II}$ atoms.

From the measured magnetic structure factors, the form factors of the $Ce_{II}$ atoms have been obtained for the two compounds. They can be compared with those calculated in an atomic model for a 4f ion. The parameters of this model based on

---

* Part of thesis work of A. Stunault (Grenoble University — 1988).

crystal field and exchange are deduced from magnetic studies [3]. In $Ce_2Sn_5$, these experiments can only be explained with an extra moment reduction of Kondo-type close to 0.8. In $Ce_3Sn_7$, no reduction coefficient is necessary. The calculated form factors are in good agreement with experimental values.

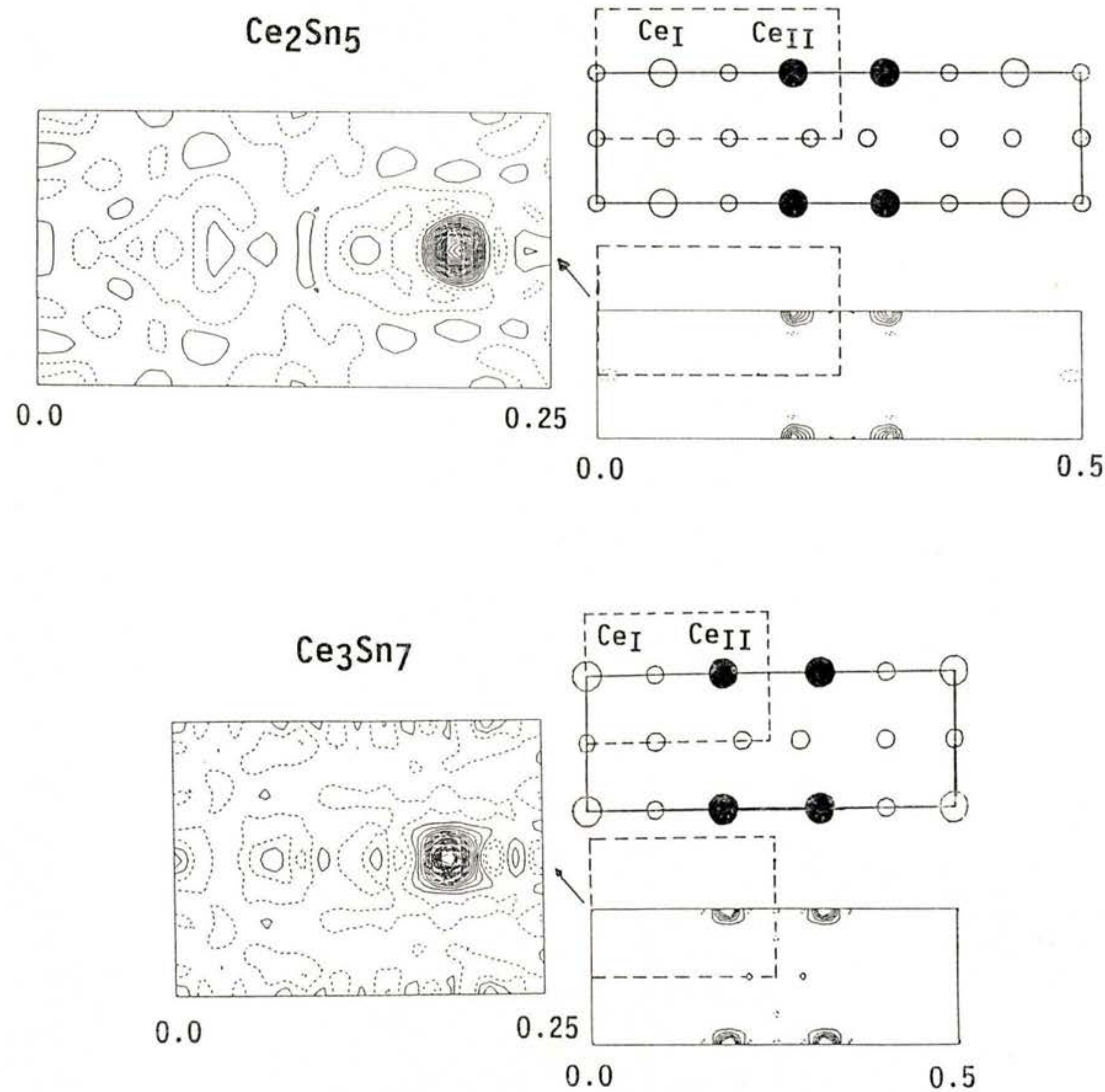

Fig. 1 — Projections of the magnetization density in the b-c plane: contours at $0.6\,\mu_B/\text{Å}^2$ for the 1/2 cell and $0.2\,\mu_B/\text{Å}^2$ for the 1/4 cell (negative contours in dashed lines).

In conclusion, the study of the magnetization density by polarized neutron diffraction was a fundamental experiment to understand the magnetic behavior of the superstructures based on the $CeSn_3$ structure. In these compounds, two types of Ce exist: one is nearly non-magnetic, of $CeSn_3$ type, the second is magnetic and can be very well described as a 4f ion. However, depending on the compound, this magnetic $Ce_{II}$ presents slightly different behaviors. In $Ce_2Sn_5$, it is affected by a Kondo reduction of the moment which can be related to the modulated magnetic structure [5] (as in $CeAl_2$). At the opposite, in $Ce_3Sn_7$ the $Ce_{II}$ has a more classical magnetic behavior. This family of compounds based on the $CeSn_3$ structure, which are characterized by different ratios of magnetic and non--magnetic Ce, is very well adapted to the study of the disappearance of magnetism in the presence of a strong interaction between 4f electrons and conduction electrons.

## REFERENCES

[1] J. G. SERENI, J. Phys. **F10** (1980) 2831.

[2] J. X. BOUCHERLE, F. GIVORD, P. LEJAY, J. SCHWEIZER, A. STUNAULT, Acta Cryst, **B44** (1988) 377.

[3] M. BONNET, J. X. BOUCHERLE, F. GIVORD, P. LEJAY, J. SCHWEIZER, A. STUNAULT, J. de Phys. **49** (1988) C8-785.

[4] J. X. BOUCHERLE, F. GIVORD, P. LEJAY, J. SCHWEIZER, A. STUNAULT, Physica B **156** & **157** (1989) 809.

[5] F. GIVORD, P. LEJAY, E. RESSOUCHE, J. SCHWEIZER, A. STUNAULT, Physica B **156** & **157** (1989) 805.

# LOCALIZED MOLECULAR ORBITAL (LMO)/MULTIPOLE (M) FORMALISM FOR CHARGE AND SPIN DENSITY IN COMBINED REFINEMENT TO THEORETICAL X-RAY AND MAGNETIC DATA

T. KORITSÁNSZKY
Central Research Institute for Chemistry, Budapest, POB 17, 1525 Hungary

P. COPPENS
Chemistry Department, SUNY/BUFFALO, NY 14214, USA

*ABSTRACT* — Simultaneous fit of decoupled majority ($\alpha$) and minority ($\beta$) spin density parameters of one (Multipole) and two center (Localized Molecular Orbital) models to the combined, theoretical (RHF) X-ray and polarized neutron data of the Iron (III) hexaaquo ion was tested. Combined refinement is shown to be powerful in gathering information on not only the metal-ligand charge and spin transfer but the degree of covalency and the radial behavior of the decoupled spin densities, as well [1].

## 1 — FORMALISM

The model applicable to bot data sets is based on the decomposition of the density into paramagnetic ($\rho^a_\alpha \neq \rho^a_\beta$) and diamagnetic ($\rho^b_\alpha = \rho^b_\beta = \rho_b$) parts [2]. Thus for the charge ($\rho_c$ and the spin density ($\rho_s$)

$$\rho_c = 2\,\rho^b + \rho^a_\alpha + \rho^a_\beta \qquad \rho_s = \rho^a_\alpha - \rho^a_\beta$$

$\rho^b$ is described in terms of real spherical harmonics [3], while the paramagnetic metal-ligand subsystem $\rho^a$ is represented by bonding ($\psi$) and antibonding ($\psi^*$) LMO's, composed of symmetry adapted linear combinations of metal ($\Psi$) and ligand ($\varphi$) atomic orbitals:

$$\psi = N(\mu\Psi + \varphi) \qquad \psi^* = N^*(\Psi - \lambda\varphi)$$

The densities for $j = \alpha$ or $\beta$ spin are given by

$$\rho^{\mathrm{LMO}}_j = \rho_j + \rho^*_j = \Sigma_k\, n_{kj}\,|\psi_{kj}|^2 + \Sigma_k\, n^*_{kj}\,|\psi^*_{kj}|^2$$

where $n_{kj}$ and $n^*_{kj}$ are the occupancies of $\psi_{kj}$ and $\psi^*_{kj}$, respectively and the summation is taken over the occupied MO's.

## 2 — DATA SET

The $Fe(H_2O)_6$ ion of $T_h$ symmetry was placed in a cubic unit cell in space group $Pmm\bar{3}$ with a = 10.0 Å. In the asymmetric unit the atoms are situated at the positions: 24(1), 6(e) and 12(j) with the site symmetry $m\bar{3}$, mm2 and m for the Fe, O and H, respectively. From the occupied HFMO's 1375 independent reflections were generated. For the details of the RHF calculation we refer to [4]. Atomic valence populations Table 1), deformation charge (Figure 1a) and total spin density maps (Figure 1b) indicate that the charge transfer is "indirect" as it occurs at the expense of the charge at the hydrogens, while the spin is much more localized on the Fe-O bonds, directly determined by the single occupied $2e_g$ and $1t_g$ MO's.

## 3 — MULTIPOLE REFINEMENT

To fit the charge and spin densities to the combined data, decoupled $\alpha$ and $\beta$ spin populations of the symmetry-allowed spherical harmonics were adjusted up to hexadecapoles, octapoles and dipoles on the Fe, O and H, respectively. Although the total charges (Table 1) are similar to those obtained directly from the wavefunction, the result does not reproduce the details of the spin density on the ligands, where insignificant spin populations were found.

TABLE 1 — Summary of refinements in terms of valence orbital populations.

| | ATOM | ORBITAL | RHF | MULTIPOLE | LMO (A) | LMO (B) |
|---|---|---|---|---|---|---|
| CHARGE | Fe | $d_\sigma$ | 2.352 | 2.307(29) | 2.237(38) | 2.182(9) |
| | | $d_\pi$ | 3.070 | 3.075(30) | 2.962(40) | 3.059(9) |
| | O | $\sigma$ | 3.524 | 3.639(19) | 3.636(3) | 3.678(3) |
| | | $\pi$ | 3.503 | 3.390(21) | 3.399(3) | 3.440(3) |
| | H | s | 0.445 | 0.448(16) | 0.460(10) | 0.414(1) |
| SPIN | Fe | $d_\sigma$ | 1.856 | 1.777(29) | 1.891(3) | 1.818(9) |
| | | $d_\pi$ | 2.957 | 3.025(30) | 2.970(3) | 2.941(9) |
| | O | $\sigma$ | 0.023 | 0.029(19) | 0.018(1) | 0.030(2) |
| | | $\pi$ | 0.006 | 0.004(21) | 0.005(1) | 0.010(2) |
| | H | s | 0.001 | 0.0 | 0.0 | 0.0 |
| | NV | | | 27 | 22 | 17 |
| | NREF | | | 741 | 741 | 741 |
| | $R_x$ | | | 0.025 | 0.027 | 0.029 |
| | $R_N$ | | | 0.011 | 0.007 | 0.010 |

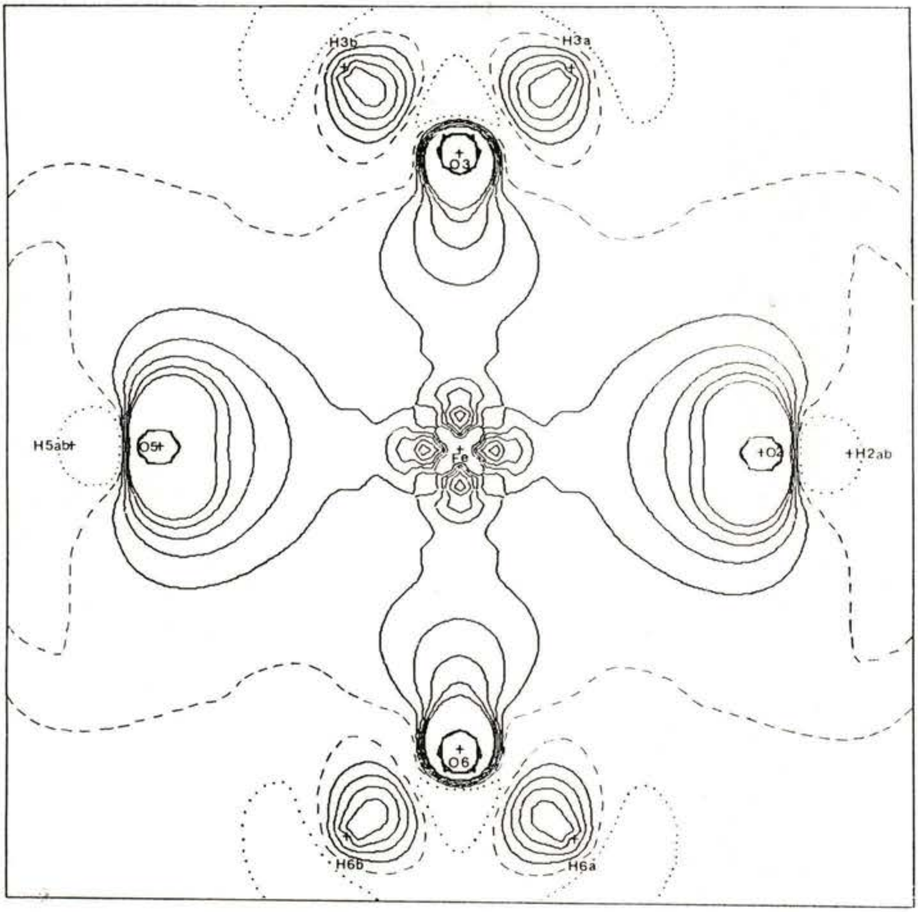

Fig. 1 (a) Deformation electron density in the X, Y plane calculated from the RHF MO's.
Contour intervals: 0.1 eÅ$^{-3}$. Negative contours dotted, zero dashed.

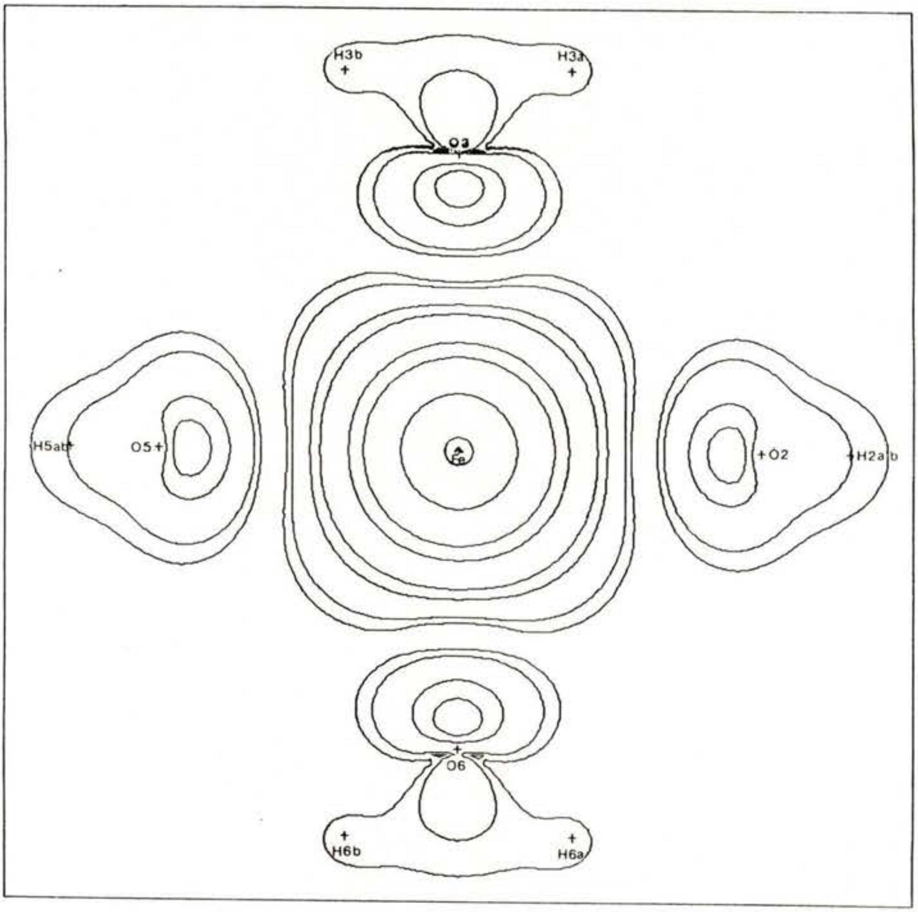

Fig. 1 (b) Total spin density in the X, Y plane calculated from the RHF MO's. Contours: (0.0, 0.005, 0.01, 0.05, 0.1, 0.5, 1.0, 5.0 μB).

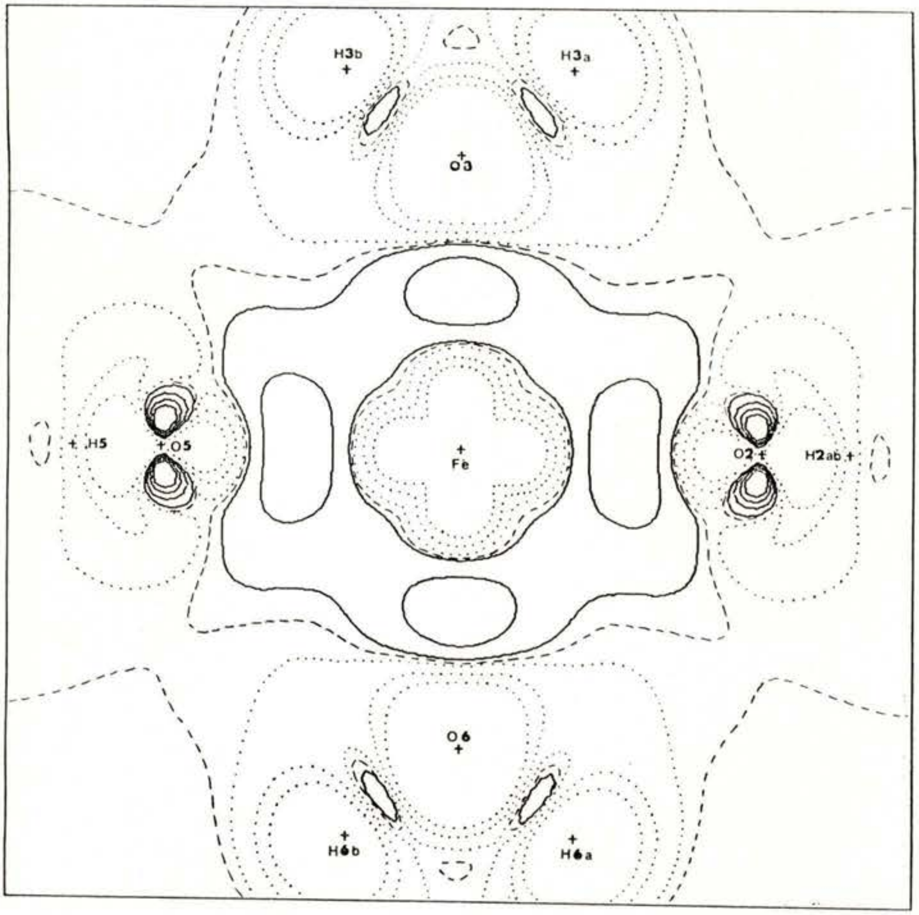

Fig. 2 (a) Residual charge density map in the X, Y plane ($\rho_c^{RHF} - \rho_c^{LMO(A)}$). Contours: (−0.1, −0.05, −0.01, 0.0, 0.01, 0.05, 0.1, 0.15 eÅ$^{-3}$).

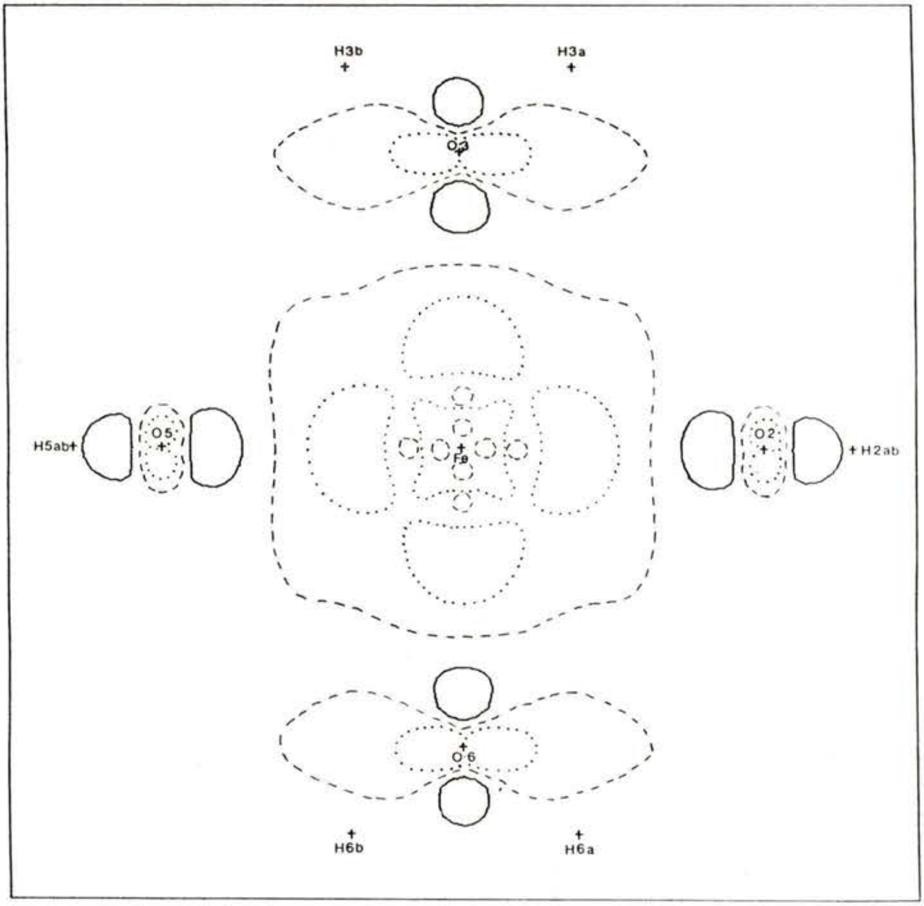

Fig. 2 (b) Residual spin density map in the X, Y plane ($\rho_s^{RHF} - \rho_s^{LMO(A)}$). Contours as in Figure 2 (a).

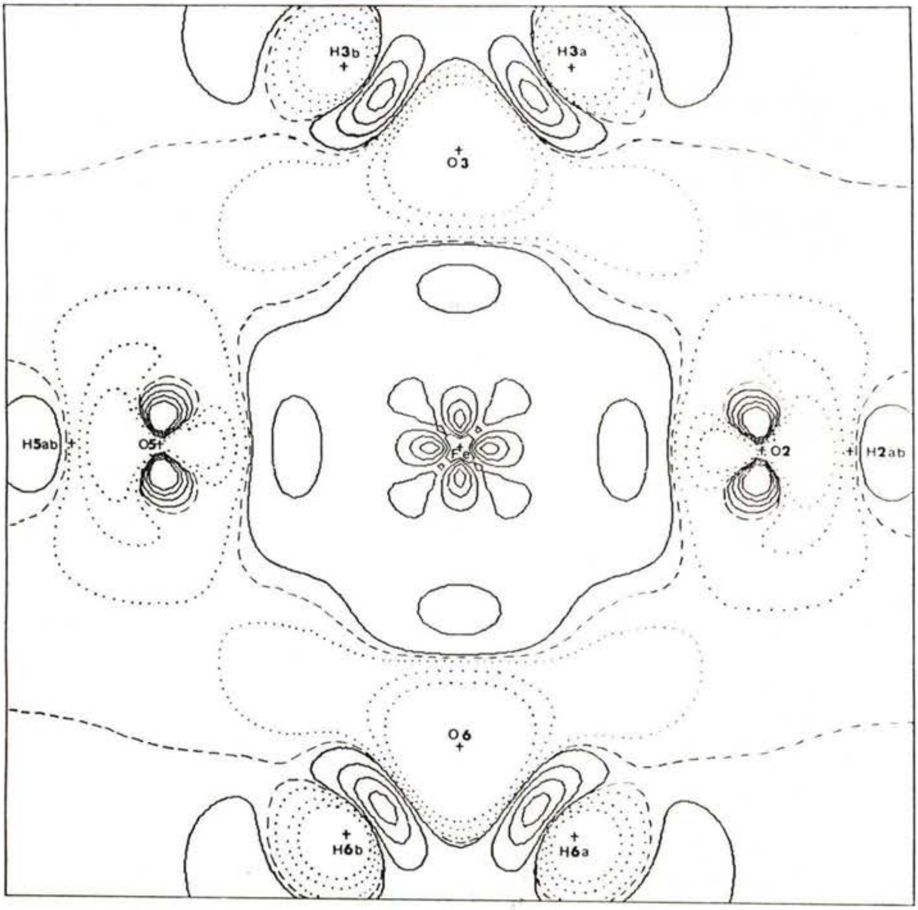

Fig. 3 (a) Residual charge density map in the X, Y plane ($\rho_c^{RHF} - \rho_c^{LMO(B)}$). Contours as in Figure 2.

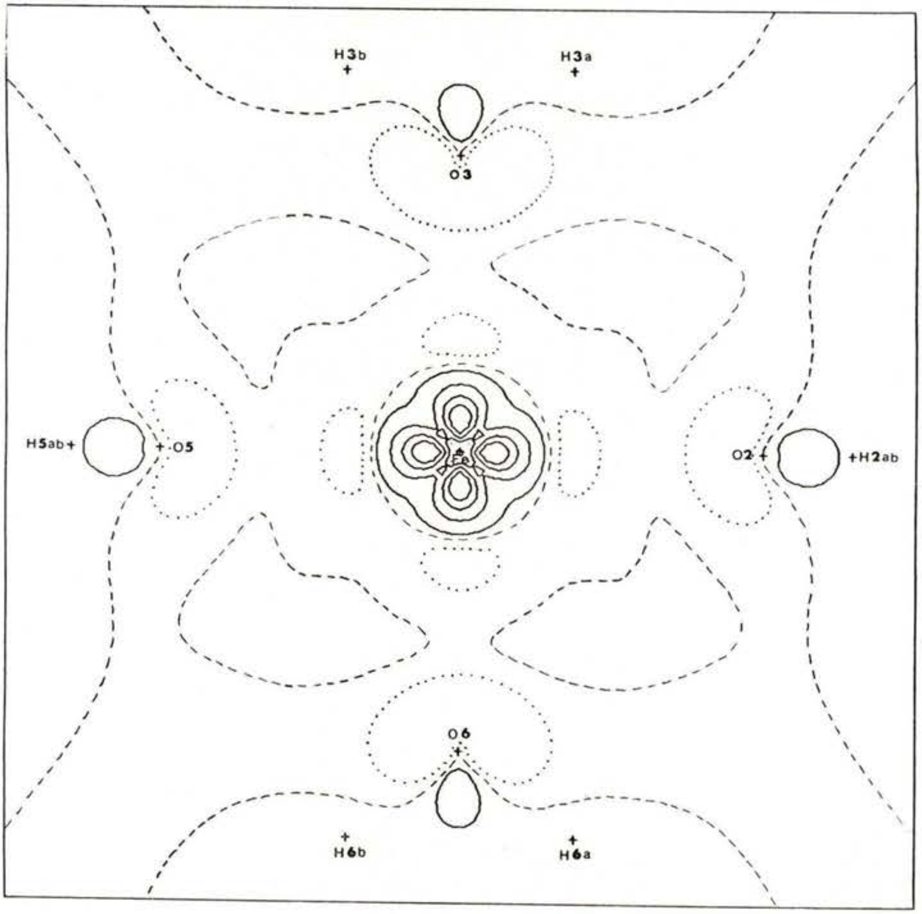

Fig. 3 (b) Residual spin density map in the X, Y plane ($\rho_s^{RHF} - \rho_s^{LMO(B)}$). Contours as in Figure 2.

## 4 — LMO REFINEMENTS

In model LMO(A) only the five d-electrons with $\alpha$ spin are treated in the MO level ($n^*_\alpha = 1$; $n_\alpha = n^*_\beta = n_\beta = 0$); the remaining part of the density representing the ligand electrons, is considered to be diamagnetic. In such a way the densities are connected through antibonding covalent interaction of the $\alpha$ electrons.

In LMO(B) a part of the diamagnetic density is represented by fully occupied bonding MO's ($n^*_\alpha = n_\alpha = n_\beta = 1, n^*_\beta = 0$). In this case $\rho^{\mathrm{LMO}}_\alpha$ corresponds to ionic configuration, thus the densities are connected through bonding covalent interaction of $\beta$ electrons. Results for both cases are summarized in Table 1.

## 5 — DISCUSSION

For transition metal complexes (orbital contribution is quenched) the magnetic properties are directly related to the highest, partially occupied MO's ($e_g$, $t_g$) of mainly antibonding, 3d character. Electrons accumulated between the atoms can only implicitly be accounted for by decomposing the density onto atomic centers. To some extent the overlap peaks can be projected to the one-center terms yielding good multipole estimation of Mulliken charges, but a loss of significant figures in the refined populations may occur. The multipole expansion may not show the local features of MO density if bond peaks have an important contribution to the scattering, as in the case of spin density.

The LMO treatment of the paramagnetic bonds turned out to be essential in modelling the spin density. The spin residual map (Figure 2b) demonstrates how well LMO(A) fits the spin distribution, but this model does not properly account for the O-Fe charge transfer, due to bonding MO's (Figure 2a). By extending the two center formalism to the bonding counterparts in LMO(B), a more satisfactory fit of charge density can be achieved (Figure 3a). This model can have special importance in representing the effect of spin polarization by the decoupled refinement of screening constants of radial functions for different spin densities ($\chi_\alpha$, $\chi_\beta$). The higher Fe-O spin transfer, demonstrated by the peak around the Iron on the spin residual map (Figure 3b), is caused by the increased $\mu_\beta$, with respect to $\mu_\alpha$ due to the different radial dependence ($\chi_\alpha > \chi_\beta$).

Support of this work by the National Science Foundation is gratefully acknowledged.

### REFERENCES

[1] Coppens, P.; Koritsánszky, T. & Becker, P., Chemica Scripta, **26**, 463-467 (1986).

[2] Becker, P. & Coppens, P., Acta Cryst. **A41**, 177-182 (1985).

[3] Hansen, N. K. & Coppens, P., Acta Cryst. **A34**, 909-921 (1978).

[4] Logan, J.; Newton, M. D. & Noell, J. O., Int. J. Quantum. Chem. Symp. **18**, 213-219 (1984).

# ELECTRON DEFORMATION DENSITY OF SACCHARIN DERIVATIVES

J. BUSCHMANN, R. RUDERT, P. LUGER
(Institut für Kristallographie, Freie Universität Berlin)

G. TRUMMLITZ
(Dr. K. Thomae GmbH, Biberach, Fed. Rep. Germany)

In the field of artificial sweeteners new non-nutritious compounds are sought which are superior to the present ones with respect to at least one property like strength and character of taste, stability against higher temperature or solubility in water. To get to the reasons why sweeteners have specific tastes we are doing structure and electron density investigations on sweet and bitter tasting saccharin derivatives.

Shallenberger and Acree (1967) [1] found that many sweet tasting compounds have two electronegative atoms with a distance of about 3 Å between them with one of them having a covalently bonded hydrogen atom, and Kier (1972) [2] added as another characteristic a hydrophobic molecular part away from the two electronegative atoms. Their AH-B-X criterion postulating two hydrogen bonds of opposite direction at that distance of about 3 Å from each other between the sweet molecule and the taste receptor can stand some substantiation from the side of quantum chemistry. Therefore, CNDO/2 calculations were done by Trummlitz (1985) [3] on several saccharin derivatives which differ in taste and rendered a higher negative charge for the keto-oxygen atom

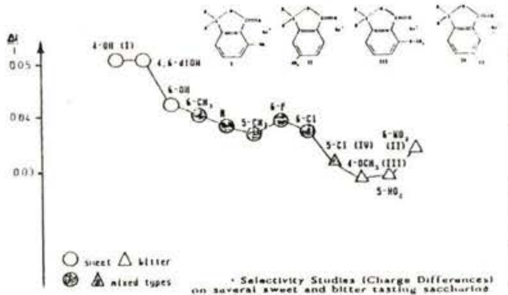

· Selectivity Studies (Charge Differences) on several sweet and bitter tasting saccharine derivatives
$I_O$, $I_N$ charge on O and N
$\frac{\Delta I}{I} = (I_O - I_N)/(I_O + I_N)$

Electron deformation density ($x$(LO)-$x$(HO)-Fourier synthesis map) in the molecular plane. Contour interval 0.1 e/Å$^3$

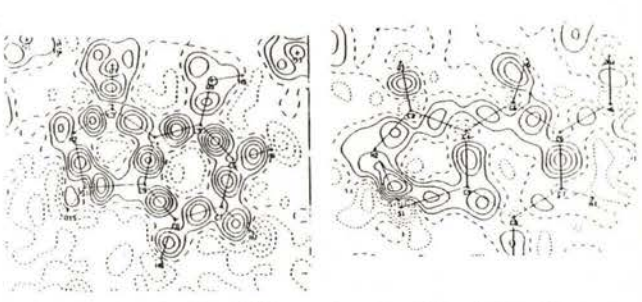

a) 4-Hydroxy-1,2-benzisothiazol-3(2H)-on-1,1-dioxide sodium salt (sweet taste)

b) 5-Nitro-1,2-benzisothiazol-3(2H)-on-1,1-dioxide sodium salt (bitter taste)

*Portgal. Phys.* — Vol. 19, fasc. 3-4, pp. 251-252, 1988

of the sweet tasting compounds than for that of the bitter tasting compounds. The left diagram shows this result, the horizontal is the taste axis — going from sweet to bitter —, and the vertical axis gives the relative charge difference between the keto-oxygen atom and the nearby nitrogen atom. On the right the cuts through the Fourier electron deformation density map in the molecular plane of one sweet and one bitter taste agent are shown. These maps are derived from X-ray data measured at 123 K. They look very different in the vicinity of the keto-oxygen atom.

The authors thank Dr. David Gregson for the experimental help at the SILOE reactor of the C. E. N. G. (France) and Prof. H. Fuess for making his low temperature single crystal diffractometer there available. This work has been funded by the German Federal Minister for Research and Technology (BMFT) under the contract number 03-LU1FUB-0, and by the Fonds der Chemischen Industrie.

## REFERENCES

[1] SHALLENBERGER, R. S., ACREE, T. E., Nature **216** (1967), 480.

[2] KIER, L. B., J. Pharm. Sci. **61** (1972), 1394.

[3] TRUMMLITZ, G. (1985), unpublished results.

# DEFORMATION DENSITY STUDIES OF TETRAMETHYLTHIURAM DISULFIDE, $(Me_2NCS_2)_2$ AND TETRAETHYLTHIURAM DISULFIDE, $(Et_2NCS_2)_2$

YU WANG and J. H. LIAO

Department of Chemistry, National Taiwan University, Taiwan, R. O. C.

*ABSTRACT* — Two thiouram disulfide compounds were studied by X-ray diffraction at low temperature. The room temperature structures were studied previously. [1]
at low temperature. The room temperature structures were studied previously. [1]
Tetramethylthiuram disulfide (1), monoclinic, C2/c; $T = 138K$, $a = 9.524\ (4)$, $b = 9.911\ (3)$, $c = 11.795\ (1)$ Å, $\beta = 99.22^\circ\ (1)$, $Z = 4$, $\lambda(MoK_\alpha) = .71069$ Å. Final $R = .031$ for 2881 reflections. Tetraethylthiuram disulfide (2), monoclinic, $P2_1/c$, $T = 105K$, $a = 10.922\ (3)$, $b = 15.946\ (4)$, $c = 8.444\ (1)$ Å, $\beta = 91.92^\circ\ (1)$, $\lambda(MoK_\alpha) = .71069$ Å. Final $R = .029$ for 5772 reflections. Both contain a disulfide bridge connecting two identical thiuram parts. Fig. 1 shows the geometry of tetraethylthiuram disulfide. The sulfur-sulfur bonds with length 2.0041(6), 2.0057 (6) Å respectively, are essentially single bonds. The tetramethyl derivative undergoes a phase transition at 133K, the high temperature molecular structure has a $C_2$ symmetry. There are $C = S$ double bond and $C - S$ single bond in both molecules. The accumulation of electron density along the $C - N$ and $C - S$ bonds in the experimental deformation density maps (see Fig. 2) are as expected. The lone pair feature around the sulfur atom is also observed (see Fig. 3). The peculiar appearance along the sulfur-sulfur bond is comparable to recent work containing the sulfur-sulfur bond [2]. Some theoretical model density calculations [3] could be adopted to give a reasonable explanation.

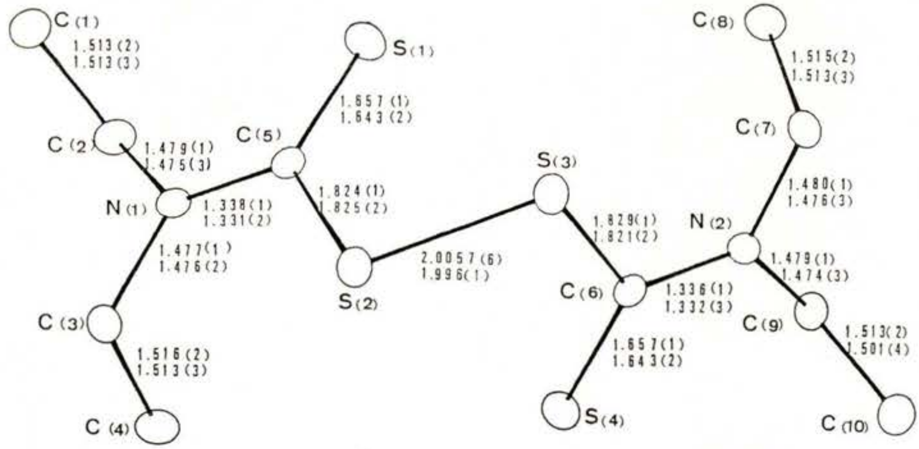

Fig. 1 — Molecular structures with selected bond lengths at both temperatures for compound 2. Top line distances are at low temperature (105K); bottom line are at room temperature.

*Portgal. Phys.* — Vol. 19, fasc. 3-4, pp. 253-254, 1988

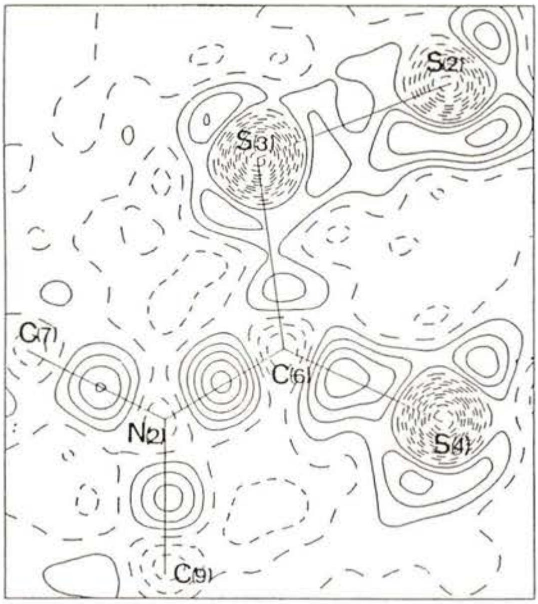

Fig. 2 — Deformation density maps af N2-C6-S4 of compound 2; solid line positive and dotted line zero and negative contours; contour interval 0.1 e$\AA^{-3}$.

In conclusion, the degree of the density accumulation at the midpoint of bonded atoms follows the order: shorter $C-N >$ $C-C \geqslant$ longer $C-N$, $C=S > C-S >$ $S-S$. Similar order was found in the other compound [4]. The features around sulfur nuclei indicate a substantial electron deficit at the center of sulfur atom and appear as residual density as expected for lone pair electron density. Similar effects were observed in other related compounds. [2, 5]

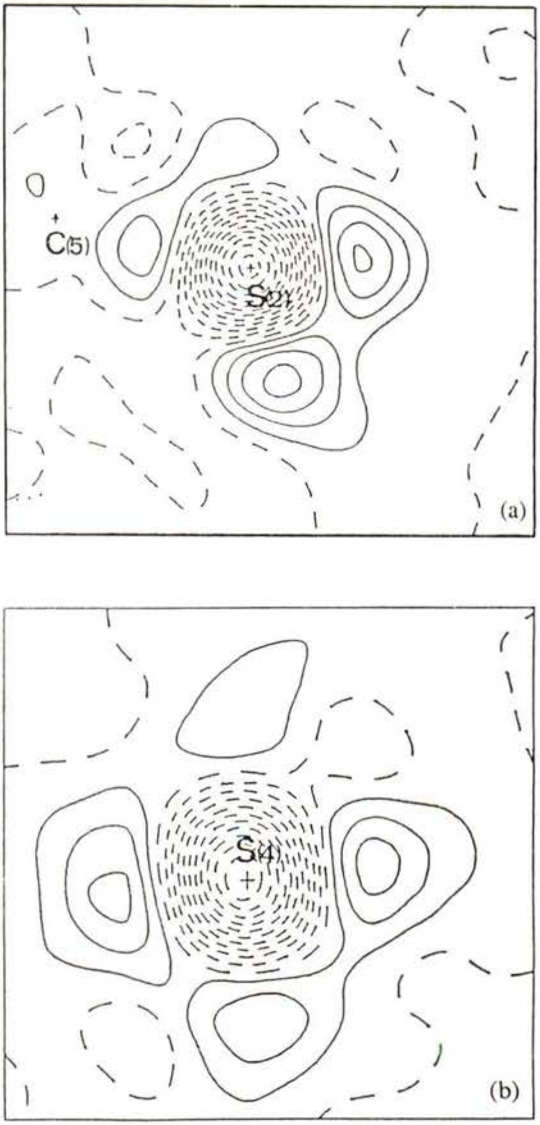

Fig. 3 — Deformation density maps *a*) at the plane which bisects C5-S2-S3; *b*) around S4 at a plane perpendicular to C6-S4; contours as in Fig. 2.

## REFERENCES

[1] WANG, Y.; LIAO, J. H. & UENG, C. H. (1986), Acta Cryst. **C42**, 1420-1423.

[2] WANG, Y.; CHEN, M. J. & WU, C. H. (1988), Acta Cryst. **B44**, 179-182.

[3] KUNZE, K. L.; HALL, M. B. (1987), J. Am. Chem. Soc. **109**, 7617-7623.

[4] DUNITZ, J. D.; SEILER, P. (1983), J. Am. Chem. Soc. **105**, 7056-7058.

[5] COHEN-ADDAD, C.; LEHMANN, M.; BECKER, P. (1984), J. Chem. Soc. Perkin II, 191-196.

# N-O BONDING ELECTRON IN p-NITROBENZENE DERIVATIVES

S. Ohba and Y. Saito

Department of Chemistry, Faculty of Science and Technology, Keio University,
Hiyoshi-3, Kohoku-ku, Yokohama 223, Japan

In the X-X and X-N maps of p-nitropyridine N-oxide at 30 K, the N-O bonding electron was not significantly observed [1]. However, the bonding peak was detected in $LiNO_2 . H_2O$ at 120 K [2]. An ab initio MO calculation using MIDI4 * basis set (double-zeta + polarization function) suggests that the deformation density is almost the same for $HNO_2$ and $NO_2^-$ [3]. The unknown factor is the interaction between the nitro group and the aromatic ring.

In the present work, the deformation densities of p-dinitrobenzene (1) and p-nitro-benzoic acid (2) has been determined at 120 K.

(1) $P2_1/n$, $Z = 2$, $2\theta_{max}$ (Mo $K\alpha$) $= 110°$, $R = 0.055$ for 2045 unique reflections.

(2) $A2/a$, $Z = 8$, $2\theta_{max} = 120°$, $R = 0.042$ for 3930 reflections.

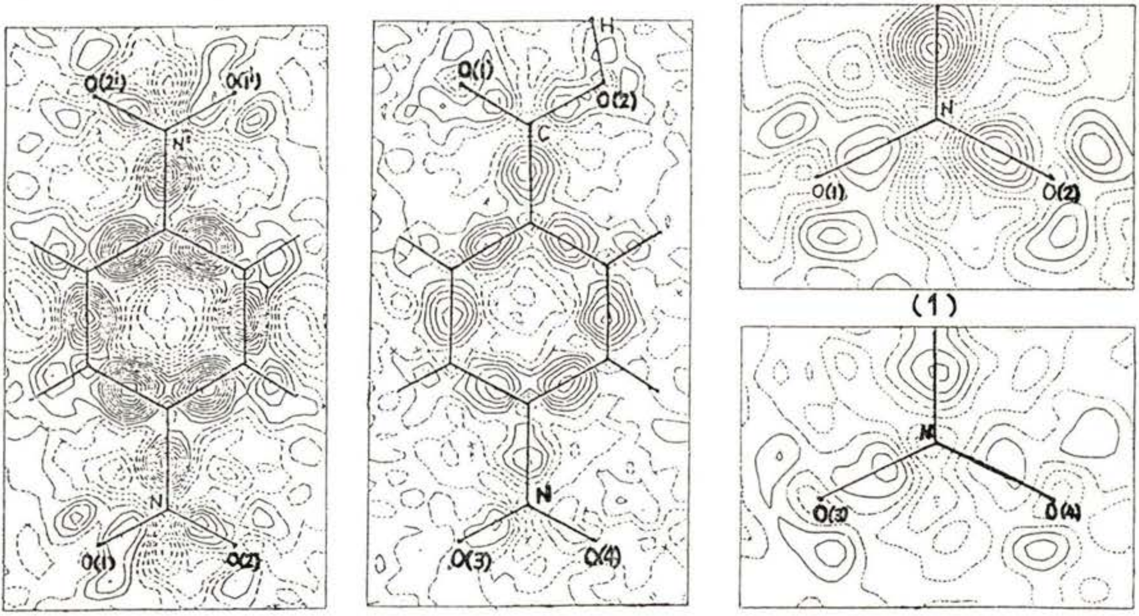

Fig. 1 — Deformation density. Contour interval 0.1 $e\text{Å}^{-3}$. $\sigma(\Delta\rho) = 0.05$ $e\text{Å}^{-3}$.

*Portgal. Phys.* — Vol. 19, fasc. 3-4, pp. 255-256, 1988

X-X maps on the benzene rings are shown in Fig. 1. The deformation densities on the nitro planes are also given, because the dihedral angles between the nitro group and the benzene ring are (1) 10.2° and (2) 14.8°. The N-O bonding peak as well as the lone-pair peaks of the terminal oxygen atoms are clearly observed.

## REFERENCES

[1] COPPENS, P. and LEHMANN, M. S., Acta Cryst., **B32**, 1777 (1976).

[2] OHBA, S., KIKKAWA, T. and SAITO, Y., Acta Cryst., **C41**, 10 (1985).

[3] KIKKAWA, T., OHBA, S., SAITO, Y., KAMATA, S. and IWATA, S., Acta Cryst. **B43**, 83 (1987).

# THE EXPERIMENTAL ELECTRON DENSITY DISTRIBUTION OF DICHLORO-BIS(TRIPHENYLPHOSPHINE)NICKEL(II)

LEE BRAMMER and EDWIN D. STEVENS

Department of Chemistry
University of New Orleans
New Orleans. Louisiana 70148, U.S.A.

*ABSTRACT* — The experimental electron density distribution of dichloro-bis (triphenylphosphine)nickel(II) has been studied using high-resolution single-crystal X-ray diffraction data. The molecule crystallizes in space group $P2/c$, with $Z = 2$, requiring two-fold molecular symmetry about the central nickel atom. The ligands adopt a tetrahedral coordination geometry leading to a paramagnetic electronic structure.

In modelling the electron density distribution, multipole deformation functions were used together with conventional structural parameters. In addition, third- and fourth-order cumulant anharmonic vibrational parameters were employed for the heavier atoms. Deformation density maps show features inconsistent with a simple tetrahedral crystal field model of metal-ligand bonding, leading to the suggestion that a degree of covalency may be present in these interactions. Supporting this assertion is the fact that the model gives a poor fit in the region around the nickel-chlorine vector leaving quite large residual features. However, an accumulation of electron density between all truly covalently bonded atom pairs is observed as there are peaks in the phosphorus lone-pair region, consistent with the principally σ-donor bonding mode of phosphine ligands.

## INTRODUCTION

It has long been noted that dihalogen-bis(tertiaryphosphine)nickel(II) complexes may exist as diamagnetic square-planar and/or paramagnetic tetrahedral isomers. The balance is a fine one and results from steric and electronic properties of the ligands as well as solvent and temperature effects [1, 2]. This balance is better documented crystallographically for the dibromo species, for which aliphatic phosphines are associated with square-planar and aromatic phosphines with tetrahedral structures [1-7]. Work on dichloro compounds supports this assertion [8-10]. Indeed the use of phosphines intermediate between aliphatic and aromatic can lead to a very delicate structural balance; for example $[NiBr_2\{PPh_2(CH_2Ph)\}_2]$ forms both square-planar and tetrahedral isomers which even cocrystallize [1].

The approximate structure of dichloro-bis(triphenylphosphine)nickel(II) and its paramagnetism were first established by Venanzi et al. [8, 11]. An accurate low-temperature structure determination has resulted from the work described here [12].

The metal has an approximately tetrahedral coordination sphere in accord with the observed paramagnetic electronic structure.

## EXPERIMENTAL

*Data Collection.* A dark blue-green crystal of $[NiCl_2(PPh_3)_2]$ with dimensions $0.47 \times 0.33 \times 0.38$ mm, grown under a nitrogen atmosphere by slow evaporation from absolute ethanol solution, was used for data collection. Having determined the unit cell parameters by a least-squares fit to 25 reflections with $48^\circ < 2\Theta < 56^\circ$, a total of 25248 intensity measurements were made (excluding those of 6 standard reflections which were remeasured every 2h to allow correction for any crystal decay or primary beam fluctuations). Data were collected at 94(1) K using an *Enraf-Nonius CAD-4* diffractometer with a locally modified low temperature device. A full sphere of data was collected in the range $\sin\Theta/\lambda < 0.704$ Å$^{-1}$ and a hemisphere in the range $0.74 \leqslant \sin\Theta/\lambda < 1.0$ Å$^{-1}$. The use of symmetry-equivalent data helps improve intensity statistics and reduce systematic errors in the data. Data were corrected for the effects of absorption based on indexed faces (max. and min. transmission coefficients 0.768 and 0.667, $\mu = 9.29$ cm$^{-1}$ for Mo$K\alpha$ X-radiation). Averaging yielded 13288 independent reflections of which 8741 $[F > 3\sigma(F)]$ were used in subsequent least-squares refinements [$R$(int) $= 0.040$, 0.018 for observed reflections].

*Least-Squares Refinements.* The quantity $w(|F_o|/k - |F_c|)^2$ with $w = 1/[\sigma^2(F_0^2) + (0.005F_0^2)^2]$ was minimized by full-matrix least-squares refinement. The estimated standard deviation of each observation, $\sigma(F_0{}^2)$ was taken as the larger, of $\sigma_{\text{counting}}$ and $\sigma_{\text{symm.}}$, where $\sigma^2_{\text{symm.}} = \sum_i^N (F^2_{0i} - < F^2_0 >)^2/(N\text{-}1)$ for $N$ measurements of symmetry-related reflections. Core valence and total atomic scattering factors for Ni, Cl, P, C and H were taken from ref. 13. Anomalous scattering factors taken from ref. 13 were also included in the calculations for Ni, Cl, P and C. An isotropic secondary extinction parameter was also refined, though the effect of extinction is a minor one in this case.

Based on structural parameters from a conventional spherical atom refinement [12], a multipole model was adopted in order to fit the aspherical features of the electron density, hence avoiding the bias in positional and vibrational parameters caused by these features in conventional refinements using X-ray diffraction data [14]. In the model used here the electron density is represented by atom-centered multipole expansions.

$$\rho\,(\mathbf{r}) = \sum_{\text{atoms}} [\,\rho_{\text{core}}(\mathbf{r}) + P_v\ \rho_{\text{valence}}(\kappa r) + \sum_{l=o}^{4} R_l(\kappa' r) \sum_{m=-l}^{l} P_{lm}\ Y_{lm}(\mathbf{r}/r)]$$

where $\rho_{\text{core}}$ and $\rho_{\text{valence}}$ are spherical Hartree-Fock core and valence densities and the $Y_{lm}$ are real space spherical harmonic angular functions. The Slater-type radial functions $R_l(r)$ are given by:

$$R_l = Nr^n \exp(\text{-}\zeta r)$$

where $N$ is a normalization factor and $n$ and $\zeta$ are chosen for each $l$ [15]. The $P_v$, $P_{lm}$, $\kappa$ and $\kappa'$ are refinable parameters.

Symmetry constraints in addition to the crystallographic molecular two-fold axis were imposed upon the multipole functions associated with the individual atoms, namely *mm* symmetry at the Ni, C and H sites and *m* symmetry at the Cl and P sites. Populations of multipoles up to order four were refined for all non-hydrogen atoms, with just a monopole and function used for the hydrogen atoms. The number of population parameters refined was also reduced by refining common parameters for atoms considered chemically equivalent. To accomodate possible deviations from harmonic vibrational motion, third-order cumulant anharmonic vibrational parameters, $C_{ijk}$ [16], were also included in refinements for the Ni, Cl and P atoms. Fourth-order cumulants were added to the phosphorous atom upon observation of surrounding residual *(i. e.* unmodelled) electron density features compatible with such anharmonic motion.

*Electron Density Maps.* The effect of chemical bonding in a molecule upon electron density distribution can be examined by ploting the deformation density, $\Delta\rho = \rho_{\mathrm{obs}}/k - \Sigma\rho_{\mathrm{spherical\ atoms}}$, which is the difference between the total observed density and the density calculated from superposition of spherical, neutral atoms (often referred to as the 'promolecule'). These density maps suffer from errors in the structure factor phases and noise generated from errors in the experimental observations. However, having fit the observed density with a multipole model, a model deformation density can be calculated, $\Delta\rho_{\mathrm{model}} = \rho_{\mathrm{model}} - \Sigma\rho_{\mathrm{spherical\ atoms}}$. Maps of the model deformation density do not suffer from the potentially high noise levels of the observed maps and are consequently more easily interpreted. Such maps are presented here. The residual density, given by $\rho\Delta_{\mathrm{residual}} = \rho_{\mathrm{obs}}/k - \rho_{\mathrm{model}}$ should also be calculated to determine how well the observed density has been modelled by the multipole functions.

## RESULTS AND DISCUSSION

Use of the multipole refinement model resulted in residual indices $R = 0.029$, $wR = 0.032$ and goodness-of-fit, $S = 1.266$ for the 8741 data $[F > 3\sigma(F)]$. This shows a substantial improvement in the fit to the electron density, over the conventional spherical atom refinement $[R = 0.038$,

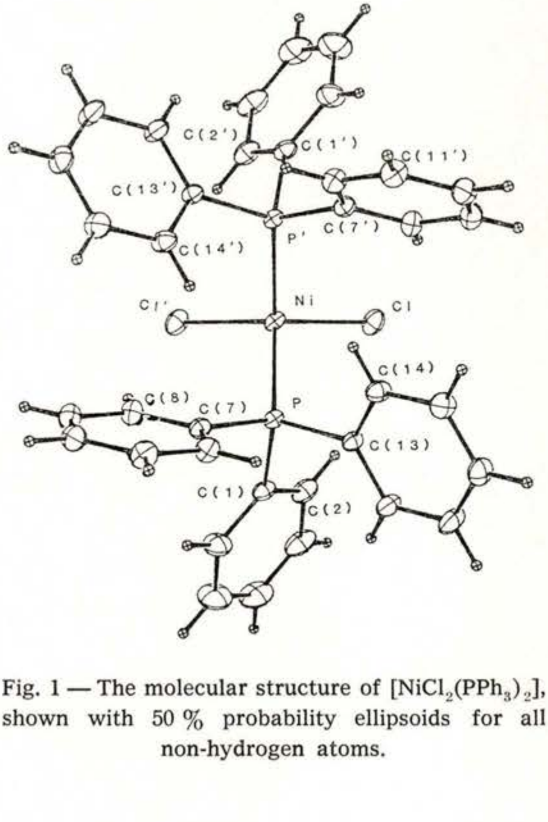

Fig. 1 — The molecular structure of $[NiCl_2(PPh_3)_2]$, shown with 50 % probability ellipsoids for all non-hydrogen atoms.

$wR = 0.052$, $S = 1.28$ for 8615 data]. Residual features are also considerably reduced in magnitude.

The molecular structure of dichloro-bis (triphenylphosphine) nickel(II) is depicted in Figure 1. The model deformation density averaged over the planes of the three separate phenyl rings is shown in Figure 2. In agreement with many previous studies on small molecules, peaks are seen in the deformation density along the interatomic vectors between all covalently bonded atoms. It is also apparent that peak heights decrease in both C-C and C-H bonds on moving from the *ipso* to the *para* end of the phenyl ring. This reflects the greater vibrational motion of atoms towards the extremities of the molecule causing increased smearing of the density features. The model deformation densities for (i) the

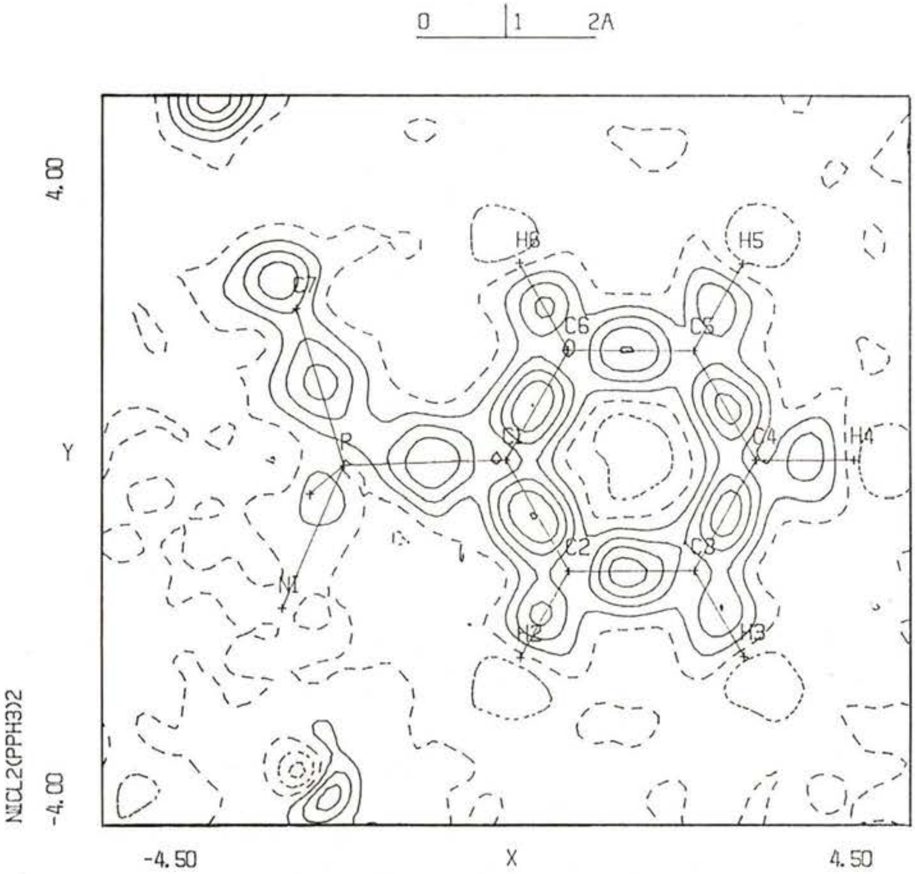

Fig. 2 — Model deformation density map, averaged over the three phenyl ring planes. Contour interval is 0.1 e/Å$^3$. Atoms other than P and the ring C, H atoms are out of the plane shown. Their projection into this plane is shown for reference.

P-Ni-P plane, (ii) the Cl-Ni-Cl plane and (iii) the plane through Ni perpendicular to the molecular two-fold axis are presented in Figures 3-5 respectively. Figure 3 indicates a build-up of density in the phosphorus lone-pair region consistent with the principally $\sigma$-donor bonding mode of phosphine ligands.

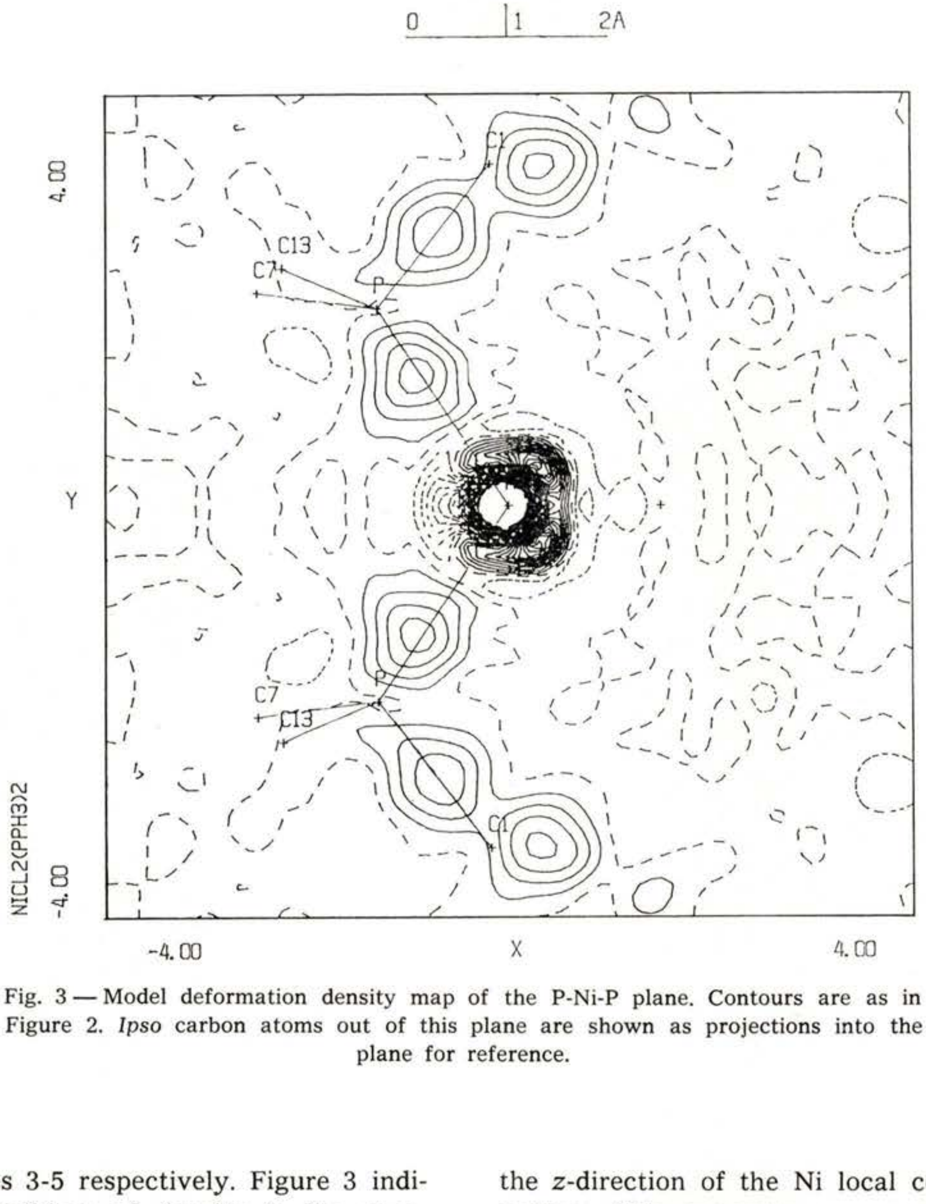

Fig. 3 — Model deformation density map of the P-Ni-P plane. Contours are as in Figure 2. *Ipso* carbon atoms out of this plane are shown as projections into the plane for reference.

Around the nickel atom, it appears (from Figures 3 and 4) that a depletion of density occurs along the two-fold axis, *i. e.* the *z*-direction of the Ni local coordinate system. This suggests an unoccupied Ni $3d_{z^2}$ orbital, an observation in contradiction to a simple tetrahedral crystal field model of metal ligand interaction. Figure 5, in the $xy$-plane of the Ni coordinate system, suggests that perhaps more electron density lies in the $d_{x^2-y^2}$ than in the $d_{xy}$ orbital of nickel, for which simple crystal field theory would provide an appropriate explanation. Hence, the implication is that crystal field theory is insufficient to rationalize metal-ligand bonding and that a degree of covalency is involved in these interactions. In support of this assertion is the fact that a diffuse positive feature (peak $> 0.5 e/Å^3$) between the Ni and Cl atoms appears in the residual map (Figure 6) as it is poorly fit by the current multipole model. The appearance of this feature reflects a very contacted radial

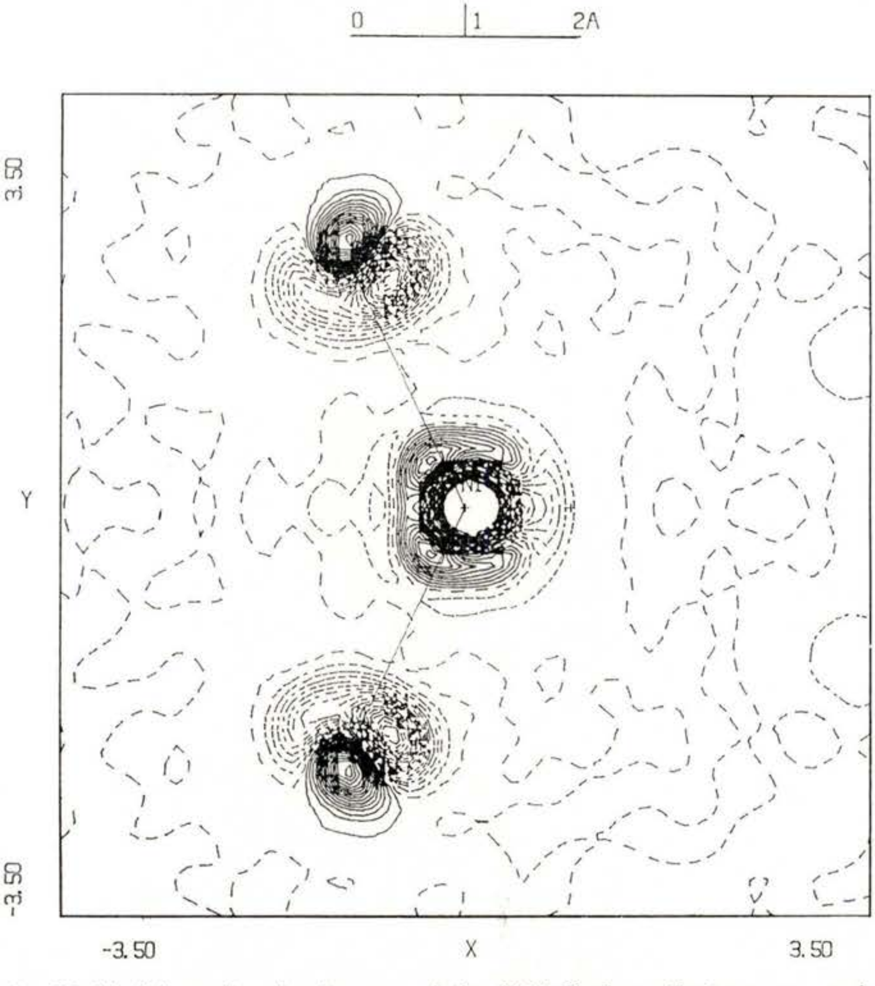

Fig. 4 — Model deformation density map of the Cl-Ni-Cl plane. Contours are as in Figure 2.

parameter associated with the chlorine atom, this contraction resulting principally from the dominance asserted by the majority of the Cl valence shell being composed of lone-pair electrons, which are closer to the nucleus than any involved in bonding. Current work is addressing the problem of modelling this residual feature using techniques applied successfully by others, namely the inclusion of additional diffuse functions on the metal atom to allow for population of 4s and 4p orbitals [17] and the inclusion in the model of a point scattering function to model the Ni-Cl two-centre term directly [18]. It is worth pointing out that the lack of such

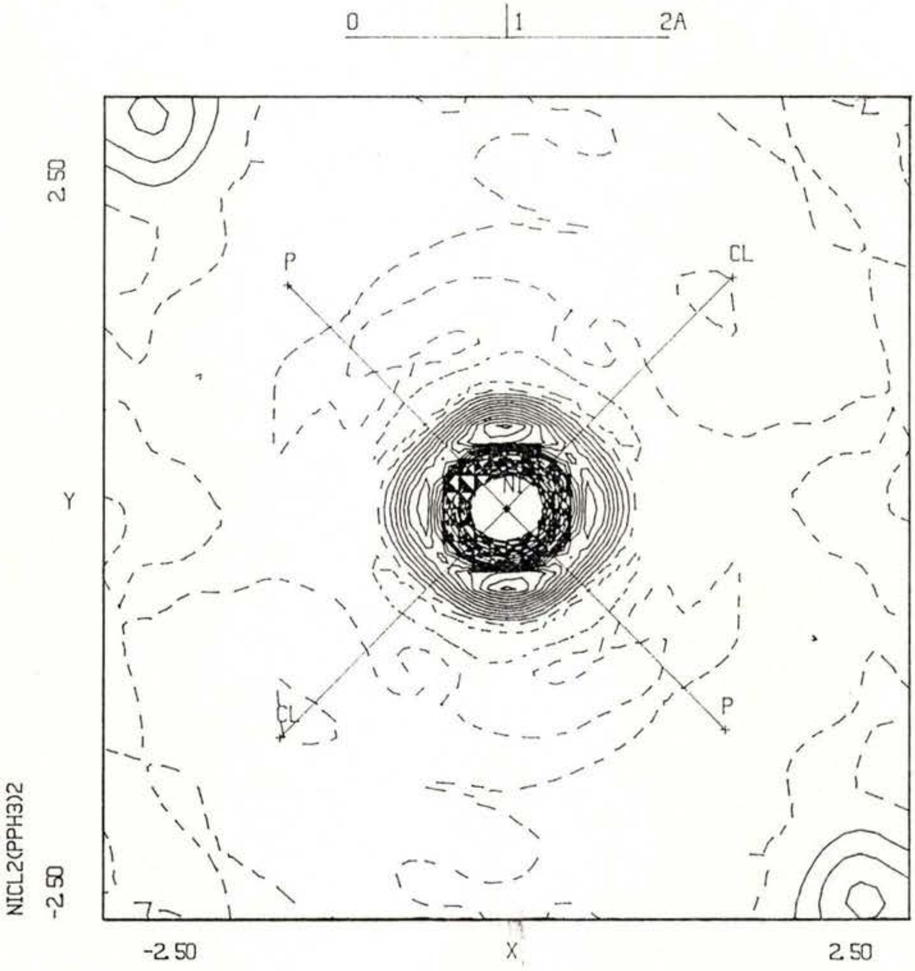

Fig. 5 — Model deformation density map of the plane through Ni perpendicular to the molecular two-fold axis. Contours are as in Figure 2. Projections of the Cl and P atom positions into the plane are shown for reference.

an unmodelled density feature in the Ni-P bonding region in no way precludes substantial Ni-P covalent bonding, but merely shows that the current model is sufficient to accomodate the deformations in the electron density in this region due to chemical bonding. Indeed this might be anticipated from the dominance of bonding electrons in the phosphorus valence shell, leading to an expanded radial parameter associated with the multipole functions.

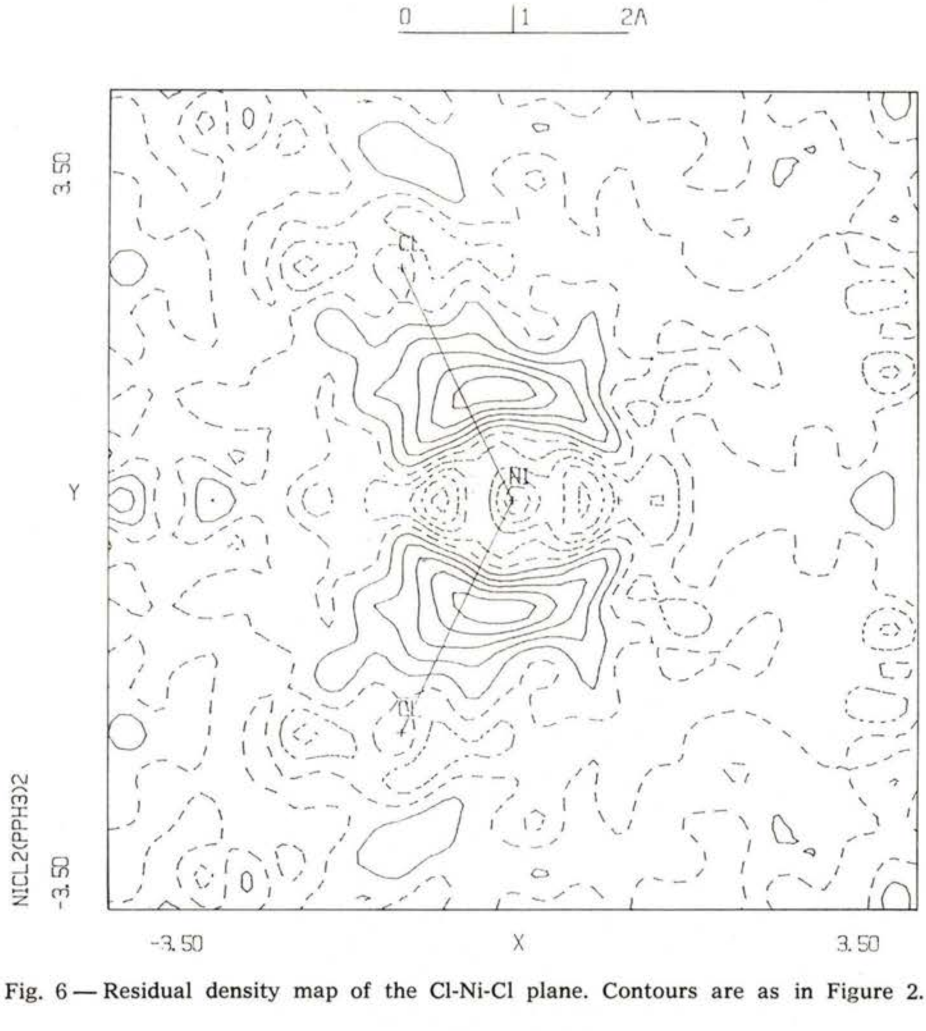

Fig. 6 — Residual density map of the Cl-Ni-Cl plane. Contours are as in Figure 2.

## CONCLUSIONS

The observed electron density distribution of dichloro-bis(triphenylphosphine) nickel(II) has been well modelled using atom-centered multipole functions, except for a diffuse region of positive density between the nickel and chlorine atoms. This residual feature may indicate a degree of covalency in the Ni-Cl interaction, not accomodated due to some inflexibility in the model used. The apparent source of this inflexibility and current work to circumvent this problem have been noted. Electron density deformation maps show an accumulation of density between all truly covalently bonded atom pairs and a build-up of density in the phosphorus lone-pair region, consistent with the well-known $\sigma$-donor nature of phosphine ligands. The failure of a simple crystal field splitting model to rationalize the deformation density around the nickel atom lends support to the assertion of covalency in the metal-ligand interactions. Intended further investigation of the electronic structure of this compound will include determination of the Ni d-orbital populations from the experimental charge distribution. It is also hoped to conduct a polarized neutron diffraction study of the paramagnetic spin density in order to more effectively examine the apparent metal-ligand bond covalency.

This work was supported in part by NSF Grant No. 8311704. L. B. wishes to thank the Science and Engineering Research Council (UK) for support in attending the Sagamore IX conference and for a NATO postdoctoral fellowship.

## REFERENCES

[1] KILBOURN, B. T. and POWELL, H. M., *J. Chem. Soc. (A)*, 1688 (1970).

[2] MARI, A., GLEIZES, M. DARTIGUENAVE, M. and DARTIGUEVANVE, Y., *Inorg. Chim. Acta.*, **52**, 83 (1981).

[3] SCATTURIN, V. and TURCO, A. *J. Inorg. Nucl. Chem.*, **8**, 447 (1958).

[4] SHELDRICK, W. S. and STELZER, O., *J. Chem. Soc., Dalton Trans.*, 926 (1973).

[5] STALICK, J. K. and IBERS, J. A., *Inorg. Chem.*, **9**, 453 (1970).

[6] JARVIS, J. A. J., MAIS, R. H. B. and OWSTON, P. G., *J. Chem. Soc. (A)*, 1473 (1968).

[7] BUTLER, I. R., CULLEN, W. R., KIM, T.-J., RETTIG, S. J. and TROTTER, J., *Organometallics*, **4**, 972 (1985).

[8] GARTON, G., HENN, D. E., POWELL, H. M. and VENANZI, L. M., *J. Chem. Soc.*, 3625 (1963).

[9] BRUINS SLOT, H. J., VAN HAVARE, W. K. L., NOORDIK, J. H., BEURSKENS, P. T. and ROYO, P., *Cryst. Spectrosc. Res.*, **14**, 623 (1984).

[10] BELLON, P. L., ALBANO, V., BIANCO, V. D., POMPA, F. and SCATTURIN, V., *Ricerca Sci.*, **33**, 1213 (1963).

[11] VENANZI, L. M., *J. Chem. Soc.*, 719 (1962).

[12] BRAMMER, L. and STEVENS, E. D., *Acta Cryst.*, *Vol. C.*, submitted for publication.

[13] International Tables for X-ray Crystallography (1974) Vol. IV, Birmingham: Kynoch Press. (Present distributor D. Reidel, Dordecht).

[14] COPPENS, P., *Acta Cryst.*, **B30**, 255 (1974); ALLEN, F. H., *Acta Cryst.*, **B42**, 515 (1986).

[15] HANSEN, N. K. and COPPENS, P., *Acta Cryst.*, **A34**, 909 (1978).

[16] JOHNSON, C. K., *Acta Cryst.*, **A25**, 187 (1969).

[17] FIGGIS, B. N. and REYNOLDS, P. A., *J. Chem. Soc., Dalton Trans.*, 125 (1986).

[18] HELLNER, E., *Acta Cryst.*, **B33**, 3813 (1977); MULLEN, D. and HELLNER, E., *Acta Cryst.*, **B33**, 3816 (1977).

# EXPERIMENTAL VS. AB INITIO THEORETICAL DEFORMATION DENSITY FOR (Z)-N-ACETYL-$\alpha$, $\beta$-DIHYDROPHENYLALANINE-METHYLAMIDE AND (Z)-N-ACETYL-TRYPTOPHANE-METHYLAMIDE

MOHAMMED SOUHASSOU, CLAUDE LECOMTE *, ROBERT BLESSING, A. AUBRY
Laboratoire de Minéralogie et Cristallographie, Université de Nancy I, URA CNRS 809
BP 239, 54506 Vandoeuvre lès Nancy Cedex, France.

ROLAND WIEST, MARIE-MADELEINE ROHMER
Laboratoire de Chimie Quantique, E. R. 139 DU CNRS,
67000 Strasbourg, France.

MARC BENARD *
Laboratoire de Chimie Quantique, E. R. 139 DU CNRS,
67000 Strasbourg, France.

## EXPERIMENTAL

A crystal of (Z)-N-acetyl-$\alpha$, $\beta$-dehydrophenylalanine-methylamide (hereafer Ac$\Delta$) and crystals of (Z)-N-acetyl-tryptophane-methylamide (hereafter AcTr) were obtained from recrystallization in methanol by Boussard and Marraud (INPL Nancy, France).

The data collections were made at $103 \pm 5$ K for both compounds on a CAD4 diffractometer on which a glove box was built to prevent ice formation on the sample [1]. At least two hkl, $hk\bar{l}$ reflections were collected up to $\sin\theta/\lambda = 1$ Å$^{-1}$. After o completion of a least squares refinement against the low order data $\sin\theta/\lambda < 0.90$ Å$^{-1}$), high order reflections were calculated up to $\sin\theta/\lambda = 1.36$ Å$^{-1}$ for Ac$\Delta$ and up to $\sin\theta/\lambda = 1.15$ Å$^{-1}$ for AcTr, and only those with an estimated intensity I greater than $5\,\sigma$(I) were measured. The full step-scan profile of each reflection was recorded. Experimental details are given in table 1. The data were processed with a new set of programs written by Blessing [2]. Cubic polynomials least squares fitted to the intensities of standard reflections showed a monotonous decline of about 6 % for Ac$\Delta$ and of 1.2 % for AcTr. The instrumental instability factor (Mc Candlish et al., 1975) was calculated to be P = 0.0071 for Ac$\Delta$ and 0.019 for AcTr. Absorption corrections were not applied, symmetry equivalent (hkl and $hk\bar{l}$) were then averaged and the internal agreement is R(F$^2$) = 1.5 %,

---

* Author to whom correspondence should be addressed.

TABLE I — Experimental details

| | Ac $\Delta$ | Ac Tr |
|---|---|---|
| Formula | $C_{12}N_2O_2H_{14}$ | $C_{14}N_3O_2H_{17}$ |
| Space group | Cc ; $Z = 2$ | $P2_12_12_1$ ; $Z = 4$ |
| Cell dimensions (103 K) | 10.193(2) ; 15.115(2) ; 8.561(2) Å<br>$\beta = 121.13°(18)$ | 8.209(3) ; 11.016(2) ; 14.760(4) |
| Crystal dimensions mm | 0.46 × 0.32 × 0.30 | 0.32 × 0.30 × 0.28 |
| Absorption coefficient (MoK$\alpha$) | 0.9 $cm^{-1}$ | 0.8 $cm^{-1}$ |
| $\theta_{min} - \theta_{max}$ ; $\sin\theta/\lambda_{MAX}$ | 1-75° ; 1.36 $Å^{-1}$ | 1-56° ; 1.17 $Å^{-1}$ |
| Standard reflections | ± 800, ± 006, 556, $5\bar{5}6$, $55\bar{6}$, $\bar{5}56$ | 555, 555, ± 600, 014, 213 |
| Scan type | $1.35 + 0.35 \text{ tg } \theta$ | $\omega/2\theta$ |
| Scan width | $\omega/2\theta$ | $1.35 + 0.35 \text{ tg } \theta$ |
| Scan speed °$min^{-1}$ | $0.5 < v < 3.5$ | $0.5 < v < 3.5$ |
| Measured reflections | 14666 | 10567 |
| Unique reflections | 7423 | 4731 |

for Ac$\Delta$ and 2.2 % for AcTr for the all data sets. Errors estimates $\sigma$(I) were calculated according to Blessing [2]. A variance analysis versus I and $\sin\theta/\lambda$ was then performed and the standard deviations were adjusted.

## STRUCTURE REFINEMENT AND THERMAL MOTION ANALYSIS

Table II gives a summary of some of the refinements made. Starting parameters for the conventionnal high order refinement were taken from Aubry et al. [3] for Ac$\Delta$; for AcTr we solved the crystal structure [11]. Spherical scattering factors for C, N, O were calculated from Clementi wave functions (Clementi, 1965). As the space group of both compounds is acentric, Hansen-Coppens [6] multipole refinements were made in order to obtain the phases of the structure factors with the best precision. A rigid bond test [7] and a T, L, S + $\Omega$ fit was applied to the thermal $U_{ij}$ parameters (table III) (Trueblood, 1987 and references therein).

The dynamic deformation density maps shown were calculated from:

$$\Delta\rho(\mathbf{r}) = \sum_{H} \frac{1}{V} \left( |F_m| e^{i\phi_m} - |F_{sph}| e^{i\phi_{sph}} \right) e^{-2i\pi \, \mathbf{H} \cdot \mathbf{r}}$$

where $F_m$ and $\phi_m$ are respectively the multipolar structure factor and phase. The Fourier series were calculated for $\sin\theta/\lambda < 0.9$ $Å^{-1}$; by using multipolar phases, the average bonding density in the phenyl ring of Ac$\Delta$ increased from 0.35 to 0.56 e/$Å^3$, and the internal standard deviation calculated on the six carbon-carbon bonds decreased from 0.06 to 0.02 e/$Å^3$, confirming the necessity of a multipole refinement for acentric structures.

TABLE II — Refinements

| Type of refinement | Ac Δ | | | | Ac Tr | | | |
|---|---|---|---|---|---|---|---|---|
| | | R % | Rw % | G. O. F. | | R % | Rw % | G. O. F. |
| H.O | $\sin\theta/\lambda > 0.9$ Å$^{-1}$<br>$I > 0$ | 7.9 | 5.3 | 0.85 | $\sin\theta/\lambda > 0.65$ Å$^{-1}$<br>$I > 3\sigma(I)$ | 4.97 | 4.77 | 0.82 |
| Spherical refinement | $\sin\theta/\lambda < 0.9$ Å$^{-1}$<br>$I > 0$ | 3.25 | 3.94 | 2.27 | All data<br>$I > 3\sigma(I)$ | 5.29 | 6.35 | 2.03 |
| All data multipole refinement | $\sin\theta/\lambda < 1.36$ Å$^{-1}$<br>$I > 0$ | 3.54 | 2.04 | 0.85 | $\sin\theta/\lambda < 1.17$ Å$^{-1}$<br>$I > 3\sigma$ | 2.91 | 2.46 | 0.84 |

TABLE III — TLS + $\Omega$ Calculations

| | | Ac Δ | | Ac Tr | |
|---|---|---|---|---|---|
| $L_{11}$ | $T_{11}$ | 2.15 | 0.114 | 2.15 | 0.138 |
| $L_{22}$ | $T_{22}$ | 1.73 | 0.105 | 1.59 | 0.115 |
| $L_{33}$ | $T_{33}$ | 1.15 | 0.089 | 0.45 | 0.107 |
| | | $\Omega_1 = 4.44$ $C_1,C_2,O_1$ about $C_3$ - $N_1$<br>$\Omega_2 = 3.46$ $O_2,N_2,C_{12}$ about $C_3$ - $C_{11}$<br>$\Omega_3 = 1.70$ phenyl about $C_3$ - $C_4$<br>$\Omega_4 = 1.46$ phenyl about $\perp$ $C_5$-$C_4$-$C_3$ through $C_4$ | | $\Omega_1 = 5.99$ $C_1,C_2,O_1$ about $C_3$ - $N_1$<br>$\Omega_2 = 4.69$ $C_5,O_2,N_2$ about $C_3$ - $C_4$<br>$\Omega_3 = 1.70$ Indole about $C_3$ - $C_6$ | |
| G. O. F. | | 2.26 | | 2.97 | |
| Number of observations | | 96 | | 114 | |
| Number of parameter (m) | | 44 | | 38 | |
| $R_w = \left( \frac{\Sigma\,(\Delta U_{ij}/\sigma(U_{ij}))^2}{\Sigma\,(U_{ij}/\sigma(U_{ij}))^2} \right)^{1/2}$ | | 4 % (Rw = 15 % for m = 20) | | 14 % (Rw = 21 % for m = 20) | |

## AB INITIO CALCULATIONS

Ab initio-MO Self-Consistent-Field (SCF) calculations (Roothaan, 1951) were carried out on both AcΔ and AcTr using basis sets composed of 9 s-type and 5 p-type Gaussian functions for first-row atoms and 4 s-type functions for hydrogen [8]. These basis sets were contracted to split-valence, that is (3s, 2p) for first-row atoms and (2s) for hydrogen. The total energies associated with the SCF wave functions were computed to be −720.4675h. for AcΔ and −852.2807h. for AcTr. The wave function of the promolecule was computed as the orthonormalized superposition of atomic wave functions obtained with the same basis sets, and at the same level of calculation. For each system, the deformation density distribution was obtained in the planes of interest by subtracting the electron densities obtained from both computed wave functions:

$$\Delta\rho(x, y, z) = \rho_{MOL}(x, y, z) - \rho_{PROMOL}(x, y, z)$$

All quantum chemical calculations were carried out using the ASTERIX program system vectorized for CRAY-2 computers (R. Ernenwein et al. [12], Rohmer et al. [13]).

## RESULTS AND DISCUSSION

Fig. 1 displays the ORTEP drawing of AcΔ (a) and AcTr (b), and fig. 2 compares the dynamical bonding densities of the two peptide groups of AcΔ (2a, 2b) and AcTr (2c, 2d). Bonding densities and oxygen lone pairs are clearly resolved for both compounds. The theoretical densities are displayed in fig. 3 for the same planes of AcΔ (3a, 3b) and AcTr (3c, 3d). Note that the respective orientations of the peptide groups are different in fig. 2 (c, d) and in fig. 3 (c, d). The depopulation region that appears on all theoretical maps along the C-O bond in the vicinity of the oxygen atom may be related to an artefact produced by medium-size basis sets and documented by Smith [10] for the isolated CO molecule. However, the subsequent displacement of the CO bonding density towards the carbon atom of the peptide groups is also observed in the experimental maps. Except for the lone pairs, the computed density peaks are quantitatively close to the observed ones, and generally underestimated by 10 to 20 %. In AcTr,

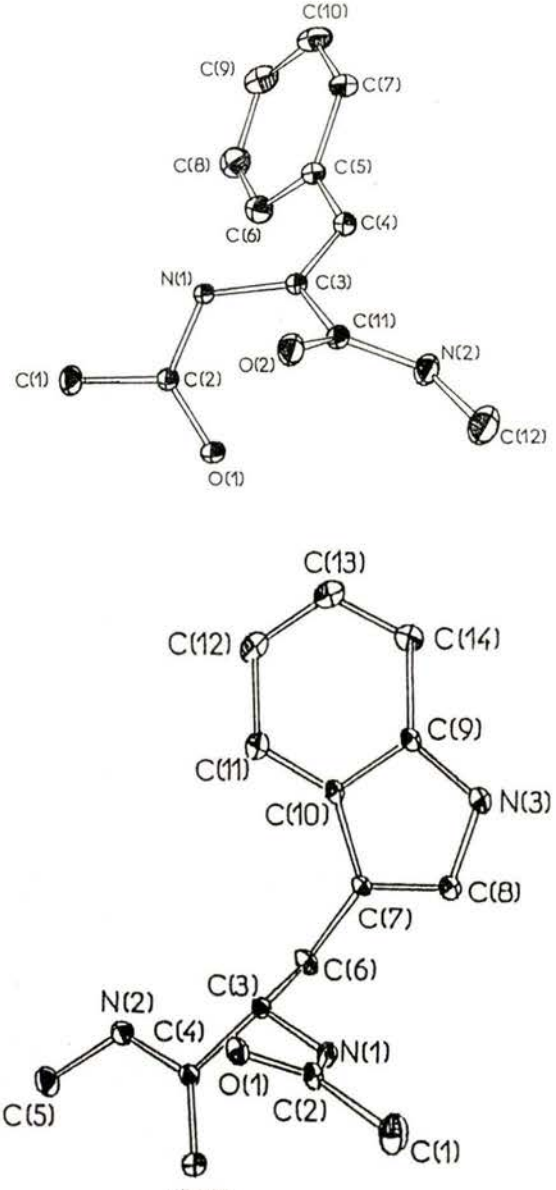

Fig. 1 — ORTEP drawing of AcΔ (a) and AcTr (b).

the deformation density observed in both peptide groups is the same for each type of bond (C = O, C − N, lone pairs) and the maximum of the density is in the middle of the bond (Fig. 2c, d). The two peptide groups appear more differenciated in AcΔ:

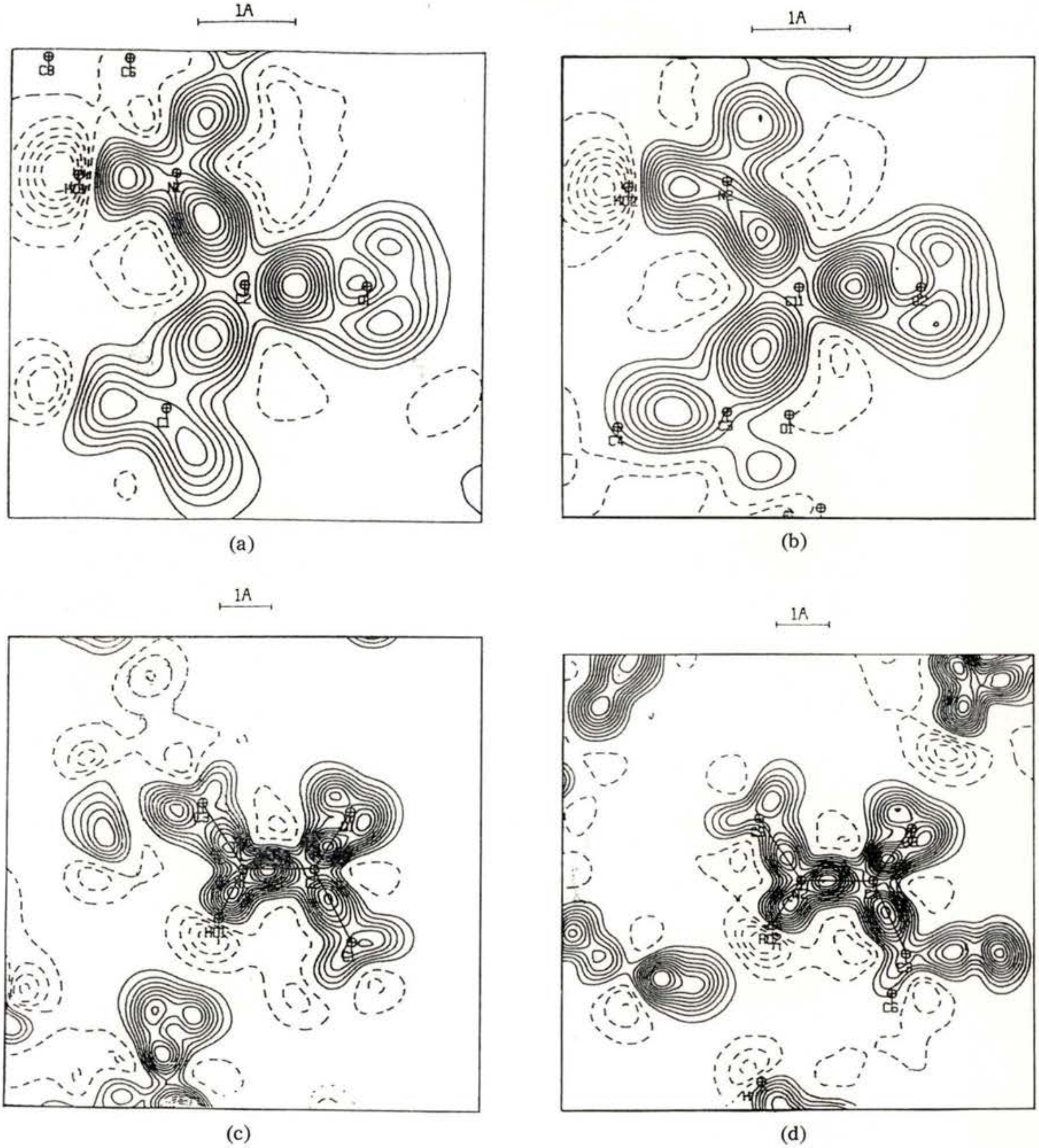

(a) (b)

(c) (d)

Fig. 2 — Model dynamical deformation densities in the planes containing the peptide groups (contour interval 0.05 e/Å$^{-3}$; no zero contour drawn) solid lines for positive contours; dotted lines for negative contours; 2a and 2b are for AcΔ, 2c and 2d for AcTr.

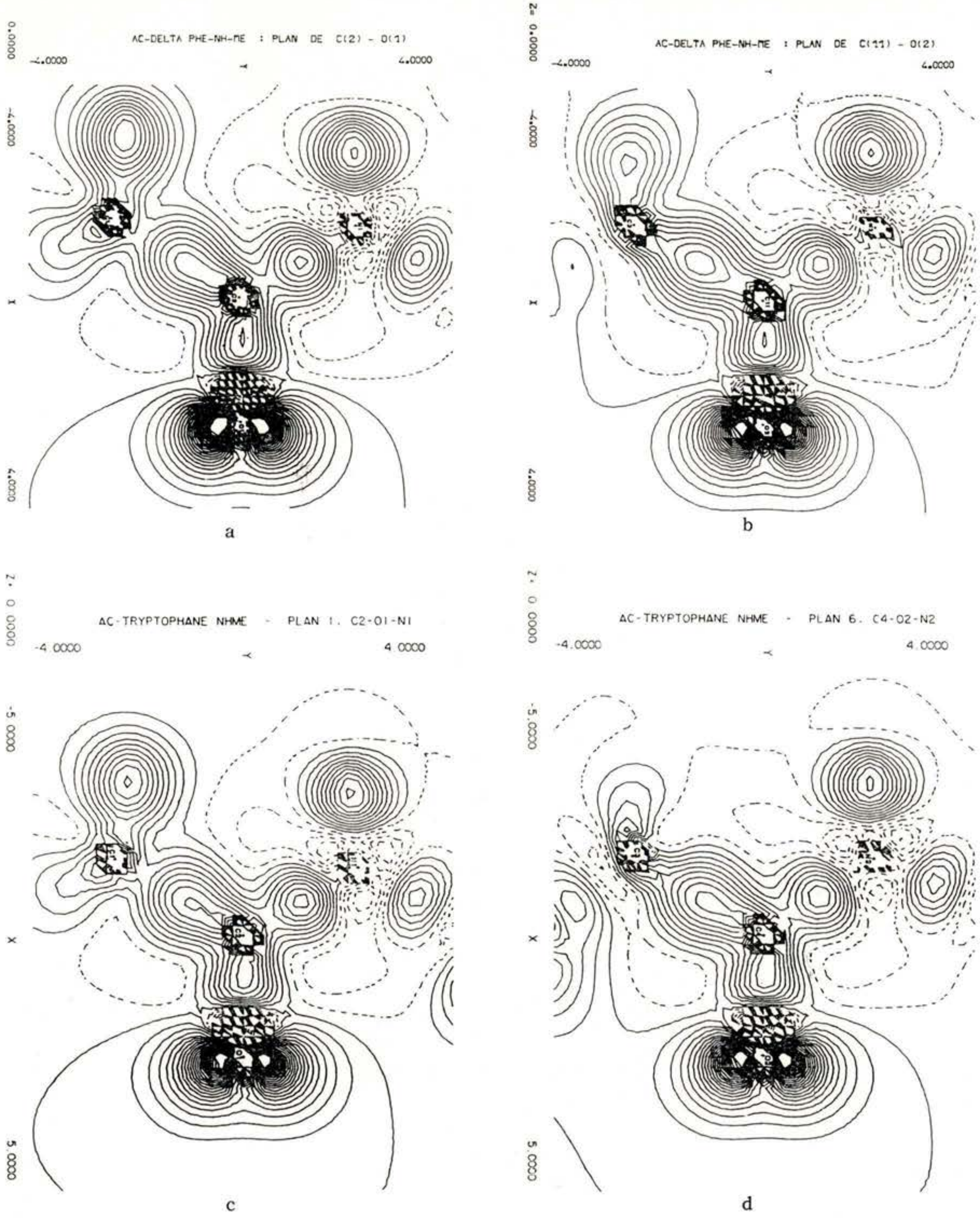

a

b

c

d

Fig. 3 — Sections of the theoretical deformation density (from ab-initio-SCF calculations) by the planes containing the peptide groups of Ac$\Delta$ (a, b) and those of AcTr (c, d). Contour interval: 0.05 e/Å$^3$. Solid lines for zero and positive contours; dotted lines for negative contours.

the bonding density in $C_{11} = O_2$ (0.6 e/Å$^3$) is larger than in $C_2 = O_1$ (0.50 e/Å$^3$) and the maximum of the bonding density of $C_2 - N_1$ is shifted towards the $N_1$ atom. It seems natural to attribute this small differenciation to the influence of the $C^{\alpha} = C^{\beta}$ double bond (in AcTr, $C^{\alpha} - C^{\beta}$ is a single bond, so that no intramolecular factor is expected to differenciate the two peptide groups). However, the theoretical maps do not agree with this rationalization: both the height and the shape of the density peaks are similar for the two peptide groups of AcΔ as for those of AcTr (Fig. 3). An influence of intermolecular factors (hydrogen bonds) should therefore be considered to explain the slight difference observed for the electron density pattern of the two peptide groups of AcΔ. Further theoretical work accounting for the influence of intermolecular interactions is being carried out.

Quantum chemical calculations have been carried out on the CRAY-2 computer of the CCVR (Palaiseau, France) through a grant of computer time from the Conseil Scientifique du Centre de Calcul Vectoriel de la Recherche.

## REFERENCES

[1] AUBRY, A. and LECOMTE, C., Internal Laboratory Report.

[2] BLESSING, R. H., Cryst. Rev., **1** (1987), 3-58. MARRAUD, M., Biopolymers, **24** (1985), 639--646.

[3] AUBRY, A., ALLIER, F., BOUSSARD, G. and

[4] CLEMENTI, E. and RAIMONDI, D. L., J. Chem. Phys., **38** (1963), 2686-2689.

[5] DUNITZ, J. D., SCHOMAKER, V. and TRUEBLOOD, K. N., Journal of Physical Chemistry, **92** (1988), 856-867.

[6] HANSEN, N. and COPPENS, P., Acta Cryst., **A34** (1978), 909-921.

[7] HIRSHFELD, F. L., Acta Cryst., **A32** (1976), 239-244.

[8] HUZINAGA, S., Approximate Atomic Functions, Technical Report, University of Alberta (1971).

[9] ROOTHAAN, C. C. J., Rev. Mod. Phys., **23** (1951), 25.

[10] SMITH, V. H., in «Electron Distributions and the Chemical Bond», P. Coppens and M. B. Hall, Eds, Plenum, New-York, 1982, p. 25.

[11] SOUHASSOU, M., AUBRY, A. and LECOMTE, C., MARRAUD, M., Acta Cryst. C (1990).

[12] ERNENWEIN, R., ROHMER, M. M. and BENARD, M., Comp. Phys. Commun. **58** (1990), 305.

[13] ROHMER, M. M., DEMUYNCK, J., BENARD, M., WIEST, R., BACHMAN, C., ERNENWEIN, R., Comp. Phys. Commun. (1990).

# TRYING TO GET INFORMATION ABOUT THE Pd-Pd BOND

JEAN-PAUL MANGEOT, CLAUDE LECOMTE *, YVES DUSAUSOY
Laboratoire de Cristallographie, UA CNRS Nº 809, University of Nancy I, B. P. 239, 54506
Vandoeuvre Cédex, France

## EXPERIMENTAL

Crystals of $Pd_2Cr_2Cp_2(\mu_3(CO)_2\mu_2(CO)_4(PEt_3)_2)$ were obtained by Bender and Braunstein (Laboratoire de Chimie de Coordination, Université Louis Pasteur, Strasbourg, France).

The data collection was made at 103 ± 5 K on a CAD4 diffractometer on which a glove box was built to prevent ice formation on the sample [1]. After completion of a least squares refinement against the low order data ($\sin\theta/\lambda < 0.80$ Å$^{-1}$), high order reflections were calculated up to $\sin\theta/\lambda = 1.35$ Å$^{-1}$, and only those with an estimated intensity I greater than $4\,\sigma(I)$ were measured. The full step-scan profile of each reflection was recorded. Experimental details are given in table 1. The data were processed with a new set of programs written by Blessing [2]. Cubic polynomials least squares fitted to the intensities of standard reflections did not show any decline about the standard. The instrumental instability factor [3] was calculated to be $P = 0.0157$; absorption corrections

TABLE I — Experimental details

| Formula Space group Z | Cell dimensions (100 K) | Crystal dimensions (mm) Absorption coefficient (mm$^{-1}$) | $\sin/\lambda_{MIN}$, $\sin\theta/\lambda_{MAX}$ Standard reflections | Scan type Scan width | Measured reflections Unique reflections $I > 4\sigma(I)$ |
|---|---|---|---|---|---|
| $C_{28}H_{40}Cr_2O_6P_2Pd_2$ | a = 10.706(2) Å | 0.12 × 0.13 × 0.23 | O – 1.35 Å$^{-1}$ | $\omega - 2\theta$ | 24181 |
| | b = 9.375(3) Å | | | | |
| $P2_1/c$ | c = 17.370(6) Å | 1.9 | 5 | $1 + 0.35\,tg\theta$ | 9138 |
| | $\beta$ = 115°38(2) | | | | |
| Z = 2 | V = 1575.14 Å$^3$ | | | | |

---

* Author to whom correspondance should be addressed.

*Portgal. Phys.* — Vol. 19, fasc. 3-4, pp. 275-281, 1988

were made by the gaussian method [4] with ABSCOR [5]; symmetry equivalent reflections were then averaged and the internal agreement was $R(F^2) = 2.3\,\%$, for the all data set (24181 measured reflections, 9138 unique). Error estimates $\sigma(I)$ were calculated according to [2]. A variance analysis versus I and $\sin\theta/\lambda$ was then performed and the standard deviations were adjusted.

## MULTIPOLAR REFINEMENT

Table II gives a summary of some of the refinements made. Starting parameters for the conventionnal high order refinement were taken from [6]. Spherical scattering factors for Pd, Cr, P, C, O were calculated from Clementi wave functions [7] Hansen-Coppens multipole refinements [8] including GRAM-CHARLIER expansion for the HO data were made. Symmetry constants were applied to the chemical equivalent atoms ($O_1 \sim O_3$; $C_1 \sim C_3$; $C_4 \sim C_5$ to $C_8$; $C_9 \sim C_{11} \sim C_{13}$; $C_{10} \sim C_{12} \sim C_{14}$; $H_1 \sim H_2$ to $H_5$; $H_6 \sim H_7$ to $H_{20}$).

The dynamic deformation density maps shown were calculated from

$$\Delta\rho(r) = \frac{1}{V} \sum_{H} \left( |F_m|\, e^{i\phi_m} - |F_{sph}|\, e^{i\phi_{sph}} \right) e^{-2i\pi\, \mathbf{H} \cdot \mathbf{r}}$$

The Fourier series were calculated for all the reflections with $\sin\theta/\lambda < 0.8$ Å$^{-1}$ ($I \geqslant 4\sigma(I)$). At the end of the multipolar refinement, residual maps were calculated and the maximum density peak is $0.25\ e/$Å$^{-3}$ close to the Pd atoms.

## RESULTS AND DISCUSSION

Figure 1 is the ORTEP drawing of the molecule (room temperature data from [6]).

TABLE II — Multipole Hansen-Coppens refinement with anharmonic GRAM-CHARLIER expansion

| | k | G. O. F. | R | Rw | Variables |
|---|---|---|---|---|---|
| High Order<br>$\sin\theta/\lambda > 0.8$ Å$^{-1}$ | 0.1355 | 0.90 | 0.0374 | 0.0419 | k, x, y, z, $U_{ij}$<br>$D_{ijkl}$ |
| Low Order<br>$\sin\theta/\lambda < 0.8$ Å$^{-1}$ | — | 1.36 | 0.0254 | 0.0315 | Hydrogen parameters |
| Low Order * | — | 0.93 | 0.0185 | 0.0216 | Multipole parameters |
| All data * | 0.1345 | 0.85 | 0.0233 | 0.0247 | All variables |

* Local m symmetry imposed to the cyclopentadienyl ring's carbons.

All the deformation maps (not given here) show the usual bonding density for the organic part of the molecule. Figure 2 shows the dynamic model density in the $C_3CrC_1$ plane. Bonding densities and carbon lone pairs are clearly resolved. The carbon lone pairs are centered on the $Cr - C$ bond at 0.5, 0.6 Å from the carbon atoms. This observation is in favor of a $\sigma$-bonding of the carbonyls to the chromium atom and not to the palladium one. Figure 2b shows the bonding density of the $\mu_3$ carbonyl group ($C_2O_2$). The $C_2$ carbon lone pair density is more diffuse extending on the $\sigma$ and $\pi$ regions towards the chromium and palladium atoms. This effect was observed before on both experimental and theoretical maps of $[\pi\ C_5H_5Fe\ (CO)_2]_2$ [9], [10].

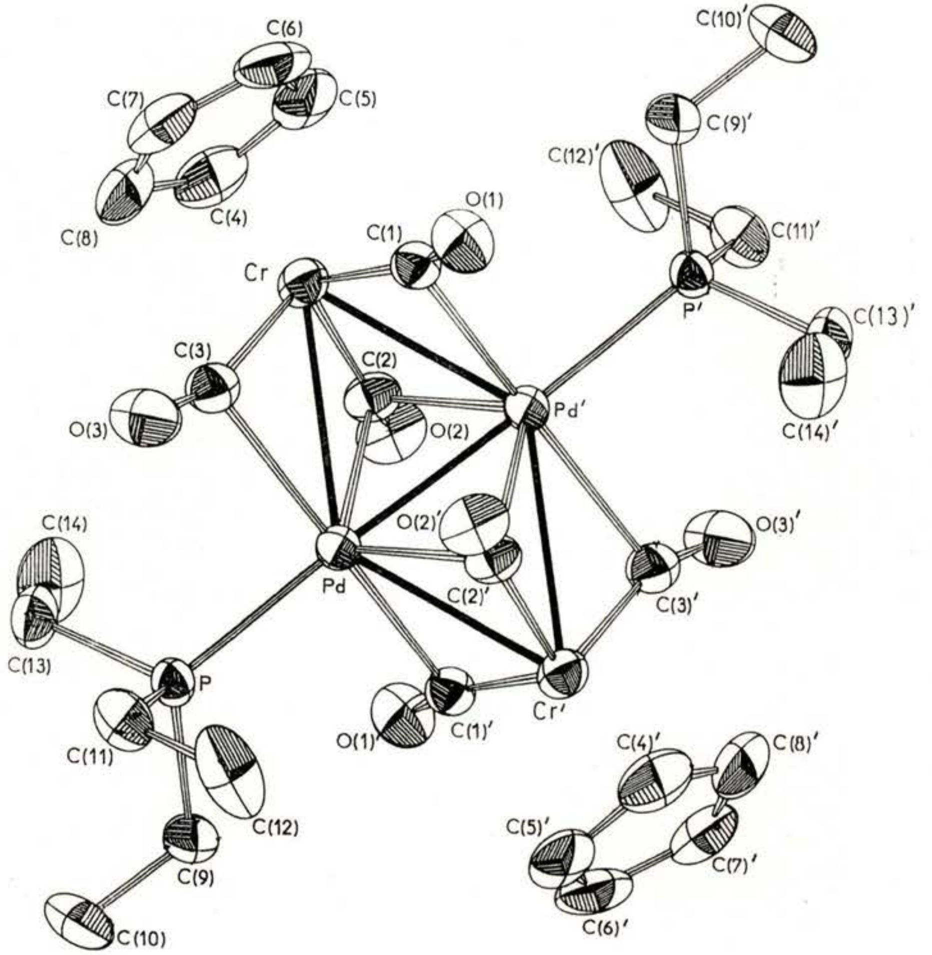

Fig. 1 — ORTEP drawing of the molecule.

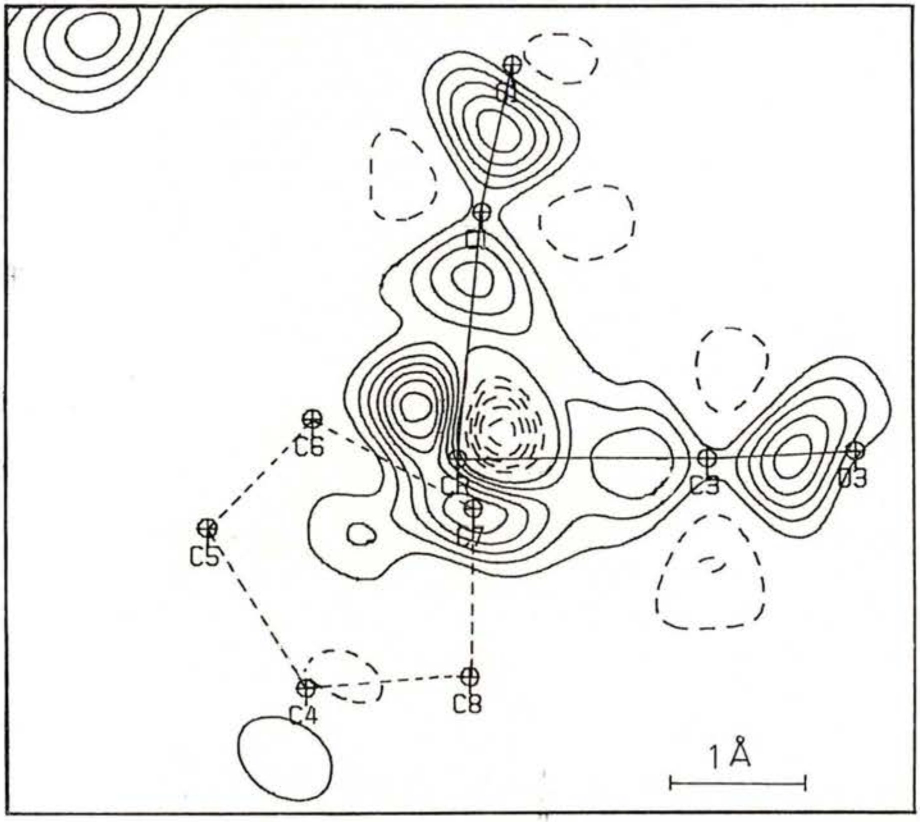

Fig. 2a — Dynamic deformation density for the $\mu_2$ carbony groups; the oxygen $O_1$ and $O_3$ are respectively 0.28 and 0.39 Å from the $C_r C_1 C_3$ plane. Contours at 0.05 e/Å$^{-3}$.

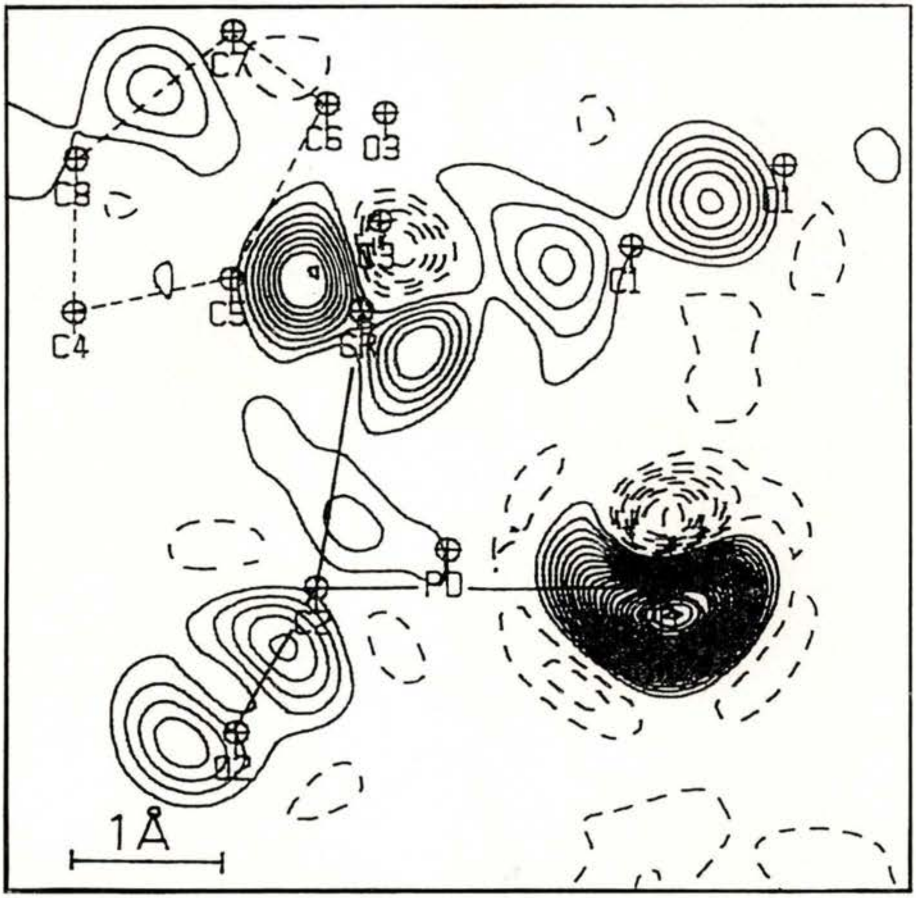

Fig. 2b — Dynamic deformation density for the $\mu_2$ ($C_2 = O_2$) carbonyl groups. Contours as in fig. 2a.

Figure 3 gives the deformation density of the $(PdC_2)_2$ plane. The Pd-Pd' distance is 2.5753(3) Å compared to 2.751 Å in the bulk metal. However very few density is observed in the Pd-Pd bond as usually found for metal-metal bonding (see for example [9]). The big accumulation region close the Pd atoms is still not explained. Further work is in progress to attempt understanding this feature which appears as an artefact or which can be due to contraction of the valence electron density associated with the bond formation. Inadequacy in the palladium form factor can also be invoked.

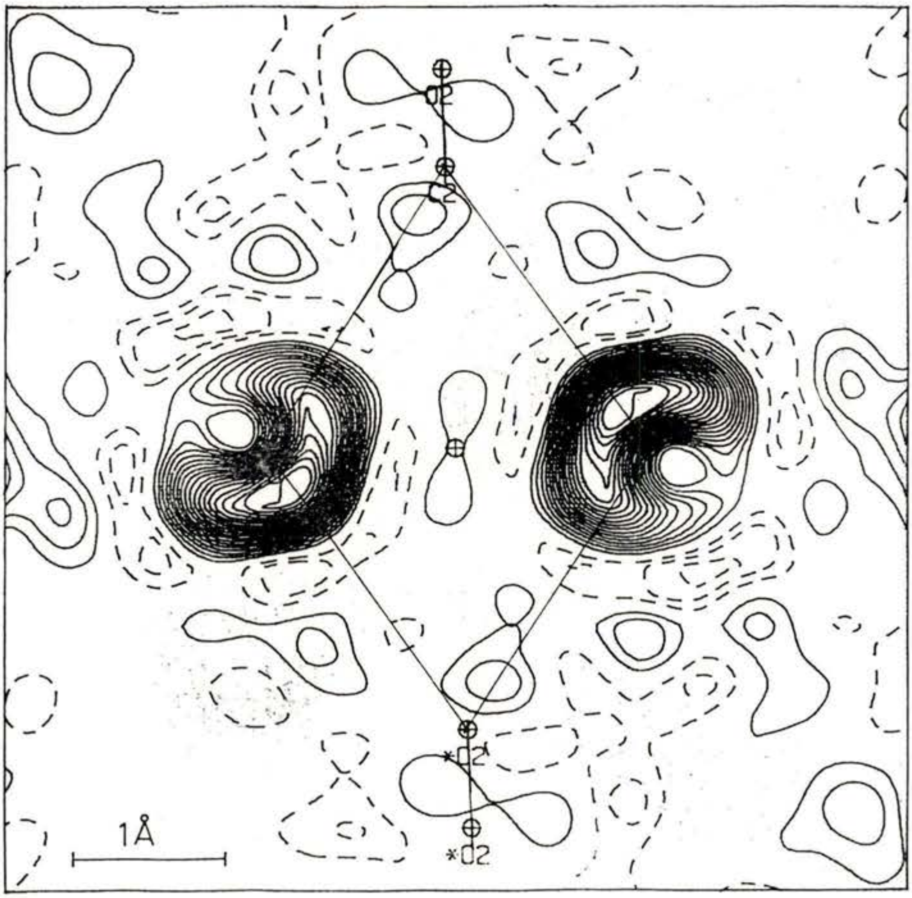

Fig. 3 — Experimental deformation density of the $(Pd\,C_2)_2$ plane.

REFERENCES

[1] AUBRY, A. and LECOMTE, C., Internal Laboratory Report, 1984.

[2] BLESSING, R. H., 1987, Cryst. Rev., **1**, 3-58.

[3] MC CANDLISH, L. E., STOUT, G. H., ANDREWS, L. C., Acta Cryst., sect. A: Cryst. Phys., Diffr., Theor. Gen. Crystallogr., 1975, **A31**, 245-249.

[4] COPPENS, P., 1970, in Crystallographic computing (p. 255), ed. by AHMED, F. R., Munksgaard, Copenhagen.

[5] DE TITTA, G. T., 1985, J. Appl. Cryst., 18, 75.

[6] BENDER, R., BRAUNSTEIN, P., JUD, J. M. and DUSAUSOY, Y., 1983, Inorg. Chem., **22**, 3394.

[7] CLEMENTI, E. and RAIMONDI, D. L., 1963, J. Chem. Phys., **38**, 2686-2689.

[8] HANSEN, N. K. and COPPENS, P., 1978, Acta Cryst., **A34**, 909-921.

[9] BENARD, M., 1982, in Electron Density Distributions and the Chemical Bond (p. 221), ed. by COOPPENS, P. and HALL, M. B., Plenum Press (N. Y.).

[10] MITSCHLER, A., REES, B. and LEHMANN, M. S., 1978, J. Am. Chem. Soc., **100**, 3390.

# 11K CHARGE DENSITY STUDY OF A SHORT NON-BONDED S...O CONTACT IN 2,5-DIAZA-1,6-DIOXA-6a-THIAPENTALENE

P. BECKER
Lab. Cristallographie, CNRS, BP 166, 38042 Grenoble, France

B. FABIUS, F. K. LARSEN
Dept. Chemistry, Aarhus Univ., DK-8000 Aarhus C, Denmark

C. COHEN-ADDAD
Lab. Spectrométrie Physique, Univ. Grenoble, BP 87, 38402 St Martin d'Hères, France

M. S. LEHMANN
Institut Laue-Langevin, BP 156, 38042 Grenoble, France

Many compounds containing the X-S...O configuration (X = O, C) exhibit very short S...O distances. In order to understand the molecular stabilization in these compounds, we have undertaken an investigation of the charge density by X-ray diffraction measurements at 11 K in 2,5-diaza-1,6-dioxa-6a-thiapentalene (S...O distance of 1.84 Å).

The charge density distribution in the molecule was not clearly understood from previous 122 K X-ray and neutron measurements [1] [2]. In the present study, results obtained with 11 K X-ray diffraction measurements and aspherical atom refinement using the program MOLLY [3] are presented.

The static deformation model maps are in good agreement with the theoretical maps obtained from a previous local-density-functional calculation. The electric dipole moment calculated from multipole parameters, $\sigma$ (11 K) = 2.0D is in good agreement with the value known from a microwave study, $\sigma$ = 2.88 (2) D [4].

The mechanism proposed to interpret the X-S...0 interaction depends on the electronegativity of X and involves a $\sigma$-type coupling between oxygen and sulphur p and a stabilization of the molecule through sulfur d orbitals. The experimental charge distribution obtained at 11 K supports this theory and leads to the rejection of the previous controversial deduction that oxygen is in a special state with little hybridization. A reinvestigation of the previous 122 K X-ray data using also the MOLLY program is qualitatively consistent with the results.

## REFERENCES

[1] BECKER, P., COHEN-ADDAD, C., DELLEY, B., HIRSHFELD, F. L., LEHMANN, M. S.,Applied Quantum Chemistry, 361, Reidel Publishing Company (1986).

[2] COHEN-ADDAD, C., LEHMANN, M. S., BECKER, P., DAVY, H., Acta Cryst. (in press).

[3] HANSEN, N. K., COPPENS, P., Acta Cryst. **A34**, 909 (1978).

[4] LARSEN, N. W., NYGAARD, T., PEDERSEN, C. TH., DAVY, H., Jour. Mol. Struct., **118**, 89 (1984).

# ELECTRON DENSITY DISTRIBUTION IN TERBIUM TRIS (TRIFLUOROMETHANESULPHONATE) NONAHYDRATE CRYSTALS

A. CHATTERJEE (*)
Crystallography Centre, The University of Western Australia,
Nedlands, Australia 6009

*ABSTRACT* — The electron density distribution in the crystalline title compound (space group $P6_3/m$, $a = 13.641(4)$, $c = 7.546(2)$ Å, $Z = 2$) has been investigated at room temperature from single crystal X-ray diffraction data. Evidence for trigonally deformed distribution of 4f electrons around the terbium atom was observed in the final difference Fourier synthesis. The deformation densities exhibit antisymmetric component with excess electron density near the terbium atom, which may be interpreted in terms of 4f-5d orbital overlapping. The residual densities were also observed to be dependent on the orientation of the water oxygen atoms.

---

(*) Present Address: Department of Physics, University of Rajshahi, Rajshahi 6205, BANGLADESH.

# ELECTRON DENSITY DISTRIBUTION IN SPINEL-LIKE $CdCr_2Se_4$

TSIREL'SON, V. G., BOROVSKAJA, T. N., OZEROV, R. P.
Mendeleev Institute of Chemical Technology Miusskaja Sq. 9,
Moscow 125820, U.S.S.R.

BUTMAN, L. A.
Institute of General and Inorganic Chemistry Leninsky P. 31,
Moscow 117071, U.S.S.R.

Semiconductor and ferrimagnetic spinel-like $CdCr_2Se_4$ has been investigated by X-ray diffraction precision experiments (Sintex P21 diffractometer, Mo-$K\alpha$ radiation, spherical sample diameter 0.13 mm, 4487 reflections in two Ewald sphere octants, $\sin\Theta/\lambda \leqslant 1.054$ Å$^{-1}$). Corrections for absorption, anomalous scattering, TDS and Becker-Coppens extinction have been applied. High angle refinements converged to $R = 0{,}013$, $R_w = 0{,}0135$, $S = 1{,}053$.

The deformation electron density distribution has been calculated in the usual way. The peculiarities have been analysed in terms of electron orbitals population. For example, the preferred occupation of $e_g$ and $a_{1g}$ orbitals has been found in $Cr^{3+}$ ion in trigonal distorted octahedron leading to uncoupled electron spins in this ion. There are no covalent peaks on the Se-Cr bond line. But the peak 0.2eÅ$^{-3}$ has been found 1.1 Å away from the $Cr^{3+}$ ion near the octahedron face. This has been attributed to the preferred occupation of $d_{xy,\ xz}$ and $d_{yz}$ orbitals with the group $\pi$ ligand orbital.

# CHARGE DENSITY STUDIES IN TWO HEXAGONAL LAVES PHASES

M. J. M. DE ALMEIDA, M. M. R. COSTA, J. A. PAIXÃO
Centro FC1, INIC — Departamento de Física, Universidade de Coimbra
3000 Coimbra, Portugal

Accurate measurements of X-ray intensities were made at room temperature on two single crystals A [1] and B of TiMn$_2$ ($0.06 \times 0.06 \times 0.10$ mm$^3$ and $0.07 \times 0.08 \times 0.08$ mm$^3$, respectively) and one single crystal of TiFe$_2$ ($0.08 \times 0.06 \times 0.05$ mm$^3$) [2]. Both structures are hexagonal Laves phases (space group $P6_3/mmc$).

Reflection intensities inside an Ewald sphere of radius 1.25 Å$^{-1}$ were accurately measured with a CAD4 diffractometer, Mo-K$\alpha$ radiation and a graphite monochromator in $\omega$-$2\theta$ scans.

The usual geometrical corrections and an psi scan absorption correction were applied to the data.

High-angle refinements ($\sin\theta/\lambda \geqslant 0.6$Å$^{-1}$) of positional and thermal parameters and a scale factor were carried out from each data set. Anomalous dispersion corrections were included in the spherical atomic scattering factors. Extinction was empirically corrected through a g parameter refined simultaneously with all data.

The refinement results are shown on table 1.

TABLE 1

| | TiMn$_2$ | | TiFe$_2$ |
|---|---|---|---|
| | C1 | C2 | |
| Atom A | | | |
| z | 0.06384(3) | 0.06389(5) | 0.06393(4) |
| $\beta_{11} = \beta_{22} = \beta_{12}$ | 0.00543(3) | 0.00533(5) | 0.00612(5) |
| $\beta_{33}$ | 0.00142(1) | 0.00159(2) | 0.00192(2) |
| Atom $B_I$ | | | |
| $\beta_{11} = \beta_{22} = \beta_{12}$ | 0.00526(3) | 0.00510(8) | 0.00609(6) |
| $\beta_{33}$ | 0.00113(2) | 0.00128(4) | 0.00142(3) |
| Atom $B_{II}$ | | | |
| x | 0.82801(2) | 0.82793(4) | 0.82940(3) |
| $\beta_{11}$ | 0.00498(3) | 0.00483(6) | 0.00507(4) |
| $\beta_{22} = \beta_{12}$ | 0.00435(4) | 0.00425(9) | 0.00386(6) |
| $\beta_{33}$ | 0.00131(1) | 0.00148(2) | 0.00182(2) |
| S | 0.4604(8) | 0.5785(13) | 0.5914(9) |
| gx$10^5$ | 0.643(15) | 0.388(16) | 0.325(10) |
| R | 1.3 % | 1.3 % | 0.9 % |
| $R_w$ | 2.0 % | 1.7 % | 1.2 % |

*Portgal. Phys.* — Vol. 19, fasc. 3-4, pp. 289-291, 1988

TABLE 2

| | | $\alpha_1$ | $\alpha_2$ | $\alpha'$ | $\alpha_3$ | $\alpha_4$ | $\alpha''$ | $\alpha_5$ | $\alpha_6$ | $\alpha_7$ | $\alpha_8$ | $\alpha'''$ |
|---|---|---|---|---|---|---|---|---|---|---|---|---|
| $TiMn_2$ | C1 | .30(14) | .27(12) | .43(13) | .40(22) | .49(17) | .11(20) | .25(3) | .22(3) | .16(3) | .24(3) | .17(3) |
| | C2 | .09(13) | .46(11) | .46(12) | .65(19) | .20(16) | .15(18) | .19(3) | .20(3) | .21(2) | .20(2) | .20(2) |
| $TiFe_2$ | | .33(7) | .29(6) | .38(7) | .37(12) | .42(10) | .21(11) | .18(2) | .16(2) | .22(1) | .21(1) | .23(2) |

Difference density maps (with corresponding error maps) were drawn. Figures 1 and 2 show the maps obtained for sections (001) $z = 1/4$ and (100) $z = 1/3$ for $TiFe_2$. The corresponding maps for both crystals of $TiMn_2$ show similar effects:

*a*) a triangle of negative peaks centered on the $Fe_{II}$ ($Mn_{II}$) triangle (fig. 1) and with smaller dimensions.

*b*) a negative density between two next Ti atoms (fig. 2).

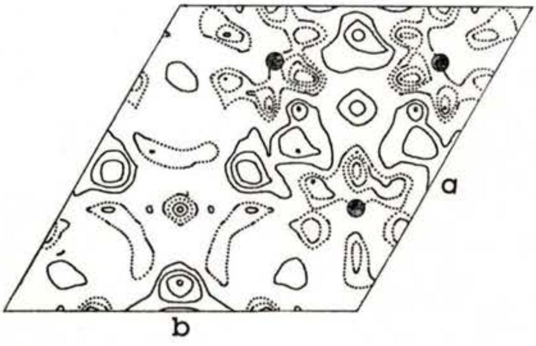

Fig. 1 — Fourier difference map, $SF_o - F_c$; section [001] of the unit cell at $z = 1/4$. Contour levels at 0.1 e/Å$^3$. Broken lines represent negative contours.

● $Fe_{II}$ atoms * Ti atoms

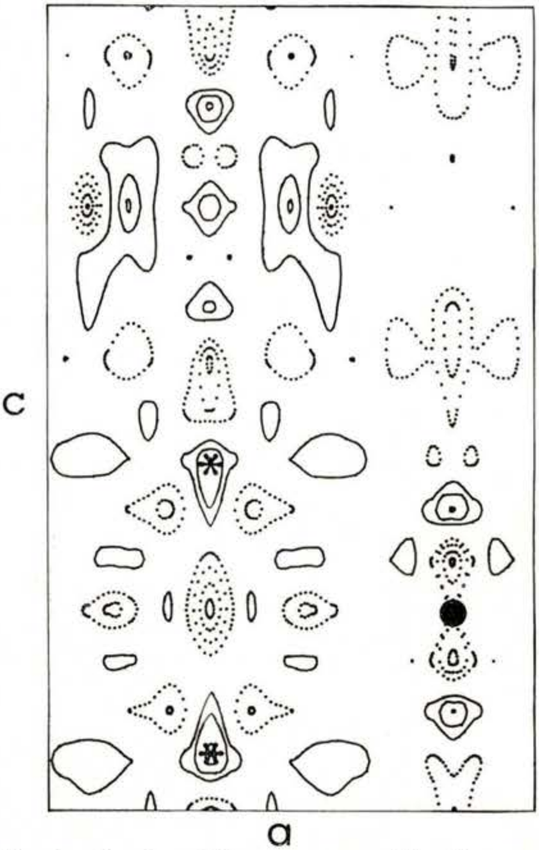

Fig. 2 — Fourier difference map, $SF_o - F_c$; section [100] of the unit cell at $x = 1/3$. Contour levels at 0.1 e/Å$^3$. Broken lines represent negative contours.

● $Fe_{II}$ atoms * Ti atoms

A refinement of 3d orbital populations was carried out. According to the site symmetry there are 8 independent $\alpha$ values for the hexagonal Laves phases, namely:

| Site A<br>symmetry 3m | | | Site $B_I$<br>symmetry 3m | | | Site $B_{II}$<br>symmetry mm | |
|---|---|---|---|---|---|---|---|
| $A_{1g}$ | $d_{z^2}$ | $\alpha_1$ | $A_{1g}$ | $d_{z^2}$ | $\alpha_3$ | $d_{z^2}$ | $\alpha_5$ |
| $E_{1g}$ | $d_{xz}$ | $\alpha_2$ | $E_{1g}$ | $d_{xz}$ | $\alpha_4$ | $d_{xy}$ | $\alpha_6$ |
| | $d_{yz}$ | | | $d_{yz}$ | | $d_{xz}$ | $\alpha_7$ |
| $E_{2g}$ | $d_{x^2-y^2}$ | $\alpha'$ | $E_{2g}$ | $d_{x^2-y^2}$ | $\alpha''$ | $d_{x^2-y^2}$ | $\alpha_8$ |
| | $d_{xy}$ | | | $d_{xy}$ | | $d_{yz}$ | $\alpha'''$ |

$$\alpha' = 1 - (\alpha_1 + \alpha_2) \qquad \alpha'' = 1 - (\alpha_3 + \alpha_4) \qquad \alpha''' = 1 - (\alpha_5 + \alpha_6 + \alpha_7 + \alpha_8)$$

Table 2 shows the 3d orbital occupancy for the three crystals studied.

## REFERENCES

[1] COSTA, M. M. R. and ALMEIDA, M. J. M., Portgal. Phys., **17**, 173-180 (1986).

[2] ALMEIDA, M. J. M., COSTA, M. M. R. and GOMES, E. M., Chemical Crystallography with Pulsed Nentrons and Synchrotron X-Rays, NATO ASI, **C221**, 586 (1988).

# ELECTRON DENSITY OF A CUBIC LAVES PHASE, $TiCo_2$

ANA MATOS BEJA, L. ALTE DA VEIGA, L. C. R. ANDRADE,
M. M. R. COSTA, J. A. PAIXÃO
Centro FC1, INIC — Departamento de Física, Universidade de Coimbra
3000 Coimbra, Portugal

The Laves phase $TiCo_2$ has a cubic structure of type $MgCu_2$ [1], space group Fd3m (8 empirical formulas per unit cell), Fig. 1.

A single crystal of $TiCo_2$ (volume: $0.10 \times 0.12 \times 0.15\ mm^3$) has been studied by X-ray diffraction, using a CAD4 diffractometer with a plane graphite monochromator and Mo(K$\alpha$) radiation; the unit cell parameters are: $a=b=c=6.7044(9)$ Å, $\alpha = \beta = \gamma = 89.99(2)°$; all the atomic positions are fixed by symmetry.

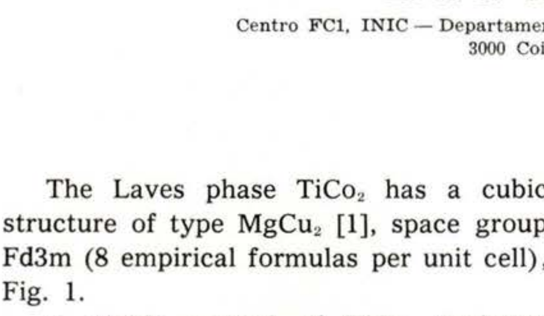

Fig. 1 — Unit cell of $TiCO_2$, showing the tetrahedra formed by Co atoms.

The diffracted intensities of the whole sphere of reflection were measured in $\omega - 2\theta$ scans, up to $\sin\theta/\lambda = 1.19$ Å$^{-1}$; the total number of independent reflections with $I \geqslant 3\sigma$ was 114.

The whole set of collected data (including weak reflections, total of 18528 reflections) was corrected for Lorentz and polarization effects and for the variation in the intensity of standard reflections; an analytical absorption correction was applied to these data.

The 114 independent «observed» reflections resulting from averaging the corrected intensities were used to carry out least squares refinements; the thermal parameters were obtained from high-angle refinements ($\sin\theta/\lambda \geqslant 0.65$ Å$^{-1}$), together with the scale factor.

An empirical extinction parameter, g, was refined afterwards (keeping all other parameters fixed) with all 114 independent reflections.

The corresponding final R-factors (wheighted and unwheighted) are respectively $R_w = 3.07\ \%$ and $R = 2.79\ \%$.

Difference density maps and the corresponding error maps were obtained; the difference maps show that there is a significant electron density (1.71 e/Å$^3$) at the center of the tetrahedra defined by Co

*Portgal. Phys.* — Vol. 19, fasc. 3-4, pp. 293-294, 1988

atoms, as observed by Ohba et al. for $MgCu_2$ [2].

A subsequent refinement of the occupation parameters of 3d orbitals has shown very small deviations from the spherically symmetrical distribution.

## REFERENCES

[1] SINHA, A. K., Progress in Mater. Sci., 15, 93 (1972).

[2] OHBA, T., KITANO, Y., KOMURA, Y., Acta Cryst., **C40**, 1-5 (1984).

# ELECTRON DENSITY OF $FeF_2$

M. J. M. de Almeida, M. M. R. Costa and J. A. Paixão
Centro FC1, INIC — Departamento de Física, Universidade de Coimbra
3000 Coimbra, Portugal

The electron density distribution of $FeF_2$ (rutile type structure, $a=b=4.7000$ Å, $c=3.3100$ Å) has been derived at room temperature from accurate X-ray diffraction measurements (CAD4 diffractometer, Mo-$K\alpha$ radiation, graphite monochromator, $\omega-2\theta$ scans, all octants of Ewald sphere out to $\sin\theta/\lambda = 1.1$ Å$^{-1}$) carried out on two single crystals A and B (with approximate dimensions $0.10\times0.11\times\times0.12$ mm$^3$ and $0.07\times0.08\times0.11$ mm$^3$, respectively).

Corrections for Lorentz, polarization and absorption were applied to 2897 reflections from crystal A and 3014 from crystal B, before averaging equivalent reflection intensities.

Atomic and temperature parameters and a scale factor were refined from high-angle data ($\sin\theta/\lambda > 0.6$ Å$^{-1}$; 123 independent reflections from crystal A and 125 from crystal B), against a spherical model with atomic scattering factors corrected for anomalous dispersion. An extinction parameter, g, was refined using the whole data set.

Difference density maps and error maps were calculated. The significant features were interpreted in terms of 3d orbitals population [1].

## REFERENCES

[1] Costa, M. M. R. and Almeida, M. J. M., Acta Cryst., **B43**, 346-352 (1987).

# ELECTRON DENSITY OF $NiF_2$

M. M. R. COSTA, M. J. M. DE ALMEIDA, J. A. PAIXÃO and L. C. R. ANDRADE
Centro FC1, INIC — Departamento de Física, Universidade de Coimbra
3000 Coimbra, Portugal

Precision X-ray diffraction measurements were carried out at room temperature on a single crystal of $NiF_2$ (rutile type structure, $a = b = 4.6499$ Å; $c = 3.0833$ Å) with approximate dimensions $0.04 \times 0.03 \times \times 0.08$ mm$^3$ (CAD4 diffractometer, Mo-K$\alpha$ radiation, graphite monochromator, $\omega - 2\theta$ scans, all octants of an Ewald sphere with radius 1.1 Å$^{-1}$).

Lorentz, polarization and analytical absorption corrections were applied to 2560 reflections.

Data processing was carried out in two different ways (DP1 and DP2):

DP1: Atomic and temperature parameters and a scale factor were refined from high-angle data (99 independent reflections with $\sin\theta/\lambda \geqslant 0.6$ Å$^{-1}$) against a spherical model with atomic scattering factors (International Tables for X-Ray Crystallography, vol. IV) corrected for anomalous dispersion.

An empirical extinction correction was applied to the data based on an extinction parameter, g, refined with the whole data set.

Difference density maps and error maps were obtained; the results were interpreted in terms of refined occupation parameters of 3d orbitals [1].

DP2: A multipole refinement of all parameters including the symmetry allowed multipole populations was made using the program MOLLY [2] and 1543 reflections with $I > 3\sigma$ corrected for isotropic, type I, Gaussian extinction.

## REFERENCES

[1] COSTA, M. M. R. and M. J. M., Acta Cryst., **B43**, 346-352 (1987).

[2] HANSEN, N. K. and COPPENS, P., Acta Cryst., **A34**, 909-921 (1978).

# DISTRIBUTION OF THE ELECTRON DENSITY IN THE A15 PHASE $Cr_3Si$

Ana Matos Beja, L. Alte da Veiga and M. M. R. Costa
Centro FC1, INIC — Departamento de Física, Universidade de Coimbra
3000 Coimbra, Portugal

One of the most interesting structural features of A15 phases is the existence of linear atomic chains in three orthogonal directions; the interatomic distances along these chains are shorter than those predicted by metallic radii criteria. Among the A15 phases (cubic, space group Pm3n), $Cr_3Si$ is one of those in which the contraction of these distances is more important [1]; the unit cell has 8 atoms with symmetry fixed positional parameters.

Previous studies of $Cr_3Si$ at room temperature have been made by Staudenmann [2].

Accurate measurements of X-ray single crystal diffraction data were undertaken. Six data sets were obtained, using four distinct crystals of the same sample and two different radiations (Ag-$K\alpha$ and Mo-$K\alpha$), at room temperature ($T \approx 291K$) and, for one of the crystals, also at low temperature ($T \approx 170K$). For every crystal, data within an Ewald sphere with radius $1.25$ Å$^{-1}$ were collected with a CAD4 diffractometer, plane graphite monochromator, in $\omega - 2\theta$ scans. The measured cell parameters were in good agreement; reflections with $I \geqslant 3\sigma$ (about 4500) have been used to perform the analysis: the usual geometrical corrections, that accounting for differences in intensities of standard reflections, and two different absorption corrections have been applied. After averaging, 145 independent reflections were used to perform least squares refinements; scale factors and thermal parameters were refined from high-order data ($\sin\theta/\lambda \geqslant 0.6$ Å$^{-1}$). An empirical extinction parameter, g, has been refined with all independent reflections.

Results obtained from different data sets were compared.

Careful measurement of absolute scale factors confirmed the values obtained from high-order refinements. The final R-factors were $1.02\,\% \leqslant R \leqslant 1.88\,\%$ and $1.40\,\% \leqslant R_w \leqslant 2.50\,\%$.

Difference density maps together with error maps were compared, and no significant covalency along the linear atomic chains was found.

## REFERENCES

[1] Nevitt, M. V., in «Electronic Structure and Alloy Chemistry of the Transition Elements», Interscience Publishers, John Wiley & Sons (1963).

[2] Staudenmann, J. L., Solid State Commun. 23, 121-125 (1977).

# ATOMIC STRUCTURE, ELECTRON DENSITY AND NON-LINEAR OPTICAL PROPERTIES OF $KTiOPO_4$ (KTP)

NIELS K. HANSEN, JEAN PROTAS and GÉRARD MARNIER
Laboratoire de Minéralogie-Cristallographie, UA-CNRS-809, Université de Nancy I,
B. P. 239, F-54506 Vandoeuvre-les-Nancy CEDEX, France

Crystalline KTP shows strong 2nd order optical properties. They were discovered about 15 years ago [1]. In the present study we have analyzed the electron density distribution with the aim of explaining these properties.

The optical property in question is the response to an applied high frequency electric field, **E** (near infrared laser light in the present case); the induced polarization, **P**, can be expressed as a Taylor series:

$$P_i = \chi_{ij}\ E_j + d_{ijk}\ E_j\ E_k + \\ + \ldots \text{(Einstein summation convention)}$$

We are interested in the coefficients $d_{ijk}$. They depend mainly on the polarizability of the valence electrons forming the bonds, so, to a good approximation, we can write:

$$d_{ijk}\,(\text{cristal}) = \sum_b g_{ijk}{}^b\, d^b/V$$

where the summation extends over the bonds within one unit cell of volume V; $d^b$ is a longitudinal 2nd order polarizability parallel to the bond axis (the other components may be taken equal to zero), and $g_{ijk}{}^b$ are geometrical factors depending solely on the orientation of the bond. For relatively simple compounds it has been observed that this type of model is appropriate for calculating the coefficients $d_{ijk}$ with an accuracy of better than 20 % when using the «Bond Charge Model» proposed by Levine [2]. In KTP the P – O and Ti – O bonds are the main contributors. From other phosphate containing materials we know that the P – O contribution is weak compared to the actual values of $d_{ijk}$ for KTP. The titanium coordination octahedra are rather irregular with bond distances varying between 1.73 and 2.15 Å. For Ti – O distances of about 2 Å, Zumsteg et al. [1] have estimated a value of $d^b$ which is far too low. It is therefore tempting to assume that the short, multiple Ti – O bonds are responsible for the pronounced non linear properties of KTP [3].

The Bragg reflections for $(\sin\theta)/\lambda < 0.9\ \text{Å}^{-1}$ have been measured at room temperature with Ag-K$\alpha$ radiation on a small, spherical single crystal [4] of radius 0.12 mm (more details to be given in [5]). It is noted that KTP crystallizes in the non centrosymmetric spacegroup $Pna2_1$. Its structure was first determined by Tordjman et al. [6]. We have determined the phases of the complex structure factors by a least-squares method fit of a multipole pseudo-atom model (computer program MOLLY [7]). The data are fitted within the limit of the experimental errors. Both Fourier and static model deformation density maps show excess electron densities in the P – O bonds and oxygen lone pair regions of the phosphate groups in good agreement with a theoretical calculation on phosphoric acid [8]. In the $TiO_6$ octahedra the most noticeable feature is a positive deformation density between the titanium and the tightly bound oxygen ion contrary to an earlier study [9]. We take our result as a confirmation of the importance of this bond for the optical properties.

We must therefore discuss the possibility of relating the ground state electron density of a crystal to its non linear dielectric properties. This problem has been considered by Flytzanis and Ducuing [10] for binary compounds with the zincblende structure. They employed a variation-perturbation approach: an operator relating the unperturbed system ground state to the perturbed system ground state is introduced; the operator is determined by minimization of a well defined energy functional depending on the operator and the ground state wavefunction, within certain approximations, on the valence electron density. Thus there is every reason to believe that the polarizability is a unique functional of the electron density; but, at present, it is not clear to us whether this procedure is of any practical use for crystals with as complex a structure as that of KTP.

## REFERENCES

[1] ZUMSTEG, F. C., BIERLEIN, J. D. and GIER, T. E., J. Appl. Phys., **47**, 4980 (1976).

[2] LEVINE, B. F., Phys. Rev., **B7**, 2600 (1973).

[3] HANSEN, N. K., PROTAS, J. and MARNIER, G., C. R. Acad. Sci. Paris Ser. II, **307**, 475 (1988).

[4] MARNIER, G., CNRS Patent (France) n.° 85, 11520 (1985).

[5] HANSEN, N. K., PROTAS, J. and MARNIER, G., to be published.

[6] TORDJMAN, J., MASSE, R. and GUITEL, J. C., Z. Kristallogr., **139**, 103 (1974).

[7] HANSEN, N. K. and COPPENS, P., Acta Cryst., **A34**, 909 (1978).

[8] MOSS, G. R. and BLESSING, R. H., Acta Cryst., **A40**, C-157 (1984): I. U. Cr. Meeting, Hamburg, August 1984, abstract n.° 06.2-1, and
BLESSING, R. H., private communication (1988).

[9] VOLOSHINA, I. V., GERR, R. G., ANTIPIN, M. YU., TSIREL'SON, V. G., PAVLOVA, N. I., STRUCHKOV, YU. T., OZEROV, R. P. and REZ, I. S., Sov. Phys. Crystallogr., **30**, 389 (1985).

[10] FLYTZANIS, C. and DUCUING, J., Phys. Rev., **178**, 1218 (1969).

# ELECTRON CORRELATION EFFECTS IN THE MOMENTUM DISTRIBUTIONS OF TRANSITION METALS

SHINYA WAKOH and MAKOTO MATSUMOTO
University of Library and Information Science,
Tsukuba 305, Japan

In the 1970' s band-theoretical calculations of Compton profiles of vanadium and chromium were published by Wakoh et al. [1], Rath et al. [2] and Wakoh et al. [3] and they were compared with the available experimental Compton profiles. Recent experimental multiple scattering profiles of vanadium by Rollason et al. [4] and chromium by Cardwell [5], and Cardwell et al. [6] have been processed by the Monte Carlo method by Folsteiner et al. [7], and therefore their single scattering profiles are very much reliable. The differences between the experiments and the theories, which were estimated by the band-theoretical one-electron approximation show a significant feature: around the origin of the momentum axis the theory is greater than the experiment, and at the higher momentum region the opposite relation occurs. The general feature has been ascribed to the electron-electron correlation effect which was not taken into account in the one-electron band scheme. So far the effect has been estimated by the Lam-Platzman [8] correction. Very roughly speaking the correction moves some amount of momentum density from the lower momentum region to the higher. This is an inherited character from the Migdal [9] function of the correlated occupation number in a correlated electron-gas system.

The difference curves (experiment--theory) are shown by dotted curves in figure 1 for vanadium. Although the effective one-electron potentials (modified $X_\alpha$-potentials) used by the APW band calculations include some correlation effects like the LSD approximation by Gunnarsson et al. [10], the APW band theoretical Compton profiles do not include any dynamical correlation effects. Therefore, the difference between experiment and theory should be due to the correlation effect and the dotted lines in figure 1 may be called experimental correlation profiles.

In order to explain the experimental correlation profiles, the Lam-Platzman correction has been used by Bauer et al. [11]. The correction is only spherically symmetrical. In the case of vanadium and chromium, therefore, realistic band structures should be used to estimate the correlation effects. Although the electron systems of transition metals are not those of the free electron-gas system, the Migdal function n(p) is used to estimate the correlation effect of vanadium and chromium. In this case, n(p) (function of momentum) should be transformed to n(E) (function of energy). A theoretical correlation profile is defined as follows:

$$J^{\mathrm{corr}}(q) = - \sum_{E=\Gamma_1}^{E_f} (1-n(E)) \times J(q,E)\,\Delta E + \sum_{E=E_f}^{\infty} n(E) \times J(p,E)\,\Delta E. \qquad (1)$$

Here, n(E) is a Migdal function and J(q, E) is a partial Compton profile contributed by the states whose energy is between $E - \Delta E/2$ and $E + \Delta E/2$. In figure 2, J(q, E)'s for vanadium along <100> scattering axis are shown. In this figure the right side axis refers to the momentum q in an atomic unit and the left side axis to the energy in an arbitrary unit; the $\Gamma_1$ energy is at 1 and the Fermi energy $E_f$ is at 22. The energy width $\Delta E$ is 0.024 Ry. The density-of-states curve

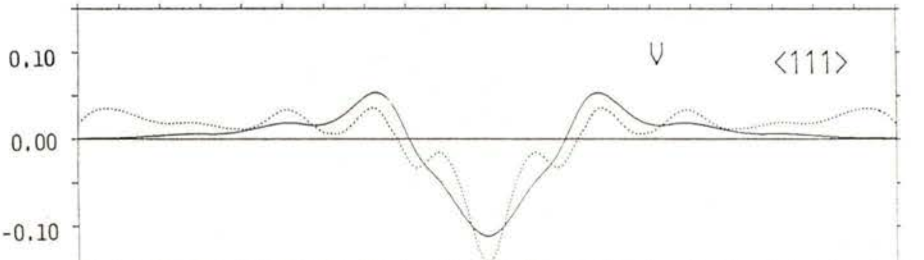

Fig. 1 — Theoretical and experimental correlation profiles along < 100 >, < 110 > and < 111 > directions for vanadium. The experimental curves (dotted lines) are the difference between the experimental Compton profiles by Rollason et al. [4] and the theoretical ones obained by the one-electron band theoretical calculation. The theoretical curves (solid lines) are only the correlation correction parts of the Compton profiles which are estimated using the Migdal function corresponding to the Wigner radius $r_s$ about 3, and real band theoretical energy dependent partial Compton profiles $J_k(q, E)$ for each scattering direction. For the experimental values only the high-energy side of the original experimental profiles are used.

N(E) is shown in figure 3. In these figures the states with energies from 13 to 33 are predominantly due to d-electrons. On the bottom of the figure 3, the Migdal function corresponding to the interelectron spacing $r_s$ whose value is about 3, is also shown. The function for vanadium is as follows:

$$n(E) = \\ = \begin{cases} 0.05+0.091\,(E/E_f) & \text{for } E<E_f \\ 0.141\times(E_b-E)^2/(E_b-E_f)^2 & \text{for } E>E_f \end{cases} \qquad (2)$$

Energies are referred to the bottom of the band ($\Gamma_1$). The lower energy part of the function n(E) and the upper one have been adjusted by the following normalisation condition:

$$\sum_{E=\Gamma_1}^{E_f} N(E)\times(1-n(E))\,\Delta E = \\ = \sum_{E=E_f}^{E_b} N(E)\times n(E)\,\Delta E \qquad (3)$$

where $E_b$ is decided to be at 60. As equation (2) has not been determined by a first principle theory, it is not so rigorous but only empirical. The theoretical correlation profiles are obtained by equation (1) using the Migdal function and J(q, E). They are shown by solid lines in figure 1.

The values of the total Comption profiles of vanadium and chromium are about 5 at the origin (q = 0), and those of the correlation effect are about 0.1. It can be said that the agreement between the theoretical correlation curve and the experimental one is very good. Although the theoretical correlation lines are almost zero at the higher momentum regions, the experimental lines are not. This fact may be due to a problem of the processing of experimental data. When the values of the experimental correlation curves at the higher momentum region become zero, the values around the origin may also be reduced a little, because the positive area

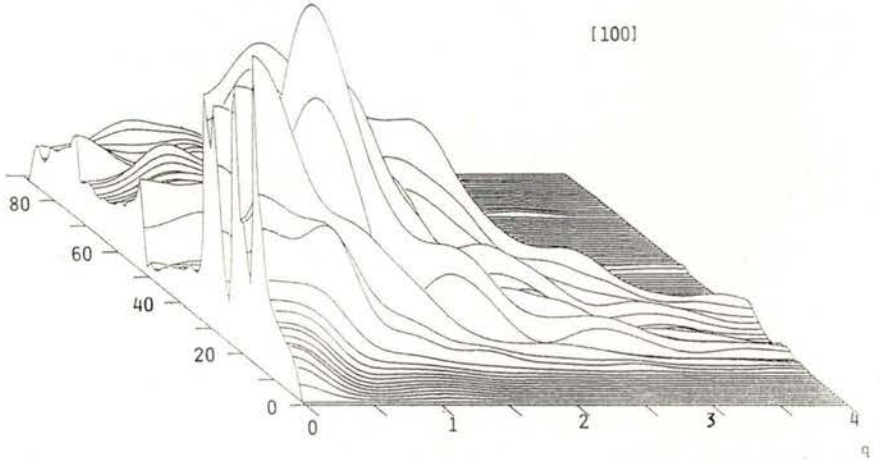

Fig. 2 — Partial Compton profiles $J_k(q, E_i)$ along < 100 > scattering direction for vanadium convoluted with a Gaussian of FWHM 0.4 a. u. The units on the right side axis q are atomic units and on the left side axis the energy E is represented (see the text). The $\Gamma_1$ energy is around 1 and the Fermi energy is at 22.

and the negative area of the lines should always cancel out. If it is true, the value of $r_s$ for the Migdal function may be a little smaller than 3 which was used for figures 1 and 3.

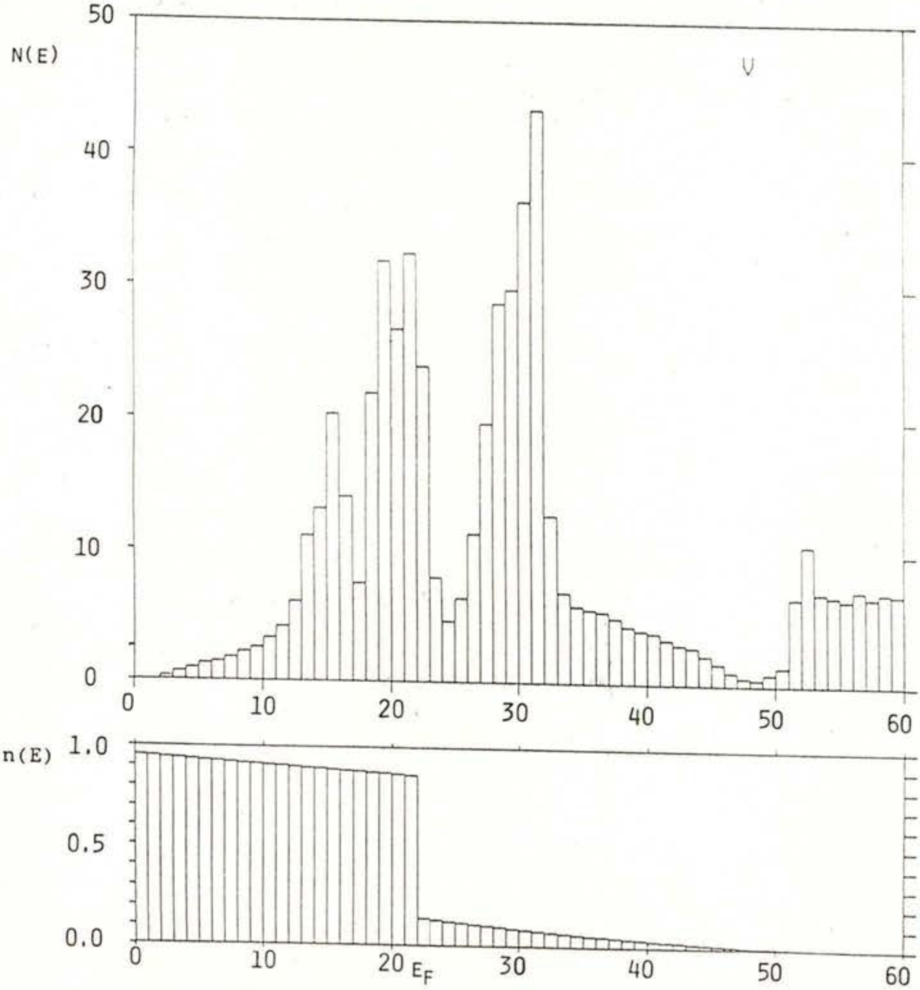

Fig. 3 — Density-of-states curve N(E) (on the top) and Migdal function n(E) (on the bottom) for vanadium. The $r_s$ value of the Migdal function is about 3.

It may be concluded that the correlation effects on the Compton profiles of vanadium and chromium, whose Fermi levels are located at the middle of the d-bands, are predominantly due to the Migdal function n(E) for the d-bands.

Thanks are due to Dr. M. J. Cooper and his Compton group at University of Warwick.

## REFERENCES

[1] WAKOH, S. and YAMASHITA, J., J. Phys. Soc. Japan, 35, 1406 (1973).

[2] RATH, J., WANG, C. S., TAWIL, R. and CALLAWAY, J., Phys. Rev., **B8**, 5139 (1973).

[3] WAKOH, S., KUBO, Y. and YAMASHITA, J., J. Phys. Japan, **40**, 1043 (1976).

[4] ROLLASON, A. J., HOLT, R. S. and COOPER, M. J., Phil. Mag. B, **47**, 51 (1983).

[5] CARDWELL, D. A., thesis at Univ. of Warwick (1987).

[6] CARDWELL, D. A., COOPER, M. J. and WAKOH, S., *J. Phys.* F., to be published.

[7] FELSTEINER, J. and PATTISON, P., Nucl. Insteum. Meths., **124**, 449 (1975).

[8] LAM, L. and PLATZMAN, P., Phys. Rev., **B9**, 5122 (1974).

[9] MIGDAL, A. B., Sov. Phys. JETP, **5**, 333 (1957).

[10] GUNNARSSON, O. and LUNDQVIST, B. I., Phys. Rev., **B13**, 4274 (1976).

[11] BAUER, G. E. W. and SCHNEIDER, J. R., Phys. Rev., **B31**, 681 (1985).

# HIGH RESOLUTION COMPTON PROFILE MEASUREMENTS USING 29.5 keV SYNCHROTRON RADIATION

ITOH, F., SAKURAI, M., SUGAWA, T. and SUZUKI, K.
Institute for Materials Research, Tohoku Univ., Sendai 980, Japan

SAKAI, N., SHIOTANI, N., MAO, O. and ITO, M.
The Institute of Physical and Chemical Research, Wakoh, Saitama 351-01, Japan

KAWATA, H., AMEMIYA, Y. and ANDO, M.
Photon Factory, National Laboratory for High Energy Physics, Tsukuba 305, Japan

*ABSTRACT* — A high resolution Compton spectrometer using 29.5 keV X-rays from synchrotron radiation has been constructed at the Photon Factory in Tsukuba, Japan. The overall momentum resolution is 0.084 a. u.. Comparison of the measured Compton profile of aluminum with the corresponding theoretical profile given by the APW calculation has suggested that the electron-electron interaction effects can be experimentally examined.

## 1 — INTRODUCTION

High resolution measurements of Compton profile are essential to study the detailed structure in the electron momentum density. There have been some reports on the design and construction of a high resolution spectrometer using synchrotron radiation [1-4]. In this paper we report further improvements on the resolution and detection efficiency for hard X-rays with use of a photo-stimulable phosphor ($BaFBr:Eu^{2+}$) film [5-7].

## 2 — EXPERIMENTAL

The present Compton spectrometer is schematically illustrated in Fig. 1. White X-rays from a vertical wiggler are monochromatized by a Ge (220) bent crystal monochromator to produce 29.5 keV X-rays with the relative band width of $1.13 \times 10^{-3}$ at 29.19 keV and the monochromatized X-rays impinge upon the sample mounted in a vacuum chamber. The inelastically scattered X-rays from the sample are energy-analyzed in the transmission mode by a Cauchois-type crystal analyzer of Si (422) bent to a radius of 2100 mm. The scattering angle is 160°. A photo-stimulable phosphor ($BaFBr:Eu^{2+}$) film [5-7], the so called Imaging Plate, is used as a detector instead of the position sensitive proportional counter (PSPC). The Imaging Plate has a large active area $(100 \times 100)$ mm$^2$ and a dynamic range of $1:10^5$. The position resolution is 100 $\mu$m. When X-rays hit the film, the X-ray image is temporarily stored on the phosphor film as a distribution of

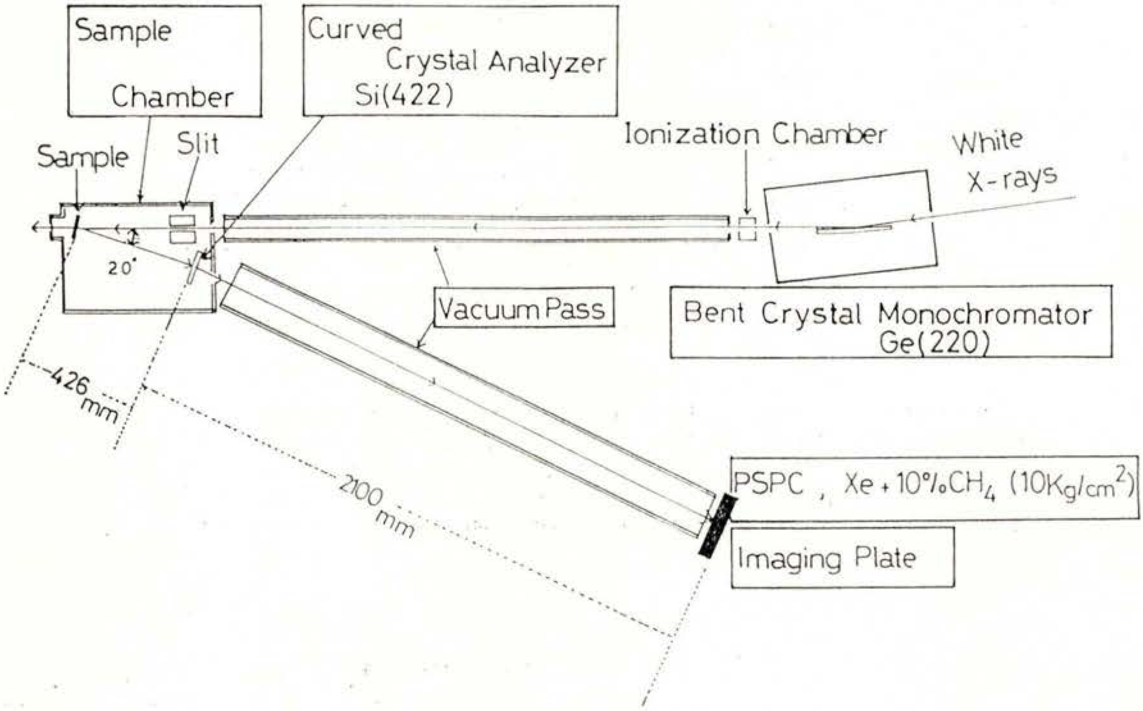

Fig. 1 — The setup of the present Compton spectrometer (top view).

quasistable color centers without any substantial fading for several days. The stored image is read out by a scanning He-Ne laser beam which releases photo-stimulated luminescence from these color centers. The luminescence is converted with a A/D converter into a time series of digital signals. One digital signal is proportional to the number of color centers in an area of 0.1 × 0.1 mm² on the Imaging Plate, thus proportional to the number of events in that area.

## 3 — RESULTS AND DISCUSSION

The Compton profiles of aluminum and silicon singe crystals were measured by this spectrometer. Since the stored data are two dimensional in this case, integration along constant-energy lines was done to obtain the Compton profile. Table 1 shows a comparison of the counting rate

TABLE 1 — A comparison of counting rates between the position sensitive proportional counter (PSPC) and the Imaging Plate (IP). The PSPC is filled with a high pressure gas (Xe + 10 % $CH_4$; 10 kg/cm²) and has a volume of 110 × 10 × 10 mm³. The dimension of the present IP is 100 mm × × 100 mm × 150 μm. The beam size on the sample is 8 × 10 mm².

| Sample | Size | PSPC (cps) | IP (cps) |
|---|---|---|---|
| Al | 12 $\phi$ × 1.8 mm | 28 | 220 |
| Si | 20 × 20 × 1.5 mm³ | 30 | 230 |

of Compton events between the Imaging Plate and the PSPC with a volume of $110 \times 10 \times 10\ \text{mm}^3$ filled with Xe + 10 % $CH_4$ gas at pressures of $10\ \text{kg/cm}^2$ in the measurements on Al and Si single crystals. It is found that the utilization of the Imaging Plate produces approximately 8 times higher counting rates than the PSPC. This comes from the wider active area of the Imaging Plate. The overall momentum resolution was determined to be 0.084 a. u. from the full width at half maximum of the elastically scattered X-ray peak at 29.5 keV.

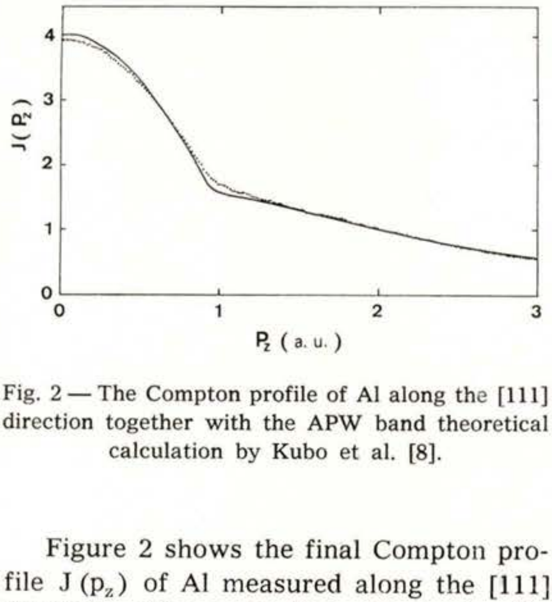

Fig. 2 — The Compton profile of Al along the [111] direction together with the APW band theoretical calculation by Kubo et al. [8].

Figure 2 shows the final Compton profile $J(p_z)$ of Al measured along the [111] direction. The solid line represents the corresponding theoretical profile by the APW method [8]. Both curves are normalized to the same area so as to give the number of total electrons in aluminum. It can be seen that in the core electron part the overall agreement between the experiment and theory is excellent, while in the valence electron part there is a definite disagreement. This disagreement seems to reflect the electron-electron interaction effects of valence electrons [9, 10].

## REFERENCES

[1] LOUPIAS, G. and PETIAU, J., J. Physique **41**, 265 (1980).

[2] ITOH, F., SAKURAI, M., SUZUKI, N., SUZUKI, K., SHIOTANI, N., SAKAI, N., FUJIMAKI, H., KAWATA, H., AMEMIYA, Y. and ANDO, M., Photon Factory Activity Report **5**, 324 (1987).

[3] SHMITZ, J. R., SCHULTE-SCHREPPING, H. and SCHULKE, W., HAYSLAB Anual Report 1987, p. 355.

[4] SHIOTANI, N., SAKAI, N., ITOH, F., SAKURAI, M., KAWATA, H., AMEMIYA, Y. and ANDO, M., to be published in Nucl. Instr. and Meth. **A275**, 447 (1989).

[5] KATO, H., MIYAHARA, J. and TAKANO, M., Neurosurg. Rev. **8**, 53 (1985).

[6] MIYAHARA, J., TAKAHASHI, K., AMEMIYA, A., KAMIYA, N. and SATOW, Y., Nucl. Instr. and Meth. **A246**, 572 (1986).

[7] AMEMIYA, Y., MASTUSHITA, T., NAKAGAWA, A., SATOW, Y., MIYAHARA, J. and CHIKAWA, J., Nucl. Instr. and Meth. **A266**, 645 (1988).

[8] KUBO, Y., WAKOH, S. and YAMASHITA, J., J. Phys. Soc. Jpn. **41**, 830 (1976).

[9] DANIEL, E. and VOSKO, S., Phys. Rev. **120**, 2041 (1960).

[10] LUNDQUIST, B. I. and LYDEN, C., Phys. Rev. **4**, 3360 (1971).

# THE COMPTON-SPECTROMETER AT THE HARWI-BEAMLINE (HASYLAB/DESY IN HAMBURG)

J. R. SCHMITZ, H. SCHULTE-SCHREPPING and W. SCHÜLKE
Institut für Physik, Universität Dortmund, FRG

The development of the Compton-spectrometer at the HARWI beamline is based on the following concept as sketched in Fig. 1:

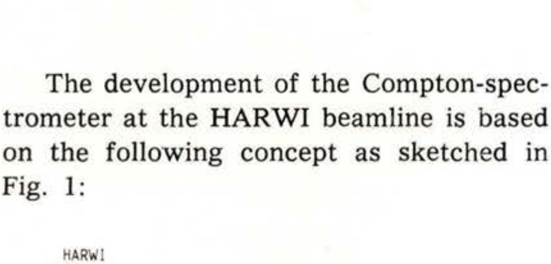

PMC = plane monochromator crystal
SFMC = sagittal focusing monochromator crystal
SS = scattering sample
CTAC = Cauchois type analyzer crystal
PSD = position sensitive detector
RC = Rowland circle

Fig. 1 — Experimental setup of the Compton-spectrometer at the HARWI-beamline, crystal-dispersive analysis.

*Monochromator:* the fixed exit double crystal monochromator consists of two Bragg-reflecting silicon crystals (140 mm × × 100 mm) together with translational and rotational stages mounted in a vacuum chamber of 750 mm diameter.

The first plane crystal is mounted on the surface of a water-cooled copper block. Gallium-metal acts to provide thermal coupling between the silicon and the copper [1]. The second crystal is cylindrically bent and groove cut on the reflecting surface to supress anticlastic bending [2]. The bending radius is determined by

$$R = \frac{2F_1F_2\sin\Theta_B}{F_1 + F_2}$$

$F_1$ and $F_2$ are the distances between the wiggler source point and the monochromator and between the monochromator and the scattering sample respectively. They are chosen to fit a 3:1-ratio [3].

Cylindrically bending is achieved by clamping the triangular shaped basis of the crystal and pressing it against an adjustable bearing at the tip of the triangle.

In cooperation with the Hahn-Meitner-Institut (Berlin) the application of specially tempered Si-crystals is considered. These crystals would make possible further improvements in intensity by broadening of the single crystal reflection curves [4].

*Analyzer:* different setups are proposed:

1. energy-dispersive analysis by means of a Ge-SSD for Compton scattering with

primary energies between 60 keV and 80 keV; momentum-resolution approximately 0.5 atomic units.

2. crystal-dispersive analysis by means of a Cauchois-type analyzing crystal for primary energies from 30 keV to 40 keV; momentum-resolution better than 0.1 atomic units, already tested at conventional X-ray sources.

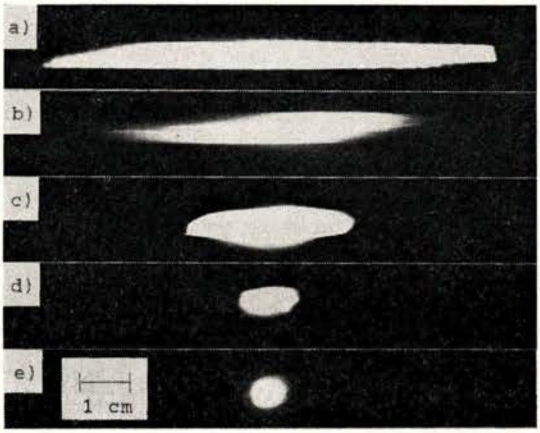

Fig. 2 — a) to e) show the decreasing size of the beam profile while the sagital focussing second crystal is bent to its proper radius of curvature of app. 90 cm.

For the present a Xe-filled position-sensitive proportional counter is used.

Enhanced efficiency and separation of higher harmonics will be obtained by a Ge-strip-detector with 200 strips, which is under development in cooperation with the Institut für Kernphysik, Kernforschungsanlage Jülich.

Fig. 2 shows a set of images of the monochromatic beam at the sample position, when the focussing crystal is bent to its proper radius of curvature.

The Compton-spectrometer at the HARWI-beamline will be available as a user-experiment in 1989.

## REFERENCES

[1] A. A. MACDOWELL, J. B. WEST, T. KOIDE, Nucl. Instr. Meth. **A246** (1986), 219-222.

[2] C. J. SPARKS, JR., G. E. ICE, J. WONG, B. W. BATTERMAN, Nucl. Instr. Meth. **194** (1982), 73-78.

[3] C. J. SPARKS, JR., B. S. BORIE, J. B. HASTINGS, Nucl. Instr. Meth. **172** (1980), 237-242.

[4] J. R. SCHNEIDER, O. D. GONÇALVES, A. J. ROLLASON, U. BONSE, J. LAUER, W. ZULEHNER, Nucl. Instr. Meth. **B29** (1988), 661-674.

# MAGNETIC X-RAY SCATTERING FACILITIES USING A HELICAL MULTIPOLE WIGGLER OF 6-GEV RING AT KEK

SAKAI, N., SHIOTANI, N. and ITO, M.
The Institute of Phys. and Chem. Research, Wako, Saitama 351-01, Japan

ITOH, F., SAKURAI, M. and SUGAWA, T.
Institute for Materials Research, Tohoku Univ., Sendai 980, Japan

KAWATA, H., AMEMIYA, Y. and ANDO, M.
Photon Factory, KEK, Oho, Tukuba 305, Japan

Magnetic systems can be studied by using circularly polarized photons, because they interact with the electron spin and the electron orbital angular momentum through the relativistic electromagnetic interaction having an order of magnitude of $E/mc^2$, where $E$ is a photon energy and $mc^2$ is the electron rest-mass energy. For the purpose of this magnetic experiment, a helical multipole wiggler will be installed soon in a 6-GeV accumulation ring at KEK, Japan, to generate eliptically polarized X-rays of energies up to 100 KeV. One of the most important characteristics of this insertion device is the high brilliance of $10^{13}$ photons/s . mm$^2$ . mrad$^2$ . 0.1 % BW (6 GeV, 50 mA) having 50 % circular polarization for 60 KeV X-rays. This will be used for the high resolution magnetic Compton profile measurement. The X-rays of lower energies with higher polarization will be used for the magnetic Bragg scattering. The ordinary high resolution Compton profile experiments can also be made by using 50-70 KeV X-rays with brilliance of about $10^{15}$ photons/s . mm$^2$ . . mrad$^2$ . 0.1 % BW (6 GeV, 50 mA). The practical designs of monochromators, a Compton scattering spectrometer, and a magnetic Bragg scattering spectrometer will be presented.

*Portgal. Phys.* — Vol. 19, fasc. 3-4, pp. 315, 1988

# CALCULATION OF COMPTON PROFILES IN FERROMAGNETIC IRON USING LMTO WAVEFUNCTIONS

A. K. SINGH, P. GENOUD and T. JARLBORG
Département de Physique de la Matière Condensée Université de Genève
24, Quai Ernest Ansermet, CH-1211 Genève 4, Switzerland

We report here the calculations of magnetic and total Compton profiles (CP) in ferromagnetic iron. A self-consistent together with a parametrized band structure calculation were performed using the linear muffin tin orbital method (LMTO). The momentum distributions were obtained using the method developed by Singh and Jarlborg [1].

As shown by the analysis of positron annihilation data made by Genoud et al. [2] on ferromagnetic iron, the Fermi surface (FS) topology given by any fully self-consistent band structure calculation is not correctly described, especially around point N of the Brillouin zone. However distributions calculated from a parametrized band structure calculation describe much better the experiment. The main difference between both corresponding FS concerns the size of the N-centred hole pocket of the 3rd minority electron band, which is large in the self-consistent calculation and very small in the parametrized one. The correct parametrization was achieved by pushing down the centre of gravity $E_\nu$ of p-bands by 35 mRy for majority p-electrons and by 57 mRy for minority ones.

The contribution of valence electrons is calculated in a sphere of radius 7.6 a. u. Core contribution is calculated self-consistently up to 12 a. u. The distributions are convolved with a gaussian of FWHM = 0.7 a. u. to take account of the experimental resolution function. Comparison of total CP with other calculations (LCAO by Callaway and Wang [3] and APW by Wakoh and Kubo [4]) indicates that our results are in very good agreement with the experimental values [5]. This is shown in fig. 1 where the difference between experiment and the calculations is pictured for three main directions. There is no direct evidence in this case to privilege the self-consistent LMTO band structure or the parametrized one.

But in the case of magnetic CP, the distributions obtained from the parametrized band structure calculation are closer to the experiment (Sakai and Sekizawa (polycrystalline) [6] and Cooper et al. (directional) [7]) than any other calculations. This is especially true in the low momentum region: the dip near $p = 0$ which is attributed to a negative polariza-

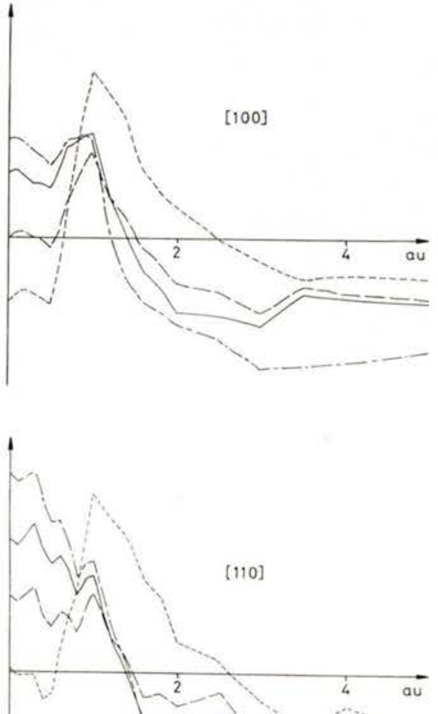

Fig. 1 — Directional total CP of ferromagnetic Fe. Difference between experiment [5] and calculations in the [100], [110] and [111] direction.

——- —— LMTO self-consistent
———— LMTO parametrized
- - - - - - - - LCAO [3]
——- · —— APW [4]

tion of s and p electrons can be correctly described only by the parametrized calculation. Corresponding curves can be

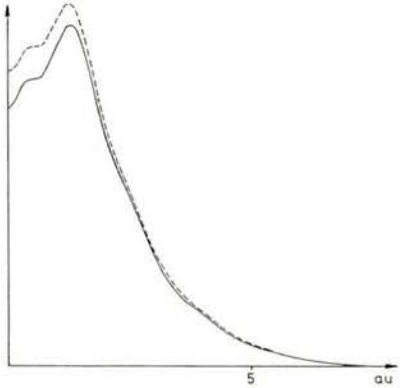

Fig. 2 — Spherically averaged magnetic CP of ferromagnetic Fe. Dashed line is for CP obtained from the LMTO self-consistent calculation and solid line for CP obtained from the parametrized one.

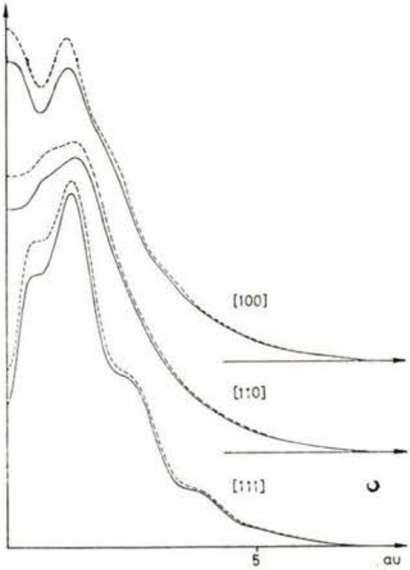

Fig. 3 — Directional magnetic CP of ferromagnetic Fe in the [100], [110] and [111] direction. Dashed line is for CP obtained from the LMTO self-consistent calculation and solid line for CP obtained from the parametrized one.

seen in fig. 2, which shows the spherically averaged magnetic CP of Fe. On fig. 3 the directional magnetic CP of Fe along three main directions are depicted.

We conclude then that the CP obtained from the parametrized LMTO band structure calculation, describe better the experimental data than these obtained from a fully self-consistent band structure calculation. This is related to the N-centred hole pocket in the 3rd minority electron band which is much too large in fully self-consistent calculations. This confirms the analysis of positron data recently made by Genoud et al. [2].

## REFERENCES

[1] SINGH, A. K. and JARLBORG, T., J. of Phys. F. **15**, 727 (1985).

[2] GENOUD, P., SINGH, A. K., MANUEL, A. A., JARLBORG, T., WALKER, E., PETER, M. and WELLER, M., J. of Phys. F. Met. Phys. **18**, 1933 (1988).

[3] CALLAWAY, J. and WANG, C. S., Phys. Rev. B. **16**, 2095 (1977).

[4] WAKOH, S. and KUBO, Y., J. Magn. Mater, **5**, 202 (1977).

[5] ROLLASON, A. J., HOLT, R. S. and COOPER, M. J., J. of Phys. F. **13**, 1807 (1983).

[6] SAKAI, N. and SEKIZAWA, H., Phys. Rev. B. **36**, 2164 (1987).

[7] COOPER, M. COLLINS, S. P., TIMMS, D. N., BRAHMIA, A., KANE, P. P., HOLT, R. S. and LAUNDY, D., Nature, **333**, 151 (1988).

# FORM FACTORS AND COMPTON PROFILES OF METALLIC Al FROM AN ATOM-IN-JELLIUM-VACANCY MODEL

S. J. MALI, R. M. SINGRU and R. R. MISHRA
Department of Physics
Indian Institute of Technology
Kanpur — 208016, India

D. G. KANHERE
Department of Physics
University of Poona
Pune — 411 007, India

*ABSTRACT* — Form factors, Compton profiles and momentum expectation values for metallic Al have been calculated using a local density approximation with the spherical atom-in-jellium-vacancy model. The theoretical results are compared with experiment and satisfactory agreement is observed.

## 1 — INTRODUCTION

The position-space density functional theory (DFT) using the electron charge density, $\rho$ ($\mathbf{r}$), as the basic variable is quite well established [1-3] as an alternate method for quantum mechanical calculations and $\rho$ ($\mathbf{r}$) is known to be directly related to some experimentally measured quantities (e. g. form factors f($\mathbf{k}$)). Similarly the DFT in the momentum space, using the electron momentum density (EMD), $\gamma(\mathbf{p})$, is also well developed [4, 5] and EMD is related to experimental measurements such as that of Compton profiles (CP), J(q). Recently some approximate methods have been developed to transform $\rho$ ($\mathbf{r}$) into $\gamma(\mathbf{p})$. In this note we present a preliminary report of our theoretical calculations of some electronic properties such as the form factor f($\mathbf{k}$), CP J(q) and expectation values $<p^n>$ in metallic Al using $\rho$ ($\mathbf{r}$). The theoretical results are compared with experiment.

## 2 — CALCULATIONS

The starting point of the present calculation was the computation of the density function $\rho$ ($\mathbf{r}$) using the atom-in-jellium vacancy (AIJV) model [6, 7]. The model uses the local density functional formalism for calculating self-consistently the non-linear response of an electron gas around a point impurity immersed in jellium. The calculational details of this model have been described elsewhere [7]. The exchange correlation term involved in these calculations was taken from the work of Vashishta and Singwi [8]. The form factors were calculated from the relation:

$$f(\mathbf{k}) = \int \rho(\mathbf{r})\ e^{i\mathbf{k}\cdot\mathbf{r}}\, d\,\mathbf{r} \qquad (1)$$

where $|\mathbf{k}| = 2\pi \sin\Theta/\lambda$.

Transformation from $\rho(\mathbf{r})$ to $\gamma(\mathbf{p})$ was carried out by using the so-called BKCM procedure [9] as developed by Gadre and Pathak [10]. It has been shown that this procedure provides satisfactory results of $\gamma(\mathbf{p})$ in metals [11]. Isotropic CP, J(q) and the momentum expectation values $< p^n >$ were calculated for metallic Al from the EMD $\gamma(\mathbf{p})$, obtained by the BKCMGP transformation.

## 3 — RESULTS AND DISCUSSION

The results of our calculations for $f(\mathbf{k})$, J(q) and $< p^n >$ for metallic Al are given in Table 1, Fig. 1 and Table 2 respectively, where a comparison with experiment [12, 13] is also provided. It is observed that the agreement between the present theory and experiment is generally satisfactory except for J(q) in the momentum range q ~ 1-2 a. u. Application of this method to other metals and a detailed discussion of these results will be presented elsewhere.

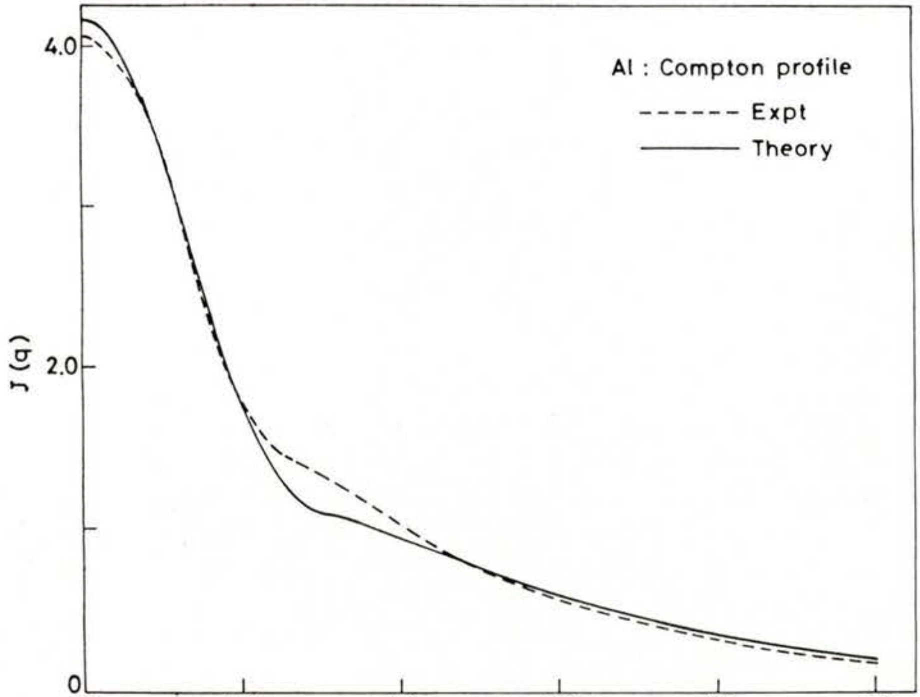

Fig. 1 — Comparison of the theoretical Compton profile J(q) for metallic Al with experimental data [13].

TABLE 1 — Comparison of theoretical form factors, f(**k**), with experiment [12]

| hkl | 111 | 200 | 220 | 311 | 222 | 400 | 331 | 420 | 422 |
|---|---|---|---|---|---|---|---|---|---|
| Present theory | 8.84 | 8.34 | 7.30 | 6.65 | 6.45 | 5.74 | 5.28 | 5.15 | 4.65 |
| Experiment | 8.80 | 8.38 | 7.27 | 6.66 | 6.48 | 5.78 | 5.33 | 5.20 | 4.66 |

The error in experimental data is ±0.06 for the first seven (hkl) values and ±0.05 for the last two (hkl) values.

TABLE 2 — Comparison of theoretical momentum expectation values $<p^{-1}>$, $<p>$ and $<p^2>$ with experiment [13]

| | $<p^{-1}>$ | $<p>$ | $<p^2>$ |
|---|---|---|---|
| Present theory | 8.37 | 31.46 | 115.47 |
| Experiment | 8.13 ± 0.14 | 31.52 | 112.85 |

## REFERENCES

[1] *Theory of Inhomogeneous Electron Gas* edited by S. LUNDQVIST and N. H. MARCH (Plenum, New York, 1983).

[2] J. CALLAWAY and N. H. MARCH, in *Solid State Physics* edited by F. SEITZ and D. TURNBULL (Academic Press, New York, 1984), Vol. 38, p. 136.

[3] J. P. PERDEW, in *Density Functional Theory* edited by J. KELLER and J. L. GAZQUEZ, Lecture Notes in Physics (Springer, Berlin, 1983), Vol. 183.

[4] *Compton Scattering* edited by B. WILLIAMS (McGRAW-HILL, New York, 1977).

[5] V. H. SMITH JR., *Local Density Approximation in Quantum Chemistry and Solid State Physics* edited by J. P. DAHL and J. AVERY (Plenum, New York, 1984), p. 1.

[6] M. MANNINEN, P. JENA, R. M. NIEMINEN and J. K. LEE, Phys. Rev. **B24**, 7057 (1981); M. J. PUSKA, R. M. NIEMINEN and M. MANNINEN, Phys. Rev. **B24**, 3037 (1981).

[7] S. J. MALI, Ph. D. Thesis, University of Poona, Pune, India (Unpublished), 1987.

[8] P. VASHISHTA and K. S. SINGWI, Phys. Rev. **B6**, 875 (1972).

[9] G. BURKHARDT, Ann. Phys. (Leipzig), **26**, 567 (1936); A. KONYA, Hung. Acta Phys. **1**, 12 (1949); C. A. COULSON and N. H. MARCH, Proc. Phys. Soc. (London), **A63**, 367 (1950).

[10] S. R. GADRE and R. K. PATHAK, Phys. Rev. **A24**, 2906 (1981).

[11] R. R. MISHRA and R. M. SINGRU, Solid State Commun. **60**, 719 (1986).

[12] P. M. RACCAH and V. E. HENRICH, Phys. Rev. **184**, 607 (1969).

[13] P. PATTISON, S. MANNINEN, J. FELSTEINER and M. COOPER, Phil. Mag. **30**, 973 (1974).

# THE ELECTRON MOMENTUM DENSITY OF GALLIUM ARSENIDE

D. N. TIMMS and M. J. COOPER
Department of Physics, University of Warwick, Coventry. CV4 7AL.

R. S. HOLT
Neutron Division, Rutherford Appleton Laboratory, Didcot, Oxon. OX11 OQX

The [100], [110], [111], [112] and [221] directional Compton profiles of gallium arsenide have been deduced from Compton scattering measurements on single crystal slices at gamma ray source energies of 412 keV and 60 keV. Both experimental systems detect profile anisotropies which are approximately 1 % of the peak height J(0). These profiles and their Fourier Transforms have been compared with the predictions of a pseudopotential band structure calculation. As expected the scale of the anisotropy is smaller than for germanium and is correctly predicted by the calculation. However, the calculation consistently underestimates the high momentum component of the charge density in all three directions.

*Portgal. Phys.* — Vol. 19, fasc. 3-4, pp. 325, 1988

# DIRECTIONAL MAGNETIC COMPTON PROFILES OF IRON

S. P. COLLINS *, D. N. TIMMS, M. J. COOPER, A. BRAHMIA and P. P. KANE **
Department of Physics, University of Warwick, Coventry. CV4 7AL

R. S. HOLT
Neutron Division, Rutherford Appleton Laboratory, Chilton, Oxon, OX11 OQX

D. LAUNDY
Daresbury Laboratory, Daresbury, Warrington, WA4, 4AD

The interference term between charge and magnetic Compton scattering amplitudes couples the circular polarization of the photon to the electron spin; it can be used to separate contributions from spin-up and spin-down electrons and obtain magnetic Compton profiles [1, 2]. We have recently measured directional magnetic Compton profiles in bcc iron for the first time [3], and we report here on further measurements with improved statistics.

The magnetic Compton profile is defined as the z-projection of the difference between spin-up and spin-down momentum densities

$$J_{\mathrm{mag}}\ (p_z) = \int_{p_x}\int_{p_y} (n\uparrow(\mathbf{p}) - n\downarrow(\mathbf{p}))\, dp_x\, dp_y \qquad \text{(i)}$$

as opposed to the usual total Compton profile which is a projection of total momentum density

$$J\,(p_z) = \int_{p_x}\int_{p_y} (n\uparrow(\mathbf{p}) + n\downarrow(\mathbf{p}))\, dp_x\, dp_y\,. \qquad \text{(ii)}$$

These profiles can be simply deduced from the measured spin-dependent and spin-independent parts of the double differential Compton cross-section.

The spin-dependent interference terms can be maximized by choosing near backscattering geometry with the sample magnetized along a direction close to the scattering vector. Under these conditions the fractional spin dependent term is given [4] by

$$\frac{\Delta\sigma}{\sigma} = 2P_c\ (\omega/m_e c^2)\ (\mu/z) \qquad \text{(iii)}$$

where $\omega$ is the incident beam energy, $\mu$ is the number of polarized electrons $P_c$ is the degree of circular polarization of the beam and z the atomic number of the scatterer.

Radiation emited out of the orbital plane of a synchrotron is eliptically

---

* Present address: Daresbury Laboratory, Daresbury, Warrington WA4 4AD, U. K.

** Department of Physico, IIT, Bombay 400 076, India.

polarized, and in this work 60 keV radiation extracted at an angle of ~ 1/10 mrad above the plane from the 5T SRS Wiggler magnet was polarized with $P_c > 0.5$. The X-ray beam was monochromated by a Si 220 crystal and scattered by 145° through a (1/4) mm thick single crystal disc of iron (containing ~ 6 % Si atoms to stabilize the bcc structure) (Figure 1). The iron disc, with the 110 crystal direction along its axis, was held across the poles of an electromagnet and the scattering vector was arranged to be along the magnetic field direction and one of the major crystal directions (100, 110 and 111). Scattered radiation was detected by a germanium SSD with an energy resolution of 0.4 keV FWHM and, after periodically reversing the magnetic field, data sets from each field direction were subtracted to yield the magnetic Compton profiles (Figure 2). Data on each crystal direction were collected for ~ 24 hours, giving around $10^6$ counts in the total profiles and a 1 % magnetic effect as predicted by (iii).

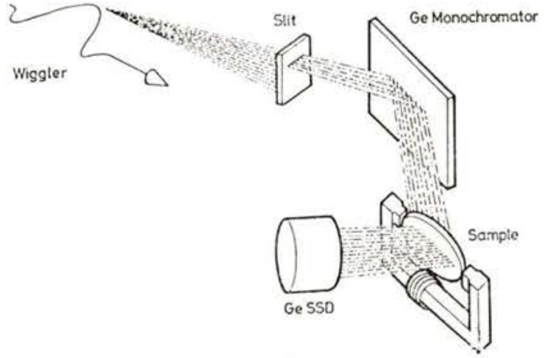

Fig. 1 — A schematic diagram of the experimental set-up, showing the transmission geometry adopted.

As in the polycrystalline measurements [1, 2] the most notable feature of the profiles is the central dip, caused by the negative polarization of conduction electrons in interatomic (low momentum) regions.

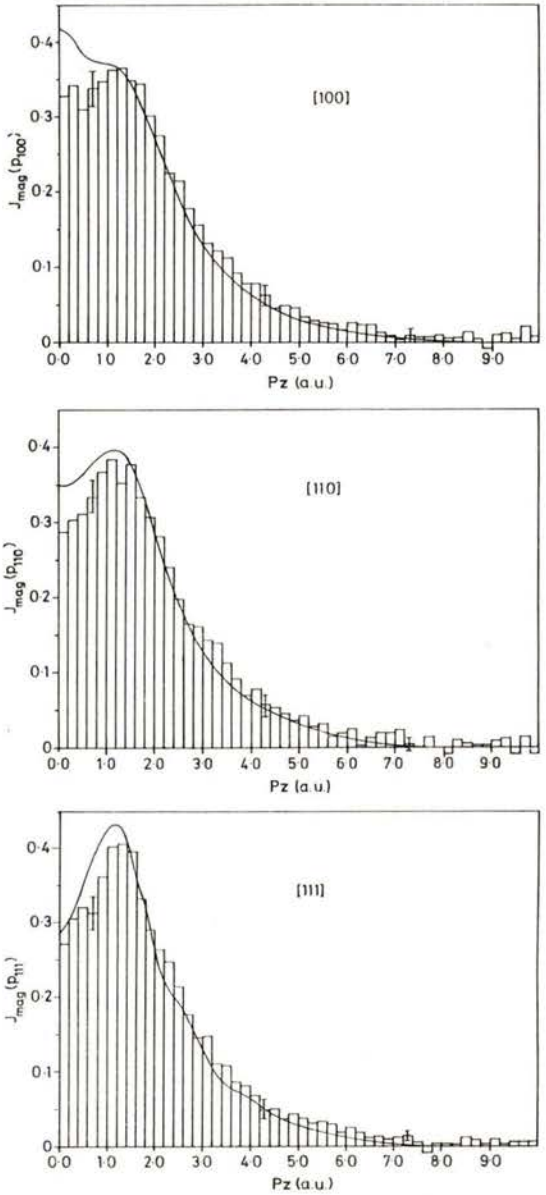

Fig. 2 — The measured directional magnetic Compton profiles (histograms) along with the results of an APW calculation [5, 6] (solid line), convoluted with a Gaussian of FWHM = 0.7 a. u. ($1.4 \times 10^{-24}$ m kg s$^{-1}$) to simulate the experimental resolution.

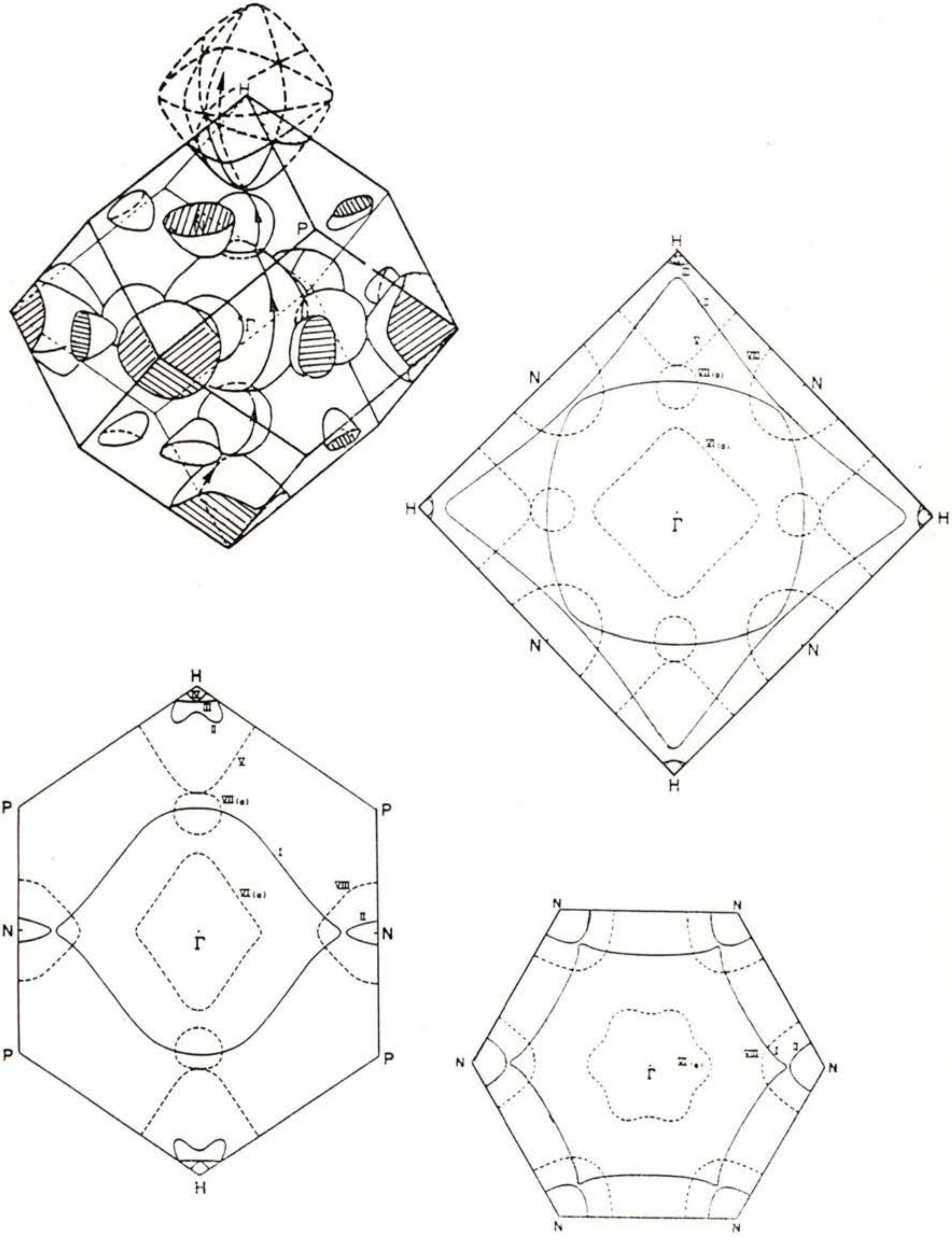

Fig. 3 — The Fermi surfaces of the majority and minority bands in iron from an APW calculation [5, 7].

The main difference between the directional profiles is in the size of the central dip, which is largest along 111 and very small along 100. This can be understood qualitatively by considering the shapes of the calculated Fermi surfaces (Figure 3). The most obvious difference between the minority and majority Fermi surfaces is that the former has large holes at the H-points on the Brillouin zone while the latter does not. The effect of these holes is to produce a positive contribution to the profile. Since electrons with wave-vectors perpendicular to the z-direction contribute to the centre of the profile, it follows that the value of $J_{mag}(0)$ will depend on the number of H-points in planes through the Brillouin zone perpendicular to each z-direction. The numbers of such points are 4, 2 and 0 for 100, 110 and 111 respectively (Figure 3), indicating that the 100 profile should be largest at the centre, and the 111 smallest, which agrees well with the experimental data.

For a more quantitative comparison the directional magnetic Compton profiles calculated by the APW method [5, 6] are shown with the experimental data (Figure 2). It can be seen that there is reasonably good agreement for 111 and 110 but the predicted central peak in the 100 profile is not observed. This may explain why the calculated central dip for polycrystalline iron is smaller than experimental data from several independent measurements suggest [1, 2]. The discrepancy is clearly associated with the 100 direction, but its origin is not yet understood.

## REFERENCES

[1] SAKAI, N., TERASHIMA, O. and SEKIZAWA, H., Nucl. Instrum. Methods, **221**, 419 (1984).

[2] COOPER, M. J., LAUNDY, D., CARDWELL, D., TIMMS, D. N., HOLT, R. S. and CLARK, G., Phys. Rev., **B34**, 5984 (1986).

[3] COOPER, M. J., COLLINS, S. P., TIMMS, D. N., BRANMIA, A., KANE, P. P., HOLT, R. S. and LAUNDY, Nature, **333**, 151 (1988).

[4] LIPPS, F. W. and TOLHOEK, H. A., Physica, **20**, 395 (1954).

[5] WAKOH, S. and KUBO, Y., J. Magn. Magn. Mater., **5**, 202 (1977).

[6] WAKOH, S., Private Communication.

[7] ROLLASON, A., Ph. D. Thesis, University of Warwick (1984).

# X-RAY INELASTIC SCATTERING INTENSITIES MEASURED BY ENERGY-DISPERSIVE DIFFRACTOMETRY

TAKAO IIJIMA and KEIKO NISHIKAWA
Department of Chemistry, Gakushuin University
Toshima-ku, Tokyo 171, Japan

*ABSTRACT* — In the energy-dispersive method, theoretical expressions of the inelastic scattering intensities to be compared with the experimental values are usually given without taking into account the width of the Compton spectrum. The validity of this approximation is numerically examined for the case of X-ray scattering from neon. It is found that the error due to the neglect of the width never exceeds 0.2 % of the total scattering intensity for scattering angles less than 35° and for the photon energy from 15 to 35 keV.

## 1 — INTRODUCTION

In the energy dispersive method, the measured inelastic intensity at a channel corresponding to the photon energy E is the sum of all the photons whose energy is reduced to just E after the energy-loss. In other words, the observed inelastic intensity is the integrated Compton spectrum over the primary energy. Usually the width of the Compton spectrum is neglected [1-5], and the inelastic scattering intensity at E is approximately given as the total inelastic scattering intensity for the primary energy E' multiplied by a band-width ratio; for the primary energy E' the Compton spectrum has the Compton peak at the energy E, i. e. at the measuring channel concerned.

In the analysis of the total scattering intensities from $N_2$, $O_2$ and Ne gases [5], a question was raised about the validity of the approximation mentioned above in order to secure the accuracy of about 0.5 %, because for the gases consisting of lighter elements as N, O and Ne, the Compton spectra have a peak with a width of about 0.5 keV and a tail extending to a few keV from the peak for the primary photon energy 30 and 45 keV and the scattering angle 43° [6]. In the present work the extent of the difference between the inelastic scattering intensity to be measured by the energy-dispersive method and the approximated intensity has been numerically estimated, in particular for the X-ray scattering from neon. A detailed account of the present study is to be published elsewhere [7].

## 2 — FORMULATION

The expression for the approximated inelastic scattering intensity from neon in terms of photon-counts per constant band-

*Portgal. Phys.* — Vol. 19, fasc. 3-4, pp. 331-333, 1988

-width at the detected photon-energy E, which has been used in the usual analysis of the data obtained by the energy-dispersive method, is given as [2, 3, 5],

$$
\begin{aligned}
I_{inel}(E) &= (dE'/dE)\, R(E, E')\, A(E, E') \times \\
&\quad \times P(E')\, I_p(E')\, S(E') \\
&= (E'/E)^2 R(E, E')\, A(E, E') \times \\
&\quad \times P(E')\, I_p(E')\, S(E')
\end{aligned}
\tag{1}
$$

where A(E, E') is the absorption factor, P(E') the polarization factor, $I_p(E')$ the intensity of the primary beam, S(E') the X-ray incoherent scattering factor of neon and R(E, E') is the recoil factor. E' is the primary photon-energy to give the Compton peak at E. The difference between E' and E is known as the Compton shift.

The inelastic intensity actually accumulated at the energy E is, however, an integral over the primary energy $E_p$:

$$
\begin{aligned}
I_{inel}(E) &= \int_{E_p > E} dE_p R(E, E_p)\, A(E, E_p) \times \\
&\quad \times P(E_p)\, I_p(E_p)\, g(E, E_p)\, S(E_p)
\end{aligned}
\tag{2}
$$

where $g(E, E_p)$ is a function which gives the shape of the Compton spectrum and it is normalized as follows:

$$\int_{E < E_p} g(E, E_p)\, dE = 1. \tag{3}$$

The Compton spectra are composed of two parts; one is the nearly symmetric part around the Compton peak which originates from the scattering by the outer electrons, and the other is the tail attributed to the scattering by the inner core (1s) electrons. Accordingly, we estimate the integral of Eq. 2 considering the contribution from the peak and tail separately.

## 3 — RESULTS AND DISCUSSION

The details of the estimation of the integral of Eq. 2 are to be reported elsewhere [7]. It turns out that the contribution to the error of Eq. 1 from the peak is very small. The dominant contribution is that from the tail. The tail function for neon was calculated by the use of the theoretical formula given by Eisenberger and Platzman [8] and Eisenberger [9], considering that the density of the final states is weighted by $4\pi p^2 dp$, p being the momentum of the recoil electron.

The final results are shown in Fig. 1 in terms of the correction factor $\alpha_{tot}$ to the total (elastic plus inelastic) scattering intensity, with the meaning that the total intensity using Eq. 1 for the inelastic part must be multiplied by $(1 + \alpha_{tot})$ to get exact values given if one used Eq. 2 for the inelastic part. At $2\theta = 45°$ the correction factor $\alpha_{tot}$ varies relatively by a maximum of 0.5 % over the range of the

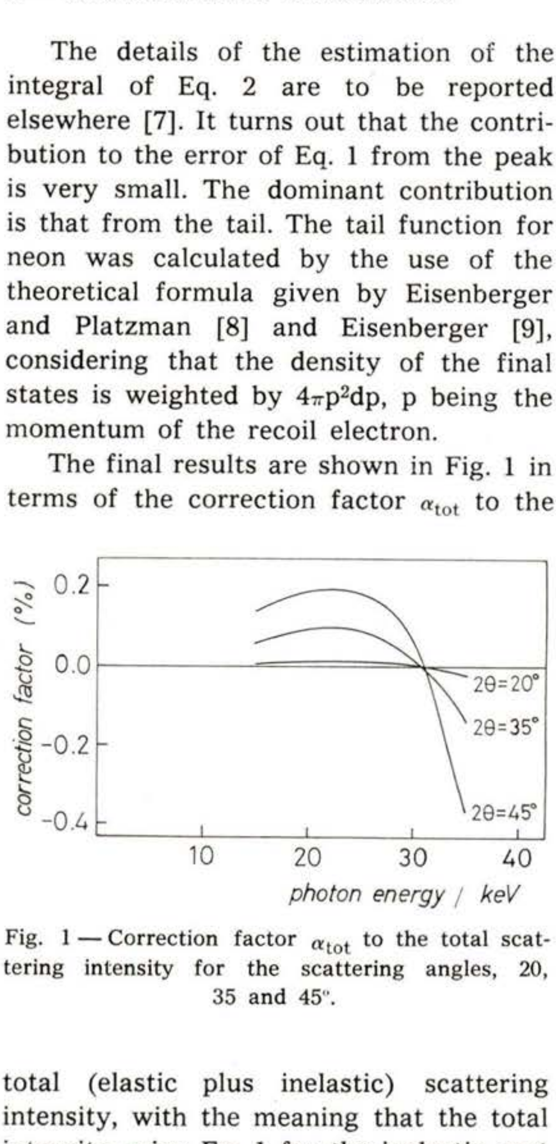

Fig. 1 — Correction factor $\alpha_{tot}$ to the total scattering intensity for the scattering angles, 20, 35 and 45°.

photon energy 15-35 keV. For $2\theta = 35°$ or smaller angles, the relative differences of $\alpha_{tot}$ are less than 0.2 % and can be safely ignored.

However, since the energy-dispersive measurements are performed in a constant-angle mode, the correction to the tabulated S(K) that is calculated at constant momentum transfer K must be applied as discussed by Bonham [10] and numerically evaluated by Sharma and Thakkar for He [11] and $H_2$ [12].

It should be noted that the present results are only applicable to the first-row elements of the periodic table, since they are based on the numerical values of the tail function of the Compton spectrum for neon. The error of the approximate equation, Eq. 1, might be larger for higher Z elements.

## REFERENCES

[1] MURATA, Y. and NISHIKAWA, K., Bull. Chem. Soc. Jpn., **51**, 411 (1978).

[2] EGAMI, T., J. Appl. Phys., **50**, 1564 (1979).

[3] NISHIKAWA, K. and IIJIMA, T., Bull. Chem. Soc. Jpn., **57**, 1750 (1984).

[4] IIJIMA, T. and MITSUHASHI, T., X-ray Instrumentation for Photon Factory, edited by HOSOYA, T., IITAKA, Y. and HASHIZUME, H., pp. 257, Tokyo, KTK Scientific Publ. (1986).

[5] NISHIKAWA, K. and IIJIMA, T., J. Chem. Phys., **87**, 3753 (1987).

[6] MITSUHASHI, T., KODERA, Y., SUZUKI, H., ISHIKAWA, T., ANDO, M. and IIJIMA, T., PF Activity Report (1984/85) vol. 3, VI, 150 (1986).

[7] IIJIMA, T. and NISHIKAWA, K., J. Appl. Cryst., **21**, 943 (1988).

[8] EISENBERGER, P. and PLATZMAN, P. M., Phys. Rev., **A2**, 415 (1970).

[9] EISENBERGER, P., Phys. Rev., **A5**, 628 (1972).

[10] BONHAM, R. A., Phys. Rev., **A23**, 2950 (1981); Erratum, Phys. Rev., **A35**, 3964 (1987).

[11] SHARMA, B. S. and THAKKAR, A. J., J. Phys., **B19**, 1049 (1986); Corrigendum, J. Phys., **B20**, 6171 (1987).

[12] SHARMA, B. S. and THAKKAR, A. J., Phys. Rev., **A31**, 5151 (1987).

# COEXISTENCE OF METALLIC AND COVALENT BONDING CHARACTERS IN InSb WITH ROCK-SALT STRUCTURE

TEIJI KOBAYASI
College of Medical Sciences
Tohoku University, Sendai 980 — Japan

HISASHI NARA
College of General Education
Tohoku University, Sendai 980 — Japan

*ABSTRACT* — The pressure-induced metallic InSb with rock-salt structure is a coexisting system of metallic and covalent bonding characters. The electronic charge distribution has been discussed within a framework of a self-consistent pseudopotential theory.

## 1 — INTRODUCTION

Pressure-induced InSb with the rock-salt (RS) structure, obtained from an amorphous phase at a pressure of ~10 kbar, is experimentally confirmed to be metallic [1]. Previously, by performing a self-consistent total energy calculation, we discussed the pressure-induced phase transition of InSb [2] and the stability of the metallic phase [3]. We found that the metallic phase is a system where metallic and covalent bonding characters coexist. In this paper we analyze the electronic charge distribution (CD) in this system. Comments on the charge transfer (CT) and the momentum distribution (MD) are given.

## 2 — ELECTRONIC CHARGE DISTRIBUTION IN THE COEXISTING SYSTEM

The CD is calculated on the basis of self-consistent band theory [3]. The higher (2nd-5th) occupied bands are separated from the lowest (lst) band. Figure 1 shows (A) the CD due to the higher occupied bands in the (100) plane and (B) the CD value along In-Sb bond. The electron distribution in the s-bonding lowest band is spherical around the Sb atom, with 5s atomic character (Fig. 2).

A massive pile of electrons is observed between In and Sb atoms. It appears around the deeper minimum of the crystal pseudopotential (PP) near the Sb atom [3]. The electrons in the bonding band tend to be attracted towards an atom of higher electronegativity. The bond-like peak, which corresponds to the covalent bond in the semiconducting InSb (ZnS-type), comes mainly from the electrons in the p-bonding part of higher bands being attracted to the valley originated from the atomic PP of Sb. The bond-like charge favours the stabilization of the metallic phase [2, 3].

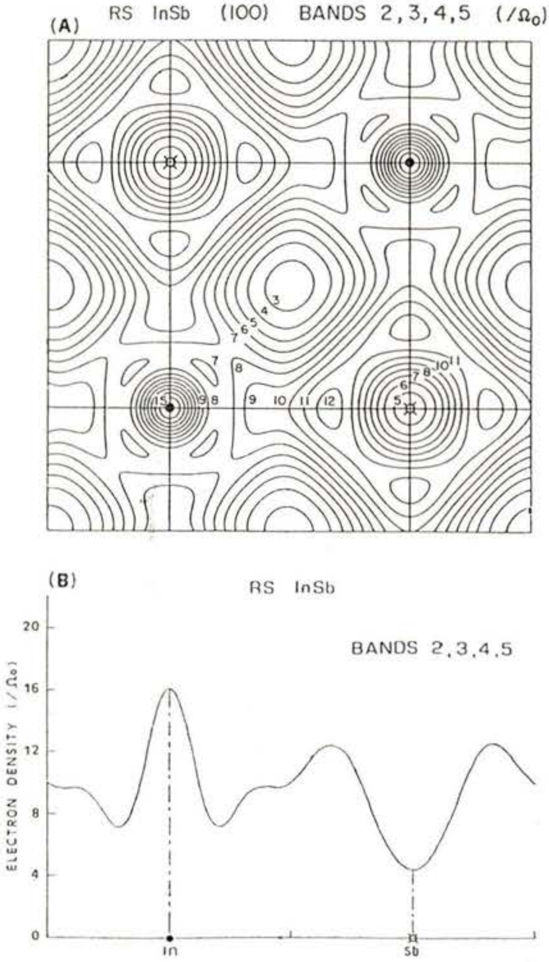

Fig. 1 — The contribution to the electron density of RS InSb from the higher occupied bands, in units of $1/\Omega_0$ ($\Omega_0$: unit cell volume). (A) The equidensity map in the (100) plane. (B) The density along the In-Sb bond.

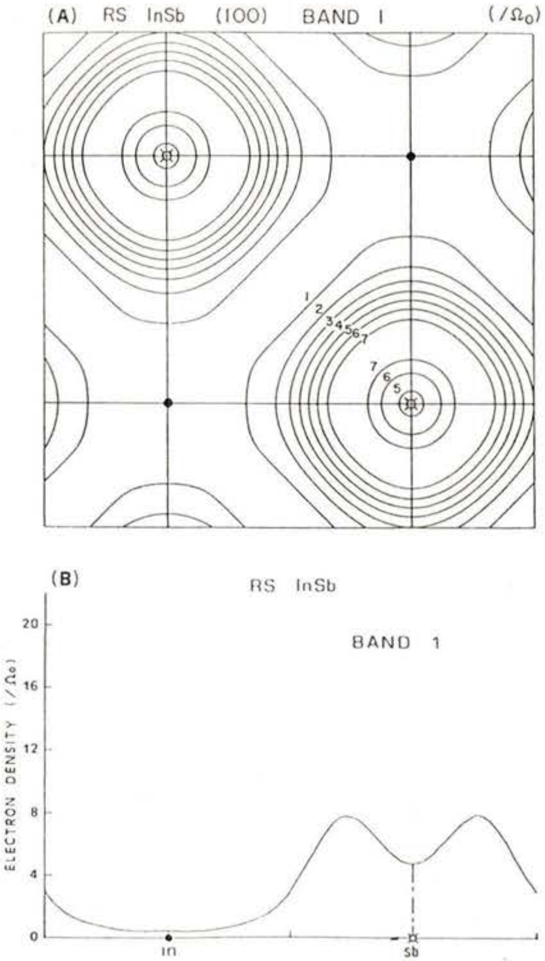

Fig. 2 — The contribution to the electron density of RS InSb from the lowest band. (A) The equidensity map in the (100) plane. (B) The density along the In-Sb bond.

We have a considerable accumulation of electrons around the In atom and a shoulder on the massive peak. The shoulder is on the shallower minimum of the crystal PP due to the atomic PP of In. These structures are due to the electrons in the s-antibonding higher bands attracted towards the In atom of lower electronegativity. The electrons in the antibonding bands behave like metallic ones. As compared with good metals, the electron distribution is considerably localized. This explains the low electric conductivity of $2.6 \times 10^4$ $\Omega^{-1}$ $\text{cm}^{-1}$.

## 3 — DISCUSSION

This material can be classified as a coexisting system of metallic and covalent bonding natures. In such a system, it is important to define CT properly as a crystalline effect, for a better understanding of its metallic behavior [3]. We define a CT by an effective charge deviation *from an atomic valence* within the Wigner-Seitz (WS) cell. The electron numbers are: 2.75 (In) and 3.25 (Sb) in the higher bands, and 0.38 (In) and 1.62 (Sb) in the lowest band. We have 0.13 electrons transferred *from the Sb-WS cell to the WS cell of metallic In.*

The MD in the typically covalent semiconductors is rather insensitive to details of valence bond structure [4]. In these materials, the bulk feature of the MD is mainly determined by the shape of Jone's zone itself. In metals, it is indeed sensitive to the electronic structure, namely to the shape of Fermi surface, many-body interactions, etc. The coexisting material may be regarded as an intermediate state between good metals and semiconductors, which calls for a systematic study of CD and MD.

## REFERENCES

[1] SHIMOMURA, O., ASAUMI, K., SAKAI, N. and MINOMURA, S., Phil. Mag., **34**, 839 (1976).

[2] SHINDO, K., SHIMAMURA, S., KOBAYASI, T. and NARA, H., J. Phys. Soc. Jpn., **49**, 2083 (1980). SHINDO, K., KOBAYASI, T. and NARA, H., J. Phys. Soc. Jpn., **50**, 2274 (1981).

[3] KOBAYASI, T., SHINDO, K. and NARA, H., «Solid State Physics under Pressure» ed. by Minomura, S. (KTK Sci. Pub., Tokyo 1985), p. 49.

[4] NARA, H., KOBAYASI, T. and SHINDO, K., J. Phys. C: Solid State Physics, **17**, 3967 (1984).

# INVESTIGATION OF THE ELECTRONIC STRUCTURE OF SOME OXIDES BY COMPTON SCATTERING TECHNIQUE

FARID M. MOHAMMAD *, B. K. SHARMA **, B. L. AHUJA and USHA MITTAL
Department of Physics, University of Rajasthan, Jaipur 302004, India

The oxides, particularly the transition-metal based ones, are an important class of materials because of their importance in industry and interesting properties. It has also been established that their characteristic behaviour is related to their electronic structure which remains less well understood. Some progress has undoubtly been made with the advent of recent techniques such as XPS, UV photoemission, XAS etc.. Regarding interpretation the Molecular Orbital approach has been mainly employed, due to difficulties with band structure methods. Recently, the Compton scattering technique has been applied successfully to probe the behaviour of valence electrons in solids including oxides [1]. In this paper we report the investigations made on three metal-oxides namely, $V_2O_5$, $Nb_2O_5$ and $MoO_3$ by means of the Compton scattering method. Preliminary results on Nb and Mo oxides were reported recently [2]. Here we also included $V_2O_5$ to see if any systematic effects could be seen.

The samples used in this work were pellets prepared by pressing polycrystalline powders, with thickness around 1.5 mm. The measurements were made with the Compton spectrometer described earlier [3]. The momentum resolution was about 0.6 a. u. and for each case more than $10^5$ counts at the Compton peak were accumulated. The signal to noise ratio varied from 750 to 250 for these samples. With the exception of $V_2O_5$, the oxides were studied with two different thicknesses to increase the reliability of the data analysis, particularly the multiple-scattering part on such systems. It was observed that after this correction was applied the data were within statistical errors. The data were corrected as usual for the effects of background, instrumental resolution, energy dependence of Compton scattering and multiple scattering (double elastic as well as inelastic events). It turned out that the correction due to double scattering was 4 %, 2.4 % and 2.5 % respectively for V, Nb and Mo oxides for J(0) value, this being 23.30, 27.53 and 14.79 with error of about 0.5 % in each case. In order to see if the free atom superposition model could predict these values, we determined theor-

---

* Ministry of Higher Education and Scientific Research, Baghdad, Iraq.

** Present address: Department of Physics, University of Helsinki, Siltavuorenpenger 20D, 00170 Helsinki, Finland.

Portgal. Phys. — Vol. 19, fasc. 3-4, pp. 339-340, 1988

etically the Compton profiles using atomic Compton profiles from the tables of Biggs et al. [4] and Weiss et al. [5]. The agreement was very poor. Then we tried various ionic models for the state of the O ion. For this, one or two electrons were added to the 2p orbital of oxygen ($O^-$ and $O^{--}$) and for the transition metal atom, the data from the metal was taken after subtracting the contribution of appropriate number of valence electrons. We thus tried two possibilities namely the transfer of one electron and two electrons per oxygen atom. In the latter case it meant complete transfer of the metal-atoms valence electrons to the oxygen atom. The results are plotted on Fig. 1 (a, b, c) for the three oxides. It is quite obvious that the model with full transfer, i. e. the $O^{-2}$ state, for these cases, seems to be supported by our data. It is worthwile pointing out that in a recent study of $MoO_3$, Werfel and Mini [6] had concluded on the basis of photoemission measurements that the bonds in this oxide should be of $d^0$ type which also agrees qualitatively with our conclusions. Since the other two oxides studied here have an identical structure, it seems logical to conclude that the same would also be valid for them. There, however, substantial differences remain between theory and experiment, particularly between 0 to 2 a. u.. This points to the need of better theoretical treatment of O-ions and perhaps measurements on crystalline samples.

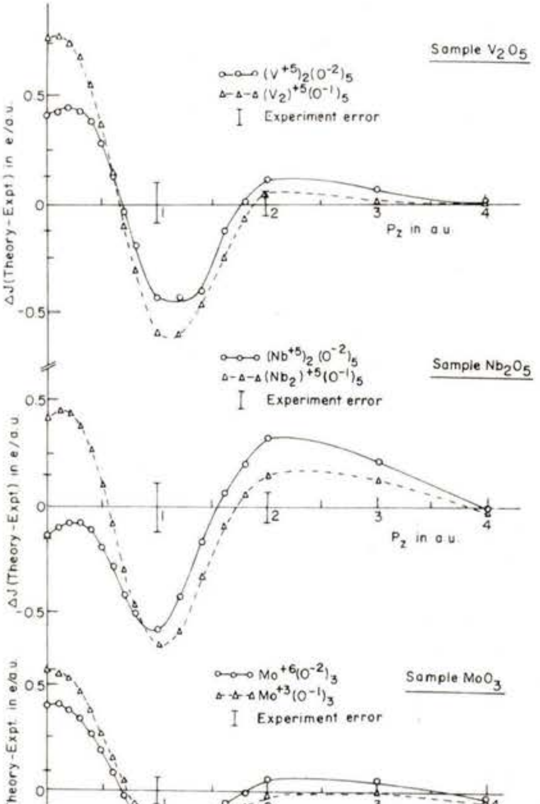

Fig. 1 — Plot of the difference between theoretical and experimental Compton profiles for $V_2O_5$, $Nb_2O_5$ and $MoO_3$. The theory has been convoluted with the RIF.

## REFERENCES

[1] See, for example, 'Compton Scattering' (Ed) B. Williams (McGraw Hill New York), 1977; Also M. Cooper Rep. Prog. Phys., **48**, 415 (1985).

[2] F. M. MOHAMMAD, B. K. SHARMA, B. L. AHUJA and U. MITTAL, Sol. Stat. Symp. **30C** (1987).

[3] M. DASGUPTA, B. K. SHARMA, B. L. AHUJA and F. M. MOHAMMAD, Am. J. Phys. **56**, 245 (1988).

[4] F. BIGGS, L. B. MENDELSOHN and J. B. MANN, At. & Nucl. Data Tab. **16**, 1975.

[5] R. J. WEISS, A. HARVEY and W. C. PHILLIPS, Phil. Mag. **17**, 241 (1968).

[6] F. WERFEL and E. MINII, J. Phys. **C16**, 6091 (1983).

# ELECTRON MOMENTUM DISTRIBUTIONS IN ZIRCONIUM AND CADMIUM

B. K. SHARMA * and B. L. AHUJA
Department of Physics, University of Rajasthan, Jaipur 302004, India

The metals zirconium and cadmium both belong to the 4d group and crystallize in H.C.P. structure [1]. Like other H.C.P. transition-metals, the electronic band structure and Fermi surface of these metals are quite complicated and less well understood [2]. Amongst these two metals, relatively more work has been reported on Zr (See Ref. 2). Within the last few years, electron momentum distributions from Compton scattering technique have been reported for a number of 4d metals [3-5]. These, however, do not include any of the H.C.P. metals and hence the present work. The measurements have been made by scattering 59.54 keV gamma-rays from polycrystalline samples of 0.1 and 1.2 mm respectively for Zr and Cd. The number of counts at the Compton peak were about 60,000 and 32,000 respectively accumulated in 48 and 24 h for Zr and Cd. The measured spectra were corrected as usual for the effects of background, instrumental resolution, sample-absorption, energy dependence of Compton scattering cross-section and elastic as well as inelastic double scattering events. The experimental profiles were normalised to 16.33 (Zr) and 18.97 (Cd) electrons these being the area of the free-atom profiles in the 0 to +7 a. u. range. In both cases the contribution of 1s electrons was not included in this normalisation as their binding energies are larger than the recoil energy in our arrangement. These 1s electrons may however contribute via double elastic scattering for which suitable correction has been made in the data analysis program.

It would have been nice if theoretical Compton profiles were available for these metals but that was not the case and we employed the simple Renormalised-Free-Atom (RFA) model which has provided reasonable compromise between the elaborate band structure calculation and free atom models. Accordingly, we followed the approach of Berggren [6] and calculated the Compton profiles for Zr choosing several 4d-5s configurations. For the case of Cd we could take only the $4d^{10}\,5s^2$ configuration but we also included the free electron and free atom models. Our results for Zr have been discussed in Ref. 2 and hence we shall skip some of the details to present the interesting aspects of the results. In Fig. 1 we compare

---

* Present address: Department of Physics, University of Helsinki, Siltavuorenpenger 20D, 00170 Helsinki, Finland.

our experiment with our calculations. In Fig. 1a we consider the case of Zr. It is seen that the difference between theory (convoluted with RIF) and experiment is quite small beyond 2 a. u. but below 2 a. u. there is considerable variation as the relative 4d-5s distribution is varied. As the number of 5s electrons is decreased from 2 to 0.6, the difference ΔJ changes and at $p_z$ equal to 0, it decreases systematically and becomes negative. On the other hand, between 1 to 2 a. u. this difference ΔJ shows the reverse behaviour. In order to find the most favoured configuration we calculated the total deviation (squared), i. e. $|\Delta J|^2$, which turned out to be lowest for $4d^4\,5s^1$ configuration. In a way, this suggests that the electron distribution in Zr metal should be close to this which turns out to be in good agreement with the conclusions of band structure calculation of Jepsen et al. [7]. Three models were considered for Cd and their relative performance is shown in Fig. 1b where we have plotted, as before, the difference between theory (convoluted with RIF) and our experiment. It is seen that the free-atom model is the poorest as is to be expected. But even the free electron model does not show good agreement. The simple RFA model shows a relatively better agreement but not as satisfactory as one would like. Thus, there is a clear need of improvement in the calculation and in particular the inclusion of 5p shell would be needed.

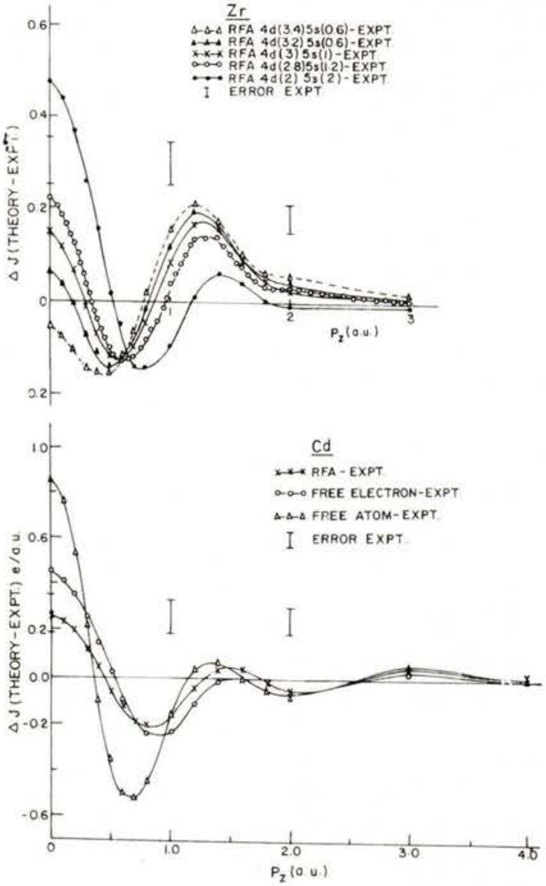

Fig. 1 — Plot of the difference between theory and experiment for polycrystalline Zr (1a) and Cd (1b). Theory has been convoluted with the RIF as discussed in the text.

REFERENCES

[1] W. B. PEARSON, «A handbook of lattice spacing and structure of Metals and Alloys» (Pergamon Press Ltd.), (1964).

[2] B. K. SHARMA and B. L. AHUJA, Phys. Rev. **B38**, 3148 (1988) and references therein.

[3] M. TOMAK, H. SINGH, B. K. SHARMA and S. MANNINEN, Phys. Stat. Sol. (b) **127**, 221 (1985).

[4] B. K. SHARMA, H. SINGH, S. PERKKIÖ, T. PAAKKARI and K. MANSIKKA, Phys. Stat. Sol. (b) **141**, 177 (1987).

[5] B. K. SHARMA, A. GUPTA, H. SINGH, S. PERKKIÖ, A. KSHIRSAGAR and D. G. KANHERE, Phys. Rev. **B37**, 6821 (1988).

[6] K. F. BERGGREN, Phys. Rev. **B6**, 2156 (1972).

[7] O. JEPSEN, O. K. ANDERSEN and A. R. MACKINTOSH, Phys. Rev. **B12**, 3084 (1975).

# COMPTON PROFILE OF POLYCRYSTALLINE TUNGSTEN

USHA MITTAL, B. K. SHARMA *, F. M. MOHAMMAD and B. L. AHUJA
Department of Physics, University of Rajasthan, Jaipur, India

In the last decade Compton scattering technique has been extensively applied to investigate the electronic structure of 3d metals [1]. Within the last few years our group has reported such results on a number of 4d metals [2]. In this paper we consider the case of tungsten for which there were theoretical calculations but no experimental data. The present measurements have been made by scattering 59.54 keV gamma-rays from a polycrystalline sample of about 0.1 mm thickness. The experimental set up has been already described (Ref. 2). It has a momentum resolution of about 0.6 a. u.. Nearly 70,000 counts/channel were accumulated near the Compton peak. The measurement time was about 48 h. The data was then corrected as usual for the effects of background, instrumental resolution, sample absorption, energy dependence of Compton scattering and elastic as well as inelastic double scattering events using the procedure described in Ref. 2. The experimental profile was normalised to an area of 25.88 electrons, this being the area of the corresponding free-atom profile in the momentum range of 0 to +7 a. u. excluding the contribution of K-shell electrons. Also the contribution of L-shell electrons has been included only up to those values for which the recoil energy exceeded their binding energies.

It was interesting to observe that our experimental values in the high momentum region, i. e. for $p_z$ above 3 a. u., were in very good agreement with the free atom values calculated from the tables of Biggs et al. [3]. This in a way was reassuring because in this region most of the contribution comes from inner electrons which are reasonably described in terms of relativistic free-atom wave functions. However, in the low momentum region there were significant deviations. It is known that the shape of Compton profile in this region is dominated by the slowly moving outer valence electrons. Therefore we consider this region more carefully in our further analysis. As mentioned before, theoretical Compton profiles for W in various crystalline directions have been published [4]. Thus it is possible to compare our results with these calculations. In order to do that we computed the spherical average using the standard formula and normalised these values properly. Thereafter, the contribution of the

---

* Department of Physics, University of Helsinki, Siltavuorenpenger 20D, 00170 Helsinki, Finland.

core electrons from the table of Biggs et al. (Ref. 3) was added. The theoretical values thus obtained were convoluted with the Residual Instrumental Function (RIF) of our instrument and compared with our data. Furthermore, in order to test if the simple Renormalised-Free-Atom (RFA) model could be employed to interpret the data in 5d metals, we calculated the Compton profile using Berggren's approach [5]. Only the 6s electron wavefunction was renormalised because most of the 5d wavefunction was contained inside the Wigner-Seitz sphere. Several 5d-6s configurations were considered and total Compton profiles were determined. Also as described above, these values were convoluted with the RIF and compared with the present measurement. In Figure 1 we have plotted the difference between the various RFA calculations and the experiment. Also plotted here are the differences between the band structure values and our experimental values. It is obvious from this figure that the agreement with the band structure values is not so good. On the other hand, the differences in the RFA values are relatively smaller. The best agreement is found for the RFA model if the configuration is chosen as $5d^{5.4}$ $6s^{0.6}$ for metal tungsten. There is, however, a need for better calculations, and new measurements with higher gamma-ray energy.

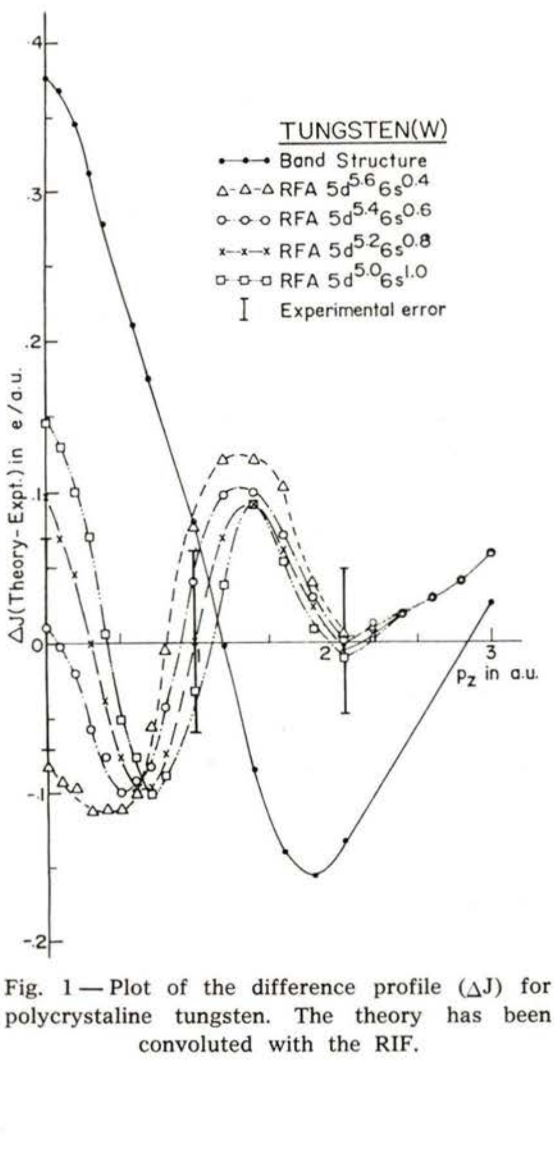

Fig. 1 — Plot of the difference profile (ΔJ) for polycrystaline tungsten. The theory has been convoluted with the RIF.

## REFERENCES

[1] See, for example, «Compton Scattering» (Ed) B. Williams (McGraw-Hill, New York, 1977), and references therein.

[2] B. K. Sharma, Anil Gupta, Hanuman Singh, S. Perkkiö, A. Kshirsagar and D. G. Kanhere, Phys. Rev. **B37**, 6821 (1988); B. K. Sharma and B. L. Ahuja, Phys. Rev. **B38**, 3148 (1988) and references therein.

[3] F. Biggs, L. B. Mendelson and J. B. Mann, At. Data and Nucl. Data Tables **16**, 264 (1975).

[4] N. I. Papanicolau, N. C. Bacalis and D. A. Papaconstantopoulos, Phys. Stat. Sol. (b) **137**, 597 (1986).

[5] K. F. Berggren, Phys. Rev. **B6**, 2156 (1972).

# THE CRYSTAL ELECTRON ENERGY AND COMPTON PROFILES FROM X-RAY DIFFRACTION DATA

ALEXANDROV JU. V., TSIRELSON V. G., OZEROV R. P.
Mendeleev Institute of Chemical Technology,
Miusskaja Sq. 9, 125820 Moscov, U.S.S.R.

There are several different quantum mechanic approaches to one-electron density matrix determination from X-ray diffraction data. The more general method of that kind which takes into account the crystal translation symmetry has been developed [1]. The method has been applied to electron energy and directed Compton profile calculations of some covalent crystals: diamond and silicon. The calculated kinetic energy (per atom in crystal) practically coincides with the theoretical one and the experimental values. The binding energies, which are determined as a difference of two very large values, coincide in a 36 %-limit; this limit is characteristic for the Hartree-Fock calculation. Coincidence with theoretical data is better.

The directed Compton profiles had been calculated in the momentum approximation. Good agreement with theory and experiment for both compounds in all regions studied has been obtained. We would like to draw attention to the fact that in the suggested approach the incoherent effects could be described starting with the coherent X-ray data. The fundamental role of the electron density can be seen here.

## REFERENCE

[1] ALEXANDROV JU. V., TSIREL'SON V. G., OZEROV R. P., Doklady Acad. Nauk 271, 1130 (1983).

# DIRECTIONAL COMPTON PROFILES AND THEIR FOURIER TRANSFORMS IN GaAs

B. K. PANDA, D. P. MAHAPATRA and H. C. PADHI
Institute of Physics, Bhubaneswar — 751005, India

Compton profiles along the (100) and (111) directions of GaAs were measured using 59.54 kev gamma-rays from a 3 Ci annular source and an HPGe detector.

Compton profile as well as Fourier transformed Compton profile anisotropies are compared with pseudopotential calculations using both local [1] as well as local plus non-local [2] potentials. The measured Compton profile anisotropy (Fig. 1) is found to be in reasonable agreement with theory for both sets of potentials. It can also be seen from Fig. 1 that the extremas in the measured anisotropy are slightly shifted to higher q values compared with theory. The autocorrelation anisotropy $\Delta B$ (111-100) as shown in Fig. 2 is dominated by the bond anisotropy as in elemental semiconductors [3] and because of resolution the effects of second neighbour interaction cannot be seen. The negative peak in the anisotropy occurs at a position lower than the bond length (4.62 a. u.). Some anisotropy is also found

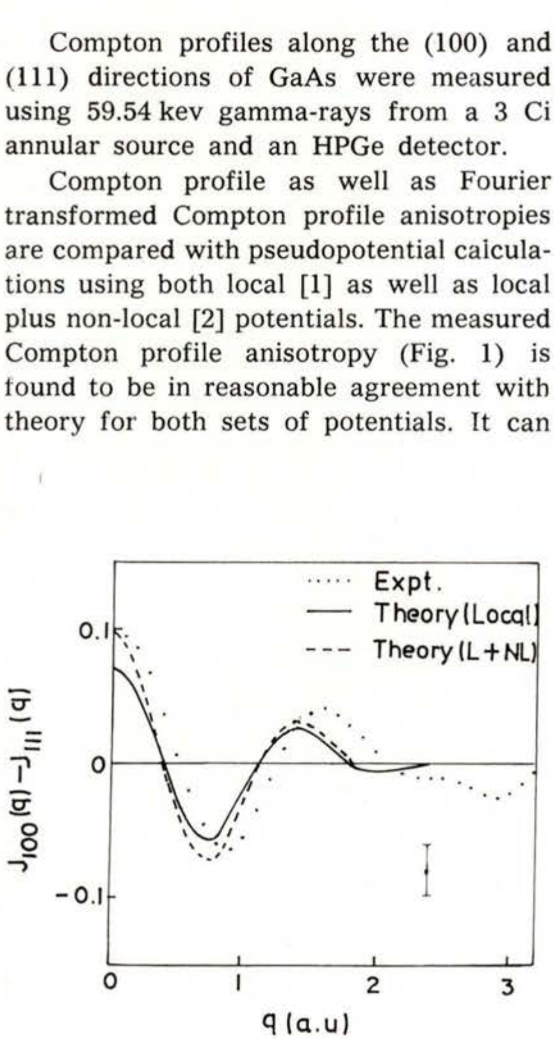

Fig. 1

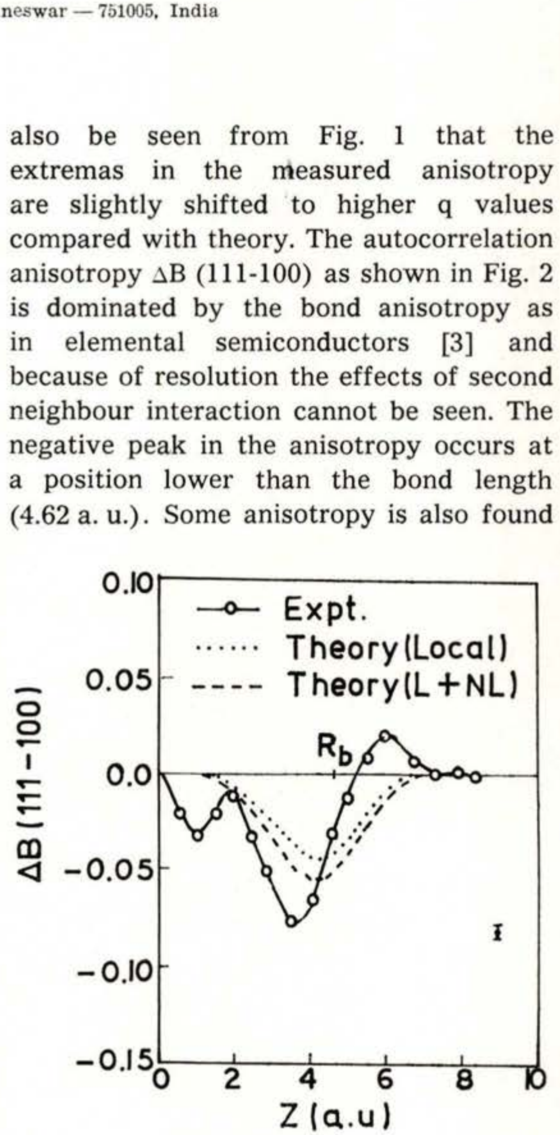

Fig. 2

*Portgal. Phys.* — Vol. 19, fasc. 3-4, pp. 347-348, 1988

at about 1 a. u. which is not predicted by the theory. This suggests that the pseudopotential wave-functions are not satisfactory near the atomic centre which perhaps is due to the fact that the wave-functions are not made orthogonal to the core electron wave-functions.

## REFERENCES

[1] COHEN, M. L., BERGSTRESSER, T. K., Phys. Rev., **141**, 789 (1966).

[2] CHELIKOWSKY, J. R., COHEN, M. L., Phys. Rev., **B14**, 556 (1976).

[3] PATTISON, P., HANSEN, N. K., SCHNEIDER, J. R., J. Chemical Phys., **59**, 231 (1981).

# PROPERTY ORIENTED BASIS-SETS USING CROSS-ENTROPY MINIMIZATION

SHRIDHAR R. GADRE, SUDHIR A. KULKARNI, INDIRA H. SHRIVASTAVA
Department of Chemistry, University of Poona
Pune — 411 007. India.

It was first axiomatically shown by Shannon [1, 2] that a suitable measure of the uncertainty associated with a finite scheme is of the form $S = -\sum_k p_k \ln p_k$ where $p_k$ is the probability of the $k^{th}$ event. The above quantity S is known as Shannon's entropy. Shannon also proved the universality of this entropy functional, which inspired Jaynes to postulate his maximum entropy principle [MEP] [3]. Jaynes' MEP states that if $P = \{p_1, p_2 \dots p_n\}$ is the probability distribution associated with experiment with data $D = \{d_1, d_2 \dots d_n\}$ then the P which best describes D is the one which maximizes $-\sum_k p_k \ln p_k$ with respect to all P satisfying D, viz. obeying the given constraints. The MEP has been successfully applied to a wide variety of problems in Science [4]. However, a problem associated with Shannon's entropy functional for a continuous case is that it is not invariant to co-ordinate transformation.

Kullaback and Leibler [5] found a solution which circumvents the invariance problem by introducing yet another measure of information, viz. the Kullback-Leibler discrimination information or cross entropy. This quantity is defined as

$$S\,[p_1 \mid p_0] = \sum_i p_{1,i} \ln \{p_{1,i}/p_{0,i}\}$$

for the discrete case. The respective quantity for a continuous one is given by $S\,[\rho_1 \mid \rho_0] = \int \rho_1(\mathbf{x}) \ln \{\rho_1(\mathbf{x}) / \rho_0(\mathbf{x})\}\, d\mathbf{x}$. Here $\rho_1(\mathbf{x})$ and $\rho_0(\mathbf{x})$ are normalized probability density functions. Thus, for a given experiment, the best way to get maximum information in an unbiased way, by employing entropy deficiency minimization,

$$\delta \left\{ \int \rho(\mathbf{x}) \ln [\rho(\mathbf{x}) / \rho_0(\mathbf{x})]\, d\mathbf{x} + \sum_{i=0}^{N} \lambda_i < F_i(\mathbf{x}) > \right\} = 0 .$$

The $\lambda_i$'s are Lagrange multipliers and $< F_i(\mathbf{x}) >$ are the constraints to which the density distribution $\rho(\mathbf{x})$ is subjected. The solution to the above equation is

$$\rho(\mathbf{x}) = \rho_0(\mathbf{x}) \exp \left[ - \sum_{i=1}^{N} \lambda_i F_i(\mathbf{x}) \right]$$

which can be employed *to refine a given density distribution* $\rho_0(\mathbf{x})$. However, there are some limitations of this approach; if

*Portgal. Phys.* — Vol. 19, fasc. 3-4, pp. 349-350, 1988

$\rho(\mathbf{x})$ is the positional electron density, then the use of kinetic energy as a constraint is impossible. Hence it is necessary to refine the 'wavefunction' enabling the imposition of constraints in position as well as momentum spaces. The minimization of cross-entropy

$$S[\rho \mid \rho_0] = \int \rho(\mathbf{r}) \ln [\rho(\mathbf{r}) / \rho_0(\mathbf{r})] \, \mathbf{dr}$$

is used in the present work for the refinement of a Near Hartree-Fock wave function. Here, $\rho_0(\mathbf{r})$ is the starting electron density and $\rho(\mathbf{r})$ is the refined one which is still obtained from a single determinantal wave function. The refined density has been obtained by constraining the wavefunction to exact / Hartree-Fock or experimentally observed $< r^2 >$ and $< p^2 >$ expectation values.

The starting wavefunctions used were the 3G basis sets of Duijneveldt [6] and Stewart [7] for hydrogen atom. Stewart's 4G basis was also used as a starting wavefunction for the hydrogen atom. The 3G and 4G basis sets of Huzinaga [8] for helium atom were used as test cases. For lithium and beryllium, 9G and 10G basis set of Huzinaga [8] respectively were employed for this purpose. The parameters, viz. the linear coefficients and exponents, were varied to within ± 15 % of their original values.

For all cases examined $< r^n >$ and $< p^n >$, expectation values extracted from the refined distribution, are in general in better agreement with the exact ones. Particularly, the percentage improvement in the expectation values of $<r^{-2}>$, $<r^3>$, $<p^3>$ and $<p^4>$ is remarkable in all the three basis sets considered here. For example, the Stewart basis for the H atom yields 1.838, 7.453, 1.577 and 3.416 (all values in a. u.) for the above expectation values, compared to 1.876, 7.473, 1.629 and 3.645 for the refined basis respectively. The corresponding exact ones are 2.0, 7.5, 1.698 and 5.0 a. u. The typical loss in energy, as compared to the corresponding Near Hartree-Fock one, was 0.03 percent for all the atoms examined.

Summarizing, one can conclude that the present method is a relatively simple one requiring just two experimentally measurable quantities. From this minimal input one can obtain a refined distribution which improves nearly all the one-electron properties with a negligible loss in energy.

## REFERENCES

[1] Shannon, C. E., Bell System Tech. J. **27**, 379, 623 (1948).

[2] Khinchin, A. I., Mathematical Foundation of information theory. Dover publications, Inc. New York (1957).

[3] Janyes, E. T. in Ray, C., Smith, W. T. Grandy. Jr. (eds.), Maximum Entropy and Bayesian Methods in Inverse Problems, 1985, D. Reidel Publishing Company.

[4] Jaynes, E. T. in Levine, R. D., Tribus, M. (eds.), The Maximum Entropy Formalism (Cambridge, Mass, M. I. T. Press).

[5] Kullback, S., Leibler, R. A., Ann. Math. Stat. **22**, 79 (1951).

[6] Duijneveldt, F. B., IBM Technical report, RJ 945 (IBM, San José, Califórnia, U.S.A., 1971).

[7] Stewart, R. F., J. Chem. Phys. **52**, 431 (1970).

[8] Huzinaga, S., J. Chem. Phys. **42**, 1293 (1965). It was observed that the 10G basis orbitals for Lithium as given by above author are not orthonormalized.

# ELECTRON MOMENTUM DISTRIBUTION AND SPIN DENSITY OF FERROMAGNETIC IRON STUDIED BY SPIN POLARIZED POSITRON ANNIHILATION

P. GENOUD, A. K. SINGH, A. A. MANUEL, T. JARLBORG, E. WALTER, M. PETER

Département de Physique de la Matière Condensée, Université de Genève
24, Quai Ernest Ansermet, CH-1211 Genève 4, Switzerland

M. WELLER

Max-Planck-Institut für Metallforchung, Institut für Werkstoffwissenschaften
Seestrasse 92, D-7000 Stuttgart, Germany

We report the study of the Fermi surface topology, electron momentum density and spin momentum density in ferromagnetic iron using two-dimensional angular correlation of (polarized) positron annihilation radiation (2D-ACPAR). The 2D-ACPAR distributions in the [110] plane of a single crystal of iron were measured at 4.2K with high-resolution (0.3 × 0.5 mrad$^2$) apparatus using two high-density proportional chambers described elsewhere [1].

In this work [2] we were mainly interested in the study of the Fermi surface (FS) topology and in the electron-positron ($e^- - e^+$) correlation effects. This was achieved by comparing the experimental data (total momentum density as well as relative spin density) with distributions obtained using the formalism of Singh and Jarlborg [3], based on linear muffin tin orbitals (LMTO) band structure calculations.

The total momentum distributions performed in the independent particle model (IPM) from a fully self-consistent LMTO band structure calculation (very similar to others [4-6]) do not give a correct description of the experimental data due to inadequate FS topology. In p-space, disagreement is particularly important near $p = 0$, as shown in fig. 1a where a line in the [100] direction is extracted from the 2D-ACPAR. The integration axis lying along the [110] direction (Γ-N direction), we can attribute this discrepancy to the large minority N-centred hole pocket (lack of contributing states at N-point). This is confirmed when folding the distributions from p- to k-space (from Lock, Crisp and West (LCW) theorem [7]), as seen in fig. 2 along some symmetry lines of the normalized distributions. There are clearly missing states near N-point. Electron-positron ($e^- - e^+$) correlation effects cannot explain such a large discrepancy. To get a correct FS description, we have performed a parametrized LMTO band structure calculation. This was achieved by treating the centre of gravity $E_\nu$ of p-bands as a parameter. Pushing down $E_\nu$ for majority p-states by 35 mRy and that of minority p-states by 57 mRy allowed us to obtain a FS topology comparable with other parametrized calculations [8-10]. The important difference between fully self-consistent and parametrized band structure calculations concerns the size (large in the first case, small in the latter) of the N-centred hole pocket in the 3rd band of minority electrons. As presented in fig. 1b, the 2D-ACPAR calculated from this parametrized band-structure gives a very good picture of the experiment. In k-space (fig. 2) the large discrepancy near point N of the BZ has almost disappeared, the remaining difference being attributed to $(e^- - e^+)$ correlation effects as described below.

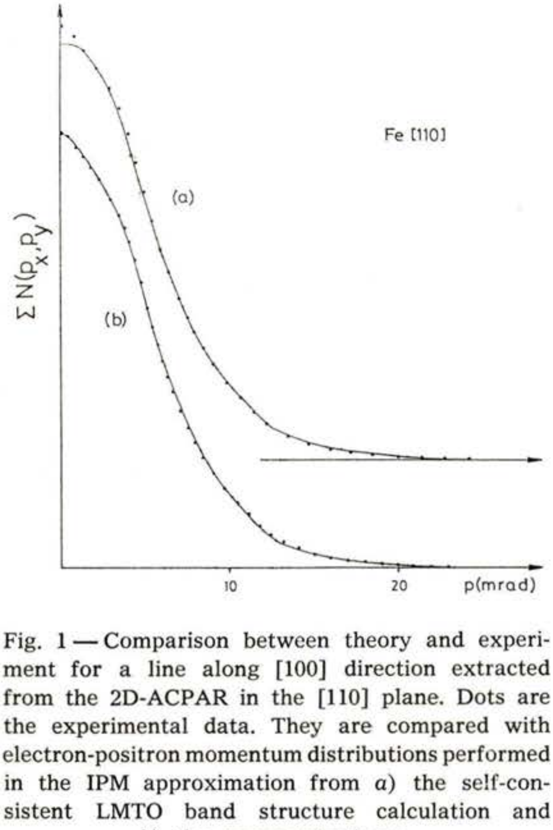

Fig. 1 — Comparison between theory and experiment for a line along [100] direction extracted from the 2D-ACPAR in the [110] plane. Dots are the experimental data. They are compared with electron-positron momentum distributions performed in the IPM approximation from *a*) the self-consistent LMTO band structure calculation and *b*) the parametrized one.

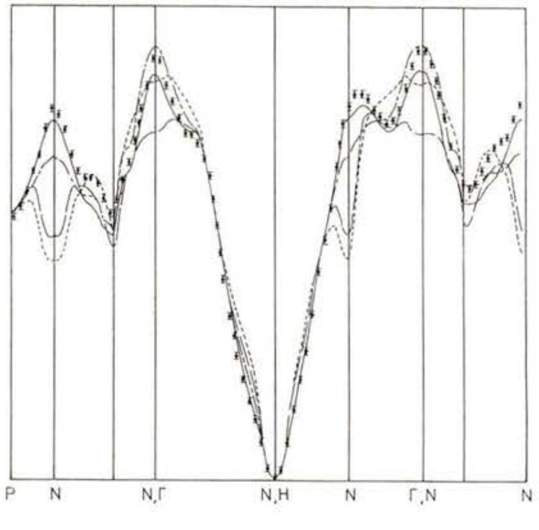

Fig. 2 — LCW analysis of the total momentum distributions of ferromagnetic Fe along some symmetry lines of the Brillouin zone. Experiment (dots) is shown together with different calculations:

| | |
|---|---|
| - - - - - - - - | self-consistent IPM |
| — —— — | self-consistent with correlations |
| —— . —— | parametrized IPM |
| ———— | parametrized with correlations |

The $(e^- - e^+)$ correlation effects were included in the calculations using a Kahana type enchancement factor similar to the one introduced by Šob [11] and independently by Mijnarends and Singru [12]. In the case of Fe, the nature of the $(e^- - e^+)$ correlation effects is found to resemble the ones which were observed by Singh et al. [13] for nickel. This confirms the systematic trends of the $(e^- - e^+)$ correlation effects for localized d electrons: the contribution of these electrons to the momentum density is overestimated in the calculations and has to be reduced. The s and p electrons have anyway to follow the usual enhancement picture.

A fine tuning of the enhancement parameter was obtained only by analyzing the relative spin momentum density distributions. This lead us to treat differently the correlations for majority and minority electron bands. Fig. 3 shows a line in the [100] direction extracted from the relative spin momentum density distributions (experiment, IPM calculation and calculation including many body effects). The negative value of the spin density at low momenta is attributed to a negative polarization of s and p electrons; positrons are much more sensitive to these electrons than to d electrons, which are positively polarized.

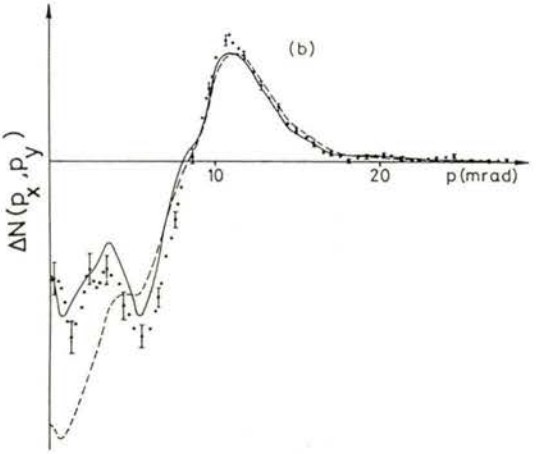

Fig. 3 — Comparison of the relative two-photon spin momentum density of ferromagnetic Fe in the [110] plane. The line is in the [110] direction. Dots are for the experiment. Dashed line is the electron-positron momentum distribution calculated from the parametrized band structure in the IPM approximation. Solid line is for the distribution including correlation effects.

## REFERENCES

[1] BISSON, P. E., DESCOUTS, P., DUPANLOUP, A., MANUEL, A. A., PERREARD, E., PETER, M. and SACHOT, R., Helv. Phys. Acta, **55**, 100 (1982).

[2] GENOUD, P., SINGH, A. K., MANUEL, A. A., JARLBORG, T., WALKER, E., PETER, M. and WELLER, M., J. of Phys. F. Met. Phys. **18**, 1933 (1988).

[3] SINGH, A. K. and JARLBORG, T., J. of Phys. F. **15**, 727 (1985).

[4] WAKOH, S. and YAMASHITA, J., J. Phys. Soc. Japan, **21**, 1712 (1966).

[5] CALLAWAY, J. and WANG, C. S., Phys. Rev. B. **16**, 2095 (1977).

[6] MORUZZI, V. L., JANAK, J. L. and WILLIAMS, A. R. in «Calculated Electronic Properties of Metals» (New York: Pergamon) (1978).

[7] LOCK, D. G., CRISP, H. and WEST, R. N., J. of Phys. F, **3**, 561 (1973).

[8] JANSEN, H. J. F. and MÜLLER, M., Phys. Rev. B, **26**, 2624 (1982).

[9] NAUTIYAL, T. and AULUCK, S., Phys. Rev. B, **32**, 6424 (1985).

[10] PAPACONSTANTOPOULOS, D. A. in «Handbook of the Band Structure of Elemental Solids» (New York and London: Plenum Press) (1986).

[11] ŠOB, M., Proc. 8th Ann. Symp. on Electronic Structure of Metals and Alloys, Gaussig (GDR), Ed. P. Ziesche 106 (1978).

[12] MIJNARENDS, P. E. and SINGRU, R. M., Phys. Rev. B, **19**, 6038 (1979).

[13] SINGH, A. K., MANUEL, A. A., JARLBORG, T., MATHYS, Y., WALKER, E. and PETER, M., Helv. Phys. Acta, **59**, 410 (1985).

# RESONANT RAMAN SCATTERING IN METALS

V. ETELÄNIEMI, K. HÄMÄLÄINEN, S. MANNINEN and P. SUORTTI
Department of Physics, University of Helsinki, Siltavuorenpenger 20 D, 00170 Helsinki, Finland

S. P. COLLINS, M. J. COOPER and P.P. KANE
Department of Physics, University of Warwick, Coventry, CV4 7AL, U.K.

In the resonant Raman scattering process (RRS) the incident X-ray photon energy is just below the absorption threshold of the target electron. The intermediate state involves a virtual hole and in the final state there is a higher shell hole, an electron in the continuum and an emitted photon. The scattered energy spectrum is continuous because the photon and the ejected electron share the available energy. RRS arises from the $\bar{p}.\ \bar{A}$ term in the interacting Hamiltonian which couples the electromagnetic field and electron, and the scattering cross section in the dipole approximation has been recently calculated [1], for example, in $(1s,2p_j)$ resonance $(j = \frac{1}{2}\ ,\ \frac{3}{2})$:

$$d^2\sigma/(d\omega_2\, d\Omega) = \{[r_0^2\, \omega_2\ (\Omega_{1s} - \Omega_{2pj})\ g_{2pj,1s}\ (\Omega_{1s} + \omega)]/[2\, \omega_1 (\Omega_{1s} - \Omega_{2pj} - \omega_2)^2 + (\Gamma_{1s}^2/4\hbar^2)]\}\ [dg_{1s}/d\omega] \quad \Omega_{1s + \omega}$$

where $\hbar\omega_1$ and $\hbar\omega_2$ are the incident and scattered photon energies, $\hbar\omega = \hbar\omega_1 - \hbar\omega_2$ the kinetic energy of the ejected electron, $\hbar\,\Omega_{1s}$ and $\hbar\,\Omega_{2pj}$ are the relevant binding energies (measured from the bottom of the conduction band), $g_{2pj,1s}$ the oscillator strength of the transition between $1s^{-1}$ and $2p_j^{-1}$ hole states, $dg_{1s}/d\omega$ is the oscillator density and $\Gamma_{1s}$ is the width of the 1s level.

In order to study the energy dependence of the RRS cross section a tunable X-ray source is required. This can now be done using synchrotron radiation. Scattering components due to the $A^2$-term can be eliminated by choosing a scattering angle of 90° and a linearly polarized incident beam. First experiments of this kind were made for Ni in LURE, Paris [2].

In this study synchrotron radiation from SRS storage ring in Daresbury, U.K., was used to measure RRS cross section for Cu ⇒ (1s,np) resonance and Ho ⇒ (2p,ns &nd) resonance. Incident energies varied from the values ~ 1 keV below the desired absorption edge up to the energies ~ 300 eV above the edge where fluorescence was excited. The differential cross section of RRS in Cu is shown at a few incident energies in figure 1. Far below the resonance which occurs at $\hbar\omega_1 = 8.98$ keV one

*Portgal. Phys.* — Vol. 19, fasc. 3-4, pp. 355-357, 1988

can see also the elastic scattering and K-fluorescence (excited by the harmonic wavelenghts passing through the monochromator) components. The line shape is dominated by the low energy tail at low energies and gets narrower when the resonance energy is approached (see Eq. 1).

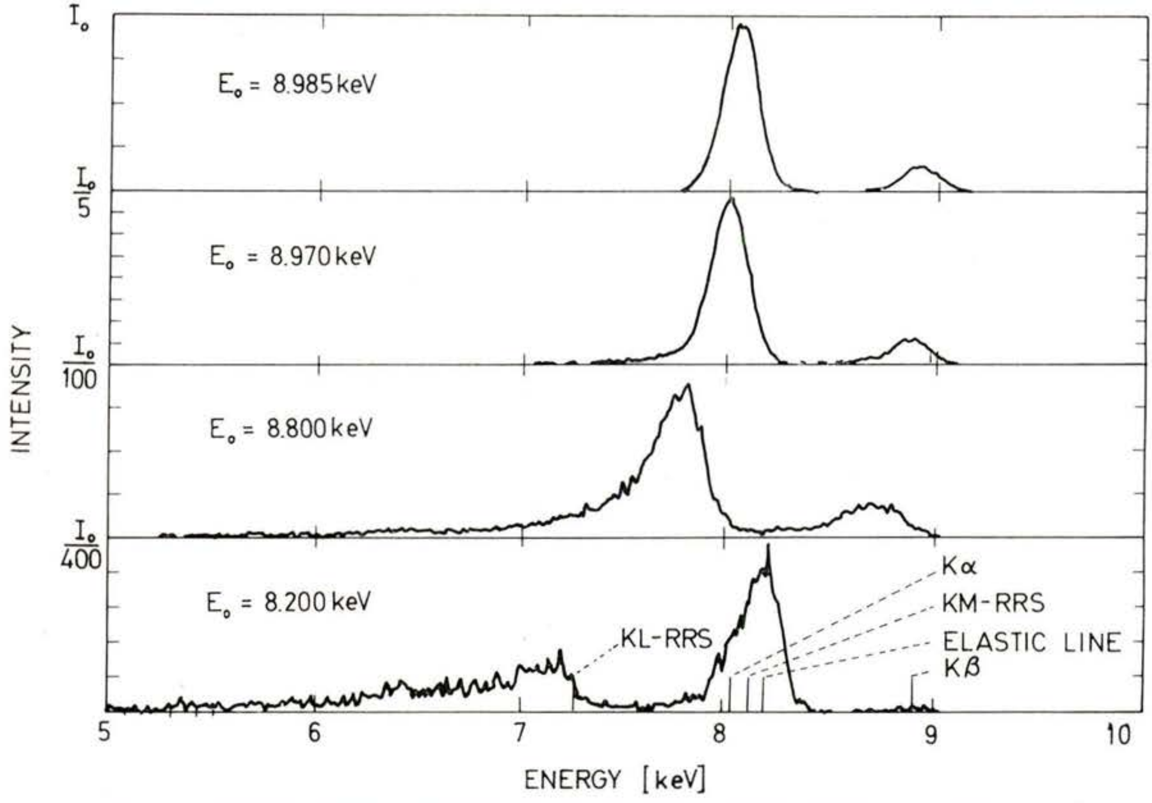

Fig. 1 — Resonant Raman spectrum of Cu at four different incident energies. The positions of the RRS edges, elastic scattering and K-fluorescence are shown on the lowest spectrum. Note the change in the vertical scale.

Instead of measuring the incident photon flux the experimental RRS cross section was put into an absolute scale by using the measured fluorescence intensities; the tabulated fluorescence yields $\omega_K$ and $\omega_{L_{III}}$ [4]. This technique has been described previously [2]. The results thus obtained were then used to determine the branching ratios and RRS yield when the resonance condition was approached.

It is seen from Eq. 1 that the double differential cross-section $d^2\sigma/d\Omega d\omega_2$ is proportional to the oscillator density $dg_{1s}/d\omega$. The spectrum of the scattered photons is a mirror image of the absorption spectrum. However, the RRS spectrum is not smeared by the width of the K-shell or L-shell hole, which makes it a potentially more sensitive probe than the absorption spectrum. Another difference is seen from Eq. 1, namely that the RRS spectrum is a superposition

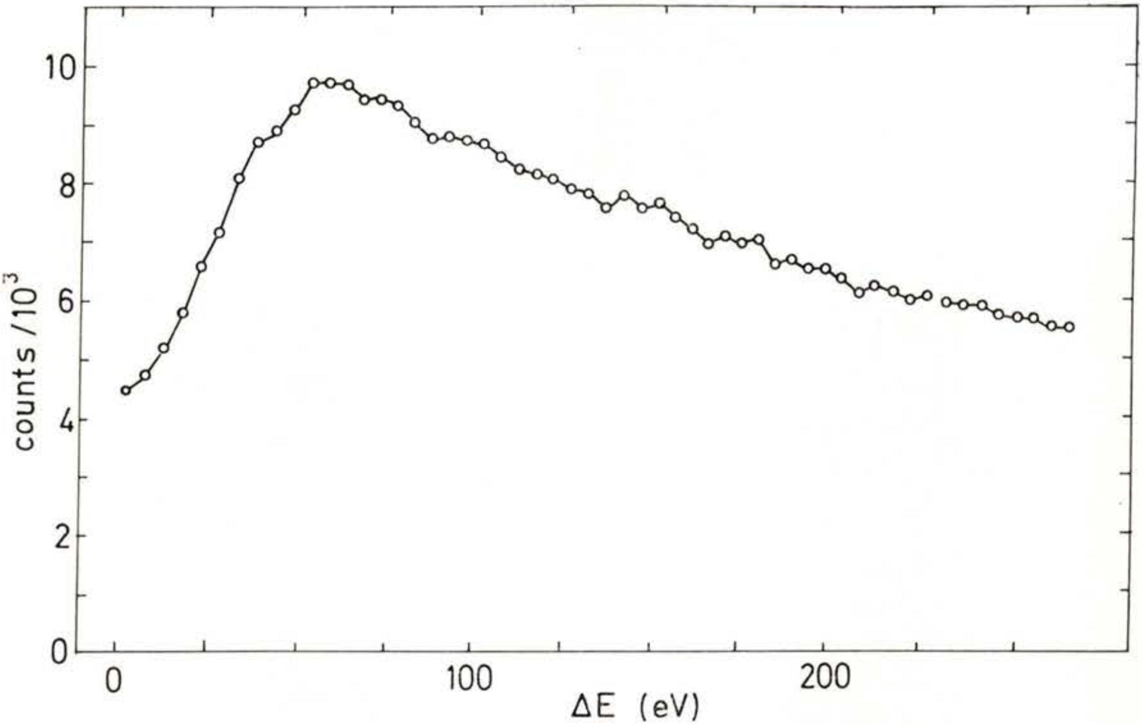

Fig. 2 — Fine structure of the KL-RRS in Ni measured using $CuK_{\alpha1}$ radiation and a focusing crystal spectrometer.

of two components, at least. In the case of the $(1s,2p_j)$ resonance the difference in energy is that between the states $2p_{1/2}$ and $2p_{3/2}$, and the intensity ratio is 1:2.

The double differential cross-section $d^2\sigma/d\Omega\, d\omega_2$ of the RRS in Ni was measured using a focusing crystal spectrometer and $CuK_{\alpha1}$-radiation from a sealed X-ray tube [3]. The resolution of the spectrometer was about 10 eV, which was sufficient to reveal the fine structure of the RRS. The modulation of the spectrum is similar to EXAFS of the absorption spectrum, but some of the features are lost because of the superposition of the $(1s,2p_{1/2})$ and $(1s,2p_{3/2})$ components. An uncorrected spectrum is shown is Fig. 2.

## REFERENCES

[1] T. ÅBERG and J. TULKKI in «Atomic Inner-Shell Physics» edited by B. Crasemann (Plenum, New York, 1985) Ch. 10.

[2] S. MANNINEN, P. SUORTTI, M. J. COOPER, J. CHOMILIER and G. LOUPIAS, Phys. Rev. **B34**, 353 (1986).

[3] P. SUORTTI, V. ETELÄNIEMI, K. HÄMÄLÄINEN and S. MANNINEN, J. Physique, **C9**, 831 (1987).

[4] P. VENUGOPALA RAO in «Atomic Inner-Shell Physics» edited by B. Crasemann (Plenum, New York, 1985), Vol. II, Ch. 1.

# BINDING AND CORRELATION EFFECTS IN SIMPLE MOLECULES AS STUDIED BY GAS-PHASE X-RAY DIFFRACTION

KEIKO NISHIKAWA and TAKAO IIJIMA

Department of Chemistry, Gakushuin University, Toshima-ku, Tokyo 171, Japan

*ABSTRACT* — In order to investigate the binding and correlation effects in charge distribution of free molecules, total X-ray scattering intensities of $N_2$, $O_2$, Ne, $C_2H_2$ and $C_2H_4$ have been measured by the use of the energy-dispersive method. Comparison of the measured intensities with Hartree-Fock independent-atom calculations has revealed the binding and correlation effects. However, the accuracy of the data in the smaller s-region has not been satisfactory. Some improvements have been made both in the experimental setup and in the analysis.

## 1 — INTRODUCTION

Investigation of the binding and correlation effects in the charge distribution of atomic and molecular systems has been extensively performed by means of high energy electron scattering [1, 2]. However, only a few studies by gas-phase X-ray scattering have been carried out, although its importance is well recognized since the papers by Bartell and Gavin [3, 4].

The present authors have carried out gas-phase X-ray diffraction experiments using the energy-dispersive method, which is suitable for the gaseous samples [5, 6]. The samples were $N_2$, $O_2$, Ne, $C_2H_2$ and $C_2H_4$. Comparison of the measured intensities with Hartree-Fock (HF) independent-atom calculations reveals the binding and correlation effects. However, it has been found that the accuracy of the data is not sufficient for the purpose of measuring the intensities from gases within the error of about 0.5 %. In the present paper, some of the results for the samples mentioned above are reported and the improvements of the experimentation and analysis are presented.

## 2 RESULTS AND DISCUSSION

The diffractometer setup is shown in Fig. 1. In the energy-dispersive method, white X-rays are used as a primary beam and photons scattered from the samples

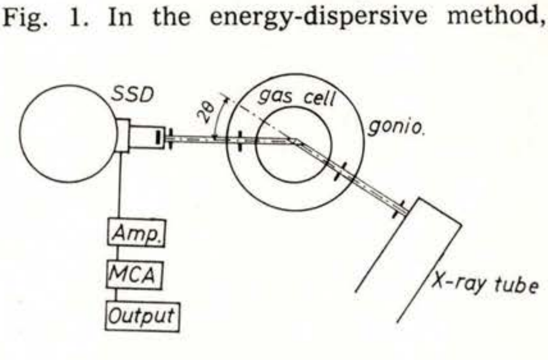

Fig. 1 — Schematic diagram of the experimental apparatus.

are energy-analyzed by a solid state detector (SSD). Because the energies of successively detected photons are distributed over the whole energy region of the primary beam, the data covering a certain region of the scattering parameters ($s = 4\pi \sin\Theta/\lambda = 4\pi E\sin\Theta/hc$, $2\Theta$: scatterring angle, $\lambda$: wavelength of X-rays, E: energy of photon) are obtained in parallel. A sealed-off tube with a tungsten target was used as the source of white X-rays. A cylindrical gas cell with an inner diameter of 60 mm was used. The pressure of the sample was 4.0 or 5.0 atm. The details of the analysis of the data obtained by the energy-dispersive method are shown elsewhere [7].

The results for $N_2$, $O_2$ and Ne were published [8]. The results for $C_2H_2$ and $C_2H_4$ are presented here. For comparison a function $\Delta\sigma_{ee}$ defined by

$$\Delta\sigma_{ee} = I^{T}_{exp} - I^{T}_{HF\text{-}IAM}$$

was obtained. This is shown in Figs. 2 (a) and (b). The dots represent our experimental data and the three curves on Fig. 2 (a) for $C_2H_2$ are calculated results by Breitenstein et al. [9], corresponding to three levels of approximation, namely HF, CI (configuration interaction), and scaled CI. In the CI calculation, about 50 or 60 % of the potential energy portion of the full empirical correlation energy is represented [9]. In the case of $N_2$, $O_2$ and Ne, the experimental values are in agreement with the CI curves rather than the scaled CI or HF curves. For $C_2H_2$ a marked characteristic of the $\Delta\sigma_{ee}$ curve, namely, a large maximum at $s = 1.8$ Å$^{-1}$ was observed experimentally. The theoretical X-ray scattering intensity of $C_2H_4$ has not been calculated.

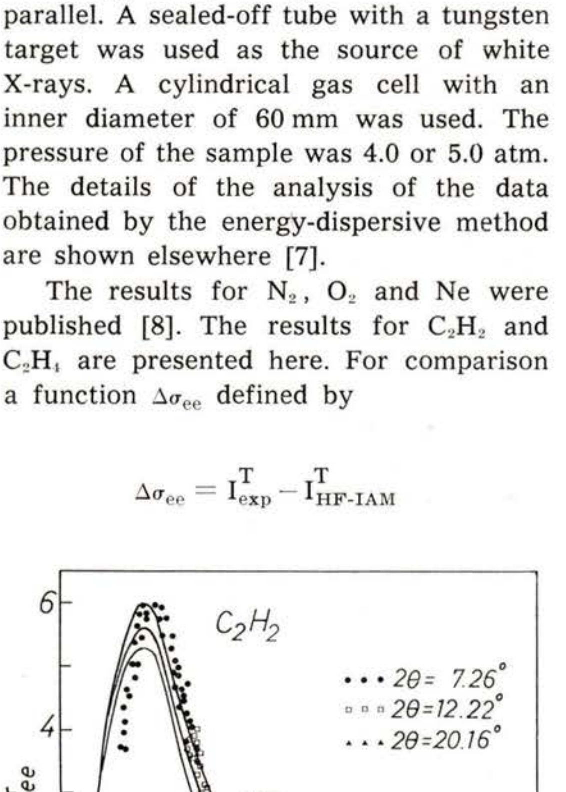

Fig. 2 (a) — Observed $\Delta\sigma_{ee}$ of $C_2H_2$ and the calculated ones by Breitenstein et al. [9] (solid curves).

In order to improve the accuracy of the data in the smaller s-region, an effort has been made to find the causes of possible systematic errors and to remove them, taking the following steps:

1) Improvement of the gas cell. The window at the incident side was changed from a 1 mm thick polyacetal sheet to a 0.2 mm thick Be plate and the beam stopper in the cell was rearranged. These changes decreased the background intensity to 1/10 of the previous values.

2) Correction for the incident beam. This correction depends on the tube current. A change in the tube current may change the energy-spectrum, because different values of the current may cause changes in the amplitude of the ripples of the imperfectly smoothed voltage applied to the X-ray tube. It was proved experimentally that the energy-spectrum of the primary beam changes by 1 % when the tube current changes from 5 mA to 30 mA.

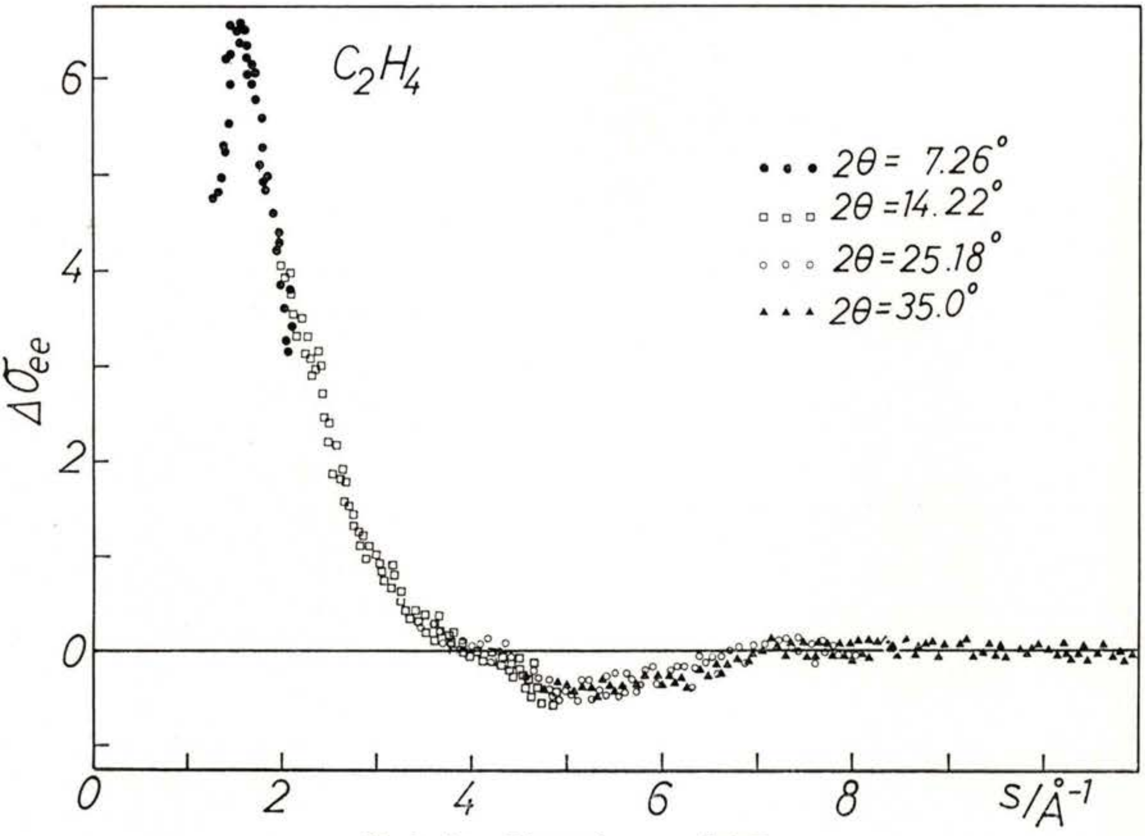

Fig. 2 (b) — Observed $\Delta\sigma_{ee}$ of $C_2H_4$.

3) Estimation of the error in the usual correction for the Compton scattering in the energy-dispersive method. The error due to the approximation in the usual correction was shown never to exceed 0.2 % of the total scattering intensity and the details are presented in this journal [10] and elsewhere [11].

4) Use of Bonham theory instead of Waller-Hartree theory for the treatment of the Compton scattering. For the inelastic scattering S(s), Bonham theory [12] for the constant scattering angle has been applied, instead of the Waller-Hartree theory, in which S(s) is calculated at constant momentum transfer s, and it has been found that the result obtained with the use of the former theory is more reasonable. It has been found that these systematic errors are not so serious for the data at relatively large s-values ($s > 3.5$ Å$^{-1}$) and that the data thus obtained is consistent with the previous measurements.

Furthermore, a slit-height correction for the scattering from the samples with finite volumes is being examined. The slit-height correction for the scattering intensities from the samples with a very large volume (the inner diameter of the gas cell is 60 mm) becomes serious also at the lower scattering angle. As a preliminary experiment, the scattering intensity at $2\Theta = 8^{\circ}$ obtained with apertures ($2\,\text{mm} \times 2\,\text{mm}$) has been compared with the one obtained when ($2\,\text{mm} \times 8\,\text{mm}$) slits were used. The smearing effect due to the slit-height is found to be 5 %. A more reliable experiment is now under way. By taking into account this effect, it is hoped that the experimental $\Delta\sigma_{ee}$ curve will be improved in the smaller s-region.

## REFERENCES

[1] BOHNAM, R. A. and FINK, M., High Energy Electron Scattering. (Van Nostrand Reinhold, New York, 1974).

[2] FINK, M. and BOHNAM, R. A., in Chemical Applications of Atomic and Molecular Electrostatic Properties, Edited by Politzer, P. and Truhler, D. G. (Plenum, New York, 1981).

[3] BARTELL, L. S. and GAVIN, Jr., R. M., J. Am. Chem. Soc., **86**, 3493 (1964); J. Chem. Phys., **43**, 856 (1965).

[4] GAVIN, Jr., R. M. and BARTELL, L. S., J. Chem. Phys., **44**, 3687 (1966); **45**, 4700 (1966).

[5] IIJIMA, T. and MITSUHASHI, T., in X-ray Instrumentation for the Photon Factory: Dynamic Analysis of Micro Structures in Matter, edited by Hosoya, S., Iitaka, Y., and Hashizume, H. (KTK Scientific, Tokyo, 1986).

[6] IIJIMA, T., NISHIKAWA, K. and MITSUHASHI, T., in Stereochemical Application of Gas-Phase Electron Diffraction, edited by Hargittai, I. and Hargittai, M. (VCH Deerfield Beach, 1988).

[7] NISHIKAWA, K. and IIJIMA, T., Bull. Chem. Soc. Jpn., **57**, 1750 (1984).

[8] NISHIKAWA, K. and IIJIMA, T., J. Chem. Phys., **87**, 3753 (1987).

[9] BREITENSTEIN, M., MEYER, H. and SCHWEIG, A., Z. Naturforsch. **A39**, 1208 (1984).

[10] IIJIMA, T. and NISHIKAWA, K., Portgal. Phys., 331 (1988).

[11] IIJIMA, T. and NISHIKAWA, K., J. Appl. Cryst., **21**, 943 (1988).

[12] BONHAM, R. A., Phys. Rev., **A23**, 2950 (1981). Erratum, Phys. Rev., **A35**, 3964 (1987).

# RECOIL SCATTERING OF HIGH ENERGY NEUTRONS IN LIQUID $^4$He

R. S. Holt, L. M. Needham and M. P. Paoli
Rutherford Appleton Laboratory, Neutron Science Division,
Chilton, Didcot, Oxon. OX11 OQX — U.K.

*ABSTRACT* — Neutron recoil scattering from liquid $^4$He at 4.2 K and 1.6 K has been observed for a momentum transfer of 150 Å$^{-1}$ using neutron resonance absorption. The experiment yielded mean kinetic energy values $< KE > = 14.8 \pm 3.0$ at 4.2 K and $14.6 \pm 3.2$ at 1.6 K. No distinct Bose condensate peak was observed below the $\lambda$ transition. Model calculations of the recoil spectra at 1.6 K indicated a standard deviation on a measurement of $n_0$ of ~12 %.

## INTRODUCTION

Liquid $^4$He exhibits a superfluid phase below 2.17 K ($\lambda$ point) and this phase is associated with a condensation of the He atoms into the zero momentum ground state [1]. Hohenberg and Platzman [2] suggested that the fraction of particles in the ground state, the Bose condensate fraction, $n_0$, could be measured using high momentum transfer inelastic neutron scattering. In this regime (of high energy and momentum transfer) the impulse approximation is approached and the measured recoil scattering spectra, $S(Q, \varepsilon)$, can then be directly related to the ground state momentum distribution, n(p), of the recoiling atoms.

The techniques of neutron resonance absorption were used on the pulsed neutron source ISIS [3] and the mean atomic kinetic energy values determined from the widths of the inelastic recoil peak, were:

$$\sigma^2 = (4/3)\ E_R < KE >$$

The variation in $< KE >$ between the normal fluid and the superfluid is however small and arises mainly from the Bose condensation rather than from a change in temperature since the zero point motion of the atoms dominates.

## RESULTS

Figure 1 shows the recoil scattering spectra below the $\lambda$ transition compared with the expected recoil line shape calculated using various condensate fractions assuming an average value for the kinetic energy of 14.6 K. The standard deviation on the measurement of $n_0$ is approximately 12 % which is in reasonable agreement with the values quoted in the literature which vary between 9 % and 12 % (see Sears [4]). A recent calculation by Olinto [4], based on an analysis of liquid $^4$He chemical potential data, has given a value of $n_0(T = 0)$ as low as 6.2 %. This is approximately 50 % lower than the values found in the present set of experiments. This indicates that data with greater statistical accuracy and higher resolution are required before the Bose condensate fraction can be accurately determined by such inelastic neutron scattering techniques.

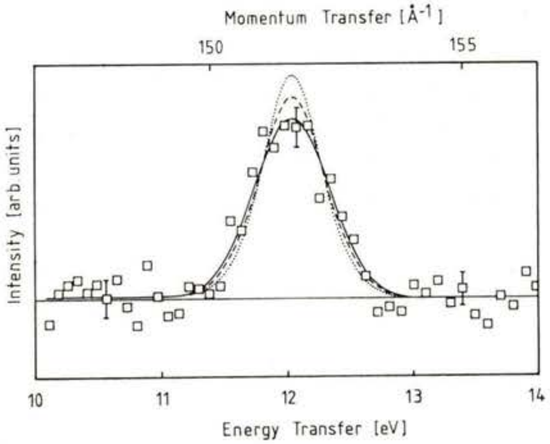

Fig. 1 — The recoil scattering spectra from $^4$He at 1.6 K compared with the expected recoil line shapes calculated using condensate fractions, $n_0$, of 0 % (———), 20 % (— — —) and 40 % (.........).

## REFERENCES

[1] LONDON, F., «Superfluids», Vol. 2, Wiley, New York (1954).

[2] HOHENBERG, P. C. and PLATZMAN, P. M., Phys. Rev. **152**, 198 (1966).

[3] HOLT, R. S., NEEDHAM, L. M. and PAOLI, M. P., Phys. Letts. **A126**, 373 (1988).

[4] SEARS, V. F., Phys. Rev. **B28**, 5109 (1983).

[5] OLINTO, A. C., Phys. Rev. **B35**, 4771 (1987).

# ATOMIC MOMENTUM DISTRIBUTION AND MEAN KINETIC ENERGY IN PYROLYTIC GRAPHITE

M. P. Paoli and R. S. Holt
Rutherford Appleton Laboratory, Neutron Science Division,
Chilton, Didcot, Oxon. OX11 OQX — U.K.

*ABSTRACT* — Mean atomic kinetic energies, < KE >, have been determined in pyrolytic and polcrystalline graphite by deep inelastic scattering of epithermal neutrons (recoil scattering). The < KE > values extracted from the recoil spectra have been compared with phonon density-of-states model calculations. Significant differences were observed for < KE > values within the hexagonal layer indicating that the phonon density-of-states extends to higher energies than those predicted.

## INTRODUCTION

Crystalline graphite has a hexagonal layer structure which exhibits strong anisotropic bonding effects. These can be readily observed by measuring the mean atomic kinetic energy within the layers and perpendicular to the layers using deep inelastic neutron scattering. The technique of resonance neutron absorption has been applied using the pulsed neutron source, ISIS [1] and the < KE > extracted from the FWHM of the recoil scattering function $S(Q, \epsilon)$. This is directly related to the atomic momentum distribution, n(p), at these high energy and momentum transfers through the impulse approximation [2].

## RESULTS

Figure 1 shows the differences in line shape for pyrolytic graphite with the momentum transfer, Q, parallel and per-

The kinetic energy values derived from Gaussian fits to the recoil scattering distributions for polycrystalline and pyrolytic graphite samples. The data shown are FWHM values. The results obtained at the WNR and KENS pulsed neutron sources using a similar technique are also shown together with the calculated values obtained from a density-of-states-calculation.

| | Experiment | <KE> K |
|---|---|---|
| $\langle KE\rangle_{\perp}$ | ISIS PG (1.6 mm thickness) | 837±30 |
| | ISIS PG (3.2 mm thickness) | 817±30 |
| | Others: KENS [3] | 825±45 |
| | WNR [4] | 750±150 |
| | Young and Koppel [5] | 825 |
| $\langle KE\rangle_{\parallel}$ | ISIS PG (1.6 mm thickness) | 1500±70 |
| | ISIS Polycrystalline Graphite | 1425±90 |
| | Others: KENS [3] | 1575±120 |
| | WNR [4] | 1650±150 |
| | Young and Koppel [5] | 1180 |

*Portgal. Phys.* — Vol. 19, fasc. 3-4, pp. 365-366, 1988

pendicular to the hexagonal planes. The < KE > values observed are summarised in the table and include data obtained on polycrystalline graphite as well as complementary data obtained on other pulsed neutron sources using similar techniques [3, 4]. The theoretical model was evaluated numerically using the density-of-states calculated by Young and Koppel [5]. The observed values with Q perpendicular to the hexagonal layers are in agreement with this model but at variance with those observed with Q parallel to the layers. The large value for the observed kinetic energy indicates that the phonon density-of-states in the hexagonal plane extends to higher energies than predicted by this and other more recent calculations [6, 7].

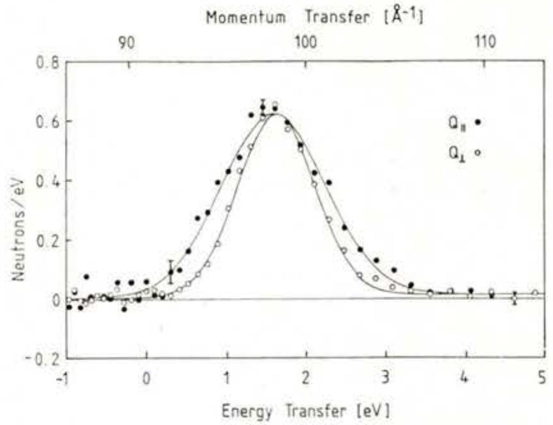

Fig. 1 — The recoil scattering spectra from pyrolytic graphite using the 4.28 eV resonance line in Ta. The momentum transfer is aligned perpendicular (o o o) and approximately parallel (● ● ●) to the hexagonal layers.

The recoil line shape is also asymmetric and the residual differences between a Gaussian recoil distribution and the observed data have been fitted to a complex first-order correction term arising from final state effects to the impulse approximation [8]. The form and magnitude of this asymmetry are in agreement with those observed and lower the predicted recoil peak centre by 25 meV. The inclusion of such corrections to the impulse approximation, even at these high momentum transfers, will become important in any future analysis where emphasis will be placed on the shape of the momentum distribution as well as on its width.

## REFERENCES

[1] NEWPORT, R. J., PAOLI, M. P., PUGH, V. T., SINCLAIR, R. N., TAYLOR, A. D. and WILLIAMS, W. G., Rutherford Appleton Laboratory Report RAL-85-110 (1985).

[2] PAOLI, M. P. and HOLT, R. S., J. Phys. C. **21**, 3633 (1988).

[3] RAUH, H. and WATANABE, N., Phys Lett., **A100**, 244 (1984).

[4] TAYLOR, A. D., Proc. Workshop High Energy Excitations in Condensed Matter, Los Alamos Report LA-10227C, 512 (1984).

[5] YOUNG, J. A. and KOPPEL, J. U., J. Chem. Phys., **42**, 357 (1965).

[6] NICKLOW, R., WAKABAYASHI, N. and SMITH, H. G., Phys. Rev. **B5**, 4951 (1972).

[7] AL-JISHI, R. and DRESSELHAUS, G., Phys. Rev. **B26**, 4514 (1982).

[8] NELKIN, M. S. and PARKS, D. E., Phys. Rev. **119**, 1060 (1960).

# DETERMINATION OF ATOMIC MOMENTUM DISTRIBUTIONS BY NEUTRON 'COMPTON' SCATTERING

R. S. HOLT and M. P. PAOLI

Rutherford Appleton Laboratory, Neutron Science Division,
Chilton, Didcot, Oxon. OX11 OQX — U.K.

*ABSTRACT* — The techniques of neutron resonance absorption have been developed to utilise the intense epithermal flux from the pulsed neutron source, ISIS. Inelastic scattering experiments have been performed in the region of high energy and high momentum transfers i. e. within the impulse approximation. A spectrometer based on a multidetector array of BGO photon detectors has been used for measuring the atomic momentum distributions in light atoms.

## INTRODUCTION

An inverse geometry spectrometer based on the $(n, \gamma)$ capture-emission process has been developed on the electron Volt Spectrometer (eVS) at the pulsed neutron source ISIS [1]. The multidetector system comprises seven bismuth germanate (BGO) photon detectors surrounding an annular foil of Ta which is used to define the scattered (final) neutron energy. The spectrometer allows both single and double coincidence counting events to be recorded simultaneously. The sample position is 1m away from the analyser foil and in back scattering geometry (where $\theta = 175^\circ$) momentum transfers, Q, in excess of 100 $\text{Å}^{-1}$ can be readily obtained at the recoil scattering centre ($E_R$). The combination of high energy and momentum transfer in such a scattering process satisfies the requirements of the impulse approximation which connects the momentum density of the atom, n(p), directly to the measured scattering function $S(Q, \varepsilon)$. A function J(y) is obtained from $S(Q, \varepsilon)$ after y-scaling [2] and this is analogous to the Compton profile in photon scattering.

With ISIS running at an average beam current of 90 $\mu$A recoil peak counting rates of 750 counts $hr^{-1}$ have been obtained for a 2 mm thick graphite sample (5 % scatterer). The eV spectrometer is calibrated using Ta and U foils at the sample and detector positions.

Figure 1 shows the results for recoil scattering from polycrystalline beryllium. Recoil peaks from the Be and from the aluminium holder are clearly visible and well separated [3]. The position of the recoil peak varies as $Q^2/2M$, where M is the atomic mass, whilst the width of the recoil line (FWHM) varies inversely with M. The recoil width provides a determination of the mean atomic kinetic energy, $< KE >$ and this can be compared to calculations of $< \mathrm{KE} >$ using various models of the phonon density-of-states. This approach has been used recently to determine the $< \mathrm{KE} >$ for pyrolytic graphite [4] and liquid $^4$He [5]. As the technique improves it should be possible to obtain information about the atomic potential through an analysis of the actual recoil line shape rather than just its width [6].

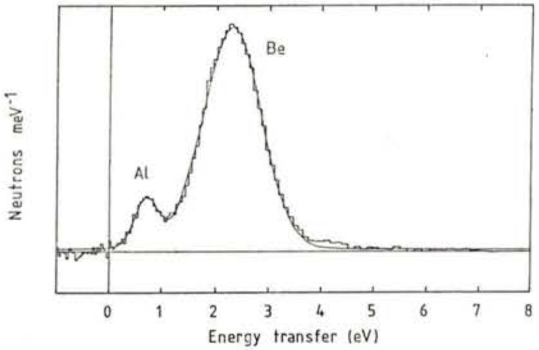

Fig. 1 — A typical recoil scattering spectrum from polycrystaline Be using the multidetector electron Volt Spectrometer on ISIS. Also shown is the recoil scattering from the aluminium holder and a two-term Gaussian fit. The inverse geometry spectrometer uses the white neutron beam and a Ta foil energy analyser with a final resonance energy of 4.28 eV.

## REFERENCES

[1] Holt, R. S. and Paoli, M. P., Nucl. Inst. Meths. (to be published)

[2] Sears, V. F., Phys. Rev. **B30**, 44 (1984).

[3] Paoli, M. P. and Holt, R. S., J. Phys. C. (to be published).

[4] Paoli, M. P. and Holt, R. S., J. Phys. C. **21**, 3633-3639 (1988).

[5] Holt, R. S., Needham, L. M. and Paoli, M. P., Phys. Letts. **A126**, 373-376 (1988).

[6] Reiter, G. and Silver, R., Phys. Rev. Letts. **54**, 1047-1050 (1985).

# ELECTRIC FIELD GRADIENTS MEASURED ON THE SYSTEMS Nb-H AND Ta-H BY PERTURBED ANGULAR CORRELATIONS

J. M. GIL, P. J. MENDES, L. P. FERREIRA, A. P. DE LIMA and N. AYRES DE CAMPOS
Physics Department, University of Coimbra, 3000 Coimbra, Portugal

Hydrogen atoms form interstitial sublattices when introduced in bcc Nb and Ta lattices, where they occupy tetrahedral sites [1]. Its structure is dependent on the hydrogen concentration and sample temperature. The phase-diagrams of these systems are known to a great extent, and some of the structures were determined by X-rays, neutron and TEM diffraction methods [1].

The Perturbed Angular Correlation techniques were applied successfully to those systems using $^{181}$Hf radiactive atoms as substitutional probes in the metal lattice [2, 3]. The technique yields information concerning the close vicinity of the probes, in the form of the electric field gradient (efg) measured at the probe nuclei. The efg is defined by two parameters in PAC measurements: the interaction strength $\nu_Q$ (MHz) $\propto V_{zz}$ and the asymmetry parameter $\eta = (V_{xx} - V_{yy})/V_{zz}$.

Although the identification of some known phases could be done by unique efg

TABLE 1

| Structure (phase) | | Nb-H | | | | | Ta-H |
|---|---|---|---|---|---|---|---|
| | | $\beta$ | $\gamma$ | $\varepsilon$ | | | $\beta$ |
| | | | | 4nnn | 3nnn | 2nnn | |
| Exp. efg | $\nu_Q$ (MHz) | 350 | 240 | 480 | 550 | — | 430 |
| | $\eta$ | 0.49 | 0.05 | 0.65 | 0.64 | — | 0.45 |
| (a) | $\nu_Q$ (MHz) | 2593 | 922 | 2461 | 2584 | 1441 | 1290 |
| | $\eta$ | 0.64 | 0.00 | 0.75 | 0.57 | 0.46 | 0.64 |
| | $q_H$ | 0.14 | 0.26 | 0.2 | | — | 0.33 |
| (b) | $r_q$ | 0.85 | 0.85 | 0.8 | 0.8 | 0.8 | 0.85 |
| | $q_H$ | 0.35 | 0.47 | 0.5 | 0.47 | — | 0.86 |

*Portgal. Phys.* — Vol. 19, fasc. 3-4, pp. 369-370, 1988

sets, the interpretation of the efg themselves is not straightforward. Point charge models have been developed in the past to explain the efg values obtained in many different PAC experiments [4].

As the Nb and Ta metal ions do not contribute to the efg at substitutional sites due to the cubic symmetry, the usually applied point charge model takes into account only the proton charge at the occupied tetrahedral sites. If a screening effect is considered, charges lower than unity are used. Table 1.a) presents the efgs calculated for various H structures compared to the values obtained experimentally. The positive charges $q_H$ necessary to reproduce the experimental $\nu_Q$ values are also shown.

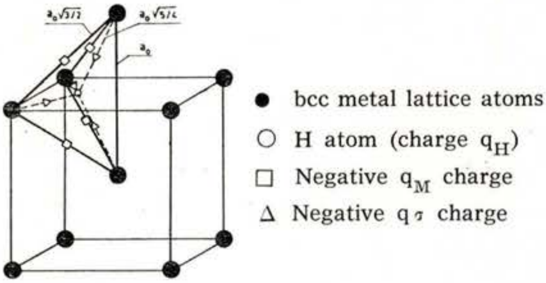

Fig. 1 — Position of point charges considered in the improved model for H in tetrahedral sites.

In the present work, the point charge model was improved by adding negative charges simulating the first moment of the electronic charge density around the probe atoms. The choice of the point charges and their localization was based on theoretical calculations of the changes induced on the electronic charge density by the introduction of a hydrogen atom in the metal lattice [5]. Fig. 1 shows the localization of the two kinds of negative charges $q_M$ and $q$ considered inside each tetrahedron. Assuming charge neutrality there are two free parameters to adjust: the positive charge $q_H$ and the ratio between the two negative charges $r_q = q_M/(q_M + q_\sigma)$.

The charge values that reproduce the experimental efgs are presented in table 1.b). The consistency of the charge values used for the different H structures shows that the point charge model was substantially improved by the addition of negative charges.

## REFERENCES

[1] SCHOBER, T., WENZL, H., «Hydrogen in Metals II», Top. in Appl. Phys., vol. 29, G. Alefeld, J. Voelkl (eds.), Springer, Berlin, 1978, p. 11.

[2] MENDES, P. J., GIL, J. M., AYRES DE CAMPOS, N., PEICHL, R., WEIDINGER, A., Hyp. Int., **15/16**, 791 (1983).

[3] GIL, J. M., MENDES, P. J., DE LIMA, A. P., AYRES DE CAMPOS, N., SHENG YUQIN, PEICHL, R., WEIDINGER, A., J. of the Less-Common Met., **129**, 145 (1987).

[4] BODENSTEDT, E., Hyp. Int., **24/26**, 521 (1985).

[5] FRITSCHE, H. G., DUEBLER, F., MUELLER, H., Z. Anorg. Allg. Chem., **513**, 46 (1984).

# HYPERFINE INTERACTIONS AND ELECTRONIC STRUCTURE OF THE $FeNH_3$ MOLECULE

JOICE TERRA and DIANA GUENZBURGER
Centro Brasileiro de Pesquisas Físicas
Rio de Janeiro — Brasil

## I — INTRODUCTION

Fe atoms, when trapped in frozen $NH_3$ matrices, react to form the molecules $FeNH_3$ [1]. This species provides a model for the study of the interactions of $NH_3$ with Fe surfaces [2]. The Mössbauer spectrum shows two narrow peaks of equal intensity, which suggests a quadrupole interaction and a well-defined Fe site. The Isomer Shift measured is different from that of Fe atoms in rare gas matrices. Mössbauer experiments in the presence of an external magnetic field reveal a large positive magnetic hyperfine field [3].

We have employed all-electron spin-polarized Discrete Variational Method (DVM) in the local density approximation, as has been described in detail elsewhere [4], to obtain values for the hyperfine parameters of $FeNH_3$ (Fig. 1), as described below.

The hyperfine parameters are:

*a*) The Isomer Shift $\delta$, which depends on the electronic density at the nuclear site:

$$\delta = 4/5\, \pi \, Ze^2 R^2 \, (\Delta R/R)\, S'(z) \times \Delta \rho\, (o), \quad (1)$$

where $\Delta R/R$ is the relative change in the nuclear radius in the Mössbauer transition, $S'(z)$ is a correction for relativistic effects and $\Delta \rho\,(o)$ is the difference in the electronic density at the nuclear site in two different chemical environments.

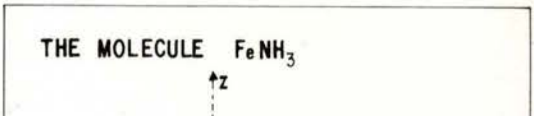

Fig. 1 — Interatomic distances: Fe — N = 2.05 Å, Fe — H = 2.59 Å, N — H = 1.00 Å and H — H = 1.61 Å.

*Portgal. Phys.* — Vol. 19, fasc. 3-4, pp. 371-372, 1988

*b*) The Quadrupole Splitting $\Delta EQ$, which depends on the electric field gradient produced by charge anisotropy around the probe nucleus. For the Mössbauer transition of $^{57}Fe$:

$$\Delta EQ = (1/2)\ e^2 q\ Q, \qquad (2)$$

where q is th eelectric field gradient and Q the quadrupole moment of the nucleus in the excited state of the nuclear transition. In Molecular Orbital (M.O.) theory [5], the electronic contribution to q is:

$$q = -\sum_i n_i < \phi_i \mid (3\cos^2 \Theta - 1)/r^3 \mid \phi_i > \qquad (3)$$

where $n_i$ is the occupation of M.O. $\phi_i$.

c) The Magnetic Hyperfine Interaction, which depends mainly on the contact hyperfine field $H_c$, a function of the spin density at the nuclear site

$$H_c = (2/3)\ g\ \mu_B S \times \chi \qquad (4)$$

where, in Molecular Orbital theory:

$$\chi = 4\pi \sum_i n_{i\uparrow} \mid \psi_{i\uparrow}(o) \mid^2 - \sum_j n_{j\downarrow} \mid \psi_{j\downarrow}(o) \mid^2 \qquad (5)$$

## II — RESULTS AND CONCLUSIONS

The configuration for Fe which gives the best agreement with the experimental sign and magnitude of all three hyperfine parameters, is:

$$\text{Fe: } 3d^{6.90}\ 4s^{1.06}\ 4p^{0.12} \quad \text{or}$$
$$\text{Fe: } 3d_{\uparrow}^{4.90}\ 3d_{\downarrow}^{2.00}\ 4s_{\uparrow}^{0.76}\ 4s_{\downarrow}^{0.30}\ 4p_{\uparrow}^{0.10}\ 4p_{\downarrow}^{0.02}$$

This configuration is similar to that found for Fe in the $Fe_2$ dimer [6].

A small negative charge (− 0.08) is found for Fe, consistent with the lone-pair donation from the N atom.

TABLE 1 — Experimental data and calculated values.

| | Calculated | Experimental<br>(E. M. B. Saitovitch, J. Terra and H. Litterst, unpublished) |
|---|---|---|
| $\delta$ (mm/s) | + 0.558 | + 0.67 |
| $\Delta EQ$ (mm/s) | − 3.36 | − 2.0 |
| $H_c$ (kOe) | + 980 | + 800 |

In Table 1 the experimental data and the calculated values for the three hyperfine parameters are shown. The large positive contact hyperfine field $H_c$ is due mainly to the large 4s (↑) population, relative to 4s (↓).

## REFERENCES

[1] E. B. SAITOVITCH, J. F. LITTERST and H. MICKLITZ, Chem. Phys. Lett. **83**, 622 (1981); P. H. BARRET and M. PASTERNAK, **71**, 3837 (1979).

[2] J. R. ANDERSON, Chemisorption and Reaction of Metallic Films (Academic, New York, 1971), p. 75.

[3] E. B. SAITOVITCH, J. TERRA and H. LITTERST, unpublished.

[4] D. E. ELLIS, Int. Quantum Chem. **S2**, 35 (1968); D. E. ELLIS and G. S. PAINTER, Phys. Rev. **B2**, 2887 (1970); A. ROSÉN, D. E. ELLIS, H. ADACHI and F. W. AVERILL, J. Chem. Phys. **85**, 3629 (1979).

[5] D. GUENZBURGER and E. B. SAITOVITCH, J. Chem. Phys, **80**, 735 (1984).

[6] D. GUENZBURGER and E. B. SAITOVITCH, Phys. Rev. **B24**, 2368 (1981).

# ELECTRONIC STRUCTURE AND ISOMER SHIFTS OF Sn HALIDES

JOICE TERRA and DIANA GUENZBURGER
Centro Brasileiro de Pesquisas Físicas
Rio de Janeiro — Brasil

## I — INTRODUCTION

The Isomer Shift $\delta$, as measured by Mössbauer spectroscopy, depends both on a nuclear factor and an electronic factor [1]:

$$\delta = 4/5\,\pi Z e^2 R^2\,(\Delta R/R)\;S'(z) \times \Delta\rho(o), \tag{1}$$

where $\Delta R/R$ is the change in the nuclear charge radius for an uniform charge distribution of $R = 1.2 \times A^{1/3}$ fm in the Mössbauer nuclear transition, $S'(z)$ is a correction for relativistic effects [2] and $\Delta\rho(o)$ is the difference between the electronic density at the nucleus in the probe atom in two different environments. In Molecular Orbital (MO) theory:

$$\Delta\rho(o) = \sum_i n_i\,|\,\psi_i(o)\,|^2_A - \sum_j n_j\,|\,\psi_j(o)\,|^2_S \tag{2}$$

where *A* and *S* refer to absorber and source and the summations are over the molecular orbitals $\psi_i$ occupied by $n_i$ electrons.

The electronic factor $\Delta\rho(o)$ can give important information about the electronic structure and chemical bonding. However, the qualitative and quantitative interpretation of this information requires a reliable value for the nuclear factor $(\Delta R/R)$. For $^{119}$Sn, a number of determinations of $\Delta R/R$ have been made, but unfortunately there has been no general agreement on its value [3]. In this work a new value of $\Delta R/R$ is presented for $^{119}$Sn. We have employed the Discrete Variational Method (DVM) LCAO Molecular Orbital method in the local density approximation, as has been described in detail elsewhere [4], to perform electronic structure calculations of clusters representing four compounds of Sn, namely $SnX_4$ ($X = F$, *Cl*, Br and I). In the M. O. calculations all electrons are taken into account, a Mulliken-type analysis is performed and an embedding scheme is used to simulate the crystal outside the cluster. We have derived $\Delta R/R$ in Eq. 1, by combining experimental measurements of $\delta$ in the four crystals studied, with the corresponding calculated values of $\rho(o)$, as in Eq. 2.

## II — RESULTS AND CONCLUSIONS

The very good correlation between $\rho(o)$ and $\delta$ (Fig. 1) obtained for the four clusters demonstrates that the method is adequate

*Portgal. Phys.* — Vol. 19, fasc. 3-4, pp. 373-374, 1988

for calculations of electronic densities at the origin.

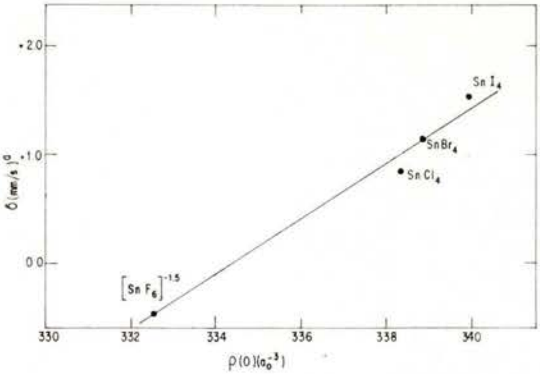

Fig. 1 — Isomer Shift x $\rho$ (o) for Sn halides.
*a*) Experimental values from Reference [1]. Related to $SnO_2$.

The increase in $\rho$ (o) along the series F, C*l*, Br and I is due mainly to an increase in the 5s population of Sn, since only s functions penetrate the nucleus, in a non-relativistic approach.

The increase in the 5s population of Sn along the series follows the decrease in the positive charge on Sn, as expected from consideration of the decrease in electronegativity of the halogens.

The value of $\Delta R/R$ derived for $^{119}Sn$ is:

$$\Delta R/R = +2.20 \times 10^{-4}$$
$$\text{with } R = 1.2 \times A^{1/3} \text{ fm.}$$

## REFERENCES

[1] N. N. GREENWOOD and T. C. GIBB, Mössbauer Spectroscopy (Chapman and Hall, London, 1971), p. 46, p. 390.

[2] D. A. SHIRLEY, Rev. Mod. Phys. **36**, 339 (1964).

[3] H. MURAMATSU, T. MIURA, H. NOKAHARA, M. FUGIOKA and E. TANAKA, Hyp. Int. **20**, 305 (1984).

[4] D. E. ELLIS, Int. J. Quantum Chem. **S2**, 35 (1968); D. E. ELLIS and G. S. PAINTER, Phys. Rev. **B2**, 2887 (1970); A. ROSÉN, D. E. ELLIS, H. ADACHI and F. W. AVERILL, J. Chem. Phys. **85**, 3629 (1976).

# LOCALIZATION OF ATOMIC IMPURITIES IN MINERALS BY PRECISION X-RAY DIFFRACTION DATA

V. S. URUSOV, E. L. BELOKONEVA
Moscow State University, Geological Faculty, Moscow

Fast improvement of X-ray diffraction experimental techniques and treatment of the data have permitted to make a precision study of the crystal structure details and peculiarities of electron density distribution, i. e. chemical bond features. A previous paper, demonstrating the principal possibility of localization of a small amount of impurity in a structure by careful analysis of $\delta\rho$-maps, dealt with ruby structure investigation [1]. The structure position of a small amount of $C^{3+}$ (0,5 wt %) was detected. Using such an approach we studied three spinels: 1) noble $MgAl_2O_4$ (0,8 wt % Fe) [2]; 2) hercynite [3]; 3) synthetic Co-spinel (*) and five beryls; 4) practically pure beryl [4]; 5) aquamarine (2,4 wt % Fe); 6) smaragd (0,3 wt % Cr, O, 3Fe, 2, OMg), synthetic; 7) Co- (1,1 wt %) and 8) Cu- (1,8 wt %)-bearing beryls. The experimental data were obtained with a «Syntex» P1 diffractometer; the structures were refined using an «Eclipse-S/200» computer with INEXTL-programs. The reliability factors R, $R_w$ and goodness-of-fit S for high-angle region of reciprocal space are given in Table 1. The structural positions of small amounts of impurities are important for physical properties interpretation, especially magnetic and spectral ones. The $\delta\rho$-maps allowed to detect chemical bond peculiarities in spinels as well as in ring-silicate beryl.

TABLE 1

| | Sample | | | | | | | |
|---|---|---|---|---|---|---|---|---|
| | 1) | 2) | 3) | 4) | 5) | 6) | 7) | 8) |
| R, % | 0.77 | 0.88 | 1.07 | 0.73 | 1.17 | 1.31 | 1.08 | 1.44 |
| $R_w$, % | 0.96 | 1.35 | 1.52 | 0.79 | 1.40 | 1.49 | 1.02 | 2.33 |
| S | 1.008 | 1.358 | 0.881 | 1.020 | 0.933 | 1.010 | 1.076 | 1.596 |

---

(*) The experimental data were kindly sent by prof. Y. Saito.

*Portgal. Phys.* — Vol. 19, fasc. 3-4, pp. 375-376, 1988

## REFERENCES

[1] TZIRELSON, V. G., ANTIPIN, M. Y., GERR, R. G., OZEROV, R. P., STRUCHKOV, Y. T. — Phys. Stat. Sol. **(a)87**, 425 (1985).

[2] TZIRELSON, V. G., BELOKONEVA, E. L., NOZIK, Y. Z., URUSOV, V. S. — Geochimija, **N7**, 1033 (1986).

[3] STRELTZOV, V. A., BELOKONEVA, E. L., TZIRELSON, V. G., URUSOV, V. S., OZEROV, R. P. — Geochimija, **N10**, 1456 (1987).

[4] EVDOKIMOVA, O. A., BELOKONEVA, E. L., TZIRELSON, V. G., URUSOV, V. S. — Geochimija, **N5** (1988).

# SUPERCONDUCTIVITY AND ZERO-POINT MOTION

R. J. WEISS
Department of Physics, King's College London
Strand, London WC2R 2LS

At temperatures nominally associated with superconductivity the quantum mechanical zero-point motion in solids accounts for the bulk of the deviation of atoms from a perfect mathematical lattice. The electron clouds follow this motion except possibly the overlapping electrons, i. e. those associated with bonding and electrical conduction.

Very little is known about zero-point motion even though there are experimental techniques for measuring it. A quantum mechanical treatment including both nuclei and electrons is beyond our capability when one wishes to include anharmonicity and both electron and nuclear correlation. The electron charge determines the zero-point motion and the zero-point motion determines to a great extent the outer electron charge. Separation is not simple. (We may find, in fact, that many more solids would be superconducting if the zero-point motion were absent.)

Superconductivity is a long range cooperative and correlated steady state of the entire system which phonons and magnetic fields only tend to destroy.

The salient experimental details piece this picture together.

1. While the Hund's rule prefers unpaired electrons for open shell on free atoms, bonding of atoms energetically favours spin-pairing for the overlapping electrons. In the 4f elements, Hund's rule is still dominant because the 4f electrons do not overlap. Some vestige of Hund's rule remains in Cr, Mn, Fe, Co and Ni where the 3d electrons divide into two groups — an overlapping group and a tightly bound group, the latter being unpaired. The Cooper pairs are a manifestation of pairing in overlapping orbitals.

2. The lambda-type anomaly in the specific heat of a superconductor suggests a long-range interaction.

3. The Meissner effect suggests long-range interactions. The ability of the surface layer of electron orbits to sacrificially enter a «normal» state with sufficient diamagnetism to exclude the magnetic field from the interior implies long range interactions of at least the thickness of the Meissner layer.

4. The relative absence of superconductivity in elements with predominant

s-like character in the overlapping electrons suggests a difficulty in correlating their motion with the zero point motion. The preference for d-like character in the current carriers comes from the more atomic-like nature of the d wave functions enabling them to more readily correlate with the zero point motion.

5. The specific heat is independent of whether current is flowing in the superconducting state. This suggests that microcurrent circuits are already present, as indeed one encounters in, say, the benzene ring. The quantum mechanical ground state arises from a well-correlated long range electron and zero-point motion. The absence of the linear term in the specific heat reflects the presence of an energy gap and the removal of the electron clouds from such thermal excitations.

6. The marked reduction in thermal conductivity in the superconducting state reinforces the concept of a quantum mechanical ground state in which the valence electrons and the zero-point motion are collectively joined and correlated.

7. The «presence» and «absence» of an isotope effects is consistent with the zero point density of states. For acoustic modes we expect an effect but for optical modes in the more complicated structures the effect may be diminished.

8. The change in $T_c$ for lanthanum, mercury, and uranium in their two crystalline states may be due to the altered zero point density of states.

9. It is clear that superconductivity is absent where there are unpaired species in the lattice such as in the rare earths beyond lanthanum and the transition metals like Mn, Cr, Fe, Ni, Co. Such unpaired spins destroy the perfect pairing of valence electrons due to exchange effects.

To gain a deeper insight into the nature of the coupled valence electron-zero point motion a number of experiments are feasible.

A. The Debye-Waller factor can be compared in the normal and superconducting state by examining the X-ray intensities at high $\sin\theta/\lambda$ ($> 3/\text{Å}$). This can be done in an energy dispersive mode.

B. Compton scattering through $T_c$ might reveal changes in the valence electron wave functions.

C. X-ray scattering factors at low $\sin\theta/\lambda$ might reveal changes in the 3d character of the wave functions.

D. Neutron Compton scattering through $T_c$, using the spallation source, would reveal changes in the zero point nuclear momenta.

E. X-ray elastic scattering through $T_c$ looking for correlations in the zero-point atomic displacements, i. e. short range order in the superconducting state.

F. Changes in $T_c$ under pressure should drive the ratio of 3d to 4s character in the valence electron wave functions one way or another.

G. Search for $T_c$ in $\varepsilon$Fe (non magnetic hexagonal phase) by applying pressure.

H. Changes in optical properties, n and k, through $T_c$. The Raman effect will reflect some details of zero-point lattice motion.

J. Precise dilatometric measurements through $T_c$. Changes in electron wave functions or zero point interactions will probably be revealed in changes in lattice parameter.

While a commercially viable room temperature superconductor may appear before an extensive research effort is made in examining the zero-point motion, it is likely that such experimental details will make the problem seem curiouser and curiouser.

In the case of vanadium ($T_c = 5.03°K$) the ratio of zero-point motion to phonon thermal motion, i. e. the mean square displacement $< u^2 >$ is given in the Table 1 as a function of T.

TABLE 1 — The ratio of the mean-squared atomic displacement of the zero-point (o) and phonon (p) activated motion based on a Debye model for vanadium ($T_c = 5.03°K$)

| T°K | $< u^2 >_o / < u^2 >_p$ |
|---|---|
| 5° | 950 |
| 20° | 59 |
| 50° | 9.5 |
| 100° | 2.4 |

If phonons only account for such a small fraction of the atomic displacement at the superconducting critical temperature, why are they so effective in destroying the superconducting state? The answer may lie in the long range nature of the superconducting state, i. e. only small displacements are needed to destroy the order.

This may not be the case in high temperature superconductors where the order is more one dimensional, particularly if the electron wave functions are correlated with zero-point optical modes which require much higher temperatures for thermal excitation.

It may be that in a «one-dimensional» superconductor, depending on the correlation of electron and zero-point motion, the destruction of the long range order at the superconducting transition temperature may lead to an insulator since other paths for normal conduction are not activated.

In summary, we are suggesting that superconductivity is a manifestation of a quantum mechanical ground state wave function in which the valence electrons and zero-point motion are correlated, and that a variety of measurements are feasible to compare the zero-point motion in the normal and superconducting states.

# Part III—Workshop on Density Matrices (Satellite Meeting)

# BASIC THEORY OF ELECTRON DENSITIES IN CRYSTALS

GERRIT E. W. BAUER
Philips Research Laboratories,
P. O. Box 80.000, 5600 JA Eindhoven, The Netherlands

JOCHEN R. SCHNEIDER
Hahn-Meitner-Institut
Glienicker Str. 100, 1000 Berlin 39, FRG

*ABSTRACT* — The elementary theory of electron densities in crystals and its relationship with other observables is reviewed, with emphasis on the effects of electron correlation.

Photon-scattering experiments yield important information on the ground-state wave function via the one-particle density matrix. In particular, the electron densities in position and momentum space (often called charge and momentum densities) can be measured with high accuracy, such that many-body effects (or the inadequacy of available theories to deal with them) can be clearly resolved (see e. g. [32], [5]).

The theory of density matrices and electron densities of the inhomogeneous electron gas is well established. Standard textbooks and review articles on many-body physics usually do not dwell upon this subject in depth, however. The present tutorial paper is hoped to fill this gap by showing how such concepts as the one-electron Green function, standardly used in spectroscopic studies, carry over to the problem of electron densities in crystals. On the other hand, some connections between effects observed in the electron densities and those observed by some other experimental techniques should become clear. As far as is needed for the critical comparison of experiment and theory, an attempt is made to give a self-contained and complete treatment of the theoretical concepts and methods involved.

Charge and momentum densities are manifestations of the one-particle density matrix, as described in Ch. 1. We will point out the interrelationship between these quantities and stress their complementarity, which provides the main motivation to measure them both.

The electronic band structure (as obtained from photoemission experiments) and the ground-state charge densities seem to be rather unrelated quantities. However, they are both special projections of the one-particle Green function, an important concept in many fields of solid-state physics. In Ch. 2 it is outlined how, by introducing the one-particle Green function, a unified treatment of the electron densities and the results of various other experiments can be achieved.

The prototype model for a metal is the homogeneous electron gas. The interaction effects in this system are relatively well understood [17], [36], [7]. The discussion of its spectral properties in Ch. 3 should be helpful in understanding the experimental results found in realistic metals.

In Ch. 4 a short review of density-functional theory is given, upon which most numerical calculations of the electronic structure of solids are founded. The so-called local density approximation to the exchange-correlation energy functional of the charge density is usually invoked. It is shown that the adequacy of the approximations can be judged by comparing experimental and theoretical electron densities only if certain exchange-correlation corrections are taken into account.

## 1 — DEFINITIONS

The N-particle density operator is defined as [9], [38]:

$$\hat{\rho}^{\,N} = e^{-\beta \hat{H}} / \mathrm{Tr}_N \{ e^{-\beta \hat{H}} \} \qquad (1)$$

where $\beta = 1/k_B T$ is the reciprocal thermodynamic temperature, $\hat{H}$ is the N-particle Hamilton operator and $\mathrm{Tr}_N$ denotes the trace over a complete N-particle basis. At zero temperature and for a non-degenerate ground-state wave function $| \Psi_0 >$, Eq. (1) reduces to

$$\hat{\rho}^{\,N} = | \Psi_0 > < \Psi_0 | . \qquad (2)$$

The one-particle density operator is obtained as the trace of the N-particle density operator with respect to a (N − 1)-particle basis:

$$\hat{\rho}^{\,1} = \mathrm{Tr}_{N-1} \{ \hat{\rho}^{\,N} \} . \qquad (3)$$

The one-particle density matrix D(i, i′) consists of the matrix elements of $\hat{\rho}^{\,1}$ for a given basis of one-particle wave functions $\{ | i > \}$. The position-space density matrix is obtained, for example, as

$$D(\mathbf{r}, \mathbf{r}') = < \mathbf{r} | \hat{\rho}^{\,1} | \mathbf{r}' > , \qquad (4)$$

and the momentum-space density matrix is a double Fourier transform of Eq. (4):

$$D(\mathbf{p}, \mathbf{p}') = \int (2\pi)^{-3/2} \, d\mathbf{r} \, \times$$

$$\times \int (2\pi)^{-3/2} \, d\mathbf{r}' \; e^{-i\mathbf{p}\mathbf{r}} \, e^{i\mathbf{p}'\mathbf{r}'} \, D(\mathbf{r}, \mathbf{r}') \qquad (5)$$

where **p** is the electron momentum divided by $\hbar$. Alternatively the density matrix can be defined as the ground-state expectation value of a pair of creation and annihilation operators. If $\hat{\psi}^{+}(\mathbf{r}), \hat{\psi}(\mathbf{r})$ create or annihilate a particle at a point **r**:

$$D(\mathbf{r}, \mathbf{r}') = < \Psi_0 | \hat{\psi}^{+}(\mathbf{r}') \, \hat{\psi}(\mathbf{r}) | \Psi_0 > . \qquad (6)$$

The diagonal parts of D may be referred to as electron densities. Of special importance are the the experimentally observable electron densities in position and momentum space. $D(\mathbf{r}, \mathbf{r}) = \rho(\mathbf{r})$ is simply the probability density of finding an electron at the position **r**. The electron density in momentum space $D(\mathbf{p}, \mathbf{p}) = \rho(\mathbf{p})$ is the probability density for an electron to have a momentum **p**.

The one-particle density matrix is diagonalized by the so-called natural orbitals $\psi_s$ [25]:

$$D(s, s') = f_s \, \delta_{s,s'} . \qquad (7)$$

The electron density in this space is identical to the so-called occupation numbers $(0 \leq f_s \leq 1, \Sigma f_s = N)$ and specifies the density matrix completely. In position space we get:

$$D(\mathbf{r}, \mathbf{r}') = \sum_s < \mathbf{r} | s > f_s < s | \mathbf{r}' > =$$

$$= \sum_s f_s \, \psi_s(\mathbf{r}) \, \psi_s^{*}(\mathbf{r}') . \qquad (8)$$

In the Hartree-Fock approximation the occupation numbers are exactly 1 for occupied orbitals and 0 for unoccupied orbitals; in the homogeneous electron gas they are identical to the momentum-space electron density.

According to Hohenberg and Kohn [19], a one-to-one mapping exists between the position-space density (or momentum-space density [18]) and the Hamiltonian of the system. In principle the complete density matrix can be reconstructed from the position-space density alone via a well-defined algorithm [3]. But in general, position and momentum operator eigenfunctions do not diagonalize the density matrix and the information lost in the form of the non-diagonal elements cannot be retrieved in any simple way. The position-space density and the momentum-space density thus provide complementary information on the density matrix, although an exact reconstruction continues to be impracticable even when both densities are available.

We shall often refer not to the densities themselves but to their Fourier transforms, i. e. the so-called form factors, which are more directly related to the experimental data. The form factor of the position-space density is defined as

$$F(\mathbf{q}) = \int d\mathbf{r}\, e^{-i\mathbf{q}\cdot\mathbf{r}}\, \rho(\mathbf{r}) = \int d\mathbf{p}\, D(\mathbf{p}, \mathbf{p}-\mathbf{q}). \tag{9}$$

The second equality follows from the convolution theorem for Fourier transforms. The form factor of the position-space density is thus the autocorrelation function of the density matrix in momentum space. For a periodic system Eq. (9) is non-zero only when $\mathbf{q}$ is a reciprocal lattice vector. The moduli of the form factors are the observables in a Bragg diffraction experiment and are also referred to as structure factors if normalized to the number of electrons in the unit cell.

The Fourier transform of the momentum density, that is the so-called reciprocal form factor $B(\mathbf{r})$, reads analogously:

$$B(\mathbf{r}) = \int d\mathbf{p}\, e^{i\mathbf{p}\cdot\mathbf{r}}\, \rho(\mathbf{p}) = \int d\mathbf{t}\, D(\mathbf{t}, \mathbf{t}-\mathbf{r}), \tag{10}$$

and may be interpreted as the autocorrelation function of the position-space density matrix [44], [39]. The reciprocal form factor has been extensively used to interpret experimental data obtained in the form of the Compton profile:

$$J_{\mathbf{h}}(q) = \int d\mathbf{p}\, \rho(\mathbf{p})\, \delta(q - \mathbf{p}\cdot\mathbf{h}), \tag{11}$$

where $\mathbf{h}$ is a unit vector determined by the experimental scattering geometry. It holds that

$$B(r\mathbf{h}) = \int dq\, J_{\mathbf{h}}(q)\, e^{-irq}. \tag{12}$$

The reciprocal form factor is especially useful in discussing results for insulators where the wave functions are more or less localized. In this case the autocorrelation of the density matrix is short-ranged and reflects the bonding or overlap interactions between the fundamental building blocks of the crystals. These effects are easier to recognize in position than in momentum space, i. e. in B rather than in J.

At the end of this section we would like to mention two recent developments in connection with the density matrix concept. Schülke [40] and Schülke and Mourikis[41], have introduced a technique to measure the non-diagonal elements of the density matrix in momentum space. Since perfect crystals are necessary, these experiments have been carried out for silicon only. Mass et al. [29] have fitted an idempotent (i.e. $D^2 = D$) density matrix to accurate experimental position-space densities. This approach is interesting since there is no *a priori* reason for the density matrix thus obtained to be worse than that constructed from the solutions of the Kohn-Sham equations (see Ch. 4). A systematic improvement of the method to include correlation effects such as non-integer occupation numbers seems unattainable, however.

## 2 — INTERRELATIONSHIP BETWEEN ELECTRON DENSITIES AND BAND STRUCTURES

The discussion of this section is centered on the one-particle Green function (see e. g. Hedin and Lundqvist [17], or textbooks like Inkson [20]), which in position space reads:

$$G(\mathbf{r}, \mathbf{r}'; t) = = -i < \Psi_0 \mid T \{ \hat{\psi} (\mathbf{r}; t) \, \hat{\psi}^+ (\mathbf{r}'; 0) \} \mid \Psi_0 >. \tag{13}$$

$i = \sqrt{-1}$, $\hat{\psi}(\mathbf{r}; t) = e^{i\hat{H}t/\hbar} \, \hat{\psi}(\mathbf{r}) \, e^{-i\hat{H}t/\hbar}$ and T denotes the fermion time-ordering operator:

$$T \{ \hat{\psi} (\mathbf{r}; t) \, \hat{\psi}^+ (\mathbf{r}'; 0) \} = = \begin{cases} \hat{\psi} (\mathbf{r}; t) \, \hat{\psi}^+ (\mathbf{r}'; 0) & t > 0 \\ -\hat{\psi}^+ (\mathbf{r}'; 0) \, \hat{\psi} (\mathbf{r}; t) & t \leq 0 \end{cases} \tag{14}$$

It follows directly that the density matrix is obtained from the Green function in the limit where t approaches zero on the negative time axis

$$D(\mathbf{r}, \mathbf{r}') = (1/i) \lim_{t \to 0^-} G(\mathbf{r}, \mathbf{r}'; t). \tag{15}$$

The Green function can be represented with respect to arbitrary one-particle bases, analogously to the density matrix.

It is usually advantageous to work with frequency instead of time variables. If a Green function is defined in the energy domain as

$$G(\mathbf{r}, \mathbf{r}'; \omega) = \int dt \, e^{i \omega t / \hbar} \, G(\mathbf{r}, \mathbf{r}'; t), \tag{16}$$

it follows, using Eq. (14), that

$$D(\mathbf{r}, \mathbf{r}') = \lim_{t \to 0^-} \int_C (1/2\pi i) \, d\omega \, G(\mathbf{r}, \mathbf{r}'; \omega) \, e^{-i\omega t/\hbar} \tag{17}$$

where the integration contour C runs along the real axis and is closed in the upper half of the complex plane.

The Green function in the frequency domain can be expanded in terms of the complete sets of (N + 1)- and (N − 1)-particle wave functions $\{ \mid \Psi_n^{N+1} > \}$ and $\{ \mid \Psi_n^{N-1} > \}$, assuming for the moment that the excitation spectrum is discrete:

$$G(\mathbf{r}, \mathbf{r}'; \omega) = \sum_n \frac{\phi_n^{N+1} (\mathbf{r}) \, \phi_n^{N+1} (\mathbf{r})^*}{\omega - E_n^{N+1} + E_0^N + i\eta} + + \sum_n \frac{\phi_n^{N-1} (\mathbf{r}) \, \phi_n^{N-1} (\mathbf{r}')^*}{\omega - E_0^N + E_n^{N-1} - i\eta} \tag{18}$$

where $E_n^{N \pm 1}$ is the energy of the n-th excited state of the $N \pm 1$ particle system and $\eta$ is a positive infinitesimal constant.

$$\phi^{N+1} (\mathbf{r}) = < \Psi_n^{N+1} \mid \hat{\psi}^+ (\mathbf{r}) \mid \Psi_0^N > \tag{19}$$

$$\phi^{N-1} (\mathbf{r}) = < \Psi_n^{N-1} \mid \hat{\psi} (\mathbf{r}) \mid \Psi_0^N > \tag{20}$$

are called quasi-particle and quasi-hole amplitudes [21]. Note that these functions are not normalized to one but that

$$0 \leq f_s^{N \pm 1} = \int d\mathbf{r} \mid \phi_n^{N \pm 1} (\mathbf{r}) \mid^2 \leq 1. \tag{21}$$

Substituting Eq. (18) into Eq. (17) and collecting the residues of the poles inside the contour C:

$$D(\mathbf{r},\mathbf{r}') = \sum_{n} \phi_n^{N-1}(\mathbf{r})\, \phi_n^{N-1}(\mathbf{r}')^{*}. \qquad (22)$$

The physical information in the Green function is thus hidden in its singularities: the position of the poles on the energy axis give the excitation spectrum, while the residues determine the density matrix.

The Green function can be calculated in principle via the following matrix («Dyson») equation:

$$G(\omega) = (\omega - h - \Sigma(\omega) + i\eta\,\mathrm{sgn}(\omega-\mu))^{-1}, \qquad (23)$$

where h is the sum of the kinetic and potential energy, sgn(x) denotes the sign of x, and $\mu$ is the chemical potential or, in a metal, the Fermi energy. Since the self-energy $\Sigma$ can be expressed as a functional of G [31], Eq. (23) is a self-consistency problem. The location of the poles of the Green function may be found by diagonalization of the matrix in Eq. (23). It is helpful to consider the eigenvalue problem of the inverse of the Green function in position space, that is the so-called quasi-particle (hole) equations:

$$\{-(\hbar^2/2m)\nabla^2 + V_{\mathrm{ext}}(\mathbf{r})\}\,\phi_i(\mathbf{r};\omega) + \int \Sigma(\mathbf{r};\mathbf{r}';\omega)\,\phi_i(\mathbf{r}';\omega)\,d\mathbf{r}' = \varepsilon_i(\omega)\,\phi_s(\mathbf{r}';\omega) \qquad (24)$$

Note that Eqs. (24) are in appearance very similar to a one-particle Schrödinger equation, but contain an effective potential in the form of the self-energy which describes the many-body effects. The poles of the Green function are at those energies $\omega_s$ where the energy argument in the self-energy agrees with one of the eigenvalues of the quasi-particle equations:

$$\varepsilon_i(\omega_s) = \omega_s \qquad (25)$$

The residues of these poles are by definition, assuming $\phi_s = \phi_i(\omega_s)$ to be normalized:

$$\begin{aligned} &\mathrm{Res}\{G(\mathbf{r},\mathbf{r}';\omega_s)\} = \\ &= \lim_{\omega\to\omega_s} (\omega-\omega_s)\, G(\mathbf{r},\mathbf{r}';\omega) = \\ &= Z_s\,\phi_s(\mathbf{r})\,\phi_s(\mathbf{r}')^{*}. \end{aligned} \qquad (26)$$

In the last step a non-degenerate spectrum has been assumed and the renormalization factor $Z_s$ has been introduced:

$$Z_s = [1 - \int d\mathbf{r}\,d\mathbf{r}'\,\phi_s(\mathbf{r})\,\frac{\partial\Sigma(\mathbf{r},\mathbf{r}';\omega)}{\partial\omega}\,\phi_s(\mathbf{r}')^{*}]_s^{-1} \qquad (27)$$

where the energy derivative has to be evaluated at $\omega = \omega_s$. The density matrix thus becomes

$$\begin{aligned} D(\mathbf{r},\mathbf{r}') &= \sum_{s}^{\omega_s \le \mu} \mathrm{Res}\{G(\mathbf{r},\mathbf{r}';\omega_s)\} = \\ &= \sum_{s}^{\omega_s \le \mu} Z_s\,\phi_s(\mathbf{r})\,\phi_s(\mathbf{r}')^{*} \end{aligned} \qquad (28)$$

We see that the renormalization factors can be interpreted as occupation numbers which may be fractional because of the energy dependence of the self-energy. In the Hartree-Fock approximation the self-energy is energy-independent and the occupation numbers can assume integer values only. Eq. (28) is very similar to the natural orbital expansion in Eq. (7). Unlike the natural orbitals, the present functions are not orthogonal because the self-energy is energy-dependent.

A complication neglected up to now is the fact that in macroscopic systems the energy spectrum is continuous which modifies the analytic properties of the Green function. In this case it is advantageous to introduce the spectral density function A:

$$A(\mathbf{r}, \mathbf{r}'; \omega) = \sum_s \phi_s^{N+1}(\mathbf{r})\, \phi_s^{N+1}(\mathbf{r}')^*\, \delta(\omega - \omega_s^{N+1}) + + \sum_s \phi_s^{N-1}(\mathbf{r})\, \phi_s^{N-1}(\mathbf{r}')^*\, \delta(\omega - \omega_s^{N-1}). \quad (29)$$

While A is a sum of δ-functions in the case of a discrete spectrum, for extended wave functions the spacing between the excitation energies becomes infinitely small and A becomes a continuous function. The Green function can be expressed in terms of A:

$$G(\mathbf{r}, \mathbf{r}'; \omega) = \int_{-\infty}^{\infty} d\omega' \{A(\mathbf{r}, \mathbf{r}'; \omega) / /[(\omega - \omega') + i\eta \operatorname{sgn}(\omega' - \mu)]\}. \quad (30)$$

It can thus be seen that the simple poles which characterize the Green function for finite systems merge to branch cuts, i. e. finite singularities when the spectrum becomes continuous. The density matrix can be obtained as an energy integral over the spectral function:

$$D(\mathbf{r}, \mathbf{r}') = \int_{-\infty}^{\mu} d\omega\, A(\mathbf{r}, \mathbf{r}'; \omega) \quad (31)$$

Fortunately the conceptually convenient picture of orbitals and energies as derived for the discrete spectrum can be restored to some extent if the spectral function can be analytically continued into the complex plane. A spectral feature in the form of a Lorentzian with halfwidth Γ corresponds to a simple pole at a distance Γ from the real axis (and vice versa). This can be interpreted as an elementary excitation («quasi-particle/hole») with a finite lifetime which is inversely proportional to the width of the spectral peak. In the quasi-particle approximation it is assumed that the prominent features in the spectrum may be replaced by complex poles. The quasi-particle equations now consist of the following non-hermitian eigenvalue problems [34]:

$$\{-(\hbar^2/2m)\nabla^2 + V_{\text{ext}}(\mathbf{r})\}\, \phi_s^l(\mathbf{r}) + + \int \Sigma(\mathbf{r}; \mathbf{r}'; \omega)\, \phi_s^l(\mathbf{r}')\, d\mathbf{r}' = \omega_s\, \phi_s^l(\mathbf{r}) \quad (32a)$$

$$\{-(\hbar^2/2m)\nabla^2 + V_{\text{ext}}(\mathbf{r})\}\, \phi_s^r(\mathbf{r}) + + \int \Sigma(\mathbf{r}'; \mathbf{r}; \omega)\, \phi_s^r(\mathbf{r}')\, d\mathbf{r}' = \omega_s\, \phi_s^r(\mathbf{r}) \quad (32b)$$

and the density matrix is constructed as follows:

$$D(\mathbf{r}, \mathbf{r}') = \sum_s^{\operatorname{Re}(\omega_s) \leq \mu} Z_s\, \phi_s^l(\mathbf{r})\, \phi_s^r(\mathbf{r}') \quad (33)$$

$$Z_s = [1 - \int d\mathbf{r}\, d\mathbf{r}'\, \phi_s^l(\mathbf{r}) \frac{\partial \Sigma(\mathbf{r}, \mathbf{r}'; \omega)}{\partial \omega} \phi_s^r(\mathbf{r}')]^{-1}. \quad (34)$$

The eigenvalues of Eqs. (32) form a band structure when the external potential is periodic. Within the assumption of analytic continuity of the spectral function they form a rather rigorous justification for treating the many-body problem as a set of one-particle Schrödinger equations [34]. But we would like to stress here that the solution of the band structure problem only gives the excitation spectrum and, if the complex part of the poles are included, the broadening of the spectral peaks. If the densities are to be calculated, the renormalization factors play an essential role and it is not sufficient to consider the amplitudes $\phi_s$ only.

## 3 — HOMOGENEOUS ELECTRON GAS AND EXPERIMENTAL SITUATION

The homogeneous electron gas is a convenient model system for the simple metals, i. e. metals which do not contain d or f-type valence electrons. While this system is of course of no use for discussing charge densities, it is a fairly adequate model for the momentum densities of simple metals.

The momentum density for the interacting homogeneous electron gas has been calculated for the first time by Daniel and Vosko (1960) [8], but we would like to focus attention on the work of Lundqvist (1967, [27], 1968, [28]), which is especially illuminating because the spectral function is given explicitly and reproduced here in Fig. 1. $A(k, \omega)$ is the Fourier transform of Eq. (29) for the homogeneous electron gas and can be interpreted as the generalization of the free-electron parabola to an interacting system. We observe two strong features in Fig. 1 which run approximately parallel. The upper curve corresponds to the quasi-hole/quasi-particle excitations, which display a significant broadening. In the absence of the electron-electron interaction this feature reduces to a $\delta$-function with a free electron dispersion in the $k, \omega$-plane. The lower parabola is a pure many-body phenomenon, i. e. it vanishes when the interaction is switched off. It has been interpreted as an elementary excitation which arises due to the coupling between a hole and the plasmons of the system and has been dubbed «plasmaron». Experimentally, analogies of the plasmaron could be identified as satellite bands in core-hole spectra (see e. g. Almbladh and Hedin, [1], but it seems to be elusive in valence-band spectra. The sharpness of the plasmaron feature in Fig. 1 might be an artifact of the random-phase approximation employed by Lundqvist, because the finite lifetime of the plasmon is neglected. While in a better approximation the plasmaron might thus be less well defined, there is little doubt concerning the existence of low energy excitations with significant oscillator strength (renormalization constants).

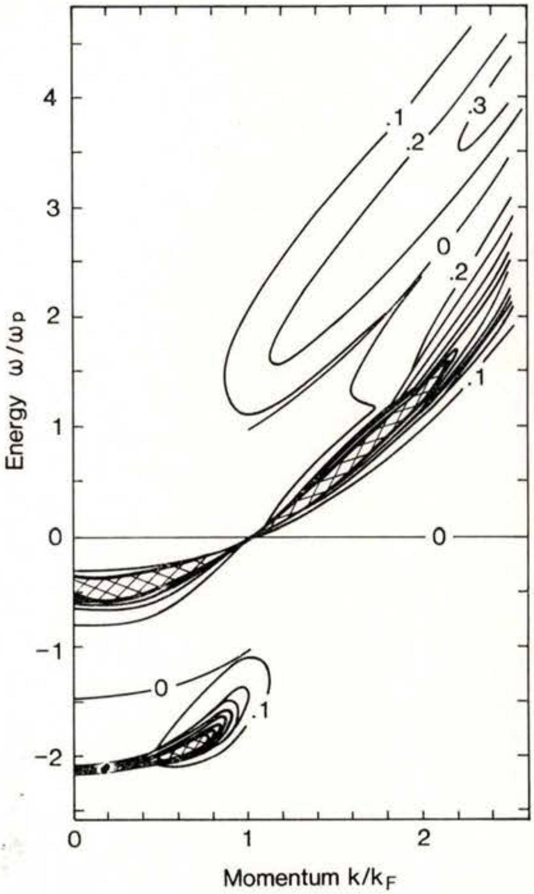

Fig. 1 — The spectral weight function of the homogeneous electron gas, given by level curves which indicate the value of $\hbar\omega_p A(k, \omega)$ for an electron density $r_s = 4$ ($\omega_p = 0.435$ Ry from [27]).

The corresponding energy density of states and momentum densities are displayed in Figs. 2 and 3. The contributions from both types of excitation described above are also roughly sketched. The quasi-hole contributes only up to the Fermi wave vector. The discontinuity of the momentum density at this wave vector is thus identical to the renormalization constant $Z_{k_f}$. It is clear that the quasi-particle alone describes the momentum density poorly, even when the renormalization is taken into account. The plasmarons contribute by a slowly varying background to the momentum density, up to momenta significantly beyond the Fermi wave vector.

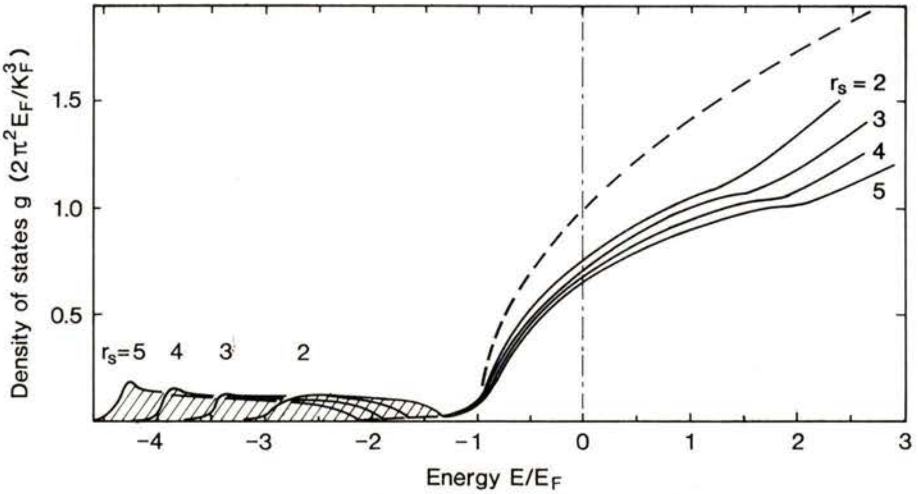

Fig. 2 — The energy density of states of the homogeneous electron gas for different densities. The dashed curve is the result of one-electron theory and the energy zero is at the Fermi level. The plasmaron contribution is shaded (from [27]).

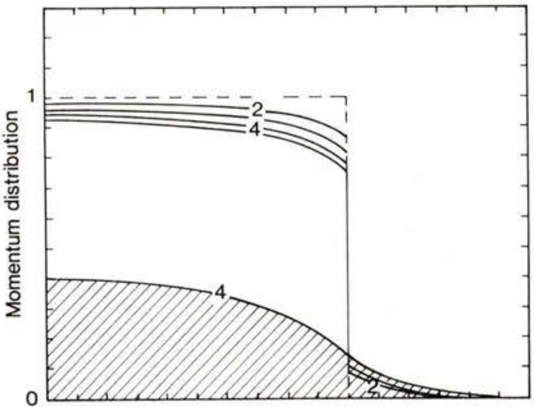

Fig. 3 — The electron momentum distribution of the homogeneous electron gas for different densities. The dashed curve is the result of one-electron theory. The contribution from the plasmaron is approximately given by the shaded area for the case $r_s = 4$ (from [27]).

*The complementarity of photoemission and Compton scattering can be described as follows. The former experiment provides information on the location of the Green-function poles, while the latter samples the magnitude of the residues. Furthermore, the densities are obtained by an energy integration over the spectral function and very broad features which cannot be seen in emission spectra may contribute significantly.*

The spectral function can in principle be obtained completely by electron or photon scattering experiments in which the recoil electron is measured in coincidence with the scattered electron or photon. Though ideally suited in principle for observation of the above mentioned many-body effects, these so-called (e, 2e) or ($\gamma$, $\gamma$e) resp. (X, Xe) spectroscopies are very difficult to carry out in condensed matter systems. Some progress has been made, however [13].

## 4 — DENSITY-FUNCTIONAL THEORY

After the general discussion of the electron densities and their interrelationship with other properties, we now turn to the problem of how to calculate them in practice. We will not dwell upon the numerical problems but concentrate on the conceptual background of modern band structure calculations. For the present purposes we may limit ourselves to the density-functional theory of Hohenberg and Kohn, [19], and Kohn and Sham, [22]. If its predecessors such as Hartree-Fock-Slater or the X$\alpha$ methods [37] are included, density-functional theory in the local density approximation is practically without contender as far as accurate electron densities in metals are concerned. (As a notable exception we would like to mention Hartree-Fock calculations of the Torino group, e. g. Dovesi et al., [10]. For details on the subject not treated here we refer to recent reviews, [23], [43], [6]).

### 4.1 — *Hohenberg-Kohn theorem*

The celebrated theorem of Hohenberg and Kohn [19] states that, for a given particle number N, an energy functional of the charge density E[$\rho$] exists which obeys the minimum principle

$$E[\rho] \leq E_0 \; ; \; E[\rho_0] = E \, , \qquad (35)$$

where $E_0$ and $\rho_0$ are the ground-state energy and charge density. We will not repeat the original proof of Eq. (35) here. Instead consider the concrete formulation of the functional as suggested by Levy [24]:

$$E[\rho] = \min_{\{\Psi_\rho\}} < \Psi_\rho \mid \hat{T} + \hat{V}_{ee} \mid \Psi_\rho > + \\ + \int dr \, V_{ext}(r) \, \rho(r), \qquad (36)$$

which holds for a system described by a Hamiltonian which consists of kinetic energy $\hat{T}$, electron-electron interaction $\hat{V}_{ee}$ and the potential of the atomic nuclei $\hat{V}_{ext}$. In the first term on the left-hand side a search for a minimum expectation value is carried out. The set denoted by $\{\Psi_\rho\}$ includes all (trial) wave functions which have the proper permutation symmetry and particle number and which correspond to the charge density $\rho$ in the argument of the energy functional. It is easily seen that Eq. (36) indeed obeys Eq. (35).

The minimum principle (35) is equivalent to the variational principle

$$\delta \{ E[\rho] - \mu \int dr \, \rho(r) \} /_{\rho=\rho_0} = 0, \qquad (37)$$

where the Lagrange multiplier of the particle number constraint $\mu = \partial E_0 / \partial N$ is the chemical potential of the system. If E[$\rho$] is known with sufficient accuracy, the solution of (37) yields the ground-state charge density and energy.

Direct computation of Eq. (35) is of course impractical and one has to resort to approximations. The so-called local density approximation

$$E[\rho] \simeq \int d\mathbf{r}\, \rho(\mathbf{r})\, \varepsilon(\rho(\mathbf{r})), \qquad (38)$$

where $\varepsilon(\rho)$ denotes the energy (per electron) of the homogeneous electron gas of density $\rho$, has a long tradition, [42], [11]. The accuracy of Eq. (38) is unsatisfactory, however, mainly because of the strong non-local character of the kinetic energy. This drawback has been remedied by Kohn and Sham [22].

### 4.2 — *Kohn-Sham equations*

The crucial assumption is the existence of a (hypothetical) model system of N non-interacting fermions, which has the same charge density as the interacting system we are interested in. If this assumption is true, we known from the Hohenberg-Kohn theorem that a unique «effective» one-particle potential must exist which generates this charge density. The energy functional may then be written as

$$E[\rho] = T_s[\rho] + U[\rho] + \\ + \int d\mathbf{r}\rho(\mathbf{r})\, V_{ext}(\rho(\mathbf{r})) + E_{xc}[\rho], \qquad (39)$$

where $T_s$ is the kinetic energy of the non-interacting system, U denotes the static Coulomb energy, and the exchange-correlation functional $E_{xc}$ representing the remaining energies is thus in fact defined by Eq. (39). The hope is now that the exchange-correlation contribution is small enough for its local density approximation not to introduce unacceptable errors. The remaining task is then the calculation of the effective potential needed for the determination of $T_s$. This can be achieved by minimizing the functional Eq. (39) with respect to (normalized) one-particle wave functions which generate the charge density:

$$\rho(\mathbf{r}) = \sum_{i}^{\varepsilon_i \leq \mu} |\phi_i(\mathbf{r})|^2. \qquad (40)$$

The corresponding Euler-Lagrange equations read

$$\{-(\hbar^2/2m)\nabla^2 + V_{eff}[\rho](\mathbf{r})\}\phi_i(\mathbf{r}) = \\ = \varepsilon_i \phi_i(\mathbf{r}), \qquad (41)$$

where the effective potential reads

$$V_{eff}[\rho](\mathbf{r}) = V_{ext}(\mathbf{r}) + \\ + \int d\mathbf{r} \frac{\rho(\mathbf{r})}{|\mathbf{r}-\mathbf{r}'|} + V_{xc}[\rho](\mathbf{r}) \qquad (42)$$

$$V_{xc}[\rho](\mathbf{r}) = \frac{\delta E_{xc}[\rho]}{\delta\rho(\mathbf{r})} \qquad (43)$$

The second term on the right-hand side of Eq. (42) is the «Hartree» Coulomb potential of the static charge distribution; $V_{xc}$ is the so-called exchange-correlation potential, which in the local density approximation reads:

$$V_{xc}(\mathbf{r}) = \varepsilon_{xc}(\rho(\mathbf{r})) + \rho(\mathbf{r}) \frac{\partial \varepsilon_{xc}(\rho(\mathbf{r}))}{\partial \rho(\mathbf{r})} \qquad (44)$$

The Kohn-Sham equations (40-44) have to be solved self-consistently for the charge density.

### 4.3 — *Integration over coupling constant*

While the exchange-correlation energy $E_{xc}[\rho]$ has been defined only indirectly by Eq. (39) and (36), an alternative and direct formulation by Harris and Jones [15], has been proven very useful for conceptual reasons. It is based on a trick of many-body theory which rests on the assumption of adiabatic connectivity of interacting and non-interacting ground states, namely that of integration over the Coulomb coupling constant. The starting point is a Hamiltonian which is a function of the Coulomb coupling g:

$$\mathscr{H}(g) = \sum_i \{ -(\hbar^2/2m) \nabla^2 + V_{eff}[\rho](g, \mathbf{r}_i) \} + g \sum_{i \neq i'} (e^2 / |\mathbf{r}_i - \mathbf{r}_{i'}|) \tag{45}$$

The one-particle effective potential $V_{eff}[\rho](g, \mathbf{r})$ is here assumed to keep the ground-state charge density for $\mathscr{H}(g)$ constant and equal to the exact charge density, thus $V_{eff}(g = 0) = V_{ext}$ and $V_{eff}(g = 1) = 0$. (This assumption is not really necessary, however. At the cost of some correction terms at a later stage, $V_{eff}(g)$ may as well be set equal to the Kohn-Sham potential Eq. (42)). The Hellmann-Feynman theorem, [16], [12], for the ground-state energy of a Hamiltonian containing a parameter $\lambda$ reads:

$$\frac{dE(\lambda)}{d\lambda} = \frac{d}{d\lambda} < \Psi_0(\lambda) \mid \mathscr{H}(\lambda) \mid \Psi_0(\lambda) > = \; = < \Psi_0(\lambda) \mid \frac{d}{d\lambda} \mathscr{H}(\lambda) \mid \Psi_0(\lambda) > \tag{46}$$

Application to the ground-state energy of $\mathscr{H}(g)$ gives:

$$\frac{dE[\rho](g)}{dg} = \; = < \Psi_0(g) \mid \{ \sum_i \frac{d}{dg} V_{eff}[\rho](g; \mathbf{r}) + \sum_{i \neq i'} \frac{e^2}{|\mathbf{r}_i - \mathbf{r}_{i'}|} \} \mid \Psi_0(g) > \tag{47}$$

$$= \int d\mathbf{r} \, \rho(\mathbf{r}) \frac{d}{dg} V_{eff}[\rho](g; \mathbf{r}) + \frac{1}{g} E_{int}[\rho](g). \tag{48}$$

$E_{int}$ denotes the interaction energy, or the expectation value of the electron-electron interaction operator. Integration of both sides over the Coulomb interaction coupling yields:

$$E[\rho](g = 1) - E[\rho](g = 0) = \; = \int_0^1 \frac{dr}{g} E_{int}[\rho](g) + \int d\mathbf{r} \, \rho(\mathbf{r}) \{ V_{eff}[\rho](g = 1; \mathbf{r}) - V_{eff}[\rho](g = 0; \mathbf{r}) \} \tag{49}$$

Since $V_{eff}(g=1)$ vanishes and $V_{eff}(g=0)$ is nothing but the Kohn-Sham potential, we get the final result for the exchange-correlation energy:

$$E_{xc}[\rho] = \int_0^1 \frac{dg}{g} E_{int}[\rho](g) - U[\rho]. \tag{50}$$

By this relationship between interaction energy and exchange-correlation energy it is possible to apply the diagrammatic methods of many-body theory also to density-functional theory [3], [33]. Gunnarson and Lundqvist [14] used this construction to express the exchange-correlation energy in terms of the exchange-correlation hole $\rho_{xc}$ which surrounds each electron.

$$E_{xc}[\rho] = \; = \int d\mathbf{r} \, d\mathbf{r}' \frac{\rho(\mathbf{r})}{|\mathbf{r} - \mathbf{r}'|} \int_0^1 \frac{dg}{g} \rho_{xc}[\rho](\mathbf{r}, \mathbf{r}'; g), \tag{51}$$

$$\rho_{xc}[\rho](\mathbf{r}, \mathbf{r}'; g) = \frac{< \Psi_0(g) \mid (\hat{\rho}(\mathbf{r}) - \rho(\mathbf{r}))(\hat{\rho}(\mathbf{r}') - \rho(\mathbf{r})) \mid \Psi_0(g) >}{\rho(\mathbf{r})} - \delta(\mathbf{r} - \mathbf{r}'). \tag{52}$$

The exchange-correlation energy is thus simply the energy of interaction of an electron with its own exchange-correlation hole integrated over the coupling constant.

The integrated interaction is smaller than that for $g = 1$ which reflects the fact that $E_{xc}$ also contains a positive kinetic energy contribution. It should be clear that a precise knowledge of the exchange-correlation hole is not necessary, since only the spherical average enters (52). The fact that the local density approximation also performs well for very inhomogeneous systems such as atoms can be tracked down to the insensitivity of $E_{xc}$ to the detailed form of $\rho_{xc}$ [14].

### 4.4 — *General expectation values*

The ground-state energy and density are, strictly speaking, the only quantities accessible via the above algorithm. As far as the charge density structure factors are concerned there is no question about the applicability of density-functional theory. In the case of the momentum density, problems arise, however. Fortunately, a functional relationship between arbitrary ground-state expectation values and the charge density exists within the Kohn-Sham formalism [3]. The application of the general theorem to the momentum density yields a correlation correction term to the Kohn-Sham theory derived earlier by Lam and Platzman [26]. The relevant expressions are most easily derived via a slight modification of the integration over the coupling constant method as described above. Consider a Hamiltonian like (45) which is coupled now by a constant $\lambda$ to an arbitrary operator $\hat{o}$ whose ground-state expectation value we want to determine.

$$\mathscr{H}(g) = \sum_i \{ -(\hbar^2/2m)\,\nabla^2 + V_{eff}[\rho](g, \lambda; \mathbf{r}_i) \} + + g \sum_{i \neq i'} e^2 / |\mathbf{r}_i - \mathbf{r}_{i'}| + \lambda \hat{o} \tag{53}$$

Again we may define a density functional for the ground-state energy which now becomes a function of the parameter $\lambda$:

$$\begin{aligned} E[\rho](\lambda, g = 1) &= E[\rho](\lambda, g = 0) + \\ &+ \int_0^1 \frac{dr}{g} E_{int}[\rho](\lambda, g) + \\ &+ \int \mathbf{dr}\, \rho(\mathbf{r}) \{ V_{eff}[\rho](\lambda, g = 1; \mathbf{r}) - \\ &- V_{eff}[\rho](\lambda, g = 0; \mathbf{r}) \}, \end{aligned} \tag{54}$$

where the condition that the charge density should be constant for all values of $\lambda$ introduces the $\lambda$-dependence of $V_{eff}$. When differentiating with respect to $\lambda$, however, all terms containing the effective potential cancel. At $\lambda = 0$ we finally get the result

$$\begin{aligned} O[\rho] &\equiv \\ \equiv &< \Psi_0 (\lambda = 0, g = 1) \,|\, \hat{o} \,| \\ &| \Psi_0 (\lambda = 0, g = 1) > = \\ &= < \Psi_0 (\lambda = 0, g = 0) \,|\, \hat{o} \,| \\ &| \Psi_0 (\lambda = 0, g = 0) > + \\ &+ \frac{d}{d\lambda} E_{ex}[\rho](\lambda) /_{\lambda = 0} \end{aligned} \tag{55}$$

We thus observe that the ground-state expectation value of the operator $\acute{o}$ is made up of the expectation value with respect to the ground state of the non-interacting Kohn-Sham system and a correlation correction term $\Delta O$ equal to the derivative of the exchange-correlation energy. $\Delta O$ is well defined and can in principle be calculated by diagrammatic perturbation theory ([3], [33]). Eq. (55) has been used by Bass [2] to derive an interesting general expression for the kinetic-energy-density functional. In the local density approximation

$$\Delta O[\rho] \simeq \int \mathbf{dr}\, \rho(\mathbf{r}) \{ o(\rho(\mathbf{r})) - o_0(\rho(\mathbf{r})) \}, \tag{56}$$

where $o$ and $o_0$ are the expectation values (per electron) of $\hat{o}$ for the homogeneous electron gas. Choosing $o = a_p^+ a_p$ we get the correction term for the momentum density

$$\Delta \rho (\mathbf{p}) [\rho] \simeq$$

$$\int d\mathbf{r}\, \rho (\mathbf{r}) \{ f_h (p; \rho (\mathbf{r})) - f_0 (p; \rho (\mathbf{r})) \}, \qquad (57)$$

which is readily calculated from the occupation numbers of the homogeneous electron gas, as in Fig. 3, and the charge density.

### 4.5 — *Beyond the local density approximation*

Finally, we would like to mention briefly attempts to go beyond the local density approximation. Without being exhaustive, there are: self-interaction corrections in different implementations ([45], [46], [47]), the weighted or average density approximation [14] and an effective gradient expansion [48]. There have been a few attempts to calculate charge densities in metals with a Langreth-Mehl corrected potential [30], although without finding a significant improvement with respect to experiment. None of the approaches improves upon the observed non-local effects in the correction term $\Delta O$ of the transition metal momentum densities ([4], [5]). Most promising for the treatment of intrinsic anisotropic correlation effects by density-functional theory are in our opinion field-theoretical methods as forwarded by Sham [33] and Sham and Schlüter [35] for the semiconductor band-gap problem.

## REFERENCES

[1] ALMBLADH, C. O. and HEDIN, L. — in *Handbook of Synchrotron Radiation*, Vol. 1B, edited by E. E. Koch, North-Holland, Amsterdam (1983).

[2] BASS, R. — *Phys. Rev.* **B32**, 2670 (1985).

[3] BAUER, G. E. W. — *Phys. Rev.* **B27**, 5912 (1983).

[4] BAUER, G. E. W. — *Phys. Rev.* **B30**, 1010 (1984).

[5] BAUER. G. E. W. and SCHNEIDER, J. R. — *Phys. Rev.* **B31**, 681 (1985).

[6] CALLAWAY, J. and MARCH, N. H. — *Solid State Physics* **38**, 136 (1984).

[7] CEPERLY, D. M. and ALDER, B. — *Science* **231**, 555 (1986).

[8] DANIEL, E. and VOSKO, S. H. — *Phys. Rev.* **120**, 2041 (1960).

[9] DAVIDSON, E. R. — *Reduced Density Matrices in Quantum Chemistry*, Academic, New York (1976).

[10] DOVESI, R., PISANI, C., RICCA, F. and ROETTI, C. — *Phys. Rev.* **B25**, 3731 (1982).

[11] FERMI, E. — *Z. Physik* **48**, 73 (1928).

[12] FEYNMAN, R. P. — *Phys. Rev.* **56**, 340 (1939).

[13] GAO, C., RITTER, A. L., DENNISON, J. R. and HOLZWARTH, N. A. W. — *Phys. Rev.* **B37**, 3914 (1988).

[14] GUNNARSON, O. and LUNDQVIST, B. I. — *Phys. Rev.* **B12**, 4274 (1976).

[15] HARRIS, J. and JONES, R. O. — *J. Phys.* **F4**, 1170 (1974).

[16] HELLMANN, H. — *Einführung in die Quantenchemie*, Deuticke, Leipzig (1937).

[17] HEDIN, L. and LUNDQVIST, S. — *Solid State Physics* **23**, 1 (1969).

[18] HENDERSON, G. A. — *Phys. Rev.* **A23**, 19 (1981).

[19] HOHENBERG, P. and KOHN, W. — *Phys. Rev.* **136**, B864 (1964).

[20] INKSON, J. C. — *Many-body Theory of Solids*, Plenum Press, New York (1984).

[21] INGLESFIELD, J. E. — *Mol. Phys.* **37**, 873 (1979).

[22] KOHN, W. and SHAM, L. J. — *Phys. Rev.* **140**, A1133 (1965).

[23] KOHN, W. and VASHISHTA, P. — *Theory of the Inhomogeneous Electron Gas*, edited by N. H. March and S. Lundqvist, Plenum, New York (1983).

[24] LEVY, M. — *Proc. Natl. Acad. Sci. USA* **76**, 6062 (1979).

[25] LÖWDIN, P. O. — *Phys. Rev.* **97**, 1474 (1955).

[26] LAM, L. and PLATZMAN, P. M. — *Phys. Rev.* **B9**, 5122 (1974).

[27] LUNDQVIST, B. I. — *Phys. Kondens. Materie* **6**, 206 (1967).

[28] LUNDQVIST, B. I. — *Phys. Kondens. Materie* **7**, 117 (1968).

[29] MASSA, L., GOLDBERG, M., FRISHBERG, C., BOEHME, R. F. and LA PLACA, S. J. — *Phys. Rev. Lett.* **55**, 622 (1985).

[30] NORMAN, M. R. and KOELLING, J. J. — *Phys. Rev.* **B28**, 4357 (1986).

[31] NOZIERES, P. — *Theory of Interacting Fermi Systems*, Benjamin, New York (1964).

[32] SCHNEIDER, J. R., HANSEN, N. K. and KRETSCHMER, H. R. — *Acta Cryst.* **A37**, 711 (1981).

[33] SHAM, L. J. — *Phys. Rev.* **B32**, 3876 (1985).

[34] SHAM, L. J. and KOHN, W. — *Phys. Rev.* **145**, 561 (1966).

[35] SHAM, L. J. and SCHLÜTER, M. — *Phys. Rev.* **B32**, 3883 (1985).

[36] SINGWI, K. S. and TOSI, M. P. — *Solid State Physics* **36**, 177 (1982).

[37] SLATER, J. C. — *Quantum Theory of Molecules and Solids*, Vol. 1-5, McGraw-Hill, New York (1960-1975).

[38] SMITH, V. H. — in *Local Density Approximations in Quantum Chemistry and Solid State Physics*, edited by J. P. Dahl and J. Avery, Plenum Press, New York (1984).

[39] SCHÜLKE, W. — *Phys. Stat. Sol.* (*b*) **82**, 229 (1977).

[40] SCHÜLKE, W. — in *Handbook of Synchrotron Radiation*, Vol. 3, edited by E. E. Koch, North-Holland, Amsterdam (1987).

[41] SCHÜLKE, W. and MOURIKIS, S. — *Acta Cryst.* **A42**, 86 (1986).

[42] THOMAS, L. H. — *Proc. Cambridge Philos. Soc.* **23**, 542 (1926).

[43] VON BARTH, U. and WILLIAMS, A. R. — in *Theory of the Inhomogeneous Electron Gas*, edited by N. H. March and S. Lundqvist, Plenum, New York (1983).

[44] WEYRICH, W., PATTISON, P. and WILLIAMS, B. G. — *Chem. Phys.* **41**, 271 (1979).

[45] PERDEW, J. P. and ZUNGER, A. — Phys. Rev. **B23**, 5048 (1981).

[46] PERDEW, J. P. and NORMAN, M. — Phys. Rev. **B26**, 5448 (1982).

[47] HEATON, R. A., HARRISON, J. G. and LIN, C. C. — Phys. Rev. **B28**, 5992 (1983).

[48] LANGRETH, D. C. and MEHL, M. J. — Phys. Rev. **B28**, 1809 (1983).

# ILLUSTRATION OF REDUCED DENSITY MATRICES AND RELATED QUANTITIES

D. FEIL and J. UITERWIJK

Chemical Physics Laboratory
University of Twente
POB 217, 7500 AE Enschede
The Netherlands

*ABSTRACT* — Second-order density matrices, conditional electron density distributions and Coulomb holes for He, $H_2$, and LiH are presented graphically.

## INTRODUCTION

To illustrate the abstract quantities discussed at this worksnop, the authors undertook to collect data on wavefunctions of small systems and to represent graphically the results on density matrices and related quantities. The systems selected are the He atom and the $H_2$, and LiH molecules. From the density matrices were derived the conditional density and the Coulomb hole.

## DEFINITIONS

Since we are not interested in spin properties, all expressions contain integration over the spin variables $\{\sigma_i\}$ and the resulting quantities are functions of the space variables $\{r_i\}$ only.

The diagonal terms of the second-order reduced density matrix are given by

$$\rho_2(r_1\ \ r_2) = \frac{n(n-1)}{2}$$

$$\int \psi^*(x_1 \ldots x_n)\,\psi(x_1 \ldots x_n)\,d\sigma_1\,d\sigma_2\,dx_3 \ldots dx_n \tag{1}$$

$\rho_2(r_1, r_2)\,dv_1\,dv_2$ represents the probability to find an electron in $dv_1$ at $r_1$ and at the same time another electron in $dv_2$ at $r_2$. The normalization is such that integration gives the number of electron pairs.

The conditional density is defined as

$$\rho^{\text{cond}}(r; r_1) = \frac{\rho_2(r_1, r)}{\rho(r_1)} \tag{2}$$

$\rho^{\text{cond}}(r; r_1)$ dv is proportional to the probability to find an electron in dv at r when an other electron is at $r_1$. Integration gives the number of electrons. The Coulomb hole is the difference between the conditional density and the normal density distribution.

Since the purpose of the contribution is to obtain qualitative understanding, all figures are in arbitrary units.

## CALCULATIONS

Computer programmes were written to calculate the diagonal terms of the second-order density matrices, the conditional density distribution and the Coulomb hole of the systems mentioned above. The electronic wave function of He was obtained from Roothaan and Weiss [1]. Kolos and Roothaan [2], provided the accurate wave function for the $H_2$ molecule. Davidson [3], snowed the advantages of using natural orbitals to represent correlated wave functions. His natural orbital analysis of LiH [4], served as basis for the work on this molecule.

## DISCUSSION OF RESULTS

Fig. 1 shows a number of cross-sections through the 6-dimensional space of $\rho^2 (r_1, r_2)$ of the He atom. Both variables are in the plane through the nucleus, with the variables of the probe electron indicated. The overall reduction of the function with increasing distance of the probe electron to the origin is of course due to the decreasing probability of finding the probe electron at increasing distances from the nucleus in fig. 2. We notice that the probe electron at the nucleus keeps the other electron away from the origin. When the probe electron moves away from the nucleus, the conditional density becomes less diffuse. This effect is better visible in fig. 3 where the Coulomb hole is shown. Note that in general the Coulomb hole is far from symmetrical about the probe electron. As long as the probe electron is not too far away from the origin, the reduction in density due to Coulomb repulsion is seen to occur where the density distribution has its maximus. This tendency is reserved when the probe electron moves into the diffuse region.

The next system to be discussed is the $H_2$ molecule. We now have two types of correlation: left-right and in-out. Since the latter is similar to the one in the He atom it will no further be discussed. Fig. 4 shows the cross-section through the space of $\rho_2 (r_1, r_2)$ in which both coordinates are on the molecular axis. The results for four different wave functions are shown. We use as reference the accurate wave function of Kolos and Roothaan. The other wave functions are Heitler and London's Valence Bond function, the Hartree-Fock determinantal wave function and the natural orbital representation of Kolos and Roothatn's results. Since the electrons in the $H_2$ molecule have opposite spins, no exchange correlation occurs, leading to a fully uncorrelated HF-wave function. The natural orbital approach is seen to yield excellent results, while the results of the HL wave function are good, with a slight over accentuation of the correlation.

The conditional density has a nice surprise. With the probe electron on one of the nuclei, one expects this nucleus to be fully screened and the conditional density to be a hydrogenic density about the other nucleus. Fig. 5, however, shows a

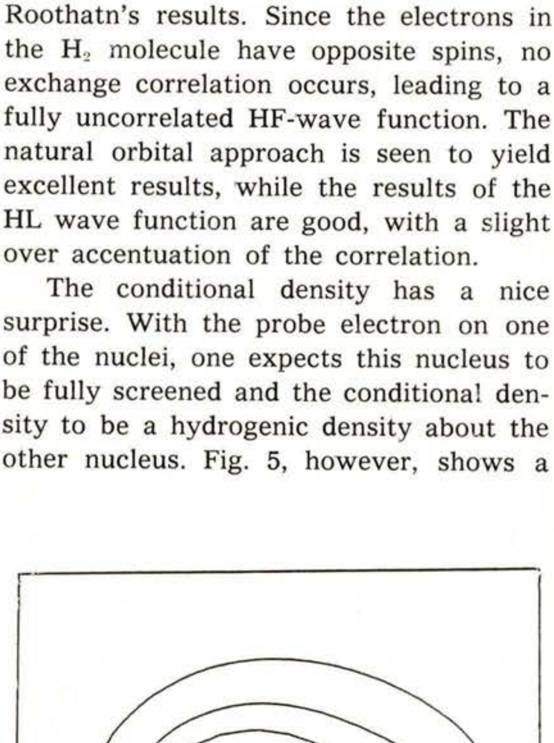

Fig. 5 — The conditional density distribution in $H_2$ with the probe electron at the nucleus on the right.

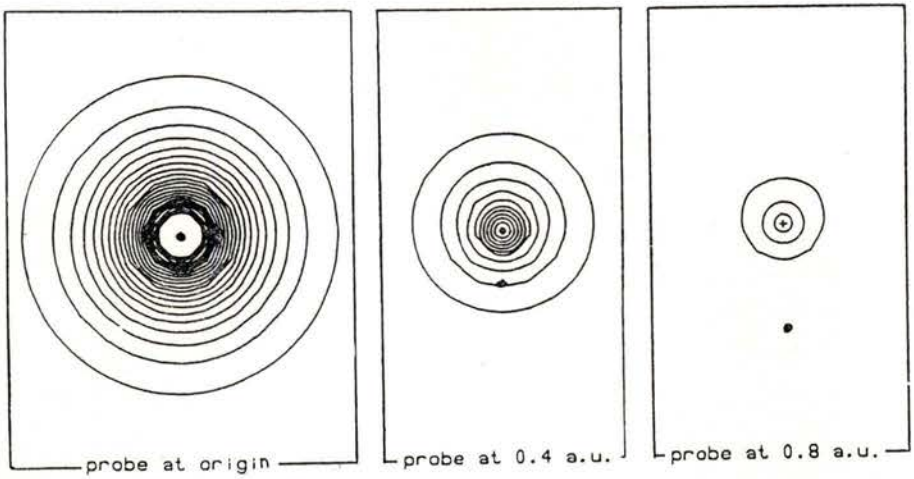

Fig. 1 — The diagonal terms of the second-order density matrix of He for different values of one of the variables. Contours in all figures are at arbitrary, but constant intervals.

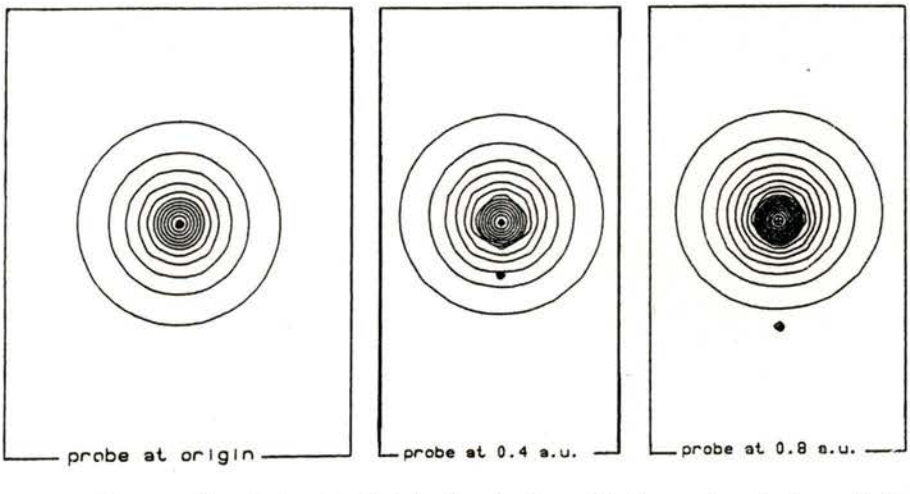

Fig. 2 — The conditional density distribution in He with the probe electron at the indicated positions.

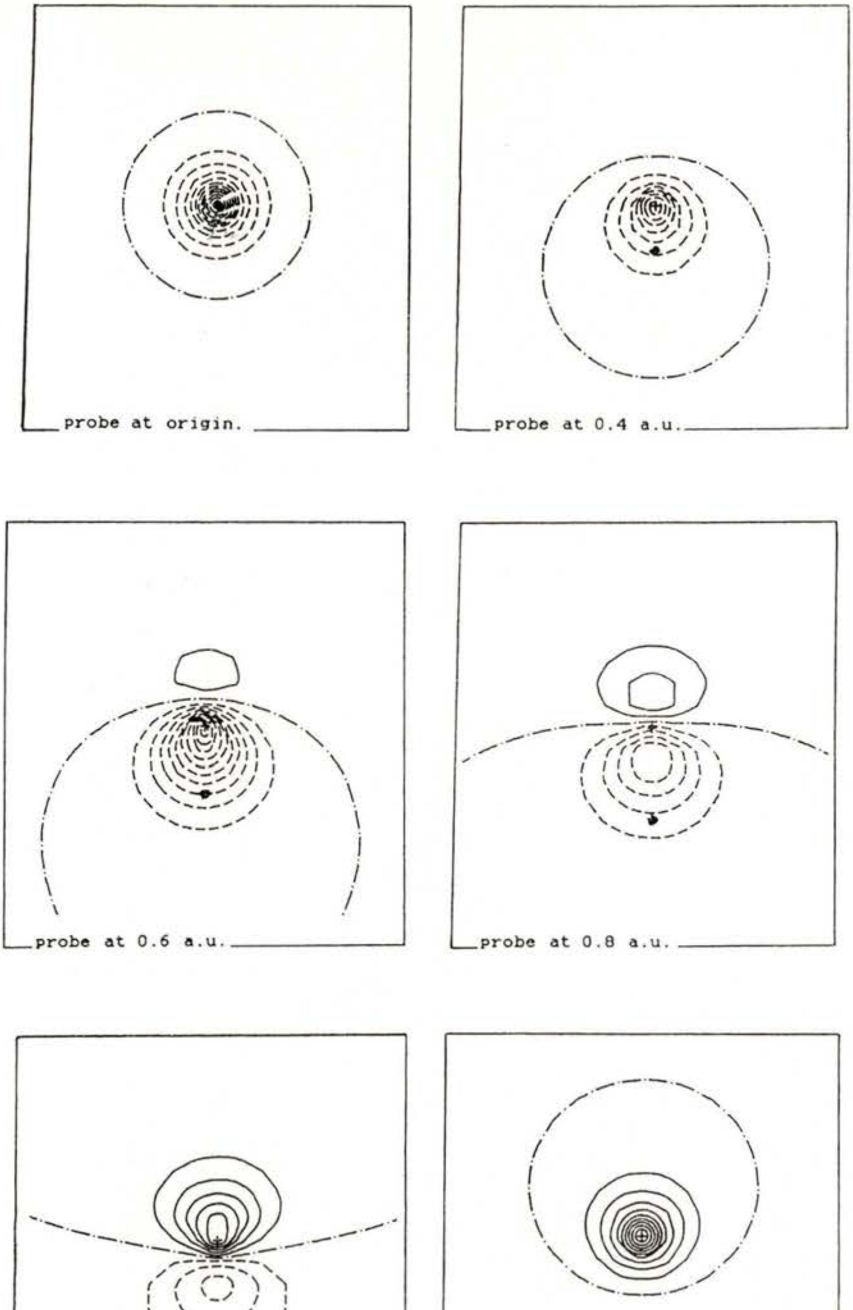

Fig. 3 — The Coulomb hole belonging to the probe electron in He.

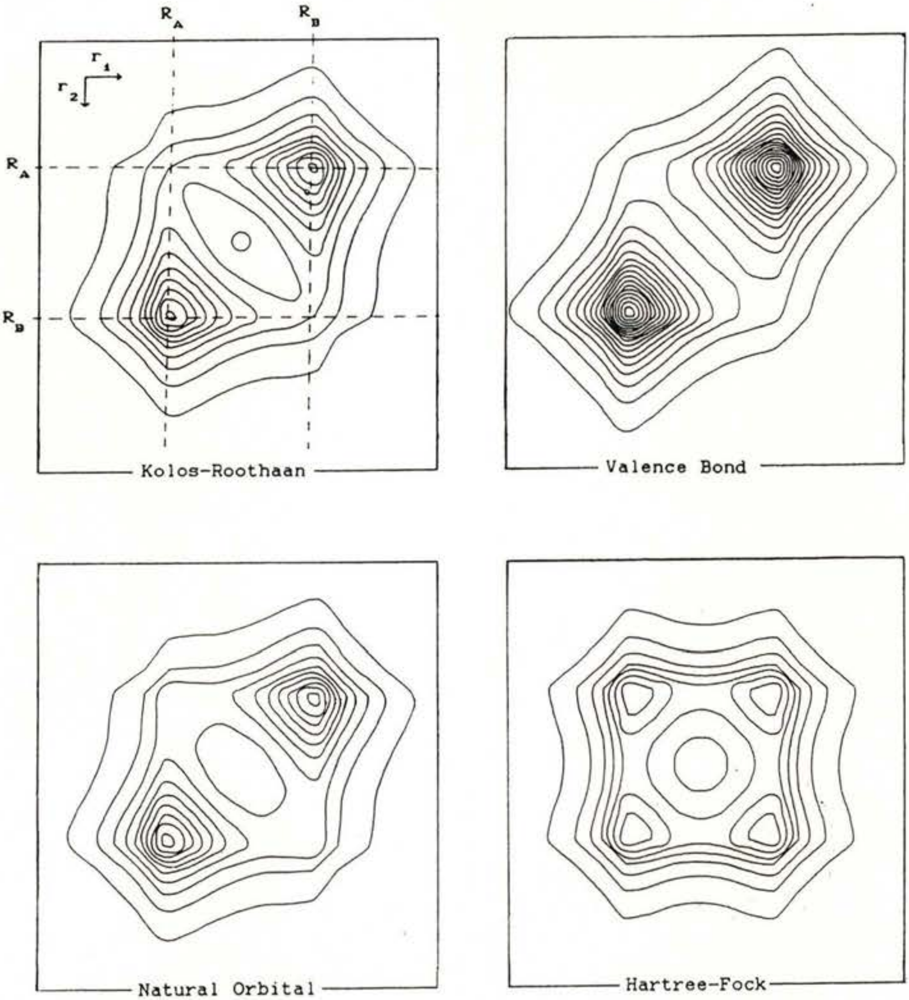

Fig. 4 — The diagonal terms of the second-order density matrix of $H_2$, calculated from different wave functions. The cross-sections shown correspond with both variables on the molecular axis.

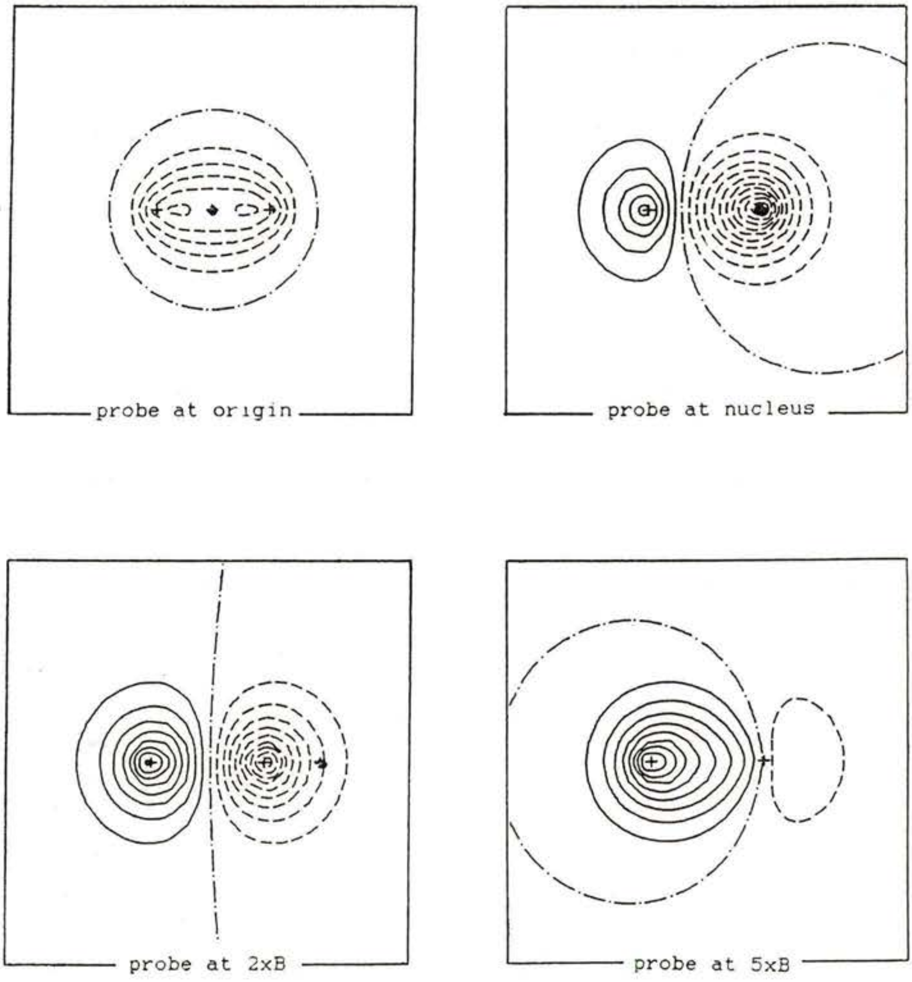

Fig. 6 — The Coulomb hole in $H_2$ with the probe electron at different positions on the molecular axis. The distance B equals R/2.

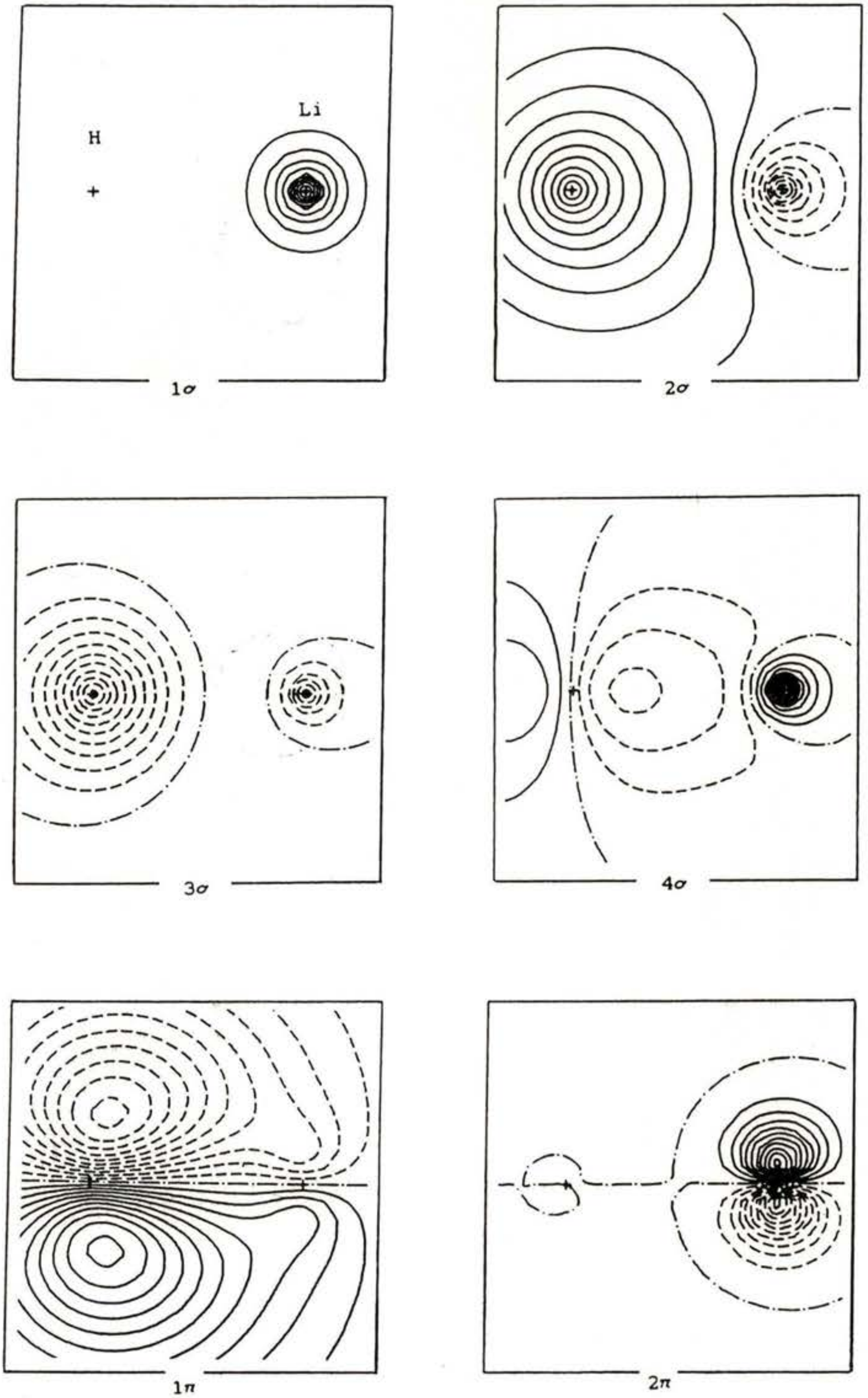

1σ 2σ 3σ 4σ 1π 2π

Fig. 7 — Some natural orbitals of the LiH molecule.

Fig. 8 — The conditional density distribution in LiH.

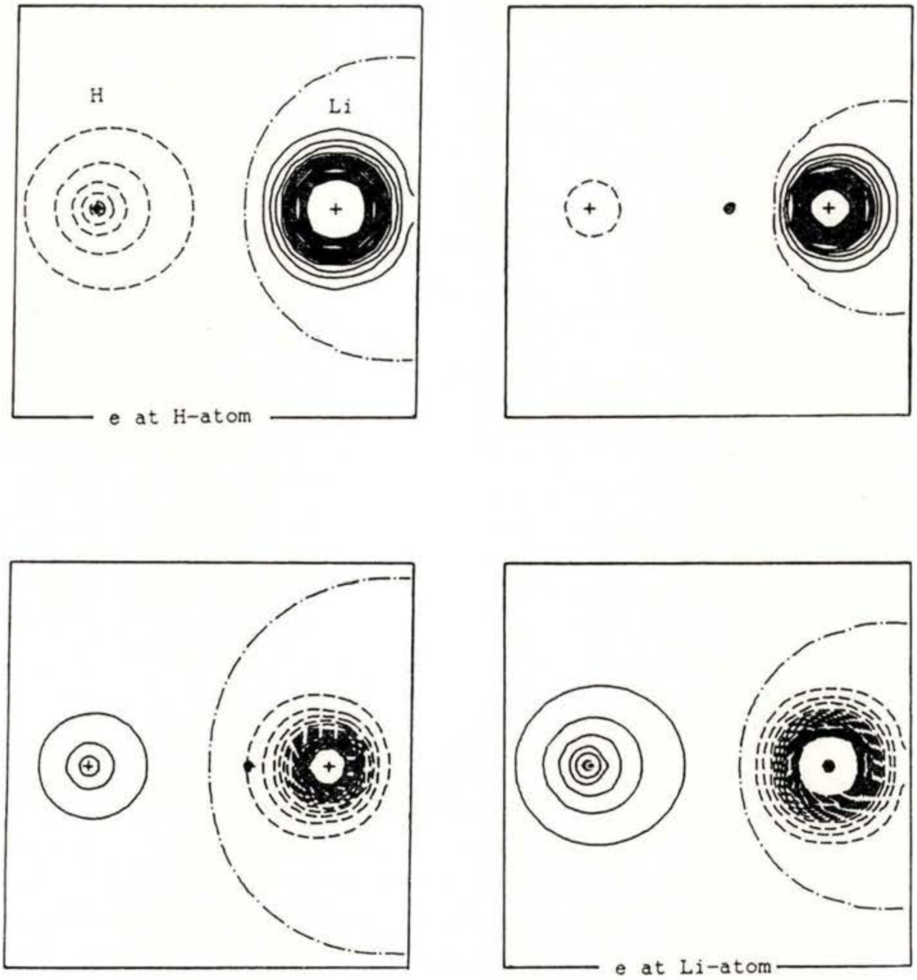

Fig. 9 — The Coulomb hole in LiH with the probe electron, indicated by •, at different positions on the molecular axis.

linear combination of hydrogenic density distributions. This result can easily be explained with the Valence Bond wave function:

$$\psi(x_1, x_2) = [s_a(r_1)\, s_b(r_2) + \\ + s_a(r_2)\, s_b(r_1)] * \text{spin} \qquad (3)$$

Assuming the probe electron to be on nucleus a, the origin, we get

$$\rho^{\text{cond}}(r; 0) = N\, [s_a(0)\, s_b(r) + \\ + s_a(r)\, s_b(0)]^2 \qquad (4)$$

$$= C\, [e^{-|r-R_b|} + e^{-|r|} * e^{-R}]^2 \qquad (5)$$

with $R = |R_a - R_b|$, the distance between the two nuclei.

We recognise the linear combination of the hydrogen density distributions. From the conditional density distribution we derive the Coulomb hole, shown in fig. 6. The hole only partly follows the probe electron.

For the calculation of the various quantities of LiH, natural orbitals were essential. A number of them are shown in fig. 7. It is known that virtual orbitals, obtained from a Hartree-Fock calculation are inefficient to account for correlation. Correlation is important in the regions of high electron density, whereas the virtual orbitals are diffuse in character. Natural orbitals are seen to be far more compact.

Fig. 8 shows the conditional density with the probe electron at different positions. The corresponding Coulomb hole, fig. 9 shows an interesting behaviour. When it is situated in a high density region, i. e. close to a nucleus, the Coulomb hole has the expected shape. From the previous examples we learned that it remains more or less centred on the nucleus even when the probe electron moves away. Since there is no low density region on the molecular axis, the Coulomb hole has to move suddenly from one nucleus to the other when the probe electron is shifted a small distance. It might be interesting to investigate if the point at which the transition takes place corresponds with the boundary between the two atoms, defined as the point at which the flux of the electron density is zero.

## REFERENCES

[1] ROOTHAAN, C. C. J., WEISS, A. W. — Rev. Mod. Phys. **32**, 194 (1960).

[2] KOLOS, W., ROOTHAAN, C. C. J. — Rev. Mod. Phys. **32**, 219 (1960).

[3] DAVIDSON, E. R. — Rev. Mod. Phys. **44**, 451 (1972).

[4] BENDER, C. F., DAVIDSON, E. R. — J. Phys. Chem. **70**, 2675 (1966).

# DEVELOPMENT OF LINKS BETWEEN ELECTRON DENSITIES IN COMPLEMENTARY SPACES

RAJEEV K. PATHAK
Departments of Physics and Chemistry

SHRIDHAR R. GADRE
Department of Chemistry, University of Poona
Pune — 411 007. India

A review of procedures for the estimation of electron momentum density for atoms, molecules and solids from the sole knowledge of the corresponding position density is presented.

These transformations can be achieved either with semiclassical phase space considerations *or* by employing more rigorous formulation of exchange hole. The former have been established by Gadre and Pathak [1] in a series of articles. These transformations are based on two reciprocal atomic relations $\rho(r) = p^3(r)/3\pi^2$ and $\gamma(p) = r^3(p)/3\pi^2$ and lead to some remarkable results, e. g. $<p>$-value being proportional to magnitude of the Slater-Dirac exchange energy. A large number of these predictions were completely missed by the earlier workers and were first pointed out by Gadre and Pathak.

A general relation

$$<r^n> = 3^{(n+3)/3} \,.\, \pi^{2n/3} \int_0^\infty \gamma^{(n+3)/3} \, d\mathbf{p}/(n+3)$$

where $\gamma(p)$ is the spherically symmetric electron momentum density, was developed by Gadre et al. [2]. An extension to molecules was pointed out by Pathak et al. [3] and tested for linear molecules. Here, it turns out that $\gamma(p) = V/4\pi^3$, V being the volume enclosed by a contour surface of electron density with value $p^3/(3\pi^2)$. This prediction is also quite successful as judged by the numerical tests.

A more rigorous strategy, viz. the conservation of exchange charge density has been employed recently by Gadre and co-workers [4]. Here, one estimates [5] the first-order reduced density matrix $\Gamma(\mathbf{r}, \mathbf{r}')$ from $\rho(\mathbf{r})$ as:

$$\Gamma(\mathbf{r}, \mathbf{r}') = [\rho(\mathbf{r})\,\rho(\mathbf{r}')]^{1/2} \; G(\mathbf{r}, \mathbf{r}').$$

$G(\mathbf{r}, \mathbf{r}')$ is related to $C_x(\mathbf{r}, \mathbf{r}')$ via
$G = (-2C)^{1/2}$ and $C_x$

incorporates an averaged charge density $\tilde{\rho}$ such that

$$\int \rho(\mathbf{r}') \; C_x^{\tilde{\rho}}(\mathbf{r}, \mathbf{r}') \; d\mathbf{r} = -1.$$

where the explicit form of $C_x$ is given by:

$$C_x(\mathbf{r}, \mathbf{r}') = -9\;[j_1(\tilde{y})/\tilde{y}]^2/2; \; \tilde{y} = (3\pi^2 \tilde{\rho})^{1/3}.$$

It is possible to obtain $\tilde{\rho}$ directly from $\rho$ by the normalization condition above [4].

Since the Fourier transformation of $\Gamma(\mathbf{r}, \mathbf{r}')$ yields the density matrix $\Gamma(\mathbf{p}, \mathbf{p}')$, one is able to estimate momentum space properties of atoms and molecules from the knowledge of the corresponding $\rho(\mathbf{r})$ alone. The formulation was applied to closed shell atomic densities and led to momentum space properties in close agreement with the respective near Hartree-Fock results. The kinetic energy anisotropy for the $H_2$ molecule is also estimated quite well via this procedure.

Gadre and co-workers have also developed novel correlations between information entropies in position and momentum spaces [1]. The information entropy sum $S[\rho] + S[\gamma]$ has a meaning of quantum-mechanical uncertainty [6] and a detailed account of the work done by the authors in this area is presented.

The financial assistance from the University Grants Commission (UGC), New Delhi under a Research Scheme *F. 12 - 43 / 86 (SR III)* is gratefully acknowledged.

## REFERENCES

[1] GADRE, S. R. and PATHAK, R. K., in Many Body Theories, Lecture Notes in Chemistry Series, ed. D. Mukherjee (Springer-Verlag, Heidelberg), **50**, 523-540 (1988) gives a detailed account of these developments.

[2] GADRE, S. R., GEJJI, S. P. and VENKATALAXMI, N., Phys. Rev. **A26**, 1768 (1982).

[3] PATHAK, R. K., GEJJI, S. P. and GADRE, S. R., Phys. Rev. **A29**, 3402 (1984). See Also Allan, N. L. and March, N. H., Intern. J. Quantum Chem. Symp. **17**, 227 (1983).

[4] GADRE, S. R. and CHAKRAVORTY, S. J., J. Chem. Phys. **86**, 2224 (1987); GADRE, S. R., KOGA, T. and CHAKRAVORTY, S. J., Phys. Rev. **A36**, 4155 (1987).

[6] BIAŁYNICKI-BIRULA, I. and MYCIELSKI, J., Commun. Math. Phys. **44**, 129 (1975).

# EXPERIMENTAL METHODS TO OBTAIN CHARGE AND MOMENTUM DENSITIES

JOCHEN R. SCHNEIDER
Hahn-Meitner-Institut, Glienicker Str. 100
D-1000 Berlin 39, FRG

In first Born approximation the double differential cross section for the interaction of photons with electrons in a solid can be written in the form [1]:

$$\frac{d^2\sigma}{d\Omega\ d\omega} = \left(\frac{d\sigma}{d\Omega}\right)_o \cdot S(\mathbf{q},\omega)$$

The intrinsic cross section $(d\sigma/d\Omega)_0$ describes only the strength of the coupling between each primary entity. The so-called dynamical structure factor $S(\mathbf{q},\omega)$ depends on the momentum $\hbar\mathbf{q}$ and the energy $\hbar\omega$ transferred to the sample in the scattering process and contains all relevant information on the structure and the dynamics of the system under investigation: $S(\mathbf{q},\omega)$ is the Fourier transform of the space time correlation function $G(\mathbf{r},t)$ which describes the correlation between the particle density at any place $\mathbf{r}'$ at any time $t = 0$ and the particle density at $\mathbf{r}' + \mathbf{r}$ at time t.

The dynamical structure factor can be expressed in the form [1]

$$S(\mathbf{q},\omega) = \sum_f \sum_i | < f | \sum_j e^{i\mathbf{q}\cdot\mathbf{r}_j} | i > |^2 \times \\ \times\ \delta(E_f - E_i - \hbar\omega)$$

where the energy $\delta$-function contains all the relevant frequency information. The sum of the matrix elements $<f | \Sigma\, e^{i\mathbf{q}\cdot\mathbf{r}_j} | i>$ has to be performed over all initial, $|i>$, and final $|f>$, states, of the system investigated in the scattering experiments; $\mathbf{r}_j$ is the position of each scatterer in the system and the factor $e^{i\mathbf{q}\cdot\mathbf{r}_j}$ represents the phase of the corresponding scattering amplitude. If the momentum transfer in the scattering experiment is small then the phase factors for many scatterers must be summed up before squaring the expression, i. e. the scattering is treated in the so-called collective regime where interference between scattering amplitudes takes place.

If $|f>$ is a continuum state the process is called Compton scattering which is interpreted within the impulse approximation [1]. The energy of recoiling electron has to be much higher than its binding energy, so that the interaction time is extremely short and the potential can be considered constant over this time; the final state of the electron is described by a plane wave. In this limit the dynamical structure factor reduces to:

$$S(\mathbf{q},\omega) = \\ = \int n(\mathbf{p})\ \delta\left(\hbar\omega - \frac{|\hbar\mathbf{q}|^2}{2m} - \frac{\hbar\mathbf{q}\cdot\mathbf{p}}{m}\right) d\mathbf{p}$$

which is the projection of the ground state electron momentum density n(**p**) onto the scattering vector **q**; **p** represents the electron momentum and m the electron mass. Therefore in a Compton scattering experiment one measures a Compton profile

$$J_{\mathbf{q}}(p_z) = \iint n(\mathbf{p})\ dp_x\, dp_z\ ;\ p_z \parallel \mathbf{q}$$

i. e. the momentum density is integrated over a plane perpendicular to the scattering vector. Because of the finite resolution in actual Compton scattering experiments the integration is not over a plane but over a sheet perpendicular to **q** with thicknesses of the order of 5 to 30 % of the diameter of the central Brillouin zone of a typical solid. If the chemical bonding is discussed in direct space the momentum density n(**p**) has to be Fourier transformed and one obtains the so-called reciprocal form factor:

$$B(\mathbf{r}) = \int n(\mathbf{p})\ e^{-i\mathbf{p}\cdot\mathbf{r}}\ d\mathbf{p}\ ,$$

which is the sum of the auto-correlation functions of the one-electron wave functions $\psi_j(\mathbf{r})$:

$$B(\mathbf{r}) = \sum_{j}^{\text{occ.}} \int \psi_j^*(\mathbf{r}' + \mathbf{r})\ \psi_j(\mathbf{r}')\ d\mathbf{r}'$$

A one dimensional Fourier transform of the Compton profile $J_{\mathbf{q}}(p_z)$ yields:

$$B_{\mathbf{q}}(z) = \int J_{\mathbf{q}}(p_z)\ e^{-ip_z\cdot z}\ dp_z$$

where z is parallel to $p_z$ [2, 3]. Assuming that the effect of resolution can be described by a convolution of the intrinsic Compton profile with a Gaussian distribution function, the finite resolution leads to an exponential damping of B(z) for increasing correlation lengths z. Therefore the bad resolution in $\gamma$-ray Compton scattering experiments can partly be compensated by high counting rates which made the $\gamma$-ray technique successful.

If $|f>$ is a discrete excited electronic state the scattering is called X-ray Raman scattering. Like in an absorption experiment a core electron is brought in a state slightly above the Fermi energy but here the energy of the incident photons is much higher than the energy transfer $\hbar\omega$, so that the spectra are measured at momentum transfer $|\hbar\mathbf{q}| > 0$. Within plausible approximations there exists a simple relation between the cross section for absorption and Raman scattering experiments [4]:

$$\left( d^2\sigma/(d\Omega\, d\omega) \right)^{\text{Raman}} \sim$$
$$(1/\hbar\omega) \left( d^2\sigma(\omega)/(d\Omega\, d\omega) \right)^{\text{absorption}}$$

Compared to soft X-ray absorption experiments, however, the Raman spectra definitely arise from the bulk of the sample which can be mounted in furnaces, cryostats or high pressure devices; surface states and impurities are of minor importance. In addition one expects new information on many-body effects in the electronic system from the **q**-dependence of the Raman spectra. Important progress has been made in the development of this technique in connection with modern synchrotron radiation sources [5].

If $|f> = |i>$, then the scattering is elastic and is called Rayleigh scattering. In a single crystal this elastic scattering from a periodic array of scatterers gives rise to Bragg peaks around reciprocal lattice vectors; the dynamical structure factor reduces to:

$$S(\mathbf{q},o) = \left| \int \psi_o^*(\mathbf{r}) e^{i\mathbf{q}\cdot\mathbf{r}}\ \psi(\mathbf{r})\ d\mathbf{r} \right|^2\ ;\ \mathbf{q} \simeq 2\pi\mathbf{H}$$

$$S(\mathbf{H},o) \simeq \left| \int_{V_{\text{cell}}} \rho(\mathbf{p})\ e^{i2\pi\mathbf{H}\cdot\mathbf{r}}\ d\mathbf{r} \right|^2 = |\mathbf{F}_H|^2$$

$\psi_0(\mathbf{r})$ represents the ground state electronic wave function and $\rho(\mathbf{r}) = \psi_0^*(\mathbf{r}) \cdot \psi_0(\mathbf{r})$ the charge density; the integral is over a crystal unit cell, $V_{cell}$. The structure factor $F_H$ is one component of the Fourier series in which the periodic charge density $\rho(\mathbf{r})$ can be developed. Once the diffraction mechanism is understood for a given sample $|F_H|$ can be determined from the Bragg scattered intensity. For a detailed discussion of diffraction physics in connection with charge density studies we refer to [6].

The cross section for X-ray scattering is small which has the advantage that many scattering experiments can be discussed in the frame of the first order Born approximation. On the other hand X-ray scattering experiments may suffer from intensity problems and therefore, in the past, special limiting cases of $S(\mathbf{q},\omega)$ have been studied extensively. Only recently, because of the availability of suitable sources of synchrotron radiation in X-ray regime, successful measurements of $S(\mathbf{q},\omega)$ over a wider range of $\mathbf{q}$ and $\omega$ have been performed [7]; they should become of increasing importance in the future.

In a way the report on the «oxalic acid project» of the IUCr Commission on Charge, Spin and Momentum Densities [8] summarizes the state of the art in experimental charge density studies on molecules in 1984. The authors conclude: «Though several chemically significant features are reproduced in all the experimental density maps, differences in detail occur which caution against overinterpretation of the maps. Large differences between vibrational tensor elements $U_{ij}$ are observed which can often not be corrected by the scaling of all temperature parameters in a set. Positional parameters are reproducible to precisions of 0.001 Å or better. The biggest discrepancies between theoretical and experimental deformation density maps occur in the lone-pair regions where peaks are higher in the theoretical maps. However, this comparison may be affected by inadequacies in the thermal-motion formalism which must be involved before experimental and theoretical maps can be compared in a quantitative way.» We cannot add to this; instead, two examples of simple solids will be discussed, namely copper and silicon.

Today, most calculations of the electronic structure of solids are performed within the Hohenberg-Kohn-Sham density functional theory (for a short review see ref. [9]). The many-body problem is transformed into a large set of one-particle eigenvalue equations, which are called the Kohn-Sham equations:

$$\{-(\hbar^2/(2m))\,\nabla^2 + V_{\text{Hartree}}\,[\rho]\,(\mathbf{r}) + + V_{\text{external}}\,(\mathbf{r}) + V_{xc}\,[\rho]\,(\mathbf{r})\}\,\phi_i(\mathbf{r}) = = \varepsilon_i\,\phi_i(\mathbf{r})$$

The eigenvalues $\varepsilon_i$ are used to calculate the energy. The eigenfunctions $\phi_i(\mathbf{r})$ have no physical meaning in themselves, however, they determine the correct charge density:

$$\rho(\mathbf{r}) = \sum_i^{\text{occ.}} |\phi_i(\mathbf{r})|^2 .$$

The exchange-correlation potential $V_{xc}(\mathbf{r})$ is approximated in the so-called local density approximation, which is based on the homogeneous interacting electron gas, i. e. it should be applied to systems with slowly varying charge density only. Following Pinder et al. [10] there are two distinct sources for discrepancies between theory and experiment in the practical implementation of density functional theory. The first because the exact exchange-correlation energy functional is not known for a real system. The second comes from the computational aspect of the problem, namely the numerical solution of the self-consistent Kohn-Sham equations for the electrons in a crystal, for which a number of approximations must be made. Since the X-ray structure factors are directly related to the electron charge density, which in principle is exactly calculable from density functional theory, these results can be used as stringent test of present day calculations of the elctronic structure of crystals. In fact X-ray structure factors provide a more severe test of the local density approximation than its very successful application to the calculation of such physical quantities as cohesive energies, compressibilities, lattice constants, etc., which are obtained from total energy differences where substantial cancellation of errors can occur. No such cancellation of errors takes place in the calculation of the structure factors.

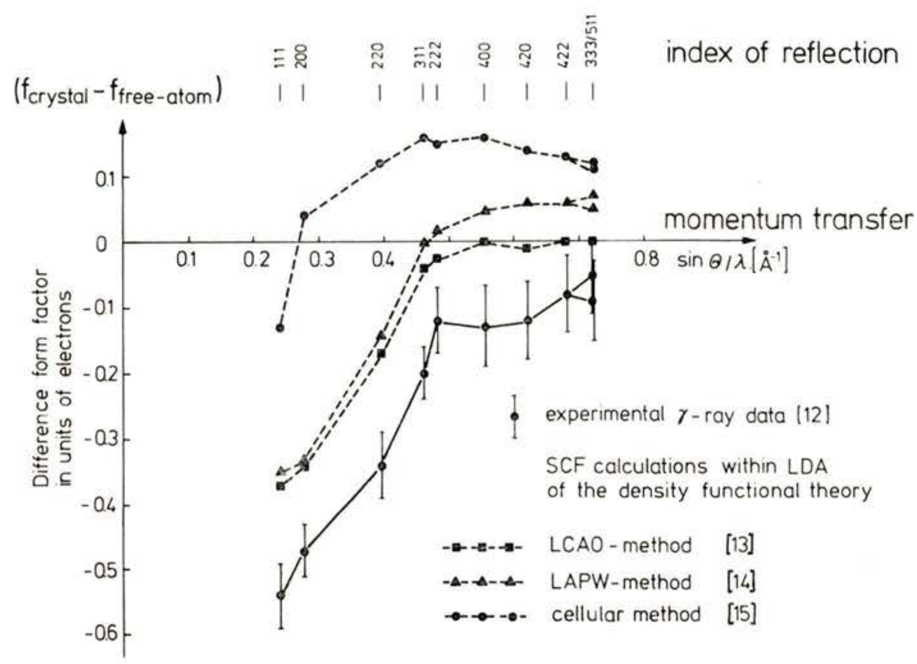

Fig. 1 — Deviation of experimental and theoretical form factors of copper from free-atom values.

In the case of copper the structure factor $F_H$ is directly proportional to the atomic scattering factor or form factor f and Fig. 1 shows the difference between the free atom form factors [11] on one hand, and experimental [12] and theoretical data [13-15] for copper single crystals on the other hand. The theoretical data from references [13] and [14] are higher than the experimental data by about 0.8 % but, nevertheless, the agreement is quite good. The energy eigenvalues of these state of the art band structure calculations, interpreted as one-electron excitation energies, do not well reproduce the band structure of copper as determined by angular resolved photoemission spectroscopy [16]. The d-bands are too high and too disperse. A more recent band structure calculation [15], again within the local density approximation to the density functional theory, but with a different construction of the periodic crystal potential, reproduces the photoemission data extremely well. However, the calculated form factors differ by about 2.2 % from the experimental data and the calculated difference density map is qualitatively different from the experimental one [16, 17]. This example demonstrates that for a comparison between experiment and theory one should not only consider physical quantities related to the eigenvalues $\varepsilon_i$ but also those directly related to the eigenfunctions $\phi_i(\mathbf{r})$.

The experimental data shown in Fig. 1 could be brought into agreement with the results from either of the three theoretical calculations by an appropriate rescaling of the measured structure factors. In other words, an accurate knowledge of the absolute scale of the measurements is crucial for a comparison between experiment and theory. In order to eliminate possible problems with the intrinsic cross section for the diffraction of $\gamma$-radiation with energies of the order of 400 keV, Pendellösung oscillations have been studied in large silicon single crystals. The integrated reflecting power measured in symmetrical Laue geometry exhibits oscil-

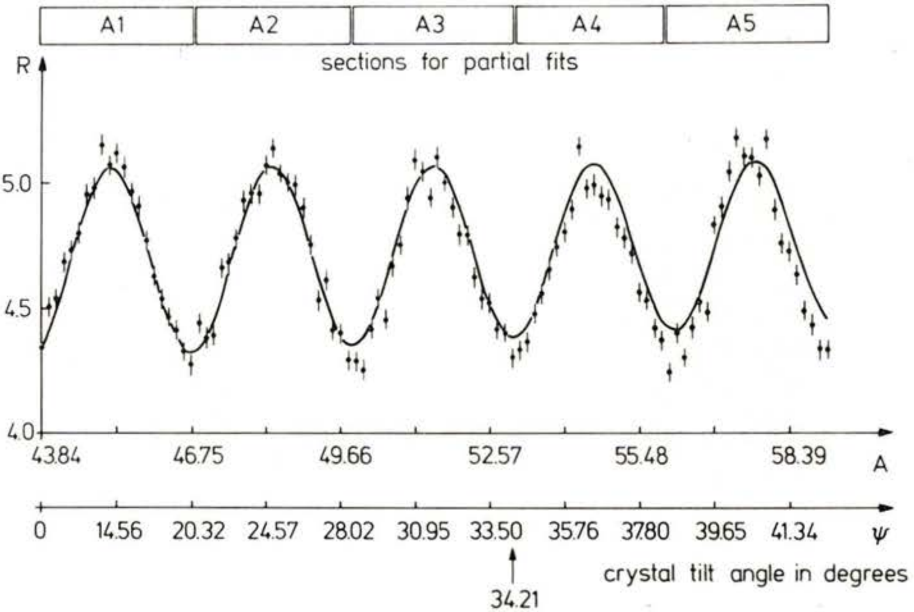

Fig. 2 — Integrated reflecting power measured with 0.0392 Å $\gamma$-radiation at the 220 reflection of a highly perfect float-zone grown Si single crystal. The experimental data are plotted as a function of the parameter A which is the ratio of sample thickness and extinction length, as well as the tilt angle $\Psi$. The solid line represents the final fit of dynamical diffraction theory to 64 data points up to $\Psi = 34.21^\circ$ [18].

lations around a constant average value as a function of sample thickness which are, for short wavelength $\gamma$-radiation, determined by the corresponding structure factor. Fig. 2 shows these oscillations measured at reflection 220 in a 1 cm thick Si crystal; the effective sample thickness has been increased by tilting the sample around the scattering vector [18]. As a result one obtains:

$$F'_{220} = 69.16 \pm 0.03 \text{ for } \lambda = 0.0392 \text{ Å}$$

$$F'_{220} = 69.21 \pm 0.06 \text{ for } \lambda = 0.0265 \text{ Å}$$

which is in perfect agreement with the X-ray Pendellösung data by Aldred & Hart [19]:

$$F'_{220} = 69.21 \pm 0.06 \text{ for X-rays}$$

Because the cross section for X-ray diffraction is not questioned we conclude that the cross section for $\gamma$-ray diffractometry is sufficiently well known.

Sets of structure factors of silicon have been determined using the different Pendellösung methods. Aldred & Hart analysed Pendellösung oscillations in the intensity diffracted from large wedge shaped crystals [19]. Teworte & Bonse deduced structure factors from the Pendellösung oscillations in the shape of the diffraction pattern [20]. Saka & Kato tilted plate like samples around the scattering vector and obtained oscillations similar to those shown in Fig. 2 [21]. The different data sets have been analysed by Cummings & Hart [22] and they conclude that the agreement between 5 independent data sets is of the order of 0.1 %. Therefore the most accurate experimental structure factors known at present are those of silicon. These data represent a real challenge for theory. Cummings & Hart compare the experimental data with the results of a pseudopotential calculation by Yin & Cohen [23] and find very good agreement. Because the requirements for the perfection of the sample increase for weak reflections, it will be difficult to measure forbidden reflections via Pendellösung methods with the accuracy obtained for ordinary reflections. Models based on Aldred & Hart data give values for the form factor $f_{220}$ between 162 and 204 milielectrons per atom [24]. By contrast, the direct $\gamma$-ray measurement gives $f_{220} = 191 \pm 1$ me per atom [25], which is in excellent agreement with the value from the pseudopotential calculation of $f_{220} = 190$ me.

Recently Deutsch & Hart [26] extended the analysis of Pendellösung oscillations in the diffraction pattern of perfect crystals using a monolitic double crystal diffractometer of novel design in an energy dispersive mode. They measured 8 high order structure factors ($0.64 \leq \sin\theta/\lambda \leq 1.56$ Å$^{-1}$) and discuss the Debye-Waller factor deduced from low and high order data via the Dawson formalism.

$$B_{\text{low}} = 0.4632 \pm 0.0041 \text{ Å}^2 \quad \sin\theta/\lambda \leq 1.04 \text{ Å}^{-1}$$

$$B_{\text{high}} = 0.5085 \pm 0.0035 \text{ Å}^2 \quad \sin\theta/\lambda \leq 1.30 \text{ Å}^{-1}$$

This result indicates that the bonding charges in silicon show smaller thermal-vibrational amplitudes than the core electrons. On the other hand a neutron diffraction study [27] yielded $B = 0.450 \pm 0.011$ Å$^2$ which is in good agreement with the B-value from the low order X-ray data. This contradiction will certainly stimulate further work and the accuracy of the available core electron X-ray form factors as well as the validity of the Born-Oppenheimer approximation may be discussed in this context.

In silicon directional Compton profiles have been measured with 412 keV $\gamma$-radiation and the 3-dimensional electron momentum distribution n(**p**), as well as the autocorrelation function of the direct space ground state wavefunction, B(**r**), have been reconstructed by Hansen et al. [28, 29]. For earlier attempts to obtain momentum densities from Compton scattering data on silicon and diamond see ref. [30-33]. For an appropriate reconstruction of the momentum density one has to optimize the strategy for Compton profile measurements with respect to the direction of **q** and the statistical accuracy aimed for. The papers by Mijnarends [34] and Hansen [35] can be consulted. As far as the reconstruction of B(**r**) from directional Compton profiles from ionic crystals is concerned, Weyrich's group in Konstanz gained a lot of experience [36]. At the synchrotron radiation facilities in Paris (Loupias et al.) and in Japan (Itoh et al.) Compton profiles of silicon are measured with about 4 times better resolution, i. e. approximately 0.1 atomic units, and the momentum density will be reconstructed. With increasing resolution the number of directional Compton profiles to be measued, in order to allow for the reconstruction of a 3-dimensional momentum distribution with the appropriate resolution, increases. In any case high resolution momentum densities will be available in the near future and because highly accurate structure factor data exist already, silicon is the most attractive candidate for the construction of a one-particle density matrix from experimental data. In addition Schülke & Mourikis [37] have performed coherent inelastic X-ray scattering experiments in perfect silicon single crystals from which they gain detailed information about the non-diagonal elements of the density matrix, which are not accessible in a classical Compton scattering experiment. For silicon a large number of good theoretical calculations of the electronic structure exist; they can be used to compare experiment and theory on the basis of one-particle density matrices. These calculations also provide detailed information about the energies which have to be considered before a statement on the relative merits of a theoretical calculation can be made.

As an example for a study of a solid in which structure factor and Compton profiles as well as the electronic band structure have been considered, we come back to copper [38-41]. Within the density functional theory only the charge density and the total energy can be calculated from the solutions of Kohn-Sham equations. For the calculation of other ground-state properties, O, as a functional of the charge density $\rho$, the following formula applies [42]:

$$O[\rho] = O_0[\rho] + \Delta O[\rho]$$

where $O_0[\rho]$ is the ground-state expectation value with respect to a N-particle Slater determinant constructed from the self-consistent solutions of the Kohn-Sham equations and $\Delta O[\rho]$ is a correction functional which can be expressed as a derivative of the exchange-correlation energy functional $E_{xc}[\rho]$; which is not known exactly. In contrast to the case of the charge density, exchange-correlation enters the calculation of the momentum density via two channels: the solutions of the Kohn-Sham equations, $\phi_i(\mathbf{r})$, depend on $V_{xc}[\rho]$ and thus on $E_{xc}[\rho]$, the correction term $\Delta O[\rho]$ also depends on $E_{XC}[\rho]$. Within the local density approximation (LDA) Lam & Platzmann [43] have calculated explicitly the correlation correction term for the momentum density:

$$\Delta n^{\mathrm{LDA}}[\rho] = \int \rho(\mathbf{r}) \cdot \left\{ n^{h}_{o}[\rho]\ (\mathbf{r}) - n^{f}_{o}[\rho]\ (\mathbf{r}) \right\} \mathbf{dr}$$

where $n^{h}_{o}[\rho](\mathbf{r}) - n^{f}_{o}[\rho](\mathbf{r})$ is the difference between the occupation numbers of the interacting and noninteracting homogeneous electron gas of density $\rho$. The correction term takes into account the effect that in the homogeneous electron gas the Coulomb correlation excites electrons from occupied plane wave states with wave vectors inside the Fermi surface into the unoccupied states outside the Fermi surface. $\Delta n^{\mathrm{LDA}}[\rho]$ is isotropic in momentum space.

Fig. 3 shows a comparison of the Cu Compton profile measured with $\mathbf{q}$ // [110] with the result of band structure calculations within the LDA of the density functional theory where the correlation correction term $\Delta n^{\mathrm{LDA}}[\rho]$, also presented in Fig. 3, was not applied [13]. Fig. 4 demonstrates that the remaining difference between experiment and theory can be

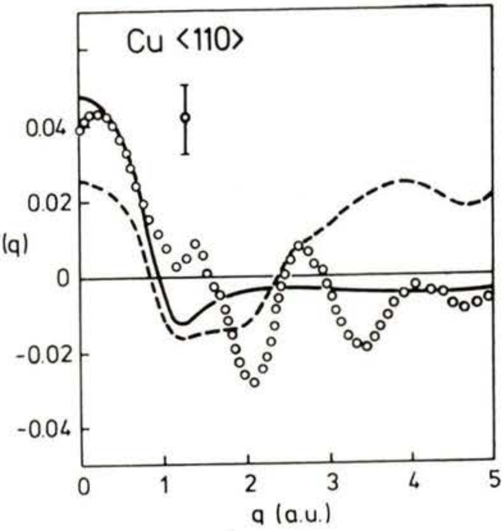

Fig. 3 — Copper < 110 > Compton profiles.

*a*) difference between the Kohn-Sham local density-functional band structure theory [13] augmented by Hartree-Fock free-atom core Compton profiles and experimental γ-ray data (open circles).

*b*) correlation correction term $-\Delta n^{\mathrm{LDA}}[\rho]$ (continuous curve).

c) difference between the Kohn-Sham local density-functional theory [13] and a MAPW Chodorow-potential band structure calculation [44].

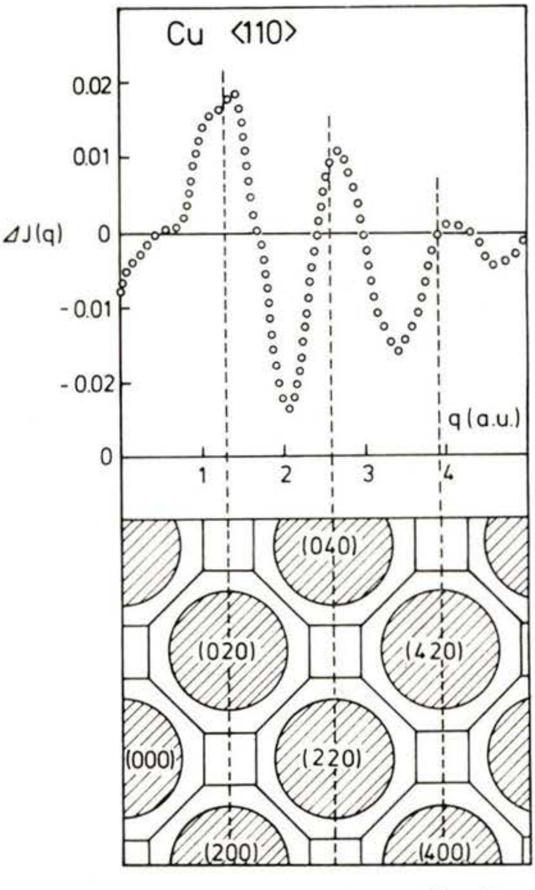

Fig. 4 — Copper < 110 > Compton profile. Upper part: difference between the local density-functional theory [13] including the correlation term $\Delta n^{\mathrm{LDA}}[\rho]$ and the experimental γ-ray data. Lower part: XY plane of the Brillouin zone and the Fermi surface of copper in the repeated zone scheme.

related to the Fermi surface topology in the extended zone scheme after incorporation of $\Delta n^{LDA}[\rho]$, for details see ref. [41]. Whenever the plane of integration perpendicular to [110] covers mainly occupied regions theory is larger than experiment; in-between the integration is essentially through unoccupied space and theory is smaller. This oscillatory function is beyond local density theory and in this sense one may consider it due to a non local correlation effect. This discrepancy almost quantitatively relates to the difference between experimental and theoretical Compton profile anisotropy shown in Fig. 5. In order to decide if these remaining discrepancies are due to problems in the exchange-correlation potential or due to deficiencies in the occupation numbers, the anisotropy has been calculated for different approximations of $V_{xc}$.

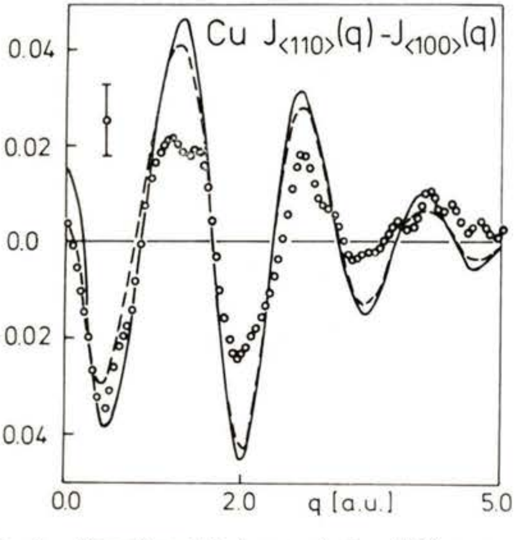

Fig. 5 — Experimental (open circles [38]) versus theoretical Compton profile anisotropies of copper. The continuous curve is the result of the Kohn-Sham local density-functional theory [13] and the dashed line is obtained by the MAPW Chodorow-potential band structure calculation [44].

Fig. 6 shows the anisotropies obtained in band structure calculations using the standard potential, the Hedin-Lundqvist potential, and the self-consistent Slater exchange potential. If concentration is on the feature at ≃ 1.25 a. u the use of the full Slater exchange potential yields the best agreement between experiment and theory. However, the band structure and the X-ray scattering factors have also been analysed and, in agreement with common experience, they exclude the use of the full Slater exchange potential. Fig. 7 shows the band structure along [100] from the origin to the boundary of the Brillouin zone. For the present purpose it may be characterised by the location of the d-bands, $E_d$, and their width, $W_d$. The use of the full Slater exchange potential increases $E_d$ by approximately 30 % and decreases $W_d$ by about 20 %, i. e. the

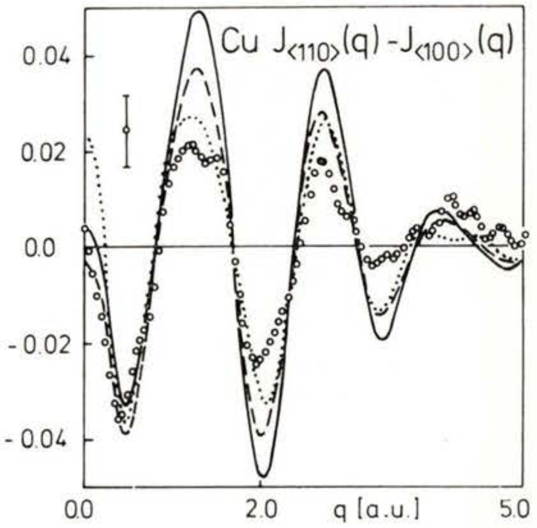

Fig. 6 — Experimental (open circles [38]) versus theoretical Compton profile anisotropies of copper obtained by the APW method and different local potentials [39]. Continuous line: standard potential, dashed line: Hedin-Lundqvist potential, dotted line: self-consistent Slater exchange potential.

d-bands are lowered in energy and reduced with respect to their dispersion by large ammounts. This is in contrast with all spectroscopic results. But also the calculated X-ray from factors show large discrepancies with experiment as demonstrated in Fig. 8. In conclusion the remaining discrepancies between experimental and theoretical Compton data on copper must be due to problems in the correlation correction term. This argument is supported by an analysis of the reciprocal form factor B(z) for a correlation length z equal to the first lattice translation $R_{110}$. Similar results have been deduced from an extensive study by Rollason et al. on nickel [47]. In the context of this work the effects of self-scattering in the $\gamma$-ray source on the measured Compton profiles, which turn out to be important especially for high energy $\gamma$-rays, have been analyzed in detail [48].

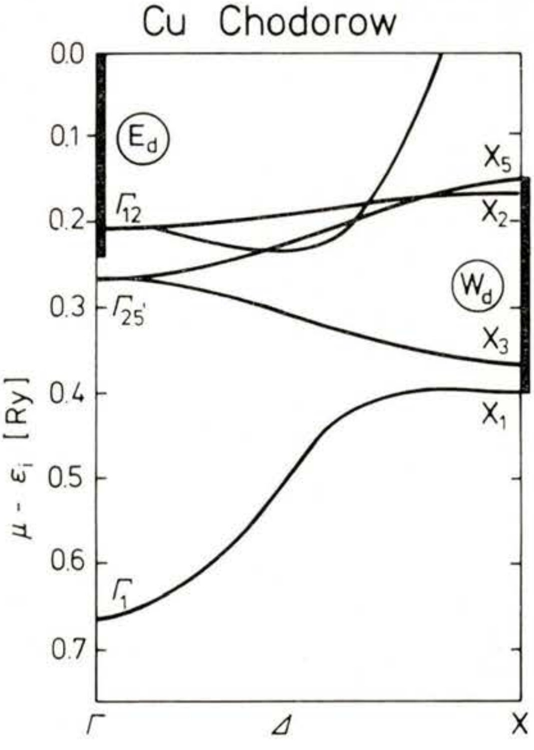

Fig. 7 — Definition of the d-band location, $E_d$, and the d-band width, $W_d$, for the Chodorow [45] band structure of copper.

In spite of their low resolution $\gamma$-ray Compton scattering experiments will continue to yield valuable information on the electronic properties of solids, especially for heavier materials. On the other hand we are convinced that the application of hard X-ray radiation from modern synchrotron radiation facilities will lead to important progress in the field and the community fully appreciates the pioneering work by G. Loupias and her co-workers in Paris [49]. Experiments performed in the laboratory at home will always be attractive and the Konstanz group has built a powerful focussing X-ray Compton spectrometer [50-52]. So far, talking about

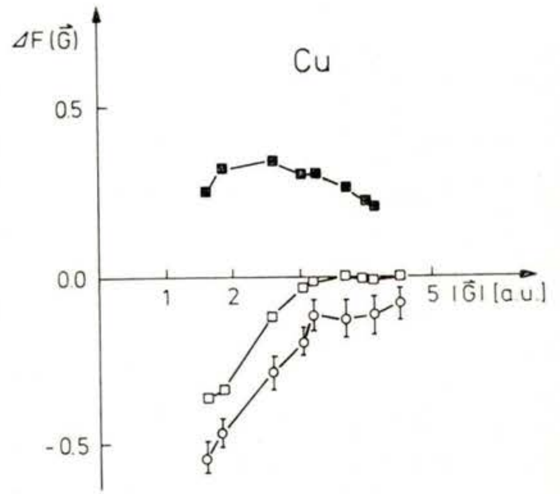

Fig. 8 — Difference between copper solid state and Hartree-Fock free-atom [11] form factors. Open circles: $\gamma$-ray experiment [12], open squares: density-functional LCGO calculation [13], filled squares: APW calculation with self-consistent Slater exchange (Snow (1968), as quoted in [12]).

high resolution Compton scattering experiments we consider a reduction of the thickness of the plane of integration in momentum space, but a lot of information on n(**p**) will always be hidden in the individual Compton profile because of this integration in itself. There is already a tremendous gain in direct information if the integration is only over a line as in 2-dimensional positron annihilation experiments [53]. The best one can think of is the measurements of the scattered photon and the recoil electron in coincidence because then the momentum density n(**p**) is measured directly. In (e,2e) scattering experiments people get there with the additional advantage that they can descriminate between the contributions from the various energy states [1]; however, it seems to be difficult to apply the technique to solids because of the strong interaction of electrons with matter. On the other hand Gao et al. [54] reported recently on (e,2e) measurements of the spectral momentum density of graphite performed on samples 100 Å thick; this is exciting! Taking advantage of the high intensity of hard X-ray beams produced by modern synchrotron radiation facilities one can consider coincidence experiments analog to (e,2e), but now with an incident photon beam, which may be called $(\gamma, e\gamma)$ scattering. At present one cannot dream of the energy resolution of the (e,2e) experiment but applications to solids should be easier. F. Bell performed a feasibility study [55] and first experiments performed with 320 keV $\gamma$-radiation from a 200 Ci Cr-51 radioactive source are under way at the Hahn-Meitner-Institut in Berlin. Even with the appropriate insertion devices at modern storage rings $(\gamma, e\gamma)$ scattering has to be considered as a border line experiment, but it is tempting for various reasons.

## REFERENCES

[1] WILLIAMS, B. G. (ed.): Compton scattering. New York: McGraw-Hill, 1977.

[2] SCHÜLKE, W., Phys. Status Solidi (b), **82**, 229 (1977).

[3] PATTISON, P. and WEYRICH, W., J. Phys. Chem. Solids, **40**, 213 (1979).

[4] SUZUKI, T., KISHIMOTO, T., KAJI, T. and SUZUKI, T., J. Phys. Soc. Japan, **29**, 730 (1970).

[5] NAGASAWA, H., J. de Physique, Colloque (C9), supplément au n° 12, **48**, C9-863 (1987).
NAGASAWA, H., MOURIKIS, S. and SCHÜLKE, W., J. Phys. Soc. Japan, in print.

[6] FEIL, D., Israel J. of Chemistry, **16**, 103 (1977).

[7] SCHÜLKE, W., NAGASAWA, H., MOURIKIS, S. and LANZKI, P., Phys. Rev. B, **33**, 6744 (1986).
SCHÜLKE, W., BONSE, U., NAGASWA, H., MOURIKIS, S. and KAPROLAT, A., Phys. Rev. Lett., **59**, 1361 (1987).

[8] COPPENS, P. (project reporter) et al., Acta Cryst. A, **40**, 184 (1984).

[9] PICKETT, W. E., Comments Solid State Physics, **12**, 1 (1985); ibid., **12**, 57 (1985).

[10] PINDOR, A. J., VOSKO, S. H. and UMRIGAR, C. J., J. Phys. F, **16**, 1207 (1986).

[11] DOYLE, P. A. and TURNER, P. S., Acta Cryst. A, **24**, 390 (1968).

[12] SCHNEIDER, J. R., HANSEN, N. K. and KRETSCHMER, H., Acta Cryst. A, **37**, 711 (1981).

[13] BAGAYOKO, D., LAURENT, D. G., SINGHAL, S. P. and CALLAWAY, J., Phys. Lett. A, **76**, 187 (1980).

[14] MAC DONALD, A. H., DAAMS, J. M., VOSKO, J. H. and KOELLING, D. D., Phys. Rev. B, **25**, 713 (1982); ibid., **26**, 3473 (1982).

[15] ECKARDT, H., FRITSCHE, L. and NOFFKE, J., Phys. F, **14**, 97 (1984).

[16] THIRY, P., CHANDESRIS, D., LECANTE, J., GUILLOT, C., PINCHAUX, R. and PÉTROFF, Y., Phys. Rev. Lett., **43**, 82 (1979).

[17] COURTHS, R., BACHELIER, V., CORD, B. and HÜFNER, S., Solid State Commun., **40**, 1059 (1981).

[18] GRAF, H. A. and SCHNEIDER, J. R., Phys. Rev. B, **34**, 8629 (1986).

[19] ALDRED, P. J. E. and HART, M., Proc. R. Soc. London, Ser. A, **332**, 223 (1973); ibid., **332**, 239 (1973).

[20] TEWORTE, R. and BONSE, U., Phys. Rev. B, **29**, 2102 (1984).

[21] SAKA, T. and KATO, N., Acta Cryst. A, **42**, 469 (1986).

[22] CUMMINGS, S. and HART, M., Proceedings of the «Symposium on Accuracy in Structure Factor Measurements», Warburton, Australia, 23.-26.8.1987.

[23] YIN, M. T. and COHEN, M. L., Phys. Rev. B, **26**, 5668 (1982).

[24] PRICE, P. F., MASLEN, E. N. and MAIR, S. L., Acta Cryst. A, **34**, 183 (1978).

[25] ALKIRE, R. W., YELON, *W*. B. and SCHNEIDER, J. R., Phys. Rev. B, **26**, 3097 (1982).

[26] DEUTSCH, M. and HART, M., Phys. Rev. B, **31**, 3846 (1985).

[27] GRAF, H. A., SCHNEIDER, J. R., FREUND, A. K. and LEHMANN, M. S., Acta Cryst. A, **37**, 863 (1981).

[28] PATTISON, P., HANSEN, N. K. and SCHNEIDER, J. R., Chem. Phys., **59**, 231 (1981).

[29] HANSEN, N. K., PATTISON, P. and SCHNEIDER, J. R., Z. Phys. B, **66**, 305 (1987).

[30] MIJNARENDS, P. E., Phys. Rev. B, **4**, 2820 (1971).

[31] SCHÜLKE, W., Phys. Stat. Sol. (b), **62**, 453 (1974).

[32] DLUBEK, G., BRÜMMER, O. and GERBER, W., Krist. Tech., **13**, 833 (1981).

[33] MUELLER, P. M., Phys. Rev. B, **15**, 3039 (1977).

[34] MIJNARENDS, P. E., Phys. Rev., **160**, 512 (1967).

[35] HANSEN, N. K., Hahn-Meitner-Institut Report, **B342** (1980).

[36] HEUSER-HOFMANN, E. and WEYRICH, W., Z. Naturforsch. **40a**, 99 (1985).

[37] SCHÜLKE, W. and MOURIKIS, S., Acta Cryst. **A42**, 86 (1986).

[38] PATTISON, P., HANSEN, N. K. and SCHNEIDER, J. R., Z. Phys. B, **46**, 285 (1982).

[39] BAUER, G. E. W. and SCHNEIDER, J. R., Z. Phys. B, **54**, 17 (1983).

[40] BAUER, G. E. W. and SCHNEIDER, J. R., J. Phys. Chem. Solids, **45**, 675 (1984).

[41] BAUER, G. E. W. and SCHNEIDER, J. R., Phys. Rev. B, **31**, 681 (1985).

[42] BAUER, G. E. W., Phys. Rev. B, **27**, 5912 (1983).

[43] LAM, L. and PLATZMAN, P. M., Phys. Rev. B, **9**, 5122 (1974).

[44] BROSS, H., J. Phys. F, **12**, 2249 (1982).

[45] CHODOROW, M. I., Ph. D. Thesis 1939 (unpublished).

[46] SNOW, E. C. (1968), as quoted in ref. 12.

[47] ROLLASON, A. J., SCHNEIDER, J. R., LAUNDY, D. S., HOLT, R. S. and COOPER, M. J., J. Phys. F, **17**, 1105 (1987).

[48] ROLLASON, A. J., FELSTEINER, J., BAUER, G. E. W. and SCHNEIDER, J. R., Nucl. Instr. Meth. in Phys. Res. A, **256**, 432 (1987).

[49] LOUPIAS, G., PETIAU, J., ISSOLAH, A. and SCHNEIDER, M., Phys. Stat. Sol. (b), **102**, 79 (1980).

[50] SUORTTI, P., PATTISON, P. and WEYRICH, W., J. Appl. Cryst., **19**, 336 (1986).

[51] SUORTTI, P., PATTISON, P. and WEYRICH, W., J. Appl. Cryst., **19**, 343 (1986).

[52] PATTISON, P., SUORTTI, P. and WEYRICH, W., J. Appl. Cryst., **19**, 353 (1986).

[53] BERKO, S., in «Positron Solid State Physics», Proceedings of the International School of Physics Enrico Fermi, ed., by W. Brandt and A. Dupasquier (North-Holland, Amsterdam, 1983).

[54] GAO, C., RITTER, A. L., DENNINSON, J. R. and HOLZWARTH, N. A. W., Phys. Rev. B, **37**, 3914 (1988).

[55] BELL, F., private communic.

# EXPERIMENTAL METHODS TO OBTAIN NONDIAGONAL TERMS OF THE DENSITY MATRIX

W. SCHÜLKE

Institute of Physics, University of Dortmund, D-4600 Dortmund 50, Fed. Rep. of Germany

*ABSTRACT* — Conventional X-ray diffraction yields information about diagonal elements of the one-particle density matrix in position space. Conventional Compton scattering provides experimental values of diagonal elements of the density matrix in momentum space. It is shown that one can get full knowledge about nondiagonal elements of the density matrix, if one measures the energy distribution of inelastically scattered X-rays under experimental conditions, where the initial photon state is represented by a standing wavefield, provided the distance of its nodal planes is commensurable with the distance of atomic planes of the crystal. An appropriate standing wavefield can be obtained by setting the sample crystal into the Bragg position, where each Bragg reflection corresponding to a reciprocal lattice vector provides information about one nondiagonal term $\Gamma(\mathbf{p}, \mathbf{p} + \mathbf{g})$ of the density matrix in momentum space. Preliminary experimental results confirm the feasibility of such an experiment.

## 1 — INTRODUCTION

There exist two complementary conventional experimental methods which provide information about the spin free one-particle density matrix: X-ray diffraction yields knowledge about the diagonal elements in position space [1], provided the phase problem can be solved; Compton scattering, within the limits of the impulse approximation, measures the diagonal elements in momentum space [2], provided reconstruction methods can be fully exploited. For sure, the knowledge of diagonal elements of the density matrix in one space includes information about nondiagonal terms in the complementary space. But this information is rather limited, since it consists in the respective spatial average over nondiagonal terms [3], as shown in section 2.

In order to get more specific information about nondiagonal terms, one has to look for experiments, where the spatial average over nondiagonal terms is replaced by a more informative method of sampling, for instance a Fourier transform.

It will be shown in section 3 that using a Bloch type photon state to act as the initial state of an inelastic X-ray scattering experiment, one gets information about the spatial Fourier transform of nondiagonal elements of the one-particle density matrix in position space.

In section 4 the experimental realization of the above suggestion is demonstrated, together with preliminary experimental results.

In section 5 a method is described to obtain the desired experimental information about nondiagonal terms also by using less perfect crystals.

## 2 — THE DENSITY MATRIX IN CONVENTIONAL EXPERIMENTS

In a conventional X-ray diffraction experiment, the Bragg diffracted intensity $I(\mathbf{g})$ corresponding to a reciprocal lattice vector $\mathbf{g}$ is proportional to the squared modulus of the form factor $F(\mathbf{g})$:

$$I(\mathbf{g}) \sim |F(\mathbf{g})|^2 \tag{1}$$

where

$$F(\mathbf{g}) = \int \rho(\mathbf{r})\, e^{i\mathbf{g}\cdot\mathbf{r}}\, d\mathbf{r} \tag{2}$$

Provided the phase $\eta(\mathbf{g})$ of $F(\mathbf{g}) = |F(\mathbf{g})|\, e^{i\eta(\mathbf{g})}$ can be determined, one obtains information about the electron density $\rho(\mathbf{r})$, the diagonal terms of the one particle density matrix $\Gamma(\mathbf{r}, \mathbf{r}')$ in position space, by means of Fourier synthesis [1]:

$$\rho(\mathbf{r}) \equiv \Gamma(\mathbf{r}, \mathbf{r}) = \sum_{\mathbf{g}} F(\mathbf{g})\, e^{-i\mathbf{g}\cdot\mathbf{r}} . \tag{3}$$

One can easily show [2] via

$$\begin{aligned} F(\mathbf{g}) &= \int \Gamma(\mathbf{r}, \mathbf{r})\, e^{i\mathbf{g}\cdot\mathbf{r}}\, d\mathbf{r} = \\ &\iiint \Gamma(\mathbf{p}, \mathbf{p}')\, e^{i\mathbf{r}\cdot(\mathbf{p}-\mathbf{p}')}\, d\mathbf{p}\, d\mathbf{p}'\, e^{i\mathbf{g}\cdot\mathbf{r}}\, d\mathbf{r} \\ &= \iint \Gamma(\mathbf{p}, \mathbf{p}')\, \delta(\mathbf{p} - \mathbf{p}' + \mathbf{g})\, d\mathbf{p}\, d\mathbf{p}' = \\ &\int \Gamma(\mathbf{p}, \mathbf{p} + \mathbf{g})\, d\mathbf{p} \end{aligned} \tag{4}$$

that the form factor contains also a limited information about nondiagonal terms of the one particle density matrix in momentum space, $\Gamma(\mathbf{p}, \mathbf{p} + \mathbf{g})$, namely about the momentum space average of the terms.

In a conventional Compton scattering experiment [3], the energy distribution, $I(\omega, \mathbf{q})$, of the inelastically scattered intensity, corresponding to a momentum transfer $\mathbf{q}$ is proportional to the so called Compton profile:

$$I(\omega, \mathbf{q}) \sim \int \rho(\mathbf{p})\, \delta\left(\hbar\omega - \frac{\hbar^2 q^2}{2m} - \frac{\hbar\, \mathbf{p}\cdot\mathbf{q}}{m}\right) d\mathbf{p} , \tag{5}$$

the one dimensional projection of the momentum space density on the direction of momentum transfer. With:

$$p_z \equiv \mathbf{p}\cdot\hat{q} \tag{6}$$

one can write the Compton profile as follows:

$$\begin{aligned} &\int \rho(\mathbf{p})\, \delta\left(\hbar\omega - \frac{\hbar^2 q^2}{2m} - \frac{\hbar\, \mathbf{p}\cdot\mathbf{q}}{m}\right) d\mathbf{p} = \\ &\iint \rho(\mathbf{p})\, dp_x\, dp_y \equiv J(p_z) \end{aligned} \tag{7}$$

where

$$p_z = \frac{m\omega}{q} - \frac{\hbar q}{2} . \tag{8}$$

Then the one-dimensional Fourier transform $B(\mathbf{r})$ of Compton profiles, the so called reciprocal form factor, turns out to be the three dimensional Fourier transform of the momentum space density [4]:

$$\begin{aligned} B(\mathbf{r}) &\equiv \int J(p_z)\, e^{ip_z r}\, dp_z = \\ &\int \rho(\mathbf{p})\, e^{i\mathbf{p}\cdot\mathbf{r}} d\mathbf{p} ;\ \mathbf{r} \,//\, \mathbf{q} , \end{aligned} \tag{9}$$

so that one can obtain

$$\rho(\mathbf{p}) \equiv \Gamma(\mathbf{p}, \mathbf{p}),$$

the diagonal terms of the one particle density matrix $\Gamma(\mathbf{p}, \mathbf{p}')$ in momentum space, by Fourier synthesis of reciprocal form factors measured for a large number of directions of $\mathbf{q}$ [5].

One can easily show, that in analogy to equation (4),

$$B(\mathbf{r}) = \int \Gamma(\mathbf{r}', \mathbf{r}' + \mathbf{r})\, d\mathbf{r}'. \qquad (10)$$

This means, that the reciprocal form factor contains also a limited information about nondiagonal terms of the one particle density matrix in position space, $\Gamma(\mathbf{r}, \mathbf{r}')$, namely about the position space average of the nondiagonal terms.

Therefore, one can conclude that conventional experimental methods do not provide information about the *full one particle density matrix* either in position or in momentum space.

Experimental methods are needed which enable measurements of the full one-particle matrix in one space. The full matrix in the complementary space can then be obtained by means of Dirac-Fourier transform [6].

## 3 — PROPOSED EXPERIMENT TO OBTAIN NONDIAGONAL TERMS OF THE ONE-PARTICLE DENSITY MATRIX IN MOMENTUM SPACE

In the case of conventional Compton scattering experiments, the initial photon state can be represented as a propagating plane wave. Therefore, each point in position space is *equally* excited. This is the physical reason for the fact that conventional Compton scattering only provides information about *position space averages* of the nondiagonal terms of the density matrix, as shown in equation (10).

In order to go beyond position space averages one has to *sample* the position space, when measuring Compton profiles, for instance by weighing certain positions within the elementary cell. A realistic way to do this is to use an initial photon state, which is represented by a standing wave with a spatial periodicity of nodal planes, commensurable with the lattice periodicity. The spatial intensity distribution of such a photon field

$$I(\mathbf{r}) = A^2 + B^2 + 2AB \cos(\mathbf{g} \cdot \mathbf{r} + \Delta\varphi) \qquad (11)$$

where $\mathbf{g}$ is a reciprocal lattice vector, would guarantee the commensurability with the lattice, the phase $\Delta\varphi$ would define the relative position of nodal planes with respect to the atomic planes of the lattice.

It will be shown in section 4 that a photon field of this kind is excited in a crystal, if the Bragg condition for a reciprocal lattice point $\mathbf{g}$ is satisfied, where $\Delta\varphi$ can be varied by changing the direction of the incident beam.

It has been shown [7, 8, 9] in terms of quantum electrodynamics that one really will obtain the desired information about nondiagonal terms of the density matrix. Here we will use a more intuitive derivation, which comes to the same result as in [7, 8, 9]:

First we write the Compton profile of equation (9) in terms of the position space density matrix:

$$J(p_z) = \iint \Gamma(\mathbf{p}, \mathbf{p})\, dp_x\, dp_y$$
$$= \iiiint \Gamma(\mathbf{r}, \mathbf{r}')\, e^{i\mathbf{p}\cdot(\mathbf{r}-\mathbf{r}')}\, d\mathbf{r}\, d\mathbf{r}'\, dp_x\, dp_y \qquad (12)$$

If we are measuring a Compton profile by using the photon field of equation (11) as initial photon state, the $\mathbf{r}$ integration in equation (12) has to be performed by taking into account a $\mathbf{r}$-dependent weight, given by the intensity distribution of the initial photon field as shown in equation (11):

$$J(p_z, \mathbf{g}, \Delta\varphi) \equiv [1/(A^2 + B^2)] \iiiint \Gamma(\mathbf{r}, \mathbf{r}')\, e^{i\mathbf{p}\cdot(\mathbf{r}-\mathbf{r}')} (A^2 + B^2 + 2AB \cos(\mathbf{g}\cdot\mathbf{r} + \Delta\varphi)\,.\,d\mathbf{r}\, d\mathbf{r}'\, dp_x\, dp_y \tag{13}$$

Writing equation (13) we have assumed that the plane wave components with amplitudes A and B, which build up the standing wave field, both transfer momenta **q** to the lattice, that are equivalent with respect to the symmetry of the crystalline scattering sample.

Assuming furthermore that one can realize two experimental situations 1 and 2 with $A_1 = A_2$; $B_1 = B_2$; $\Delta\varphi_1 = 0$, $\Delta\varphi_2 = \pi$, then the difference of the two Compton profiles reads as follows:

$$\Delta J \equiv J(p_z, \mathbf{g}, 0) - J(p_z, \mathbf{g}, \pi) = [2AB/(A^2 + B^2)] \iiiint \Gamma(\mathbf{r}, \mathbf{r}')\, e^{i\mathbf{p}\cdot(\mathbf{r}-\mathbf{r}')} (e^{i\mathbf{g}\cdot\mathbf{r}} + e^{-i\mathbf{g}\cdot\mathbf{r}})\, d\mathbf{r}\, d\mathbf{r}'\, dp_x\, dp_y = [2AB/(A^2 + B^2)]\, \mathrm{Re} \iint \Gamma(\mathbf{p} + \mathbf{g}, \mathbf{p})\, dp_x\, dp_y\,. \tag{14}$$

The desired information about nondiagonal terms of the density matrix is comprised in the so called nondiagonal Compton profile:

$$J(p_z ; \mathbf{g}) \equiv \int \Gamma(\mathbf{p} + \mathbf{g}, \mathbf{p})\, dp_x\, dp_y \tag{15}$$

of equation (14).

In order to demonstrate the surplus of information about density matrices, one can calculate the 1D-Fourier transform, $B(\mathbf{t}, \mathbf{g})$ of $\Delta J$:

$$B(\mathbf{t}, \mathbf{g}) \equiv \int \Delta J e^{ip_z t}\, dp_z = [4AB/(A^2 + B^2)] \int \Gamma(\mathbf{r}, \mathbf{r} + \mathbf{t}) \cos(\mathbf{g}\cdot\mathbf{r})\, d\mathbf{r};\ \mathbf{t} \,//\, \mathbf{q}\,. \tag{16}$$

By comparing equation (16) with equation (10), the increase in information becomes evident.

Conventional Compton scattering yields only position space averages of nondiagonal terms of the one-particle density matrix in position space, whereas Compton scattering of photons from standing wave fields, the so called coherent Compton scattering [10], provides spatial Fourier transforms of nondiagonal terms, making feasible the measurement of complete nondiagonal terms of the one-particle density matrix by Fourier synthesis.

Under the conditions of coherent Compton scattering (the initial photon state is a standing wave field) the measured Compton profile $J(p_z, \mathbf{g}\ \Delta\varphi)$ for a given relative phase $\Delta\varphi$ is composed of diagonal and nondiagonal Compton profiles, where their contributions depend on A, B and $\Delta\varphi$. From equation (13) one obtains:

$$J(p_z, \mathbf{g}, \Delta\varphi) = [1/(A^2 + B^2] \{(A^2 + B^2)\ J(p_z) + 2AB \cos\Delta\varphi\, \mathrm{Re}\, J(p_z, \mathbf{g}) - 2AB \sin\Delta\varphi\, \mathrm{Im}\, J(p_z, \mathbf{g})\}. \tag{17}$$

## 4 — REALIZATION OF THE PROPOSED EXPERIMENT

The proposed experiment has been realized for the first time in 1981 independently by Golovchenkov et al. [10] and Schülke et al. [8, 9]. Both groups have utilized the standing wave field which is built up by the coherent superposition of the incident and the Bragg diffracted wave in the Bragg case of diffraction according to the two beam approximation of the dynamical theory of X-ray diffraction [11]. Both the amplitude ratio A/B and the phase $\Delta\varphi$ are functions of the angle of incidence assuming a plane wave incident beam, where $\Delta\varphi$ changes from 0 to $\pi$, when going from one side of the total Bragg reflection range to the other. As a consequence of this phase shift the position of the antinodes of the standing wave field is moving from the atomic planes into their interstices as shown in Fig. 1.

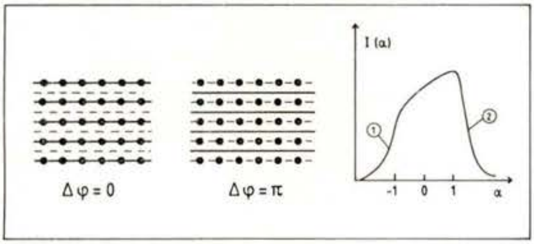

Fig. 1

*a*) Relative position of the antinodes (solid lines) and nodes (broken lines) of a standing wave field with respect to atomic planes (dots) for the two extreme values of the relative phase $\Delta\varphi$.

*b*) Sketch of the corresponding rocking curve. Position 1 corresponds to $\Delta\varphi = o$; position 2 corresponds to $\Delta\varphi = \pi$ ; $\alpha$ in units of half of the Darwin width.

The angle of incidence has been controlled by means of a nondispersive double crystal setting with a highly asymmetrically cut first crystal and the second crystal acting as the scattering sample (see Fig. 2). The so called rocking-curve of this special double crystal setting, this means the Bragg diffracted intensity $I(\alpha)$ of the second crystal (measured by means of detector 1) as a function of its angular position $\alpha$ relative to the first crystal, is very similar to the intrinsic reflection curve, as deduced for the plane incident wave case [12]. Therefore, the amplitude ratio A/B and the phase $\Delta\varphi$ can be deduced from this rocking curve as decribed in more detail in ref. [9] (see Fig. 1). The beam of photons inelastically scattered from the standing wave field within the second (sample) crystal is energy analyzed by means of a solid state detector (D2 in Fig. 2). In ref. [9] the direction of the scattered beam is chosen in such a manner that the scattering angles for the incident and the Bragg diffracted beam are identical and that furthermore the corresponding vectors **q** of momentum transfer are crystal symmetry equivalent.

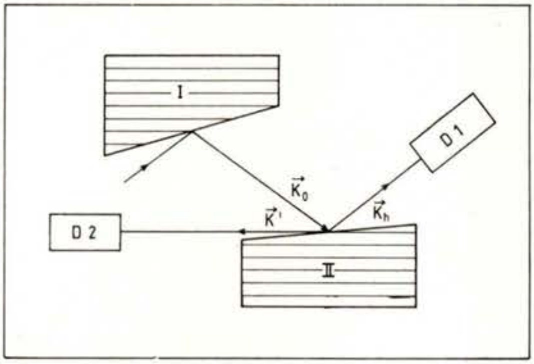

Fig. 2 — Schmatic of an experimental set-up for coherent Compton scattering: Crystal I is highly asymmetrically cut, crystal II is the sample crystal. $\mathbf{K}_o$ is the incident beam, $\mathbf{K}_h$ is the Bragg diffrac- $\mathbf{K}'$ is the inelastically scattered beam. Detector 1 measures the diffracted intensity, Detector 2 is a Ge solid state detector (energy analyzing system).

Fig. 3, shows two experimental Compton profiles of Si for two different positions on the (220)-rocking curve (MoK$\alpha$-radiation) corresponding nearly to $\Delta\varphi = o$ and

$\Delta\varphi = \pi$ respectively. The momentum space resolution of this preliminary experiment was rather poor, roughly 1.5 a. u., because of the low energy recolution of the Ge solid state deterctor for MoK$\alpha$-radiation. Nevertheless a decomposition of diagonal ($J(p_z)$) and nondiagonal Compton profiles ($J(p_z, \mathbf{g})$) could be performed according to equation (17). The result is shown for the valence electrons in Fig. 4 for $\mathbf{g} = (2\pi/a)\,(1, 1, 1)$. A crucial test for the reliability of the decomposition procedure results from the sum rule [2]:

$$\int J(p_z, \mathbf{g})\, dp_z = \int \Gamma(\mathbf{p}, \mathbf{p} + \mathbf{g})\, d\mathbf{p} = F(\mathbf{g}) \qquad (18)$$

where $F(\mathbf{g})$ is the X-ray form factor (see equation (4)).

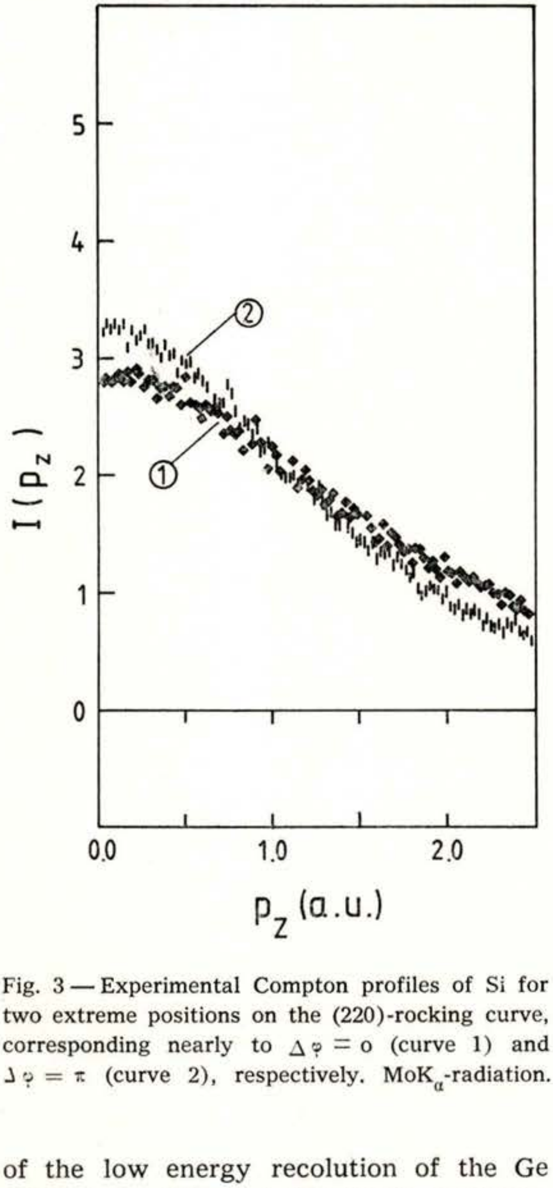

Fig. 3 — Experimental Compton profiles of Si for two extreme positions on the (220)-rocking curve, corresponding nearly to $\Delta\varphi = o$ (curve 1) and $\Delta\varphi = \pi$ (curve 2), respectively. MoK$_\alpha$-radiation.

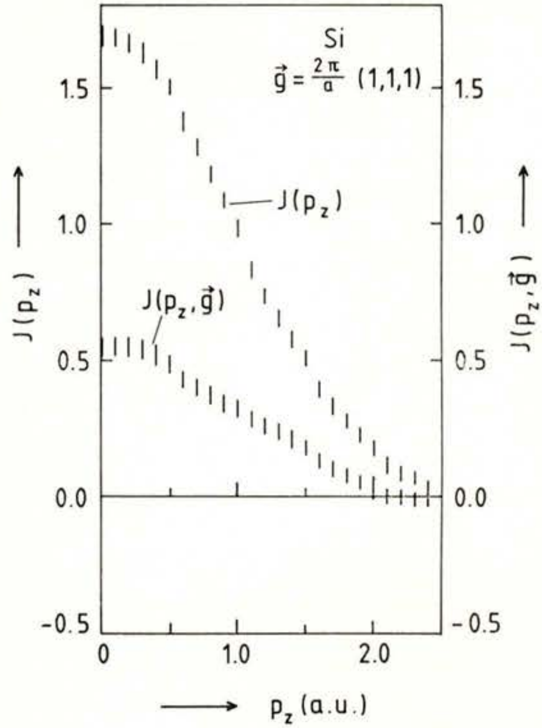

Fig. 4 — Experimental valence electron part of the diagonal Compton profile $J(p_z)$ and the nondiagonal Compton profile $J(p_z, \mathbf{g})$ for $\mathbf{g} = (2\ \ /a)\,(1,1,1)$.

## 5 — PROCEDURE FOR LESS PERFECT CRYSTALS

It was assumed in section 4 that the amplitudes A and B as well as the relative phase $\Delta\varphi$ of the two plane wave components of the wave field could be read directly from the rocking curve position. This is possible only with nearly perfect crystals. For less perfect crystals, where the mosaic spread is comparable or even somewhat larger than the **g**-dependent Darwin-width, another procedure seems feasible. Utilizing the unique properties of synchrotron radiation it should always be possiible to produce a well collimated X-ray beam by means of Bragg diffraction on a nearly perfect monochomator crystal with an interplanar spacing $d_M$ very near to $d_s$, the interplanar spacing corresponding to the desired **g** of the less perfect sample crystal. Combining the monochomator crystal with the sample crystal in a weak dispersive set-up the effective collimation of the beam hitting the sample crystal could be made comparable with its Darwin width and mosaic sprear, respectively. Therefore, one can be sure that the effective phase $\Delta\varphi$ is different on the opposite sides of the rocking curve.

Based on this assumption, one has to measure the intensity distribution $I(p_z)$ at least for three different positions on the rocking curve, where one measurement (number 1 in equations (19)) should be far outside the Bragg condition and number 2 and 3 on opposite sides of the rocking curve. Following equation (17) one can write down the following system of linear equations, three at a time for each sampling point $p_z$:

$$\begin{aligned} I_1(p_z) &= a\,J(p_z) \\ I_2(p_z) &= b\,J(p_z) + c\,\mathrm{Re}\,J(p_z, \mathbf{g}) + \\ &\quad + d\,\mathrm{Im}\,J(p_z, \mathbf{g}) \\ I_3(p_z) &= e\,J(p_z) + f\,\mathrm{Re}\,J(p_z, \mathbf{g}) + \\ &\quad + h\,\mathrm{Im}\,J(p_z, \mathbf{g}). \end{aligned} \tag{19}$$

Equations (19) can be considered as a system of linear equations for determining the unknown coefficients a to h, if one inserts the well known values both of $J(p_z)$ and $J(p_z, \mathbf{g})$ of the free atomic cores for $p_z > p_{zc}$, where for $p_z > p_{zc}$ practiically only the atomic cores contribute to $I(p_z)$.

If the coefficients a to h have been determined, one can calculate the *three* quantities $J(p_z)$, Re $J(p_z, \mathbf{g}$ and Im $J(p_z, \mathbf{g})$ for each sampling point $p_z$ from the respective three equations (19).

## 6 — CONCLUSIONS

It has been demonstrated that it is feasible to get *direct experimental information about nondiagonal elements* of the one-particle density matrix, not only for nearly perfect crystals but also for less perfect ones. This direct experimental information can be used as a crucial test of the reliability of methods put forward at this workshop, which claim to reconstruct the complete density matrix from conventional experimental data of diagonal elements both in position and momentum space.

This work has been funded by the German Federal Minister of Research and Technology under Contract No. 05 334 AX B2.

## REFERENCES

[1] see for a review Schneider J. R., Fortschr. Miner. **61**, 85 (1983) and references given therein.

[2] BENESCH, R., SNIGH, S. R. and SMITH, V. H. Jr., Chem. Phys. Lett. **10**, 151 (1971).

[3] see for a review Cooper, M. J., Rep. Prog. Phys. **48**, 415 (1985) and references given therein.

[4] PATTISON, P., WEYRICH, W., and WILLIAMS, B. G., Solid State Commun. **21**, 967 (1977). SCHÜLKE, W., Phys. Stat. Sol. (b), **82**, 229 (1977).

[5] HANSEN, N. K., Reconstruction of EMD from a set or difectional Compton profiles, Hahn-Meitner-Institut, Berlin, Rep. HMI B 342 (1980).

[6] SMITH, V. J. Jr. in «Electron and Magnetization Densities in Molecules and Crystals» ed. P. Becker, New York, Plenum press, p. 3-25.

[7] SCHÜLKE, W., Phys. Lett. **A83a**, 451 (1981).

[8] SCHÜLKE, W., BONSE, U. and MOURIKIS, S., Phys. Rev. Lett. **47**, 1209 (1981).

[9] SCHÜLKE, W. and MOURIKIS, S., Acta Cryst. **A42**, 86 (1986).

[10] GOLOVCHENKO, J. A., KAPLAN, D. R., KINCAID, B., LEVESQUE, R., MEIXNER, A., ROBBINGS, M. P., and FELSTEINER, J., Phys. Rev. Lett. **46**, 1454 (1981).

[11] LAUE, M. V., «Rontgenstrahlinterferenzen», Frankfurt/Main, 1960, Akademische Verlagsgesellschaft.

[12] RENNINGER, M., Z. Naturforsch. **16a**, 1110 (1961).

# ZEROTH ORDER DENSITY MATRICES OF MOLECULES FROM UNIQUELY DEFINED ATOMIC GROUND STATES

W. H. E. SCHWARZ

Theoretische Chemie, Universität, POB 101240, D-5900 Siegen-West Germany

*(Received — September, 1988)*

*ABSTRACT* — The zeroth-order approximation to the molecular density operator is defined as the superposition of the density operators of the noninteracting atoms. The positions and orientations of the ground states of the free atoms «in the molecule» are uniquely determined by minimizing the norm of the corresponding one-electron difference density.

## 1 — INTRODUCTION

The basis of scientific chemistry since Dalton [1] is the concept that matter consists of atoms. In quantum mechanics parts of matter, for instance atoms or molecules, are described by density operators [2]

$$\hat{D} = \sum_{i,\,j}^{\infty} | \psi_i > D_{ij} < \psi_i | \, . \qquad (1)$$

$\psi_i$ are orthonormalized many-electron-nuclear wavefunctions [3]. A wavefunction is only suitable to describe pure states, which do not interact with any surrounding, e. g. the background radiation, nor even matrix $D$ with eigenvalues $D_k$. The mon-the elements of the many-particle density matrix $D$ with eigenvalues $D_k$. The non-idempotent matrix $D$ must fulfill the three conditions:

$$D = D^{+}, \quad \mathrm{tr}(D) = 1, \quad 0 \leq D_k \leq 1 \qquad (2)$$

The electronic ground states of most atoms are degenerate or quasi-degenerate (e. g. $C(p^2)\,^3P$ or $O(p^4)\,^3P$, which are spanned by three equivalent nonspherical states $P_x$, $P_y$, $P_z$). Therefore, free atoms under realistic conditions, e. g. in a physical vacuum with 3K-radiation, are to be described by a density operator from a few ground state functions $\psi_i$, $i = 1, \ldots, N$. Free atoms are characterized by having no specified nuclear position nor specified electronic $D_{ij}$-parameters. The $D_{ij}$ describe the population, orientation and shape of the degenerate open valence shells of the atomic ground state.

The zeroth-order approximation of a molecule is the superposition of free atoms, between which the interactions have been switched off artificially, but where the nuclear and electronic distributions have been specified. In X-ray crystallography it is customary to specify the «positional parameters» (mean position $\mathbf{r}$, vibrational amplitude tensor $\beta$) so that the nuclei (or atomic cores) coincide optimally with the molecule, while the «orientational parameters» $D_{ij}$ are left un-specified [5]. Since atoms are extended objects, which have core and valence shells, it seems more consistent to specify both the «core positional parameters» and the «valence shell orientational parameters» of the atomic ground states in the promolecule.

## 2 — APPROXIMATE DENSITY MATRIX FROM THE MOLECULAR ELECTRON DENSITY

Integrating the n-particle density operator $\hat{D}$ over all but one coordinate, one obtains the one-density operator $\hat{\rho}$ [5]:

$$(\mathbf{x}_1 ; \mathbf{y}_1) = \int \hat{D}(\mathbf{x}_1 , \mathbf{x}_2 ,.. , \mathbf{x}_n ; \mathbf{y}_1 , \mathbf{y}_2 ,.. , \mathbf{y}_r) \times \times \delta(\mathbf{x}_2 - \mathbf{y}_2)\, d\mathbf{x}_2\, d\mathbf{y}_2 \ldots \delta(\mathbf{x}_n - \mathbf{y}_n)\, d\mathbf{x}_n\, d\mathbf{y}_n \tag{3}$$

which can be represented in terms of orbitals $\varphi_i$ as

$$\hat{\rho} = \sum_{i,j}^{\infty} | \varphi_i > d_{ij} < \varphi_j | \, . \tag{4}$$

The one-matrix elements $d_{ij}$ depend linearly on the $D_{ij}$ yielding restrictions similar to those of eq. (2) [6]. We note that neither $D_{ij}$ nor $d_{ij}$ are idempotent.

If the molecular density $\rho^M(\mathbf{x}) = \hat{\rho}^M(\mathbf{x}; \mathbf{x})$ is known, we can determine a zeroth-order one-density operator of the molecule

$$\hat{\rho}_0^M (\mathbf{x}; \mathbf{y}) = \sum_{A}^{\text{atoms}} \hat{\rho}^A (\mathbf{x}; \mathbf{y}) \tag{5}$$

by minimizing the norm of the difference density $\Delta \rho$ :

$$\text{Diff} = \| \Delta \rho (\mathbf{x}; \mathbf{r}, \beta, d) \| = = \| \rho^M ((\mathbf{x}) - \hat{\rho}_0^M (\mathbf{x}; \mathbf{x}) \| = \text{Min}_{\mathbf{r},\, \beta,\, d} \tag{6}$$

in a least squares sense with respect to both the *positions* **r** (and the vibrational both the *positions* **r** of the $\varphi_i$ (and the vibrational parameters $\beta_{ij}$) and the *orienta-* the $\hat{\rho}^A$ on the rhs. of eq. (5). The corresponding algorithm is described in Ref. [6]. (We note that the Pauli principle may impose additional restrictions on the $d_{ij}$ if $\varphi_i$, $\varphi_k$ with same spin from different atoms overlap. These latter restrictions are easily accounted for if one uses orthogonalized atomic spin-orbitals instead of the original $\varphi_i$.) This recipe to determine an approximate one-density matrix *d* has two advantages, concerning energies and densities.

According to the virial theorem, the kinetic energy T of a bound state is higher than that of the separated atoms. While some other approximate methods may produce density operators which yield drastically reduced T [7], the present method (eqs. 5, 6) yields at least unchanged T (or slightly increased T in the case of overlapping occupied shells). Furthermore, Spackman and Maslen have shown [8] that the classical electrostatic interaction energies of the atoms are of the same order of magnitude as the bond energies.

## 3 — DIFFERENT DIFFERENCE DENSITIES FOR DIFFERENT PURPOSES

If one is interested in the field *around* a molecule, or above the surface of a crystal, an appropriate procedure is to determine the «conventional difference density», which is defined with respect to the density of the spherically averaged free atoms superimposed at the optimized positions [5]. Spherically averaged neutral atoms do not contribute to the electric field at the outside of the system, so that the «conventional difference density» is the *minimal* charge distribution, which fully determines the field in the surrounding, and is uniquely defined thereby.

If one is interested in chemical bonding effects *inside* the molecule, another kind of difference density is more appropriate. For this purpose, we have defined the «chemical deformation density» [6] according to eqs. (5, 6) with respect to free atoms, which are positioned *and* oriented optimally in the molecule. The chemical deformation density is the *minimal* difference distribution between the molecule and its constituent free atoms, and is uniquely defined thereby.

Both the positional parameters and the orientational parameters describe quantitatively, how the free atoms have to be constrained in order to be optimally prepared for bond formation. The resulting chemical deformation density indicates the formation of covalencies and the «existence» of lone pair dipoles. These features are no longer covered by the much larger quadrupolar distributions of the free degenerate atoms [9], as is often the case in the conventional difference densities [10].

## REFERENCES

[1] DALTON, J. — A New System of Chemical Philosophy, Part I. London, 1808.

[2] ZIMAN, J. M. — Elements of Advanced Quantum Theory, Chp. 4. Cambridge University Press, 1969.
COHEN-TANNOUDJI, C., DIU, B., LALOE, F. — Quantum Mechanics, Chp. $E_{III}$ Hermann — Paris and John Wiley — New York, 1977.

[3] The Born-Oppenheimer approximation is assumed in order to introduce the classical concept of molecular structure [4].

[4] PRIMAS, H. — Chemistry, Quantum Mechanics and Reductionism, 2nd Ed. Chp. 6.4. Berlin, Springer, 1983.

[5] HIRSHFELD, F. L. — in Electron and Magnetization Densities in Molecules and Crystals, Ed. Becker P., p. 47. New York and London, Plenum, 1980.
SMITH, V. H. — in Electron and Magnetization Densities in Molecules and Crystals, Ed. Becker P., p. 3. New York and London, Plenum, 1980.

[6] SCHWARZ, W. H. E., RUEDENBERG, K., MENSCHING, L. — J. Am. Chem. Soc. **111**, 6926, 1989. RUEDENBERG, K., SCHWARZ, W. H. E. — J. Chem. Phys. **92**, 4956, 1990.

[7] MASSA, L., GOLDBERG, M., FRISHBERG, C., BOEHME, R. F., LA PLACA, S. J. — Phys. Rev. Lett. **55**, 622, 1985. Instead of a T-increase of about +0.1 a. u., a decrease of nearly −1 a. u. was obtained.

[8] SPACKMAN, M. A., MASLEN, E. N. — J. Phys. Chem. **90**, 2020, 1986.

[9] MENSCHING, L., VONNIESSEN, W., VALTAZANOS, P., RUEDENBERG, K., SCHWARZ, W. H. E. — J. Am. Chem. Soc. **111**, 6933, 1989.

[10] DUNITZ, J. D., SEILER, P. — J. Am. Chem. Soc. **105**, 7056, 1983.

# STATE-DEPENDENT CORRELATION EFFECTS ON THE COMPTON PROFILES OF THE TRANSITION METALS

SHINYA WAKOH, MAKOTO MATSUMOTO and FUYUE YOSHIMURA
University of Library and Information Science, Tsukuba 305, Japan

So far electron correlation effects on the Compton profiles have been estimated by a local density approximation proposed by Bauer and Schneider [1]. Their definition of the correlation effects is as follows:

$$\Delta J(q) = \int_{\text{unit cell}} \Delta J(q, \rho(\mathbf{r}))\ dr$$

where $\Delta J(q, \rho(\mathbf{r}))$ is a correlation effect due to the electron gas system whose density is $\rho$. In this approximation the density of all core electrons is included in the $\rho$ used.

In SAGAMORE IX we [2] propose another approach to estimate the electron correlation effect by empirical fit to the difference between theory and experiment. The definition is as follows:

$$\Delta J(q) = -\int_{\Gamma_1}^{E_f} (1 - n(E)) \times J(q, E)\ dE + \\ + \int_{E_f}^{\infty} n(E) \times J(q, E)\ dE$$

where n(E) is an occupation number, i. e. Migdal function, and J(q, E) is a partial Compton profile due to the states whose energies are at E. In this approximation the contribution from the core electrons is totally negrected. In the case of vanadium and chromium, whose Fermi energies are located at the middle of the d-bands, this approximation has given very good results [2].

On the other hand, however, when we use the similar Migdal functions also in the case of copper and nickel whose Fermi levels are located closed to the top of the d-bands, we can not obtain such good results as in the case of vanadium and chromium. The reason is understood by the following explanation. In the free electron system, i. e. s-p band, the momentum of the higher energy state is larger than that of the lower energy state. It is also the case with d-band electrons. Therefore, in the case of vanadium and chromium, the correlation effect due to the Migdal functions moves some amount of momentum density from the lower momentum region to the higher one, and we can make a good agreement between theory and experiment. In the case of copper and nickel the similar Migdal function shifts some amount of occupation in the d-bands to the higher s-p bands. It moves momentum density from the higher region to the lower. In figure 1, the experimental correlation profile for copper whose experiment has been measured by Rollason et al. [3] is shown by a dotted line, together with a theoretical one (a solid

*Portgal. Phys.* — Vol. 19, fasc. 3-4, pp. 433-439, 1988

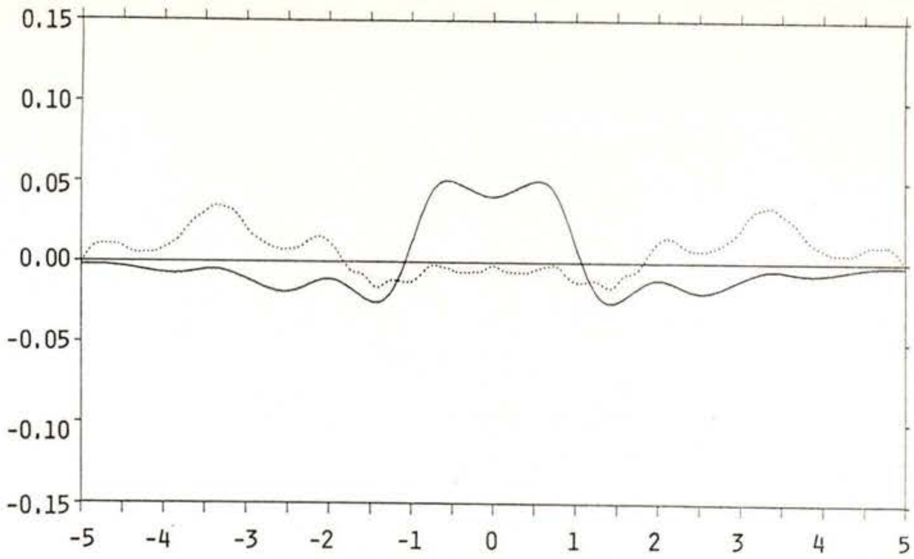

Fig. 1 — Theoretical and experimental correlation profiles along < 110 > direction for copper. The experimental curve (dotted line) is the difference between the experimental Compton profile by Rollason et al. [3] and the theoretical one obtained by the one-electron band theoretical calculation. The theoretical curve (solid line) is only correlation correction part of the Compton profiles which are estimated using the Migdal function shown in figure 2 and real band theoretical energy dependent partial Compton profiles $J_k(q, E)$ for < 110 > scattering direction.

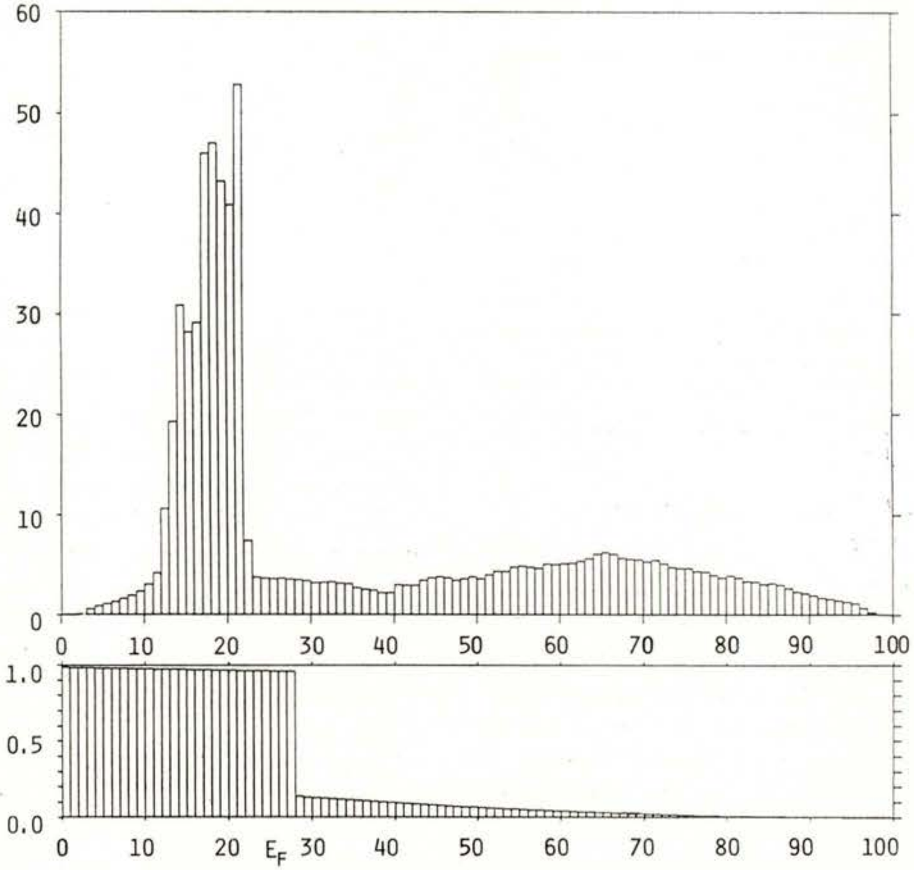

Fig. 2 — Density-of-states curve N(E) (on the top) and Migdal function n(E) (on the bottom) for copper.

line) obtained by using a Migdal function defined by similar parameters to those used for vanadium and chromium. The Migdal function and density-of-states histogram for copper are shown in figure 2.

In figure 3, the experimental and theoretical correlation correction profiles for ferromagnetic iron are shown for the three major orientations. The experiment was carried out by Rollason et al. [4]. The

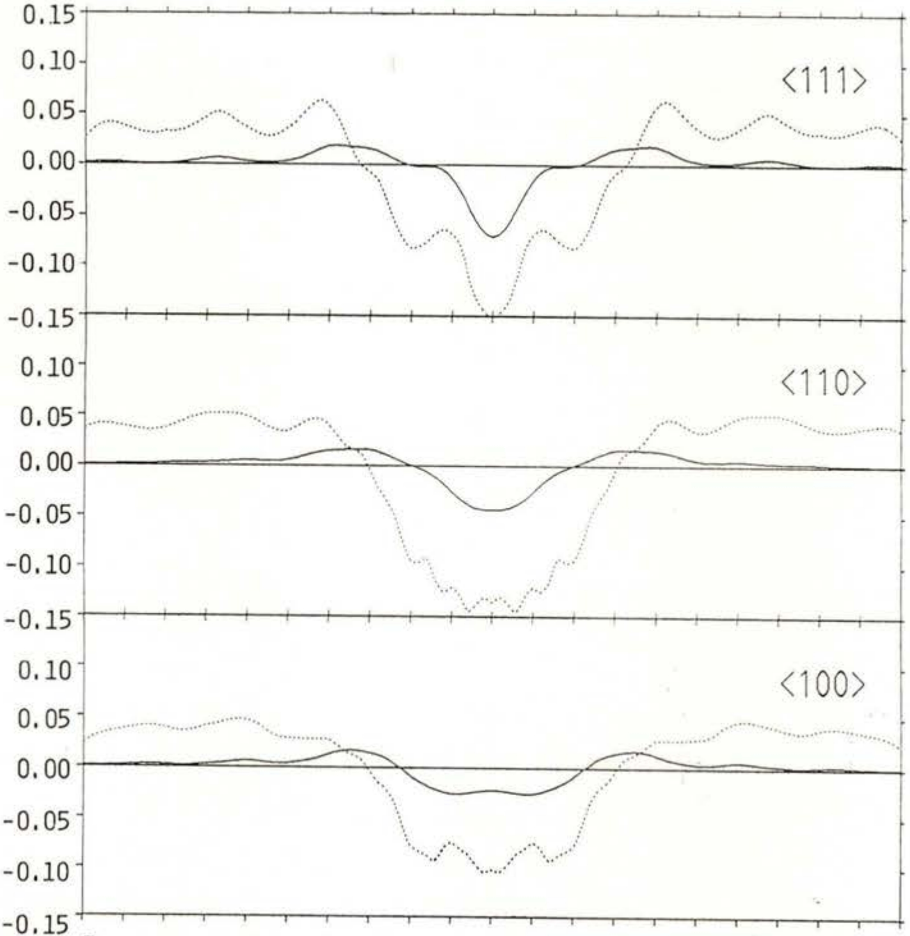

Fig. 3 — Theoretical and experimental correlation profiles along < 100 >, < 110 > and < 111 > directions for ferromagnetic iron. The experimental curves (dotted lines) are the difference between the experimental Compton profiles by Rollason et al. [4] and the theoretical ones obtained by the one-electron band theoretical calculation. The theoretical curves (solid lines) are only correlation correction part of the Compton profiles which are estimated using the Migdal functions shown in figure 4 and real band theoretical energy dependent partial Compton profiles $J_k(q, E)$ for < 100 >, < 110 > and < 111 > scattering directions for both spin-bands.

theoretical curves are determined by using two Migdal functions for the minority spin-bands shown in figure 4(a) and the majority spin-bands figure 4(b). The agreement between theory and experiment is not so good again.

In order to obtain better agreement state dependent Migdal functions are introduced. For the minority bands a similar Migdal function to those for vanadium and chromium is used, because the Fermi level of the minority bands is located at the middle of the d-bands. The Migdal function is shown in figure 5(a) and shows that the correlation effect among the minority spin d-electron is fairly strong and the Migdal discontinuity is reduced very much. On the other hand, the Migdal function for the majority band shown in figure 5(b) is state-dependent. As the majority d-bands are almost full, the correlation effect among the majority d-electrons may not be as strong as that of the minority d-electrons. Although there may be any other better choice of Migdal functions, when these Migdal functions are used the

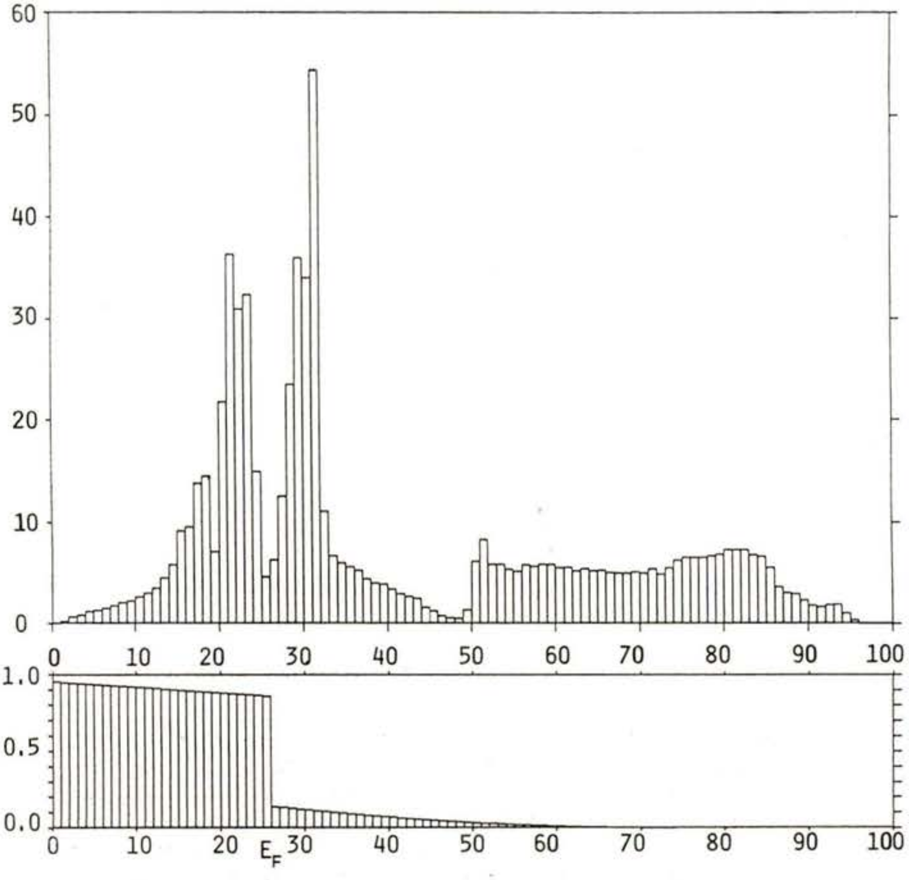

Fig. 4a — Density-of-states curve N(E) (on the top) and Migdal function n(E) (on the bottom) for minority spin-bands.

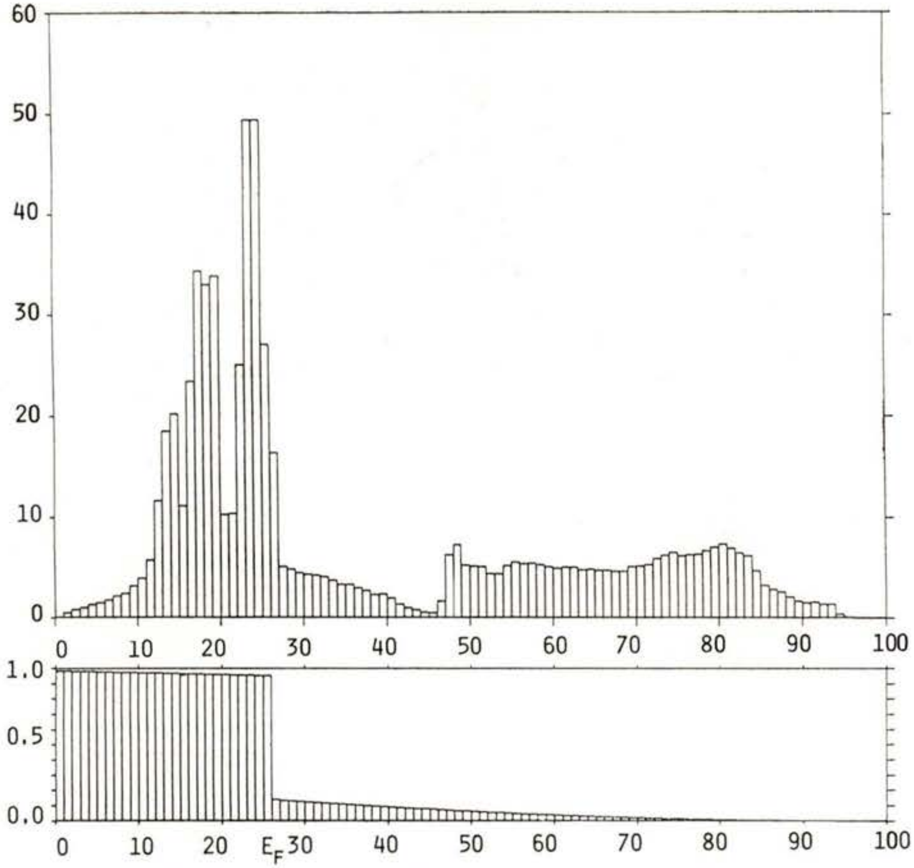

Fig. 4b — Density of states curve N(E) and Migdal function n(E) (on the bottom) for majority spin bands.

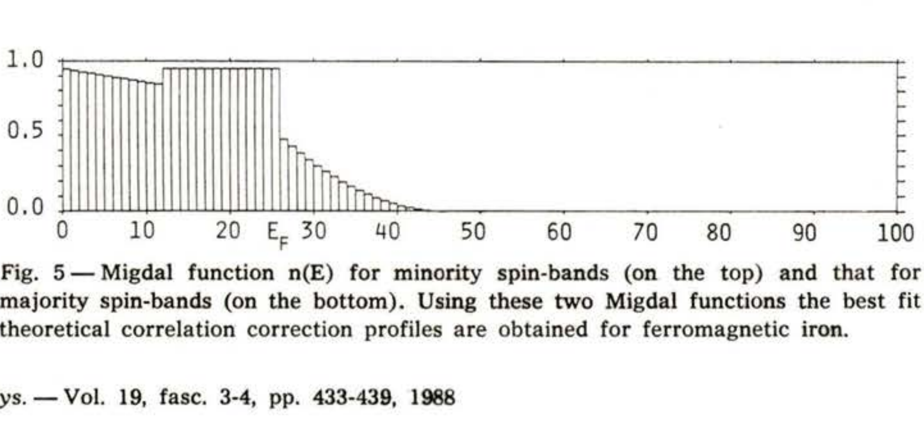

Fig. 5 — Migdal function n(E) for minority spin-bands (on the top) and that for majority spin-bands (on the bottom). Using these two Migdal functions the best fit theoretical correlation correction profiles are obtained for ferromagnetic iron.

agreement between theoretical correlation correction profiles and the experimental ones is fairly improved as shown in figure 6. On ferromagnetic iron we have obtained a fairly good result, but there should be many arguments about its physical explanation.

In order to obtain more conclusive results, we need more experiments on copper other than $< 110 >$ direction. When we can use more reliable magnetic Compton profiles on iron and nickel, we can estimate the correlation effects spin-dependently and obtain more reliable estimations on the correlation effects.

In this paper we used state-dependent Migdal functions. For the majority spin-band, especially, it is band-dependent, i. e.

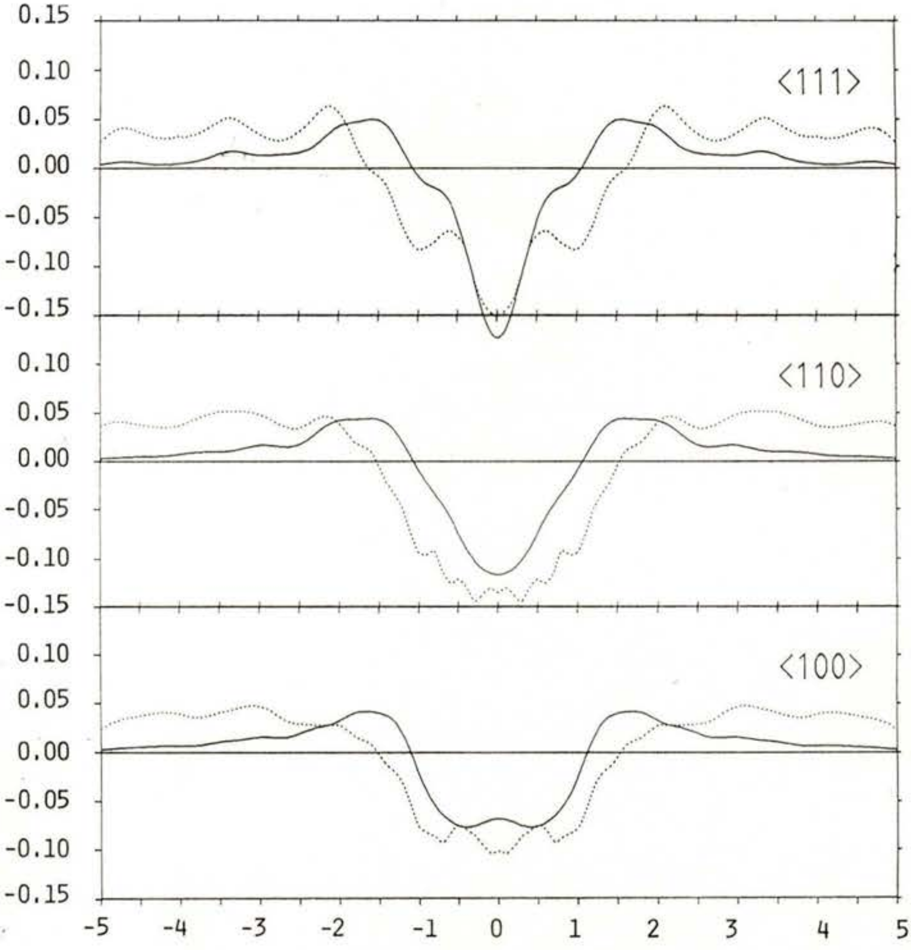

Fig. 6 — Theoretical and experimental correlation profiles along $< 100 >$, $< 110 >$ and $< 111 >$ directions for ferromagnetic iron. The experimental curves (dotted lines) are the same as those shown in figure 3. The theoretical curves (solid lines) are the theoretical correlation correction part of the Compton profiles which are determined to fit to the experimental ones best using the Migdal functions shown in figure 5.

the correlation effect for the energy region where d-bands are predominant is assumed to be small. As it is not so much rigorous, when some character-dependent Migdal functions are used the result may be improved very much. But it is a problem in the near future.

## REFERENCES

[1] BAUER, G. E. R. and SCHNEIDER, J. R., Phys. Rev. **B31**, 681 (1985).

[2] WAKOH, S. and MATSUMOTO, M., Proceedings of SAGAMORE IX, Portgal. Phys. (1988).

[3] ROLLASON, A. J. et al., private communication.

[4] ROLLASON, A. J., HOLT, R. S. and COOPER, M. J., J. Phys. F., **13**, 1807 (1983).

## CONTENTS

### FASCÍCULO 1-2

### PART I — INVITED LECTURES

# CONTENTS

## FASCÍCULO 3-4

## PART II — POSTER COMMUNICATIONS

## PART III — WORKSHOP ON DENSITY MATRICES

# AUTHOR INDEX

Composição, Impressão e Acabamento
na
*Imprensa Portuguesa* • Rua Formosa, 108-116 • 4000 PORTO

SOCIEDADE PORTUGUESA DE FÍSICA
AV. REPÚBLICA 37-4.º, 1000 LISBOA, PORTUGAL

PORTUGALIAE PHYSICA publishes articles or research notes with original results in theoretical, experimental or applied physics; invited review articles may also be included.

Manuscripts, with an abstract, may be written in English or French; they should be typewritten with two spaces and in duplicate. Figures or photographs must be presented in separate sheets and be suitable for reproduction with eventual reduction in size; captions should make the figures intelligible without reference to the text. Authors are requested to comply with the accepted codes concerning references.

There is no page charge. Author(s) will get 50 free reprints (without covers); these are to be shared among all the authors of the article. Authors interested in more reprints should say so when sending their manuscripts; quotations shall be sent with the proofs.

Subscription rates for volume 19:

3.600 Escudos (US$24) — individuals
9.000 Escudos (US$60) — libraries

PORTUGALIAE PHYSICA may also be sent on an exchange basis; we wellcome all suggestions to such effect.

All mail to be addressed to

PORTUGALIAE PHYSICA

C/O LABORATÓRIO DE FÍSICA, FACULDADE DE CIÊNCIAS
PRAÇA GOMES TEIXEIRA
4000 PORTO PORTUGAL

# PORTUGALIAE PHYSICA

VOL. 19 · NUMB 3/4 · 1988

## CONTENTS

ISSN 0048-4903

POPYA4 19 (3/4) 185-454 (1988)